12-WTP-0220

JUN 2 7 2012

The Honorable Peter S. Winokur
Chairman
Defense Nuclear Facilities Safety Board
625 Indiana Avenue, NW, Suite 700
Washington. DC 20004-2901

Dear Mr. Chairman:

TRANSMITTAL OF DEFENSE NUCLEAR FACILITIES SAFETY BOARD (DNFSB)
RECOMMENDATION 2010-2 IMPLEMENTATION PLAN (IP) DELIVERABLE 5.5.3.2

This letter provides you the deliverable responsive to Commitment 5.5.3.2 of the U.S.
Department of Energy plan to address Waste Treatment and Immobilization Plant (WTP)
Vessels Mixing Issues; IP for DNFSB 2010-2

The attached document defines the range of physical properties for waste that is anticipated to be
transferred to WTP over the mission duration. Ranges of waste physical properties include
particle size, particle density, and rheology. This assessment is based on available
characterization information, including PNNL-20646 EMSP-RPT-006, *Hanford Waste Physical
and Rheological Properties: Data and Gaps*, qualitative and quantitative uncertainties
(including sampling and analytical error) in the report and the physical capabilities of the
retrieval and transfer systems. The analysis provided is a key input to Commitment 5.5.3.1
"Initial Gap Analysis between WTP WAC and Tank Farm Sampling and Transfer Capability,"
due in December 2012.

If you have any questions, please contact me at (509) 372-2315, or your staff may contact Ben
Harp, WTP Start-up and Commissioning Integration Manager at (509) 376-1462.

Sincerely,

Scott L. Samuelson, Manager
Office of River Protection

WTP:WRW

Attachment

cc w/attachment: See page 2

cc w/attachment:
D. M. Busche, BNI
W. W. Gay, BNI
F. M. Russo, BNI
D. McDonald, Ecology
D. G. Huizenga, EM-1
J. D. Lorence, EM-41
M. B. Moury, EM-1
T. P. Mustin, EM-1
K. G. Picha, EM-1
C. S. Trummell, EM-1
A. C. Williams, EM-2.1
D. Chung, HS-1
M. N. Campagnone, HS-1.1
R. H. Lagdon, Jr., US
M. D. Johnson, WRPS
S. A. Saunders, WRPS
R. G. Skwarek, WRPS
M. G. Thien, WRPS
BNI Correspondence
WRPS Correspondence

Attachment
12-WTP-0220

**TRANSMITTAL OF DEFENSE NUCLEAR FACILITIES
SAFETY BOARD (DNFSB) RECOMMENDATION 2010-2
IMPLEMENTATION PLAN (IP) DELIVERABLE 5.5.3.2**

RPP-RPT-50642
**One System Evaluation of Waste Transferred to the Waste
Treatment Plant**

Pages: 249 (including Coversheet)

DOCUMENT RELEASE FORM

(1) Document Number: RPP-RPT-51652	(2) Revision Number: 0	(3) Effective Date: 06/25/2012

(4) Document Type: ☐ Digital Image ☒ Hard copy ☐ PDF ☐ Video	(a) Number of pages (including the DRF) or number of digital images 247 248 mw 6/26/2012

(5) Release Type:	☒ New	☐ Cancel	☐ Page Change	☐ Complete Revision

(6) Document Title: One System Evaluation of Waste Transferred to the Waste Treatment Plant

(7) Change/Release Description: Initial release of document.

(8) Change Justification: Not applicable (N/A).

(9) Associated Structure, System, and Component (SSC) and Building Number:	(a) Structure Location: N/A	(c) Building Number: N/A	(e) Project Number: N/A
	(b) System Designator: N/A	(d) Equipment ID Number (EIN): N/A	

(10) Impacted Documents:	(a) Document Type	(b) Document Number	(c) Document Revision
	N/A	N/A	N/A
	N/A	N/A	N/A
	N/A	N/A	N/A

(11) Approvals:

(a) Author (Print/Sign): J. E. Meacham	Date: 06/26/2012

(b) Reviewer (Optional, Print/Sign): M. G. Thien   Date: 6/26/12

(c) Responsible Manager (Print/Sign): FOR T. L. Sams   D.H. Shuford   David H. Shuford   Date: 26 JUNE 2012

(12) Distribution:

(a) Name	(b) MSIN	(a) Name	(b) MSIN
B. E. Wells	K7-15	S. J. Harrington	R2-58
J. S. Rodriguez	H3-20	V. C. Nguyen	B1-55
G. F. Piepel	K7-20	S. K. Cooley	K7-20
C. W. Enderlin	K7-15	D, R. Rector	K7-15
J. Chun	K6-24	A. Heredia-Langner	K7-20
R. F. Gimpel	B1-55	M. G. Thien	B1-55
T. L. Sams	R2-52	R. A. Gilbert	H6-60

Release Stamp

DATE: Jun 26, 2012   HANFORD RELEASE

(13) Clearance	(a) Cleared for Public Release ☑ Yes ☐ No	(b) Restricted Information? ☐ Yes ☑ No	(c) Restriction Type:

(14) Clearance Review (Print/Sign):	APPROVED By G. E. Bratton at 1:28 pm, Jun 26, 2012	Date:

A-6003-881 (REV 3)

RPP-RPT-51652, Rev. 0

One System Evaluation of Waste Transferred to the Waste Treatment Plant

J. E Meacham

Washington River Protection Solutions, LLC
Richland, WA 99352
U.S. Department of Energy Contract DE-AC27-08RV14800

EDT/ECN:	N/A	UC:	N/A	
Cost Center:	N/A	Charge Code:	N/A	248
B&R Code:	N/A	Total Pages:	~~248~~ ~~247~~	mw 6/26/2012

Key Words: Waste, double-shell tank, particle size, density, waste feed delivery, Hanford Tank Waste Treatment and Immobilization Plant, WTP, WFD

Abstract: This report provides a preliminary examination of the ranges of physical properties for waste that could be transferred to the Hanford Tank Waste Treatment and Immobilization Plant (WTP) using current design concepts for waste retrieval, staging, and transfer. This report is part of the U.S. Department of Energy's response to Defense Nuclear Facilities Safety Board (DNFSB) Recommendation 2010-2, "PulseJet Mixing at the Waste Treatment and Immobilization Plant, issued on December 17, 2010". This document fulfills the requirements of DNFSB Recommendation 2010-2 Implementation Plan Commitment 5.5.3.2.

DATE:

Jun 26, 2012

HANFORD
RELEASE

APPROVED
By G. E. Bratton at 1:29 pm, Jun 26, 2012

Release Approval	Date	Release Stamp

Approved For Public Release

A-6002-767 (REV 2)

One System Evaluation of Waste Transferred to the Waste Treatment Plant

J. E. Meacham
S. J. Harrington
J. S. Rodriguez
V. C. Nguyen
J. G. Reynolds

Washington River Protection Solutions, LLC

B. E. Wells
G. F. Piepel
S. K. Cooley
C. W. Enderlin
D. R. Rector
J. Chun
A. Heredia-Langner
Pacific Northwest National Laboratory

R. F. Gimpel
URS Corporation

Date Published
June 2012

Prepared for the U.S. Department of Energy
Office of River Protection

Contract No. DE-AC27-08RV14800

EXECUTIVE SUMMARY

This report provides a preliminary examination of the ranges of physical properties for waste that could be transferred to the Hanford Tank Waste Treatment and Immobilization Plant (WTP) using current design concepts for waste retrieval, staging, and transfer. This report is part of the U.S. Department of Energy's response to Defense Nuclear Facilities Safety Board (DNFSB) Recommendation 2010-2, "PulseJet Mixing at the Waste Treatment and Immobilization Plant, issued on December 17, 2010". This document fulfills the requirements of DNFSB Recommendation 2010-2 Implementation Plan Commitment 5.5.3.2. The following are included in this report:

- A review of the retrieval and transfer system.

- A description of waste undissolved solids, characterization uncertainties, and variation.

- A description of waste liquid, characterization uncertainties, and variation.

- A description of waste rheology, characterization uncertainties, and variation.

- A determination of retrieval and transfer system capabilities.

Each bullet above represents a major section in this report and a summary for each is provided below. See the list of terms for how the terms uncertainties and variation are used in this report.

WASTE FEED DELIVERY SYSTEM

The waste feed delivery (WFD) system is summarized, including initial concepts for mixer pumps, transfers pumps and a flow loop with remote sampling capability. Transfer line pipe lengths that are used in the retrieval and transfer system capabilities section are also reviewed. Mixer pump performance parameters include the ability to discharge fluid at a velocity of 59 ft/s through two opposite 6-inch nozzles. The transfer pump specifications include the ability to transfer slurries of up to 1.5 SpG with a viscosity of up to 20 cP. The transfer line lengths from the proposed feed tanks to WTP range from 3,758 to 6,917 feet and are limited to a pressure of no more than 400 psig.

UNDISOLVED SOLIDS

Mineralogy, density, and particle size for Hanford Site tank farm waste are reviewed to provide inputs for the retrieval and transfer system capabilities calculations. Specifically, the following are considered in this report:

- The densest primary particle and its largest size.

- The largest primary particle and its density based on scanning electron microscopy data.

- The largest particle observed coupled with the highest crystal density observed in AY-102 waste.

- The largest agglomerate and its density based on particle size distribution analyses.

- The largest particle observed coupled with the highest crystal density observed in AZ-101 waste.

- The hypothetical largest agglomerate and its density based on transfer equipment limitations (i.e., pump screen mesh size).

Table ES-1 summarizes the results. The most dense particle is plutonium metal (19 g/mL) and is hypothesized to be as large as 100 μm. The largest undissolved solids waste particle that might hypothetically be transferred in waste feed is 9,525 μm (⅜-inch), and would most likely have a density of an agglomerate of gibbsite (1.43 g/mL). Large agglomerates have been found in single-shell tank heel samples and some large particles will likely be in the high-activity waste feed double-shell tanks. Long-term waste storage in double-shell tanks and planned WFD operations are judged not likely to eliminate large particles and agglomerates.

Table ES-1. Particle Size and Density Combinations Used in Calculations

Particle	Diameter (μm)	Density (g/mL)
Most dense primary particle (Pu)	100	19
Largest primary particle observed by SEM (gibbsite)	200	2.4
Largest particle hypothetically combined with highest density (Bi_2O_3) in AY-102	1,268	8.9
Agglomerate based on PSD limit (gibbsite)	1,441	1.6
Largest particle hypothetically combined with highest density (Ag_2O) in AZ-101	1,441	7.14
Largest agglomerate based on pump screen mesh (gibbsite)	9,525*	1.43

Notes: *9,525 μm = ⅜-inch.

LIQUID WASTE

The available data, models, and model predictions for physical properties of the liquid phase of Hanford tank wastes are examined. The physical properties include the liquid density and liquid viscosity. Uncertainties in property data or model predictions and variation in properties are discussed and quantified. Replicate measurements of specific gravity (SpG) available for a large number of liquid-waste samples from Hanford tanks were used to quantify the measurement uncertainty.

For individual SpG measurements, the standard deviation (SD) was 0.0146 and the 95% prediction interval (PI) was ±0.0286. A data set that had complete compositions of dissolved solids, as well as measured SpGs (ranging from 0.97 to 1.58), was used to assess the performance of the liquid-density model included in Hanford Tank Waste Operations Simulator (HTWOS). The liquid density model tends to: slightly over-predict SpGs below 1.08, accurately predict for 1.08 to 1.34, over-predict for 1.34 to 1.54, and possibly under-predict above 1.54. The random uncertainty of SpG model predictions was SD = 0.0293 and 95% PI = ±0.0574 for SpG ≤ 1.27, and SD = 0.0489 and 95% PI = 0.0958 for SpG > 1.27.

A new model for liquid viscosity as a function of temperature and liquid density was developed to improve some aspects of the model used in PNNL-20646, *Hanford Waste Physical and Rheological Properties: Data and Gaps*. The new liquid-viscosity model is still subject to considerable uncertainty, because liquid density is an imperfect representative for the effects of dissolved solids on liquid viscosity. The data used to develop the model did not have complete compositions of dissolved solids, so it was not possible to develop a model as a function of dissolved solids composition. The models for liquid density and viscosity were applied to waste

feed batches from the HTWOS run of the Baseline Case in ORP-11242. For batches dated from 5/31/2018 to 4/24/2039 (prior to the end-of-mission activities), the model-predicted values ranged from 1.14 to 1.37 kg/L for liquid density and 2.44 to 8.00 cP for liquid viscosity. Accounting for model uncertainties, the ranges are 1.08 to 1.47 kg/L for liquid density and 0.80 to 13.54 cP for liquid viscosity.

RHEOLOGY

The available rheology data were reviewed and separate plots were produced for each tank with data. For the sludge waste (i.e., undissolved solids), viscosity ranged from near 1 cP at 0.1-wt% solids to slightly more than 100 cP at 18-wt% solids. Yield stress data ranged from near 0.1 Pa at 1-wt% solids to near 80 Pa at 18-wt% solids. Yield stress data were fit with a power law function for various temperature ranges, and viscosity data were fit with an exponential function for various temperature ranges. These fits were then used to predict yield stress and viscosity at 10-wt% undissolved solids through interpolation or extrapolation. Except for one outlier (C-109), yield stress predictions at 10-wt% undissolved solids fell within a range of less than 0.01 to 12 Pa. The tank data suggest some feed batches would exceed a yield stress of 1 Pa. Similarly, viscosity predictions fell within a range (except for the same C-109 outlier) of 0.42 to 7.1 cP.

A literature review for the potential effects from waste mixing and blending suggests a complicated relationship between particles sizes, solids fraction, particle and liquid densities, and repulsive and attractive forces. No good predictive tool exists for estimating yield stress and viscosity in mixed/blended wastes. Waste feed samples taken from the flow loop with the remote sampler will be tested for rheological properties. There will be about 600 mixed and blended HLW feed batches during waste feed delivery, and current data on blended waste is limited. It is likely that the ranges of yield stress and viscosity for all feed batches will be greater than the data ranges presented in this document.
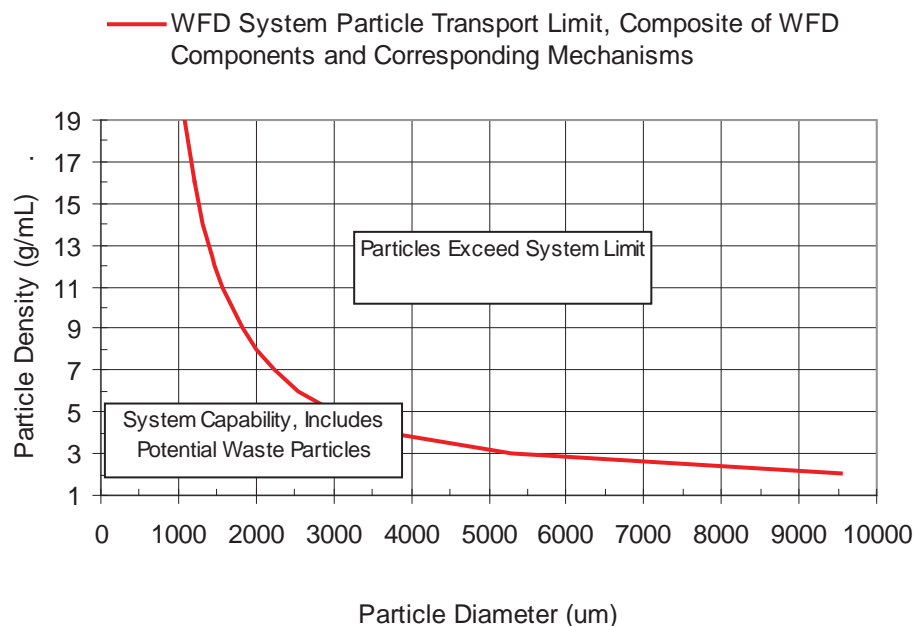
RETRIEVAL AND TRANSFER SYSTEM CAPABILTIES

Retrieval and transfer system capabilities were evaluated using simple models from the literature. The evaluation identified the limits of performance of the WFD system, including the mixer pumps and the vertical and horizontal legs of the transfer pipeline, with respect to undissolved solids particle size and density. Where possible, a simple model approach was compared to full-scale process data and scaled test data, and reasonable agreement was demonstrated.

Waste feed delivery system components, analyzed for limits of performance with respect to the particle size and density of undissolved solids include:

- Jet mobilization and transport of particles to the transfer pump.

- Particle entrainment into the transfer pump.

- Particle motion in the vertical transfer pipeline.

- Particle transfer in the horizontal pipeline.

- The WFD system transport limit capabilities are determined for waste properties established by characterization of the Hanford waste and the evaluated uncertainties of that characterization data. The limits of performance of the WFD system, as shown in Figure ES-1, exceed the identified potential limiting waste particles, which are particles at the density and size that might occur in the waste. That is, transport of the postulated 100-μm 19 g/mL plutonium metal particle from a DST to WTP is possible. Similarly, transport of the postulated large 9,525-μm 1.43 g/mL gibbsite agglomerate is also possible. The limiting component and associated mechanism is the transport of particulate via the jet mixer pump to the transfer pump inlet assuming that transfer in the horizontal pipeline can occur via sliding particulate. The influence of non-Newtonian yield stress fluid properties (Bingham plastic modeled fluid) on the evaluations is considered. While the influence of non-Newtonian fluid properties may increase the capability of one or more components in the WFD system, the potential limiting waste particles are always exceeded by the limits of performance with a Newtonian fluid. Thus the Newtonian fluid limits of performance provide a suitable upper bound for the WFD system capabilities. Because the identified WFD system limit exceeded the potential limiting waste particles, other potential less-limiting mechanisms for particle transport that exist were not considered as relevant.

Figure ES-1. WFD System Particle Transport Limit. Representative Bounding Liquid (1.37 g/mL, 14 cP), Limiting Pipeline Length and Pressure, 0.99 miles, 400 psig

CONTENTS

APPENDICES

FIGURES

TABLES

LIST OF TERMS

Terms

Bias is the difference in the long-term mean value of estimates of a quantity and the true, unknown value of the quantity.

Random uncertainty occurs when repeated observations (e.g., measurements) of a quantity differ because of uncontrollable, random effects in the observation process.

Systematic uncertainty occurs when estimates of a quantity (e.g., measurements or model predictions) has a long-term mean value that differs from the true, unknown value of the quantity.

Uncertainty refers to the lack of knowledge of the true value of a quantity. Uncertainty can be systematic or random.

Variation or Variability refers to differences in the true value of a quantity over time and/or space and is distinct from uncertainty.

Abbreviations and Acronyms (2 pages)

Ar	Archimedes Number
CUF	Cell-Unit Filter
DNFSB	Defense Nuclear Facilities Safety Board
DOE	U.S. Department of Energy
DLVO	Derjaguin-Landau-Verwey-Overbeek
DQO	Data Quality Objectives
DST	Double-Shell Tank
DWP	Dangerous Waste Permit
ECR	Effective Cleaning Radius
EDS	Energy Dispersive Spectroscopy
ENRAF	Enraf-Nonius Series 854
GLM	Generalized Linear Models
gpm	gallons per minute
HLW	High-Level Waste
HTWOS	Hanford Tank Waste Operations Simulator
ICD	Interface Control Document
IEP	Isoelectric Point
IHLW	Immobilized High-Level Waste
LAW	Low-Activity Waste
OLS	Ordinary Least Squares
NPS	nominal pipe size
PFP	Plutonium Finishing Plant
PI	Prediction Interval
PLM	Polarized Light Microscopy
PSD	Particle Size Distribution
PUREX	Plutonium-Uranium Extraction
RCSTS	Replacement Cross-Site Transfer System

Re	Reynolds Number
REDOX	Reduction-Oxidation
RMS	Root mean square
RPP	River Protection Project
RSD	Relative Standard Deviation
SD	Standard Deviation
SE	Standard Error
SEI	Scanning Electron Imaging
SEM	Scanning Electron Microscopy
SpG	Specific Gravity
SS	Stainless Steel
SSMD	Small-Scale Mixing Demonstration
SSP	Suspended Solids Profiler
SST	Single-Shell Tank
TBP	Tri-Butyl Phosphate
TEM	Transmission Electron Microscopy
TRU	Transuranic
TWINS	Tank Waste Information Network System
UDS	Undissolved Solids
vol%	Percent By Volume
WAC	Waste Acceptance Criteria
WFD	Waste Feed Delivery
WRSS	Waste Retrieval Sluicing System
wt%	Percent by Weight
WTP	Hanford Tank Waste Treatment and Immobilization Plant
XRD	X-Ray Diffraction
ZPC	Zero Point of Charge

Units

cm	centimeter
cP	centipoise
ft	foot
g	gram
gal	gallon
hp	horsepower
J	Joule
kg	kilogram
L	liter
m	meter
mL	milliliter
mm	millimeter
min	minute
Pa	Pascal
psi	pounds per square inch
psig	pounds per square inch gage
s	second
Sv	sievert

1.0   INTRODUCTION

1.1   PURPOSE

This document was written to satisfy Defense Nuclear Facilities Safety Board (DNFSB) Commitment 5.5.3.2 "Evaluation of Waste Transferred to WTP" contained in the *Department of Energy Plan to Address Waste Treatment and Immobilization Plant Vessel Mixing Issues*. The analysis provided here also supports Commitment 5.5.3.1 "Initial Gap Analysis between WTP WAC and Tank Farm Sampling and Transfer Capability."

This report is a preliminary examination of the range of physical properties for waste that could be transferred to the Hanford Tank Waste Treatment and Immobilization Plant (WTP) using current design concepts for waste retrieval, staging, and transfer. Models from the literature and calculations are used to determine the largest and densest, undissolved solid particles that the Waste Feed Delivery (WFD) system might hypothetically deliver to WTP.

1.2   SCOPE

This document examines the WFD system as currently envisioned in the three volumes of the RPP-40149, *Integrated Waste Feed Delivery Plan* and does not address how WFD will meet Waste Acceptance Criteria (WAC) or Interface Control Document (ICD) limits (24590-WTP-ICD-MG-01-019, "ICD 19, Interface Control Document for Waste Feed").

In cases where methods exist and have been applied to predict physical properties of waste batches to be transferred to WTP, the data, uncertainties, and variation[1] over the WTP mission are presented (including the means and methods for determining the uncertainties). In other cases, the data, uncertainties, and variation of physical properties of waste samples from single-shell tanks (SST) and double-shell tanks (DST) are presented.

A limits-of-performance approach was used to provide upper bounds on waste properties. Conclusions should not be interpreted as expectations during day-to-day WFD operations or that physical property extremes will occur. In particular, the analyses provided here are not meant to imply that all large, dense particles will be delivered to WTP.

---

[1] The distinct meanings of "uncertainty" and "variation" used in this report are given in the Terms area at the beginning of the report. The term "uncertainties" used in DNFSB Commitment 5.5.3.2 was interpreted as referring to both uncertainties and variation as defined and discussed in this report.

1.3   REPORT ORGANIZATION

Section 1.0 describes report objectives and scope, as well as an overview of the report contents. Section 2.0 provides background information and context for the report objectives. The WFD infrastructure and equipment are summarized in Section 3.0. Data, uncertainties, and variation of the properties of the waste to be transported are examined in Section 4.0 (solids), Section 5.0 (liquids), and Section 6.0 (slurry). This information is then used in the preliminary, simplified assessment of WFD capabilities in Section 7.0.

The document is organized in approximately the same order as the requirements in Commitment 5.5.3.2 (see Section 2.4). After the introduction and background sections, Section 3.0 describes the WFD system to address the requirement "A definition of the retrieval and transfer system" listed in Commitment 5.5.3.2. Sections 4.0 through 6.0 describe and analyze waste properties to address the requirement "A description of the means and method for determining the standard uncertainties in characterization data that support the physical capabilities of the retrieval and transfer system." Section 7.0 provides an upper bound on particle size, particle density, and rheology to address the requirement "A determination of the performance capabilities of the retrieval and transfer system."

For the work in this report, the term "uncertainties" was interpreted as including both uncertainties and variation. Where possible, uncertainties are quantified. The available data did not always allow quantitation of uncertainties; therefore, data are assessed qualitatively in some sections. Table 1-1 shows the sections where uncertainties are analyzed and whether the analysis is quantitative, qualitative or both.

Table 1-1. Report Sections Showing Uncertainty Analyses

Data Examined	Report Section Number(s)	Method(s) for Determining Uncertainty
Mineralogy and density	4.2.2 and 4.2.3	Quantitative and qualitative
Particle size and shape	4.3.2 and 4.3.3	Qualitative
Specific gravity (tank data)	5.1.2 and 5.1.3	Quantitative
Liquid density predictions (feed batches)	5.2.3, 5.2.4 and 5.2.5	Quantitative
Liquid waste viscosity	5.3.2 and 5.3.3	Quantitative
Liquid waste viscosity predictions	5.4.2 and 5.4.3	Quantitative
Slurry rheology	6.2.2, 6.2.3 and 6.3.3	Qualitative

2.0 BACKGROUND

2.1 TANK FARMS

Radioactive and chemical wastes from nuclear fuel processing are stored in large underground storage tanks at the Hanford Site. There are 149 older SSTs built in the 1940's through 1960's and 28 newer DSTs built in the 1970's and 1980's. The SSTs contain little drainable liquid waste and the Tank Operations Contractor is continuing a program of moving solid wastes from SSTs to DSTs and preparing for WFD. Some DSTs store only liquid waste, while others contain both liquid and a layer of settled solids. Solid wastes can be divided into saltcake and sludge. Saltcake is mostly soluble sodium nitrate and nitrite salts with some interstitial liquid consisting of concentrated salt solutions. Sludge is mostly low solubility aluminum and iron compounds with relatively dilute interstitial liquid. The predominant radioisotope in low-activity waste (LAW) feed is cesium-137 (^{137}Cs), while the predominant radioisotope in the high-activity waste (HLW) feed is strontium-90 (^{90}Sr).

Waste feed from the DSTs must be delivered to the WTP in a manner that assures continuous WTP operations over the life cycle of the treatment mission. The DSTs are used for various roles throughout the mission and the role performed by a DST may change over time. A key challenge in supporting the mission is to manage the use of the DSTs and the rest of the WFD system efficiently. This includes the following:

- Safely storing the existing tank waste.

- Receiving, storing, and transferring wastes from sources outside of the WFD system (e.g., the 222-S Laboratory and the SSTs).

- Staging feed and receiving concentrated waste from the 242-A Evaporator.

- Incidental and intentional blending or segregation, staging and delivering solids and supernatant tank waste to the WTP.

- Accepting emergency returns from the WTP, if necessary.

Low-activity waste feed is staged in DSTs with provisions to minimize solids transfer. Specifically, LAW waste is staged in a DST with the mixing system off to allow solids settling. Liquid waste is decanted from an elevation above the settled solids layer to minimize solids entrainment. High-level waste feed is a slurry of liquid and insoluble solids. The planned configuration and operation of the WFD system has been established to perform these functions within the DST system (RPP-40149).

2.2   WASTE TREATMENT PLANT

The WTP is being designed and built to process and vitrify highly radioactive and mixed hazardous waste stored in the Hanford Site underground storage tanks. The scope of work in the WTP Contract is to design, construct, commission, and complete the transition of the plant to the long-term operating contractor to process the wastes that are stored in the underground tanks.

There are three facilities in WTP for processing waste feed from the tank farms. The received feed is separated into LAW and HLW fractions in the pretreatment facility. Following pretreatment, the HLW fraction is transferred to the HLW facility, combined with glass former material, and sent to high temperature melters for formation of HLW glass product. The LAW fraction is transferred to the LAW facility, combined with glass former material, and sent to high temperature melters for formation of the LAW glass product.

2.3   WASTE ACCEPTANCE CRITERIA

Waste Acceptance Criteria were developed through the interface control process to ensure that feed transfer and receipt will not exceed WTP plant design, safety, and processing limits. An initial Data Quality Objectives (DQO) document was written (Initial Data Quality Objectives for WTP Feed Acceptance Criteria, 24590-WTP-RPT-MGT-11-014) based on parameters identified in the following documents:

- Waste Treatment and Immobilization Plant (WTP) Contract, Contract No. DE AC27 01RV14136 (Contract).

- Interface Control Document for Waste Feed, 24590-WTP-ICD-MG-01-019, Rev. 5 (ICD-19).

- Regulatory Data Quality Objectives Optimization Report, 24590-WTP-RPT-MGT-04-001, Rev. 0 (RDQO).

- IHLW Waste Form Compliance Plan for the Hanford Tank Waste Treatment and Immobilization Plant, 24590-HLW-PL-RT-07-0001, Rev. 3 (IHLW).

- Final Waste Treatment and Immobilization Plant Dangerous Waste Permit, Ecology, as amended through the most recent version, Washington Department of Ecology, Olympia, Washington (DWP).

Changes are planned to the WAC DQO as additional information is identified. Table 2-1shows a partial list of the initial WAC at the release of this document. Density, solids content, viscosity, and yield stress are discussed further in this document.

Table 2-1. Waste Acceptance Criteria Documented in the Initial DQO for WTP Feed Acceptance Criteria (24590-WTP-RPT-MGT-11-014)

Description	LAW Feed Action Limit	HLW Feed Action Limit	Requirement Source			
			DWP	RDQO	ICD-19	Contract
Bulk density	< 1.46 kg/L	< 1.5 kg/L	---	---	X	---
pH	> 7	> 7	X	---	X	---
Maximum solids wt.	≤ 3.8 wt%	N/A	---	---	X	---
Maximum solids conc.	NA	≤ 200 g/L	---	---	X	X
Feed unit dose	< 1,500 Sv/L	< 270 Sv/g (dry basis)	---	---	X	---
Viscosity (consistency)	N/A	< 10 cP	---	---	X	---
Yield stress	N/A	< 1.0 Pa	---	---	X	---
Ammonia	< 0.04 M	< 0.04 M	---	X	X	X
Separable organic	Non-Visible	Non-Visible	---	---	X	---
PCBs	< 50 ppm	< 50 ppm	X	---	X	---
Total organic carbon	< 10 wt%	< 10 wt%	X	---	---	X
Pu to metals ratio	< 6.20 g/kg	< 6.20 g/kg	---	---	X	---
$U_{Fissile}$ to U_{Total} ratio	< 8.4 g/kg	< 8.4 g/kg	---	---	X	---
Pu conc of liquids	< 0.013 g/L	< 0.013 g/L	---	---	X	---
Na molarity	< 10 mol/L	< 10 mol/L	---	---	---	X
Hydrogen generation	< 3.7E-07 mol/L-hr (at 120°F)	< 2.1E-06 mol/L-hr (at 150°F)	---	---	X	---
Feed temperature	< 120 °F	< 150°F	---	---	X	---
Critical velocity	N/A	≤ 4.0 ft/s	---	---	X	---
Temperature change	± 20°C	± 20°C	X	---	---	---

Notes: N/A= not applicable

2.4 DEFENSE NUCLEAR FACILITES SAFETY BOARD RECOMMENDATION 2010-2

On December 17, 2010, the DNFSB issued Recommendation 2010-2, "PulseJet Mixing at the Waste Treatment and Immobilization Plant", which identified technical and safety issues related to performance of the pulsejet mixing and transfer systems in the WTP. The Secretary of Energy accepted Recommendation 2010-2 on February 10, 2011, with clarifications to ensure that the U.S. Department of Energy (DOE) was clear on the scope of commitments to be addressed in the DOE's implementation plan. On May 20, 2011, the DNFSB notified DOE that the initial communication was a partial rejection of the recommendation and reaffirmed the primary elements of the recommendation. On November 10, 2011 DOE issued the Implementation Plan that responds to DNFSB Recommendation 2010-2.

Recommendation 2010-2 provided seven sub-recommendations to address technical concerns and safety issues. This report partially addresses the fifth sub-recommendation, which reads as follows:

> "Define the impact on the waste retrieval, feed delivery and feed certification processes due to any limitations of the WTP mixing and transfer systems and demonstrate the ability to obtain adequately representative samples from the waste feed tanks to ensure the WTP WAC can be reliably enforced."

The DNFSB Recommendation 2010-2 implementation plan has 10 commitments under sub-recommendation 5. Specifically, this report was written to satisfy the second commitment in sub-recommendation 5 (Commitment 5.5.3.2) which reads as follows:

> "The range of physical properties for waste that is anticipated to be transferred to WTP over the mission will be defined. This assessment will be based on available characterization information including PNNL-20646 EMSP-RPT-006, uncertainties (including sampling and analytical error) in the report and the physical capabilities of the retrieval and transfer systems. Based on available information this assessment will define the preliminary range of physical properties including particle size, particle density, and rheology for waste anticipated to be delivered to WTP with the current feed staging and transfer concepts.

> The evaluation will include:

> - A definition of the retrieval and transfer system.
> - A description of the means and method for determining the standard uncertainties in characterization data that support the physical capabilities of the retrieval and transfer system.
> - A determination of the performance capabilities of the retrieval and transfer system."

For the work in this report, the term "uncertainties" above was interpreted as including both uncertainties and variation, as defined in the List of Terms.

3.0   DEFINITION OF THE RETRIEVAL AND TRANSFER SYSTEM

The WFD system includes DSTs, flow loops, mixer pumps, transfer pumps, and transfer lines. The purpose of Section 3.0 is to provide sufficient detail about the WFD system to support the preliminary calculations in Section 7.0. Section 3.1 reviews the DSTs currently selected to feed LAW and HLW to WTP. Section 3.2 summarizes the sampling loop that will be used for feed testing to ensure WAC compliance. Section 3.3 describes the mixer pumps that will produce slurry DST waste. Section 3.4 reviews the transfer pumps that transport slurries from the DSTs. Section 3.5 describes the transfer lines to be used during WFD. The complete WFD system contains many more components then the truncated list here (e.g., 242-A evaporator, pits, diversion boxes, jumpers, etc.), but only detailed information on mixer pumps, transfer pumps and transfer lines is needed for the simplified preliminary calculations in Section 7.

The WFD system components are in various stages of design, fabrication, upgrade, and procurement that are subject to change as information is gathered and projects mature. The preliminary assessment presented here represents a snapshot in time. Detailed WFD descriptions are provided in three volumes: RPP-40149-VOL1, *Integrated Waste Feed Delivery Plan, Volume 1 - Process Strategy*, RPP-40149-VOL2, *Integrated Waste Feed Delivery Plan, Volume 2 - Campaign Plan*, and RPP-40149-VOL3, *Integrated Waste Feed Delivery Plan, Volume 3 - Project Plan*, which are periodically updated.

3.1   DOUBLE-SHELL TANKS

3.1.1   Hot Commissioning Feed Tank

Originally, Tank C-106 was selected by the Tank Waste Remediation System Privatization Contractor for the HLW commissioning feed (WHC-SD-WM-ES-370, *Phase I High-Level Waste Pretreatment and Feed Staging Plan*) as the first HLW feed tank. When Tank C-106 was retrieved into Tank AY-102, AY-102 tank took over as the designated HLW commissioning tank. Iterations to determine the initial LAW hot commissioning feed source eventually settled on the supernatant in Tank AP-101. To create more DST space for SST retrievals, a baseline change request was prepared in October 2003 to consolidate DST waste. At the approval and direction of the U.S. DOE, Tank AP-101 was consolidated with the waste in Tank AY-102. This permitted Tank AY-102 to become the sole source for HLW and LAW hot commissioning feed, which is detailed in HNF-SD-WM-SP-012, *Tank Farm Contractor Operation and Utilization Plan*.

The WFD strategy is to transfer the waste currently in Tank AY-102 to the WTP to support hot commissioning activities. Some evaporation is anticipated in AY-102 during interim storage, so dilution water will be added to the contents as needed to bring sodium and solids concentrations to proper levels prior to hot commissioning. The waste staged in Tank AY-102 will be mixed and sampled for acceptance based on the WTP WAC for HLW and LAW feed, respectively. A process control sample will be taken to confirm sodium and solids concentrations after

completing the required time for sampling and characterization, and immediately before delivery. A portion of the AY-102 supernatant will be delivered to the WTP LAW feed receipt tanks. The remaining waste in Tank AY-102 will be mixed, a process control sample taken to confirm sodium and solids concentrations, and multiple HLW batches will be transferred to the WTP HLW feed receipt tank.

3.1.2   Low-Activity Waste Feed Delivery

Tanks AP-102, AP-104, AP-106, and AP-108 are the early candidates for LAW feed tanks because of a direct path to the dedicated LAW feed line. Waste compatibility and process control samples are taken prior to filling the LAW feed tank to generate a waste compatibility assessment and to assist in developing the process control plan for the identified LAW feed tank. Additional process control samples may be taken during and after process control plan development to identify if the plan has adequately addressed the process controls necessary for delivering the designated LAW feed.

After the LAW campaign is fully prepared, the LAW feed tank will undergo a prescribed hold time of 30 days to allow for solids settling, sampling, and an additional 180 days for waste characterization to confirm the feed meets the WAC. A pre-transfer flush of water will precede the designated waste transfer; this preheats the transfer line and helps prevent solids precipitation during the waste transfer. The LAW feed campaign is then transferred to WTP LAW feed receipt tanks.

After a transfer is complete, the transfer line will be flushed to clear it of any remaining waste. The received LAW may then be transferred by WTP to either the feed evaporator process or ultrafiltration process system, depending on the SpG and weight percent (wt%) solids in the waste. This process is then repeated for each LAW campaign, with a goal of ensuring that the steps required for the next LAW campaign to be transferred are completed prior to WTP requesting the feed.

3.1.3   High-Level Waste Feed Delivery

Tanks AN-101, AN-102, AN-103, AN-105, AN-106, AW-103, AW-104, AW-105, AY-101, AY-102, AZ-101, and AZ-102 are the preliminary candidates for HLW feed tanks. The general strategy for delivering HLW feed to the WTP is expected to proceed as follows. A tank operating as a HLW feed tank is identified to receive staged waste, from one or more tanks operating as HLW feed staging tanks, for delivery to the HLW receipt tank in WTP. Waste compatibility and process control samples are taken prior to filling the HLW feed tank to generate a waste compatibility assessment, and to assist in the development of the process control plan for the identified HLW feed tank. Additional process control samples may be taken during and after the process control plan is developed to identify if the plan has adequately addressed the process controls necessary for delivering the designated HLW feed.

After the feed is fully prepared, the HLW feed tank undergoes a prescribed hold time of 30 days for mixing, sampling, and an additional 180 days for waste characterization to confirm the feed meets the WAC. A pre-transfer flush of water precedes the designated waste transfer; this

preheats the transfer line and helps prevent solids precipitation during the waste transfer. The HLW feed campaign is then transferred to WTP HLW feed receipt in multiple batches.

The HLW feed tank is mixed prior to each HLW batch delivery to the WTP and the transfer line is flushed to clear it of any remaining waste following each HLW batch transfer. The received HLW feed is transferred by WTP to system UFP until the HLW feed receipt vessel is ready to receive an additional transfer. This process is then repeated for each HLW campaign, with a goal of ensuring that the steps required for the next campaign of HLW batches to be transferred are completed prior to WTP requesting the feed. Figure 3-1 summarizes the preliminary plan for DSTs. The special waste handling in the legend represents those tanks that require mitigation because of flammable gas concerns before the DST space can be fully utilized (RPP-40149VOL1).

Figure 3-1. Double-Shell Tank Usage for Waste Feed Delivery
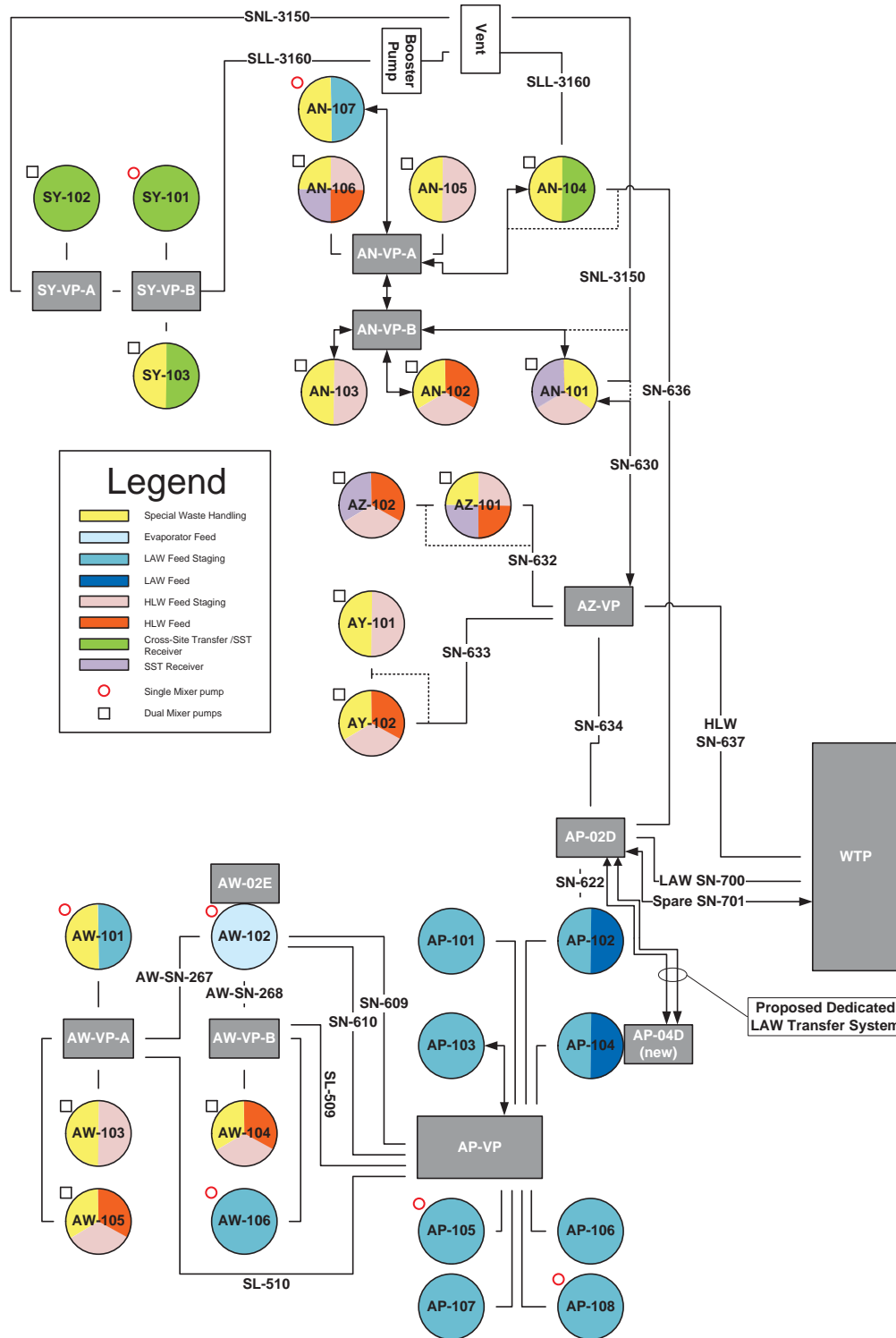
3.2   FLOW LOOP AND REMOTE SAMPLING

High-activity waste will need to be sampled, tested, and accepted to the WTP WAC standards. Current sampling methods are core and grab sampling in a static DST. These methods likely will not collect slurry samples representative of WFD. A flow loop with remote sampling is being developed to include slurry-sampling capability. Figure 3-2 shows the envisioned mixing and sample loop systems.

Figure 3-2. Waste Feed Acceptance Flow Loop and Remote Sampler System
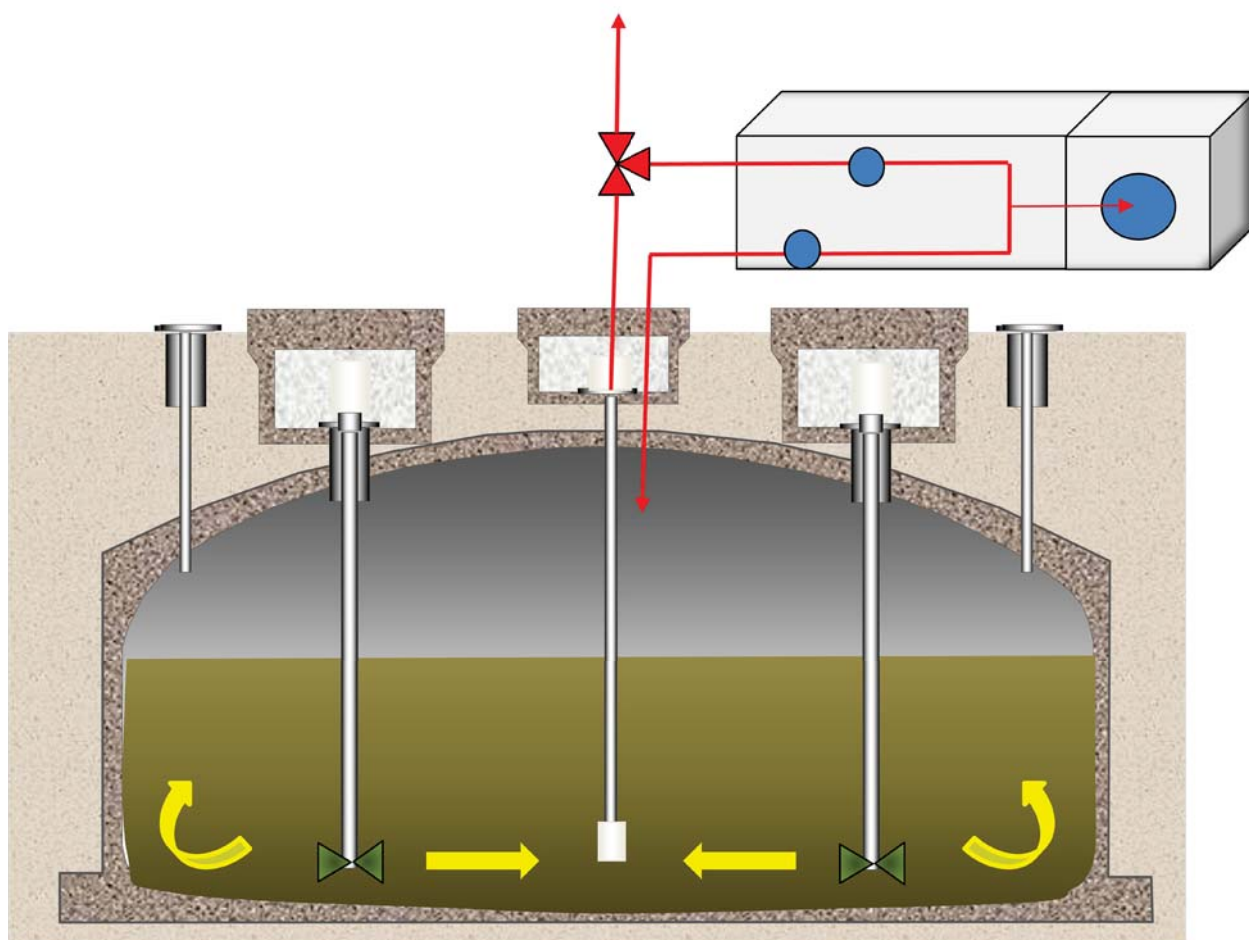
The waste feed flow loop/remote sampler system will include an instrumented spool piece (pulse Echo system) for measuring critical velocity and a remote sampler (Isolok®[2] Sampler) for sample collection. The flow loop will allow the contents of each feed tank to be transferred through the sampler and critical velocity measurement device and returned back to the same tank. HLW slurry samples will be collected and critical velocity measurements taken in real time while both mixer and transfer pumps are operating. The system will provide for safely collecting representative HLW slurry samples for laboratory analysis. Data collection, sample

---

[2] Isolok® is a registered trademark of the Sentry Equipment Corporation, Yorkville, Illinois.

collection, and handling will be performed remotely except for loading clean sample bottles and securing lids on transportation casks.

3.3   DOUBLE-SHELL TANK MIXER PUMPS

3.3.1   Mixer Pump Procurement Specifications

Mixer pumps are designed to operate in the high-dose radioactive process fluid for a minimum of 10,000 hours of intermittent operation at 100% rated capacity with minimal maintenance. Materials used in the design were selected to survive 10 years of total exposure in the waste tank environment described and summarized in Table 3-1 (RPP-SPEC-43262, *Procurement Specification for Hanford Double-Shell Tank Submersible Mixer Pumps*).

Table 3-1. Mixer Pump Design Specifications

Parameter	Minimum	Rated	Maximum
Operating (process fluid) temperature	50°F	---	190°F
Outside ambient temperature	-25°F	---	115°F
Process fluid specific gravity	1.0	1.5	2.0
Process fluid viscosity	1.0 cP	20 cP	50 cP
pH	7	---	14
Solids mass loading	0 g/L	---	300 g/L
Solids volume fraction	0	---	0.11
Particle size	1 μm	95% < 50 μm	4,000 μm
Yield stress	0 Pa	---	16 Pa
Miller number (ASTM G75)	---	---	100
Radiation dose rate in process fluid	---	1,000 Rad/hr	---
Radiation dose rate above mounting foundation	---	0.0005 Rad/hr	---
Elevation	---	650 feet above sea level	

3.3.2   Mixer Pump Placement

The conceptual mixer pump arrangement in a DST is shown in Figure 3-3 and Figure 3-4. At the riser opening, the column is 30 inches in diameter to prevent any potential interference as the turntable rotates the column assembly. The maximum diameter on the mixer pump is 32 inches, which should provide sufficient clearance as it passes through the riser.

Figure 3-3. Mixer Pump Conceptual Arrangement (Pump Mounted at Grade)
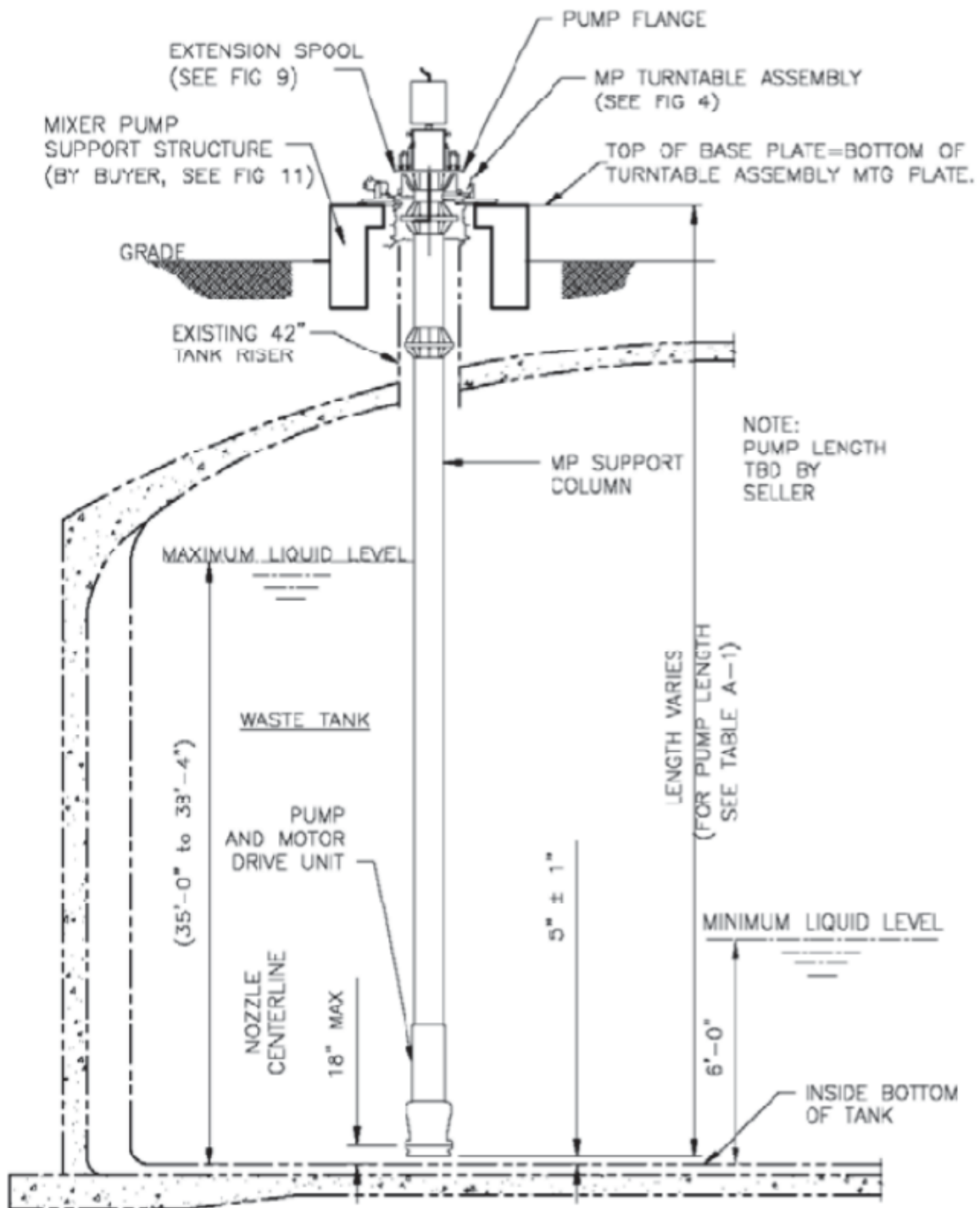
Figure 3-4. Mixer Pump Conceptual Arrangement (Pump Mounted on Pit)
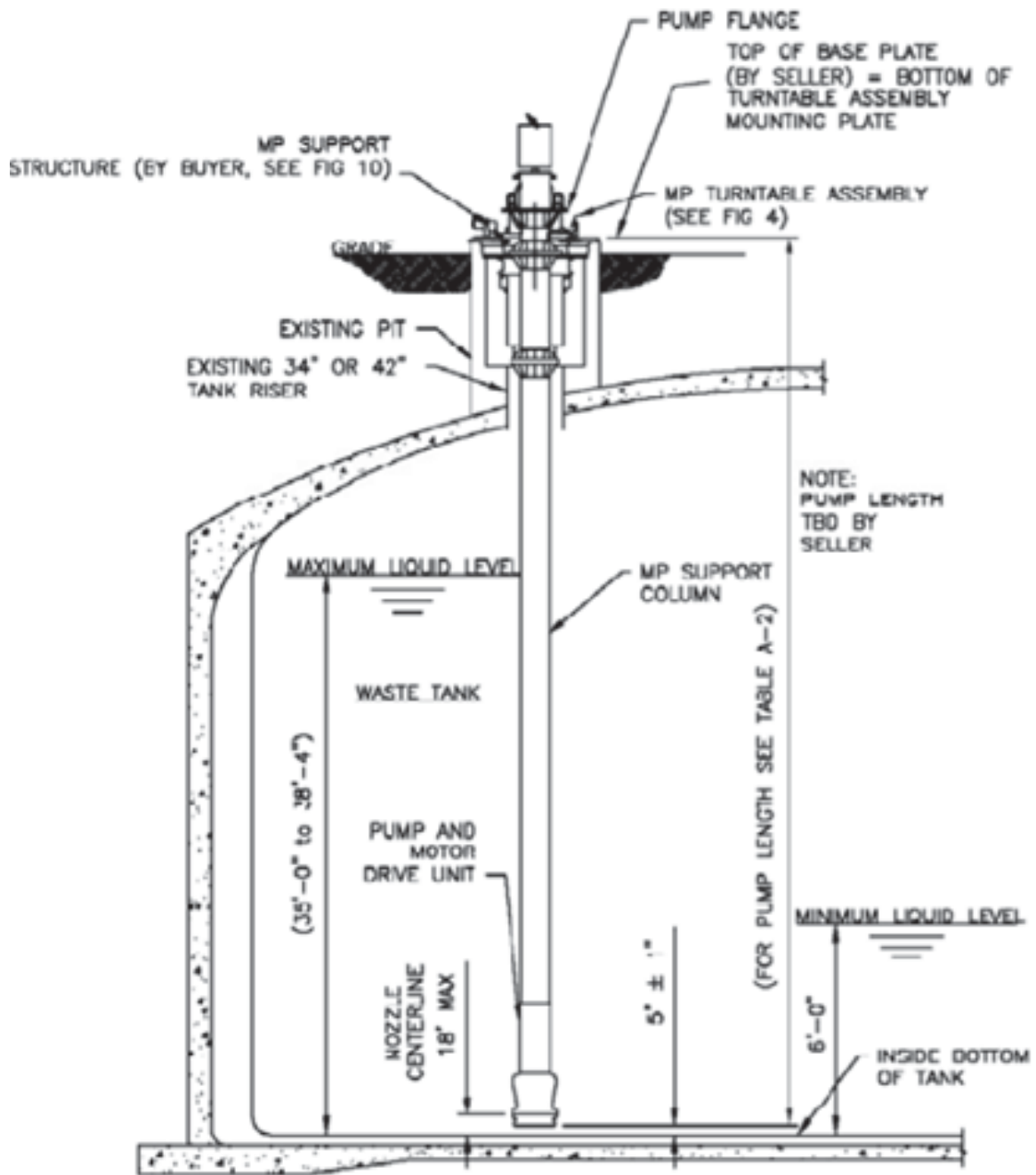
3.3.3 Mixer Pump Operation

Mixer pumps are designed to operate with a variable frequency drive so that the operating speed can be adjusted to suit DST conditions. The rated design point (nozzle discharge coefficient of 29.4 ft^2/s, process fluid SpG, and viscosity of 1.5 and 20 cP) is 1,035 RPM. The primary geometric and performance parameters are summarized in Table 3-2 (RPP-SPEC-43262).

Table 3-2. Mixer Pump Performance Parameters

Parameter	Units	Value
Suction geometry	---	Bottom
Maximum pump diameter	inch	32
Nozzle diameter	inch	6.0
Nozzle discharge height	inch	18.0
U_0D	ft^2/s	29.5
U_0 (average at nozzle exit)	ft/s	59
Nozzle area	$inch^2$	28.3
Nozzle flowrate	gal/min	5,200
Pump head	ft	54
Speed	rpm	1,035
Impeller head	ft	63

The mixer pumps are designed to be suspended vertically and submersed in the process fluid. The process fluid is drawn through an inlet suction screen, vertically upward into a suction barrel and into the impeller (Figure 3-5). The inlet screen is designed to prevent large objects from entering and potentially damaging the pump internals, as well as to control vortex formation at the pump inlet. The process fluid passes through the impeller into an annular space that accommodates both diffuser vanes and channel vanes that guide the process fluid to the two nozzles that are located below the impeller.

Figure 3-5. Illustration of Mixer Pump Internal Circulation
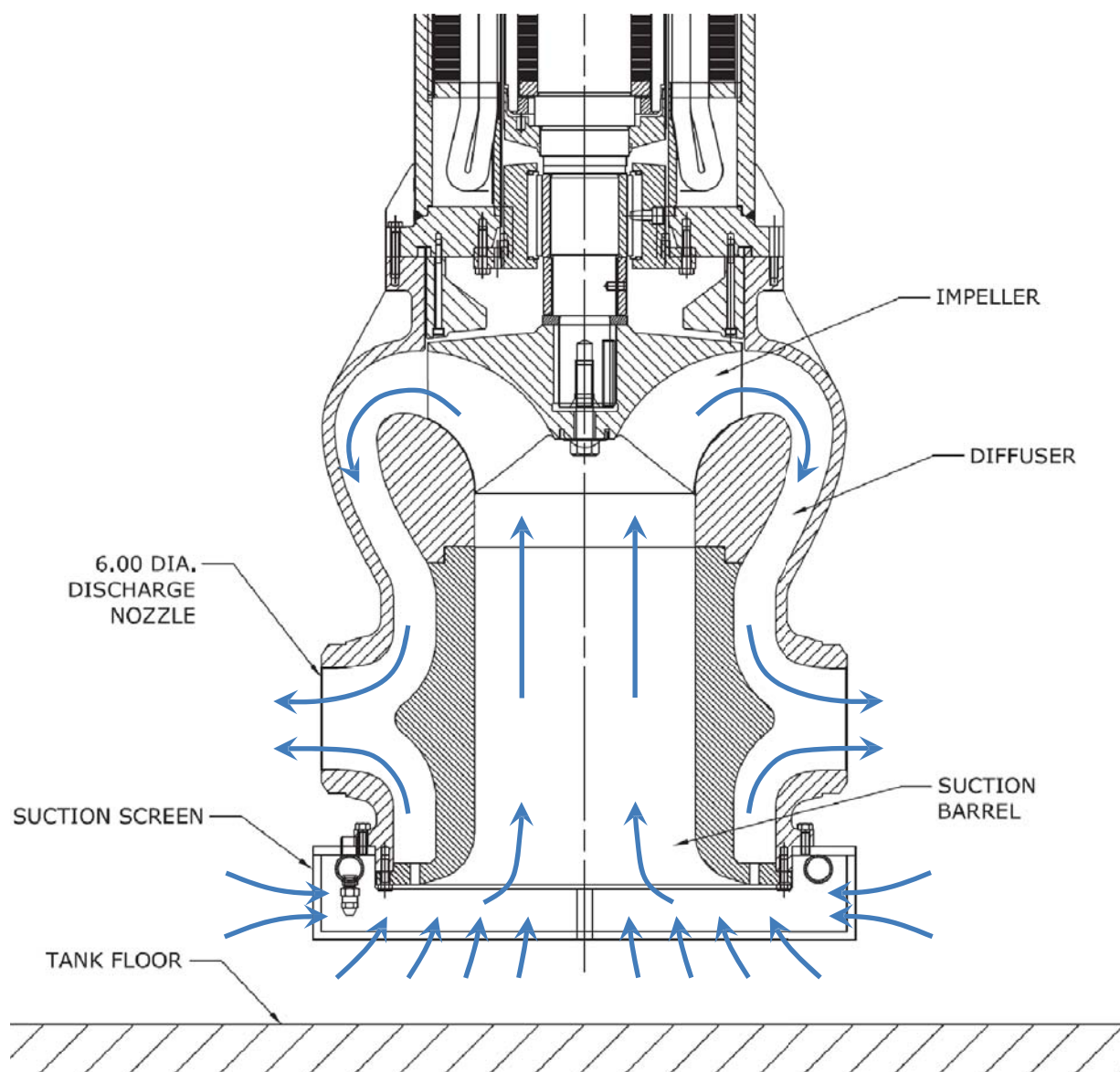
3.4   TRANSFER PUMPS

3.4.1   Transfer Pump Procurement Specifications

Procurement specifications (*Design of Hanford Submersible Transfer Pump*, Requisition 244607) for these pumps specify a capacity of transferring slurry (see Table 3-3) a vertical distance of approximately 80 feet, through a 3-inch nominal pipe size (NPS), schedule 40, carbon or stainless steel pipe at a minimum flow rate of 90 gal/min (4 ft/s) and with a maximum flow rate of 140 gal/min (6.1 ft/sec). See RPP-5346, *Waste Feed Delivery Transfer System Analysis*. The diameter of the suction inlet will be approximately 2.40 (± 0.1) inches.

The pump will also include a suction intake-screen sized to prevent particles greater than ⅜-inches from entering the pump. Electrical horsepower is constrained by a 150 hp adjustable frequency drive.

Table 3-3. Waste Properties Specifications for Transfer Pump Procurement

Property	Range
Specific gravity	1 to 1.5
Viscosity	1 to 20 cP
Temperature	< 190°F
Solids content	0 to 300 g/L
pH	7 to 14
Maximum particle size	⅜-inch
Average particle size	80 μm

3.4.2 Transfer Pump Placement

Initial transfer pump deployments will consist of a single assembly in a 42-inch diameter riser. Figure 3-6 depicts the general configuration of the DST Transfer Pump. The pump will be positioned near the center of the tank between the two mixer pumps (in those tanks that will have two). The pump height is adjustable, so that the inlet can be lowered to 6 inches above the tank bottom and raised to a little more than 13 ft from the tank bottom.

Figure 3-6. Illustration Showing Transfer Pump Placement (Raised Position)
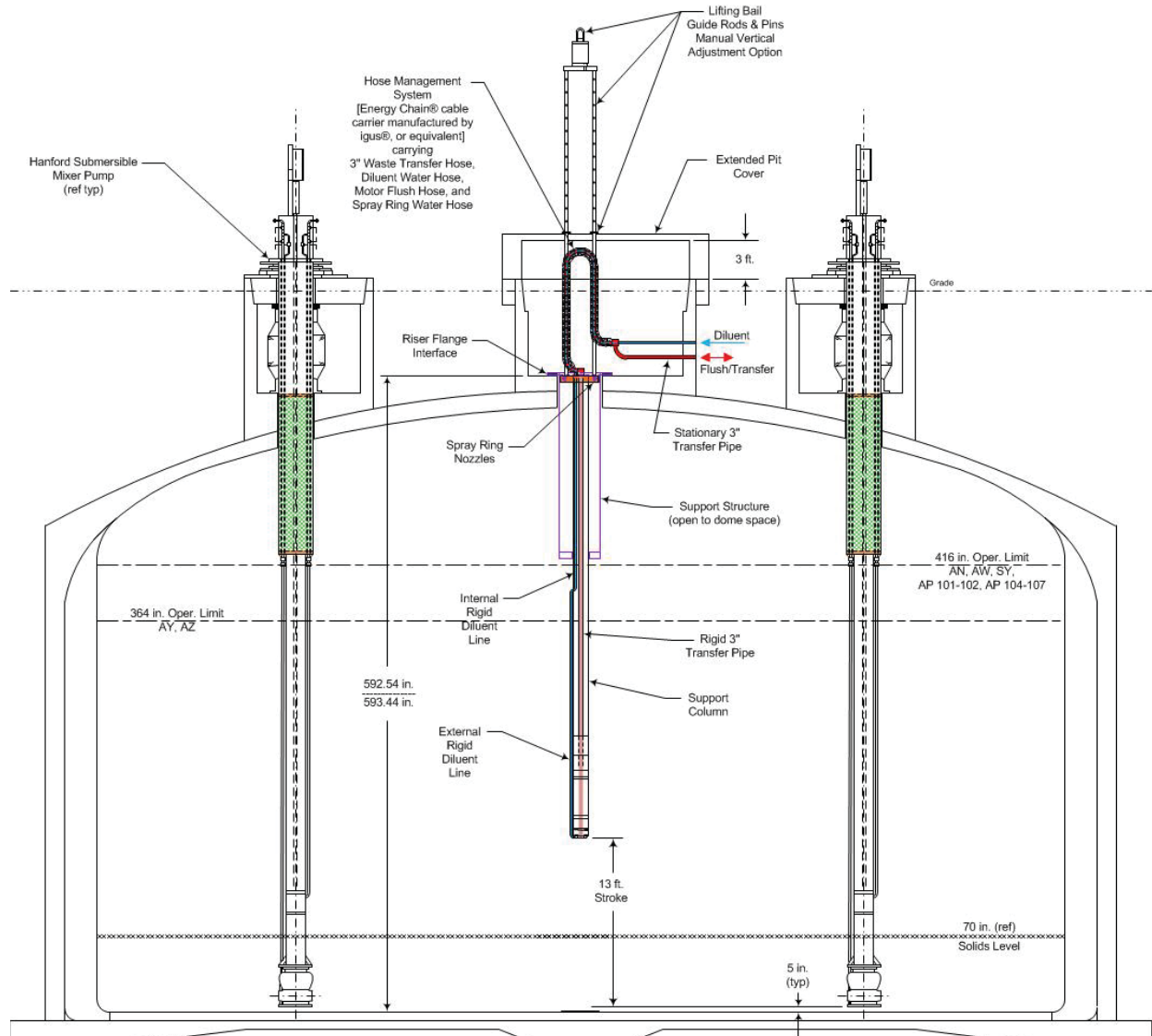
3.4.3   Transfer Pump Operation

The recommended transfer pump configuration represents a merger and enhancement of design features from all adaptations of the technology to date. The transfer pumps are a more powerful version of the C-Farm Retrieval motor/pump unit, including the "dry" bearing startup and integral motor flush capabilities, combined with a vertically adjustable column and support structure configuration that is capable of withstanding direct jet impingement forces from operating mixer pumps. The transfer pumps will be multi-staged vertical, bottom suction, side, or top discharge. Also, dilution water will be added, as required, at the suction to adjust rheological properties.

The transfer pumps can differ in design and capability for each DST depending on whether the transfer pump is to be operated concurrently with mixer pumps, the waste type being pumped (supernatant, dissolved salts, or suspended solids) and the depth from which the waste must be pumped. Figure 3-7 shows conceptual design of the pump inlet and flow patterns during flushing, in-line dilution, and waste transfers. Scenarios examined in Section 7.0 assume the pump inlet is placed near the bottom of the tank.

Figure 3-7. Transfer Pump Inlet Conceptual Design
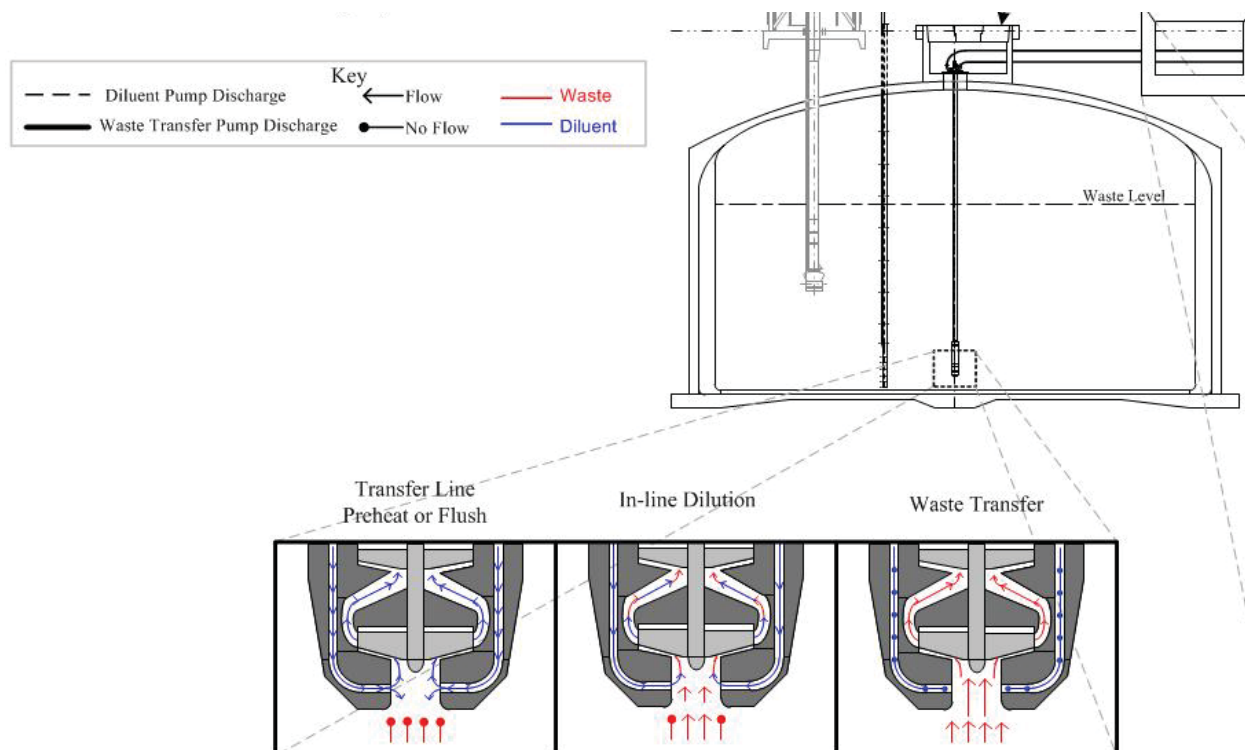
3.5 TRANSFER LINES

3.5.1 Transfer Line Descriptions

Waste Feed Delivery will transport liquid/slurry wastes among the 28 tanks comprising the six DST farms in preparation for transport of batches of the waste out of the DST system as feed to the WTP. This mission will take decades with current plans projecting over 1,300 individual waste transfers. The current Tank Farm pipeline infrastructure for these transfers consists of a network of inter-farm (within a farm) pipelines connected to intra-farm (between farms) pipelines connected to WTP feed pipelines. Elements of this pipeline network were constructed over decades to evolving codes and standards, from varying materials of construction and to varying pressure ratings. In general, the lowest pressure rated lines (275 psig) exist within the inter-farm pipelines and the higher-pressure rated lines (400 psig) connect the farms together and to the WTP. The transfer lines consist of process piping components like encased piping, valve

manifold/jumper assemblies, encased over-ground hoses, and transfer pumps. Figure 3-8 illustrates the waste transfer system and the transfer line routes.

Figure 3-8. Illustration Showing Waste Transfer Routes
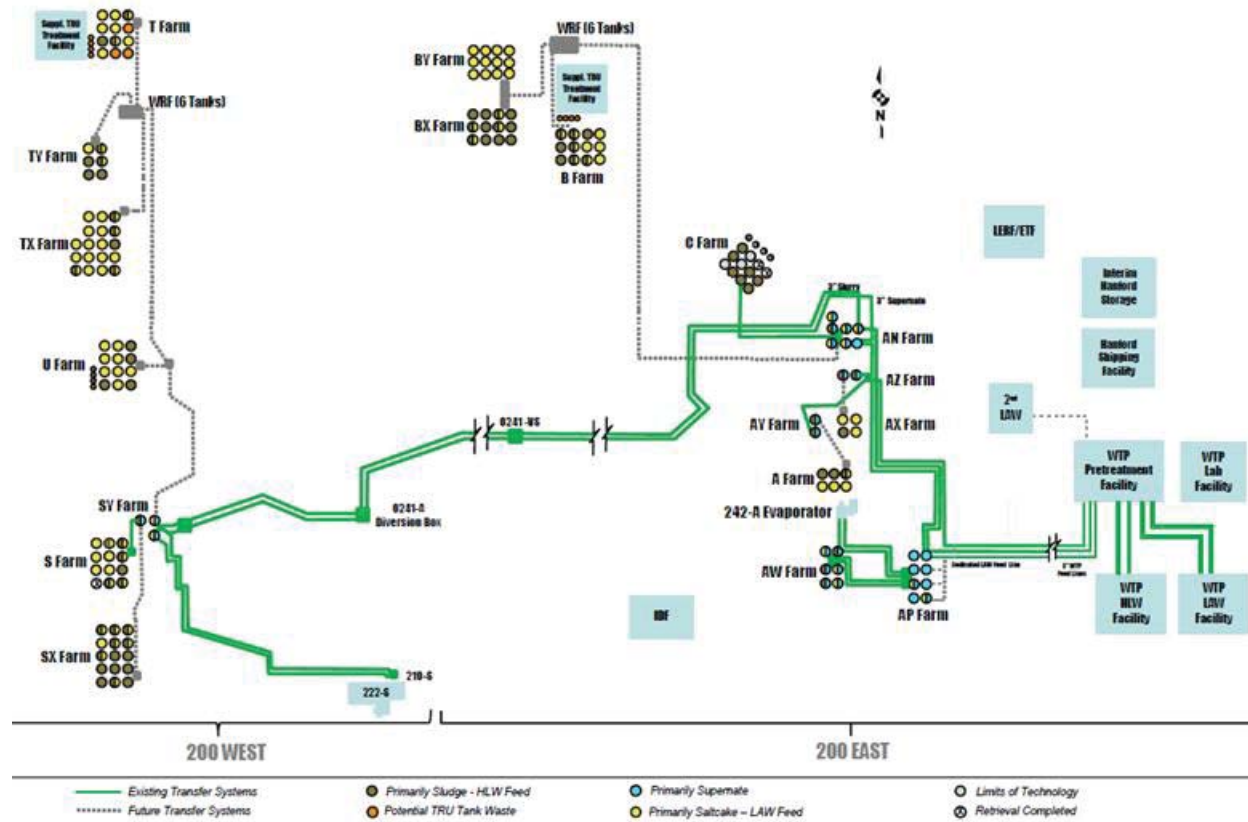
The 200 Area DSTs generally use buried supernatant and slurry transfer lines to transfer waste from tank farm to tank farm. All of the DST transfer lines are of double-wall construction, with the innermost waste-carrying pipe encased within a larger pipe that provides the secondary containment barrier. The outer containment pipe is non-pressurized and includes leak detection.

Tank Farms AN, AP, and AW have transfer lines that are made entirely out of carbon steel with one exception: supernatant transfer line SN-274 in AW Farm uses 304L stainless steel for the inner pipe. All of the transfer lines within tank farms AY and AZ are virtually identical to SN-274 with schedule 40, 304L stainless steel inner pipe and carbon steel encasements, as documented in RPP-27591, Volume 2 *IQRPE DST System Integrity Assessment – Pipeline Integrity* and RPP-15137, *System Design Description for 200 Area Double-Shell Tank Waste Transfer System (DSA-Based)*. In September of 2011, project W-566, *Transfer Line Upgrades Project*, completed the installation of four refurbished and four new SY transfer lines with schedule 40, 304L stainless inner pipe and carbon steel encasements. Both SL-178 and SL-179 transfer lines were not replace by project W-566 and are therefore still made entirely out of carbon steel.

Typically, the supernatant transfer lines are 3-inch NPS with 6-inch NPS encasements and the slurry transfer lines are 2-inch NPS with 4-inch NPS encasements. These inter-farm transfer lines interface at the tank farm valve pits or pump pits and depending on the route required, pass through valve pits or pump pits of tank farms not designated as the originating or receiving tank farm.

It is assumed that the transfers pass through two three-way valves (run), one three-way valve (branch), three Plutonium-Uranium Extraction (PUREX) connectors and five long-radius elbows. The largest pressure drops in the pits occur in the PUREX connectors and in the three-way valves with the flow through the branch. The elevations of the end points of the transfer lines were determined from the elevations of the nozzles inside the pump or valve pits.

Should the inner pipe of a double-walled transfer line develop a leak, the outer encasement directs the leakage into the waste transfer structure via a drain line. The transfer lines are all sloped back to these structures so that leakage can flow to a leak detector by gravity. Each waste transfer structure has a leak detector installed at the lowest point near the floor drain. The diversion box and vent station structures for the Replacement Cross-Site Transfer System (RCSTS) both have sumps installed to collect fluids, with low-point leak detectors installed inside each sump. In addition, a continuous leak detection cable runs along the inside of each RCSTS transfer line encasement below the inner pipe. Approximately 30% of the transfer line encasements have either leak detectors installed in their drain lines or continuous leak detection cable that runs along the entire length of the encasement, which is the case for the RCSTS lines, (RPP-15136, *System Design Description for the Replacement Cross-Site Transfer System between 200 West and 200East Tank Farms*). Encasement leak detection capability permits the immediate identification of a failed transfer line.

The cross-site slurry line (SLL-3160) is not currently authorized for use, and requires a separate approval from DOE before commencement of slurry transfer operations take place. An activation evaluation[3] has been issued that describes the required needs, actions, and recommendations for the cross-site slurry transfer system to be operational. It should also be noted that the installation of two booster pumps in series inside DB 6241-A are a unique feature of the SLL-3160 line.

3.5.2   Transfer Line Lengths

Most transfer line lengths were measured from Hanford drawings, but some lengths were estimated from the lengths of their leak detection cables, which run along the inside of the encasements. Equivalent pipe lengths are also based on the number of linear feet of pipe in each transfer route plus the number of feet of pipe that will provide a pressure drop equivalent to the pressure drop that would be experienced through a pipefitting or valve.

---

[3] RPP-RPT-47572, 2012, *Cross-Site Slurry Line Evaluation Report*, Rev. 0, Washington River Protection Solutions, LLC, Richland, Washington.

Transfer lines from DST to DST and from DST to WTP are detailed in RPP-RPT-46112, *Transfer Line Reliability for the Waste Feed Delivery Operations Research Model Phase 2*. Among these transfer lines, the Tank Operations Contractor will provide three transfer lines to WTP and the WTP contractor will connect to these three lines. Each of the three transfer lines will be capable of transporting LAW, HLW, and returned waste between the Tank Farms and the WTP Pretreatment facility.

RPP-5346 shows the plan for general transfer routes from DST to DST and from DST to WTP. Many of these transfer routes, analyzed a decade ago, are the same transfer routes used in the *River Protection Project System Plan* (ORP-11242). Transfer line lengths and maximum pressures for transfers from Tank Farms to WTP are shown in Table 3-4.

Table 3-4. WFD Transfer Routes, Pipe Line Lengths, and Pressure Ratings

From Tank	To Tank	Carbon Steel Total Route Length (feet)	Stainless Steel Total Route Length (feet)	Total Route Pipe Length (feet)	Pressure Limits* (psig)
AN-101	WTP	0	6,102	6,102	400
AN-102	WTP	405	6,512	6,917	275/400
AN-103	WTP	376	6,512	6,888	275/400
AN-104	WTP	0	5,999	5,999	400
AN-105	WTP	452	6,717	7,169	275/400
AN-106	WTP	442	6,717	7,159	275/400
AN-107	WTP	557	6,814	7,371	275/400
AP-101	WTP	1,050	3,858	4,908	400
AP-102	WTP	0	3,758	3,758	400
AP-104	WTP	950	3,858	4,808	400
AP-105	WTP	938	3,858	4,796	400
AP-106	WTP	976	3,858	4,834	400
AP-108	WTP	1,079	3,858	4,937	400
AW-101	WTP	1,630	4,268	5,898	275/400
AW-102	WTP	1,472	4,063	5,535	275/400
AW-103	WTP	1,648	3,584	5,232	275/400
AW-104	WTP	1,434	4,268	5,702	275/400
AW-105	WTP	1,556	4,268	5,824	275/400
AY-101	WTP	0	6,674	6,674	400
AY-102	WTP	0	6,133	6,133	400
AZ-101	WTP	0	5,444	5,444	400
AZ-102	WTP	0	5,674	5,674	400

Notes:

*When two pressures are presented, the first is the within tank farm limit and the second is the tank farm to WTP limit.

4.0 UNDISSOLVED SOLIDS WASTE DATA, VARIATIONS AND UNCERTAINTIES

This section discusses the existing analytical data for physical properties of undissolved solids, including particle size, mineralogy, solid density, and solid particle shape. These properties are important in waste transfer to the WTP, as well as the operation of the WTP. The uncertainties and variation[4] in the existing physical properties data are also discussed.

Section 4.1 contains general discussion of the available data and the information on the waste types (sludge and saltcake) included in each Hanford tank. Section 4.2 presents data, uncertainties, and variation information on primary particle density and mineralogy. Section 4.3 presents data, uncertainties, and variation information on particle shape and size. Section 5 presents density calculations and assumptions for the largest primary particle and largest agglomerate.

4.1 AVAILABLE DATA AND WASTE TYPES

4.1.1 Available Data

The data presented and discussed in this section should not be evaluated independently of the environment in which the measurements were obtained. Solid properties depend on the liquid in contact with the solid's surface. The liquid impacts the surface charge and cohesive properties of the solid particles, as well as the dissolution and precipitation kinetics of the slurry system. With a surface charge, particles may agglomerate because of cohesive forces and form larger solid masses with entrained interstitial liquid. A larger agglomerated particle has a different size, shape, and density than the individual particles and liquid of which it is made. The physical properties of agglomerates are intermediate to the physical properties of the various solids and liquid that forms the agglomerate.

Adjustments in the solid surface charge occur because of environment changes. These changes in environment lead to changes in the strength of cohesive particle interactions. As cohesive forces increase, solid agglomerates are formed as particles attach to one another. Smaller agglomerates exhibit solid properties more typical of individual primary particles because the particles make up more of the total volume of an agglomerate.

Most data in the following sections are from archived solid waste samples from SSTs and DSTs. Tank waste samples were taken using core, auger, clamshell, finger trap, or other solids sampling devices. Archived samples typically were reconstituted using deionized water, a 0.1 mole/L sodium hydroxide solution, or a 0.01 mole/L solution of sodium hydroxide and sodium nitrite. During reconstitution it was assumed that a majority of the dissolvable solids, which may have precipitated from the interstitial liquid during storage, were re-dissolved.

---

[4] See the definitions of "uncertainty" and "variation" in the Terms section at the start of the report.

Solid agglomerates may have been broken apart during sampling or formed from aqueous environment changes. It was uncertain whether the data obtained from archived solids were characteristic of what would have been observed immediately following sample delivery to the laboratory because solid property analyses (e.g., particle size, shape and mineralogy) were not frequently performed prior to archive storage. The term "apparent" particle size distribution (PSD) has been used to describe the data available to date (PNNL-20646) and may be a more appropriate term for the analytical results presented here.

The Hanford sample archive was designed (nearly 20 years ago) as a repository with an effective life span of no more than 5 years (WHC-SD-W079-ES-001, *Hot Sample Archiving/W-079*). Samples were stored in borosilicate glass with plastic screw thread caps. Opening and closing these lids over time has led to evaporation and precipitation of salts, often along the rim. The necessity of handling these jars with hot cell manipulators has resulted in broken caps. Jars with poorly closed caps have led to further evaporation. Reconstitution of the archived solids has been hypothesized as dissolving precipitated salts, but its effect on particle size and aggregate formation cannot be determined. Further, the presence of caustic solutions in many archive samples has led to the dissolution of boron and silicon from the glass, with subsequent precipitation of Cancrinite or other silicates. The effect of these post-retrieval processes on waste particle properties cannot be easily assessed at present.

Additional data were available for chemically adjusted sludge, composite sludge, and dissolved saltcake samples. These samples were taken using the same solids sampling devices outlined above. These data, although not characteristic of the solids currently in the tank(s), were relevant to include in particle analyses. This is because of the many processes might take place before WFD, including sluicing, caustic dissolution, evaporation, and waste blending.

Mixing and chemical adjustments were used during SST retrieval and DST operations. These adjustments are anticipated to continue during WFD. The exact retrieval technologies used on individual tanks will depend on the waste and how easily it is mobilized and transferred. Deployment of new retrieval technologies to enable faster and/or more efficient solid mobilization are likely during the mission. These process modifications will ultimately affect the resultant particle properties that are discussed in this section.

4.1.2 Waste Types

Knowing which tanks contain low solubility sludge and/or high solubility saltcake is necessary to evaluate the available data. Waste types (see Table 3.2 of PNNL-20646) have been used to distinguish various wastes based on the Hanford processing facility and various chemical technologies that created the waste initially. Extrapolation of tank waste types to predict WFD batch properties may not be appropriate for a number of reasons:

- Several Hanford tanks were connected in series with cascade lines between tanks. These cascades allowed solids to settle in the first tank, while the more buoyant solids and supernatant were transported to subsequent tanks as the initial tanks became full.

- As tank contents are retrieved and transferred, multiple waste types will be mixed. These mixtures do not necessarily maintain the characteristics of the individual waste types. Chemical reactions, which occur as the waste mixes, establish a new equilibrium that makes the original waste type labeling invalid.

Table 4-1 summarizes inventory data for the 177 Hanford DSTs and SSTs (HNF-EP-0182). Tank inventories are updated monthly, taking into consideration any changes because of retrievals, transfers, evaporations, chemical adjustments, etc. The information in Table 4-1 is the inventory in all of the 200 area SSTs and DSTs as of December 31, 2011. The inventories of all of the waste volumes can be summed to determine the total volume of each waste phase (Table 4-2). A single waste tank can contain single or multiple waste phases as evidenced by those tanks with both sludge and saltcake.

Table 4-1. Approximate Waste Phase Volumes for Hanford SSTs and DSTs (4 pages)

Tank	Sludge (kgal)	Saltcake (kgal)	Supernatant (kgal)
241-A-101	3	317	0
241-A-102	0	37	3
241-A-103	2	372	4
241-A-104	28	0	0
241-A-105	37	0	0
241-A-106	50	29	0
241-AN-101	255	31	366
241-AN-102	0	154	890
241-AN-103	0	486	474
241-AN-104	0	443	606
241-AN-105	0	536	588
241-AN-106	370	17	251
241-AN-107	0	241	843
241-AP-101	0	33	1075
241-AP-102	28	0	1051
241-AP-103	0	52	1184
241-AP-104	0	100	716
241-AP-105	0	105	1030
241-AP-106	0	0	1133
241-AP-107	0	0	1092
241-AP-108	0	112	1131
241-AW-101	0	396	737
241-AW-102	52	0	174
241-AW-103	280	40	766
241-AW-104	97	157	807
241-AW-105	248	0	159
241-AW-106	0	264	371
241-AX-101	3	355	0
241-AX-102	6	24	0
241-AX-103	8	99	0
241-AX-104	7	0	0
241-AY-101	105	0	797
241-AY-102	151	0	715
241-AZ-101	52	0	847
241-AZ-102	105	0	837
241-B-101	28	81	0
241-B-102	0	28	4
241-B-103	1	55	0
241-B-104	309	65	0
241-B-105	28	262	0
241-B-106	122	0	1
241-B-107	86	75	0
241-B-108	27	65	0
241-B-109	50	76	0
241-B-110	244	0	1
241-B-111	241	0	1
241-B-112	15	17	3
241-B-201	29	0	0
241-B-202	28	0	0
241-B-203	49	0	1
241-B-204	49	0	1

Table 4-1. Approximate Waste Phase Volumes for Hanford SSTs and DSTs (4 pages)

Tank	Sludge (kgal)	Saltcake (kgal)	Supernatant (kgal)
241-BX-101	48	0	0
241-BX-102	79	0	0
241-BX-103	62	0	13
241-BX-104	97	0	3
241-BX-105	42	25	5
241-BX-106	10	28	0
241-BX-107	347	0	0
241-BX-108	31	0	0
241-BX-109	193	0	0
241-BX-110	65	148	1
241-BX-111	32	156	0
241-BX-112	163	0	1
241-BY-101	37	333	0
241-BY-102	0	278	0
241-BY-103	9	405	0
241-BY-104	46	359	0
241-BY-105	48	433	0
241-BY-106	32	398	0
241-BY-107	15	256	0
241-BY-108	40	182	0
241-BY-109	24	263	0
241-BY-110	43	323	0
241-BY-111	0	402	0
241-BY-112	2	284	0
241-C-101	88	0	0
241-C-102	316	0	0
241-C-103	Retrieval completed 08/26/06[a]		
241-C-104	Retrieved to limit of modified sluicing technology 6/17/11 [b]		
241-C-105	132	0	0
241-C-106	Retrieval completed 12/31/03 [c]		
241-C-107	Retrieval in progress [d]		
241-C-108	Retrieved to limit of modified sluicing technology 4/27/07 [e]		
241-C-109	Retrieved to limit of modified sluicing technology 8/23/07 [f]		
241-C-110	Retrieved to limit of modified sluicing technology 4/27/09 [g]		
241-C-111	Retrieval in progress [h]		
241-C-112	Retrieval in progress [i]		
241-C-201	Retrieval completed 03/23/06 [j]		
241-C-202	Retrieval completed 08/11/05 [k]		
241-C-203	Retrieval completed 03/24/05 [l]		
241-C-204	Retrieval completed 12/11/06 [m]		
241-S-101	235	117	0
241-S-102	22	69	2
241-S-103	9	227	1
241-S-104	132	156	0
241-S-105	2	404	0
241-S-106	0	455	0
241-S-107	320	38	0
241-S-108	5	545	0
241-S-109	13	520	0
241-S-110	96	293	0
241-S-111	76	325	0

Table 4-1. Approximate Waste Phase Volumes for Hanford SSTs and DSTs (4 pages)

Tank	Sludge (kgal)	Saltcake (kgal)	Supernatant (kgal)
241-S-112	Retrieval completed 03/02/07 [n]		
241-SX-101	144	276	0
241-SX-102	55	287	0
241-SX-103	78	431	0
241-SX-104	136	310	0
241-SX-105	63	312	0
241-SX-106	0	396	0
241-SX-107	94	0	0
241-SX-108	74	0	0
241-SX-109	66	175	0
241-SX-110	49	7	0
241-SX-111	97	18	0
241-SX-112	75	0	0
241-SX-113	19	0	0
241-SX-114	126	29	0
241-SX-115	4	0	0
241-SY-101	232	0	857
241-SY-102	0	199	348
241-SY-103	332	0	381
241-T-101	37	62	0
241-T-102	19	0	13
241-T-103	23	0	4
241-T-104	317	0	0
241-T-105	98	0	0
241-T-106	22	0	0
241-T-107	173	0	0
241-T-108	5	11	0
241-T-109	0	62	0
241-T-110	369	0	1
241-T-111	447	0	0
241-T-112	60	0	7
241-T-201	28	0	2
241-T-202	20	0	0
241-T-203	36	0	0
241-T-204	36	0	0
241-TX-101	74	17	0
241-TX-102	2	215	0
241-TX-103	0	145	0
241-TX-104	34	33	2
241-TX-105	8	568	0
241-TX-106	5	343	0
241-TX-107	0	30	0
241-TX-108	6	121	0
241-TX-109	363	0	0
241-TX-110	37	430	0
241-TX-111	43	321	0
241-TX-112	0	634	0
241-TX-113	93	545	0
241-TX-114	4	528	0
241-TX-115	8	545	0
241-TX-116	66	533	0

Table 4-1. Approximate Waste Phase Volumes for Hanford SSTs and DSTs (4 pages)

Tank	Sludge (kgal)	Saltcake (kgal)	Supernatant (kgal)
241-TX-117	29	597	0
241-TX-118	0	247	0
241-TY-101	42	76	0
241-TY-102	0	69	0
241-TY-103	103	51	0
241-TY-104	43	0	1
241-TY-105	231	0	0
241-TY-106	16	0	0
241-U-101	23	0	0
241-U-102	43	283	1
241-U-103	11	405	1
241-U-104	54	0	0
241-U-105	32	321	0
241-U-106	0	168	2
241-U-107	15	279	0
241-U-108	29	405	0
241-U-109	35	366	0
241-U-110	176	0	0
241-U-111	26	196	0
241-U-112	45	0	0
241-U-201	3	0	1
241-U-202	3	0	1
241-U-203	2	0	1
241-U-204	2	0	1

Notes:

a.   Total waste 2,529 gallons; sludge 2282 gallons; supernatant 247 gallons.

b.   4,710 gallons of sludge remained in tank 241-C-104 after retrieval operations came to a halt.

c.   Total waste 2,771 gallons; sludge 2,686 gallons; supernatant 85 gallons.

d.   Total waste 186,379 gallons sludge remaining at the end of November 2011, according to a Retrieval & Closure status report email dated 10/31/2011 stating that 185,699 gallons remained in the tank, plus a flush of 710 gallons on November 3, 2011.

e.   Final estimate of 8.1 kgals includes 5.6 kgals of sludge solids, 1.2 kgals of sludge interstitial liquid, and 1.3 kgals of water assumed to have drained to 241-C-108 during leak checks during July 2011.

f.   First Quarter fiscal year 2011 Best-Basis Inventory update: sludge 7,800 gallons.

g.   17,200 gallons of sludge remains in tank 241-C-110 after retrieval operations came to a halt.

h.   Total waste 32170 gallons remaining at the end of November 2010.

i.   Total sludge waste approximately 121,700 gallons remaining at the end of December 2011.

j.   Total waste 144 gallons; sludge 142 gallons; supernatant 2 gallons.

k.   Total waste 147 gallons; sludge 145 gallons; supernatant 2 gallons.

l.   Total waste 139 gallons; sludge 126 gallons; supernatant 13 gallons.

m.   Total waste 137 gallons; sludge 134 gallons; supernatant 3 gallons.

n.   Total waste 2,387 gallons; sludge/saltcake 2,263 gallons; supernatant 124 gallons.

Table 4-2. Total Volumes of Waste Phases for Hanford 200-series SSTs and DSTs

Total Sludge Volume (kgal)	Total Saltcake Volume (kgal)	Total Supernatant Volume (kgal)
12,550	23,592	19,338

Sludge and saltcake waste phases can be further delineated into waste types. This information can be obtained from the Tank Waste Information Network System (TWINS; https://twins.pnl.gov) under the Best-Basis Inventory tab as Waste Type Volumes by Tank. Sludge volumes by waste type are provided in Table 4-3. The information in TWINS is updated quarterly to reflect ongoing changing tank conditions (e.g., SST retrievals, DST-to-DST transfers, evaporation, and chemical adjustments). Although Tank Farms waste data and characteristics are assigned to waste types, the current waste type categories will be of limited use as ongoing operations blend several waste types together in preparation for WFD. Blended sludges receive a "NA" waste type designation (see Table 4-3) because the mixture no longer fits a Hanford Defined Waste type.

Table 4-3. Sludge Volumes by Waste Type for Hanford SSTs and DSTs

Waste Phase	Waste Type	Total (kgal)
Sludge (Liquid & Solid)	1C (Solid)	2,092
Sludge (Liquid & Solid)	1CFeCN (Solid)	147
Sludge (Liquid & Solid)	224-1 (Solid)	58
Sludge (Liquid & Solid)	224-2 (Solid)	492
Sludge (Liquid & Solid)	2C (Solid)	1,345
Sludge (Liquid & Solid)	AR (Solid)	23
Sludge (Liquid & Solid)	B (Solid)	41
Sludge (Liquid & Solid)	BL (Solid)	40
Sludge (Liquid & Solid)	CWP1 (Solid)	227
Sludge (Liquid & Solid)	CWP2 (Solid)	528
Sludge (Liquid & Solid)	CWR1 (Solid)	378
Sludge (Liquid & Solid)	CWR2 (Solid)	124
Sludge (Liquid & Solid)	CWZr1 (Solid)	34
Sludge (Liquid & Solid)	CWZr2 (Solid)	502
Sludge (Liquid & Solid)	DE (Solid)	160
Sludge (Liquid & Solid)	HS (Solid)	6
Sludge (Liquid & Solid)	MW1 (Solid)	52
Sludge (Liquid & Solid)	MW2 (Solid)	23
Sludge (Liquid & Solid)	NA (Sludge)	927
Sludge (Liquid & Solid)	P2 (Solid)	11
Sludge (Liquid & Solid)	P3AZ1 (Solid)	44
Sludge (Liquid & Solid)	P3AZ2 (Solid)	73
Sludge (Liquid & Solid)	PFeCN (Solid)	252
Sludge (Liquid & Solid)	PL2 (Solid)	30
Sludge (Liquid & Solid)	Portland Cement (Solid)	8
Sludge (Liquid & Solid)	R1 (Solid)	1,418
Sludge (Liquid & Solid)	R2 (Solid)	182

Table 4-3. Sludge Volumes by Waste Type for Hanford SSTs and DSTs

Waste Phase	Waste Type	Total (kgal)
Sludge (Liquid & Solid)	SRR (Solid)	147
Sludge (Liquid & Solid)	TBP (Solid)	745
Sludge (Liquid & Solid)	TFeCN (Solid)	82
Sludge (Liquid & Solid)	TH1 (Solid)	26
Sludge (Liquid & Solid)	Z (Solid)	8
Sludge Solid	AR (Solid)	27
Sludge Solid	BL (Solid)	20
Sludge Solid	CWP2 (Solid)	21
Sludge Solid	DE (Solid)	56
Sludge Solid	NA (Sludge)	277
Sludge Solid	P1 (Solid)	1
Sludge Solid	P2 (Solid)	44
Sludge Solid	PL2 (Solid)	67
Sludge Solid	R1 (Solid)	96
Sludge Solid	R2 (Solid)	99
Sludge Solid	TBP (Solid)	18
Sludge Solid	Z (Solid)	48

4.2 MINERALOGY AND DENSITY OF UNDISSOLVED SOLIDS

Particle grain densities in Hanford tank waste can be considered identical for agglomerates or individual primary particles. Solid tank waste has been observed in the form of agglomerates. Agglomerates are combinations of two or more solid primary particles attached because of attractive forces (e.g., adhesion/cohesion, pressure, cementation, and/or sintering). The agglomerates may be combinations of the same or different mineral primary particles, with void spaces making up the remainder of the volume. Void spaces are filled with interstitial liquid and/or a gas phase. Agglomerates have different bulk densities than the primary particles from which they are formed because of the combination of dissolved minerals and interstitial liquids and/or gases residing in the resultant void spaces. Agglomerate density will depend on the combination of insoluble and dissolved solids, liquids, and/or gases that make up the final solid mass.

Technical reports that characterize solid particles have mainly analyzed the individual primary particles and their characteristic densities. Agglomerated particle densities can be calculated as a bulk density (composite density of the solids plus any liquid/gas filling the void space) or with knowledge of the individual particles that comprise them, along with the characteristics of the fluids and/or gas phases filling the interstitial void space.

If it is assumed that an agglomerate can be characterized by a single or representative primary particle type and size and one liquid or gas, the following equation can be used to calculate the agglomerate density as described in PNNL-20646 (pg. 3.230):

$$\rho = \left(\frac{r}{R}\right)^{3-D_F} (\rho_S - \rho_L) + \rho_L \qquad\qquad (4-1)$$

where ρ =   agglomerate density (mass/volume)
             D_F =   fractal dimension (dimensionless)
              r =   primary particle size (characteristic length)
             R =   agglomerate size (characteristic length)
            ρ_L =   density of the liquid or gas filling the pore space (mass/volume)
            ρ_S =   density of the solid primary particle (mass/volume)

The primary particle size (r) is less than the agglomerate size (R), leading to the first term being less than 1. Similarly, the density of the primary particle is greater than the liquid density, leading to the second term in parentheses being greater than 0. The fractal dimension (D_F) is a measure of the void space within the agglomerate. For densely packed agglomerates, the value of D_F is closer to 3, whereas for loosely packed agglomerates with more pore space, the value of D_F is closer to 1.6 to 1.8. As reported in PNNL-20646, a value of $D_F = 2.25$ has been used in previous studies describing agglomeration of Hanford tank waste. However, there is large uncertainty in this value given the wide range of primary particles forming agglomerates and in the conditions wherein the agglomerates are formed. Application of a fractal dimension other than 3 has several limitations and necessary assumptions as described in PNNL-20646 that are not defined for Hanford waste particulate including:

- An agglomerate can be comprised of more than one solid phase compound. Agglomerates of different compounds and primary particle sizes likely have unique fractal dimensions.

- The fractal dimension can be a function of agglomerate size.

- It is assumed that the diameter of an equilibrium sphere represents a non-spherical primary particle.

- It is assumed that all primary particles form agglomerates of any size within a measured solid size range, regardless of the size of primary particles.

- Due to shear and normal forces acting on it, waste may have different agglomerate sizes and associated fractal dimensions during retrieval and transport processes as compared to *in situ* conditions.

The effect of varied fractal dimensions on particle density is illustrated in PNNL-20646. In using $D_F = 2.25$ in the agglomerate density calculations, the product of the first two terms will be less than the density of the primary particle. Therefore, agglomerate density (e.g., ρ) will decrease as its size (e.g., R) increases for a constant value of D_F (PNNL-20646).

4.2.1   Mineralogy and Density Data for Primary Particles

Primary particle density and mineralogy data are interdependent; the density of the primary particle depends on its mineral composition. Individual mineral densities were obtained from PNNL-20646 or SciFinder (https://scifinder.cas.org). Mineral phases have primarily been identified using a variety of techniques, such as x-ray diffraction (XRD), Polarized Light

Microscopy (PLM), Scanning Electron Microscopy (SEM) with Secondary Electron Imaging (SEI) and Backscatter Electron Imaging, Energy Dispersive Spectroscopy (EDS), and Transmission Electron Microscopy (TEM) with Selected Area Electron Diffraction among others. Selective dissolution, where specific solid phases are dissolved using strong reagents, has also been used to provide information that can assist with solid phase identification. The compiled Hanford mineralogy data have been documented in RPP-RPT-46618, *Hanford Waste Mineralogy Reference Report*, which has been updated to include additional data since it was used in PNNL-20646. Additional information concerning Pu specific minerals has been documented in RPP-RPT-50941, *Review of Plutonium Oxide Receipts into Hanford Tank Farms*. This information is summarized Table 4-4.

Density values for the primary particles range from 1.8 g/mL (and aluminum phosphate) to 19 g/mL (Pu metal). Table 4-4 also shows the number of tanks in which each mineral phase has been reported to occur. Densities of some poorly characterized chemical compounds are included even though those phases have not yet been definitively identified in any Hanford solid samples. This was done because phases exist in the Hanford tanks that have never been definitively classified other than by elemental composition or inferred in chemical analyses. Additional mineral phases that do not have documented observations are from expert panel elicitations (PNNL-20646 and RPP-RPT-50941).

Table 4-4. Density and Mineralogy by Element and Number of Tanks (2 pages)

Element	Mineral Density (g/mL) [a]	Observed Phases	# Tanks with Phase Observed [b]
Ag	7.1	Ag_2O	2
	[c]	(Ag, Hg) oxide	1
	10.5	Ag (zero valence)	2
Al	4.1	Barton 36CG garnet abrasive: $Fe_sO_3Al_2(SiO_4)_3$	2
	2.4	Gibbsite $Al(OH)_3$	28
	2.4-2.8	Cancrinite, zeolite, and other aluminosilicates	32
	3.0	Boehmite AlOOH	16
	[d]	Compounds of Al and Cr, Fe, U, Bi, or mixtures of their compounds	9
	1.8-2.6		5
	3.4	Aluminum phosphates	1
	2.4	Diaspore AlO(OH)	7
	3.0	Dawsonite $NaAlCO_3(OH)_2$	1
	2.5	Cryolite Na_3AlF_6	[d]
		$(NaAlO_2)_2 \cdot 2.5H_2O$	
Bi	7.9	$BiFeO_3$	[d]
	6.3	$BiPO_4$	1
	8.9	Bi_2O_3	3
	[c]	Compounds of bismuth combined with Al, Cr, Fe compounds	6
Ca	3.1	Hydroxylapatite $Ca_5OH(PO_4)_3$	3
	[c]	Other apatites $Ca_x(OH,F,Cl,Br)_x(PO_4)_x$	3
	2.7	Calcite $CaCO_3$	2
	2.2	Whewellite $CaC_2O_4 \cdot H_2O$	3
	2.2	Portlandite $Ca(OH)_2$ Calcium Phosphates (e.g., $CaPO_4$)	[d]
	2.4	Calcium sulfates (e.g., $CaSO_4$)	1
	2.3-3.0	Ca-U compounds or mixtures [g]	[d]
	4.1	Ca-Cr compounds or mixtures	1
	~3.0	Compounds of calcium combined with aluminum compound	3
	~3.0	$[e.g., (Ca,Sr)_3(Cr,Al)_2(OH)_{12}]$ [g]	10
Ce	6.0-7.2	CeO_2 [e]	1
Cr	5.2	Cr_2O_3	[d]
	4.1	CrOOH	1
	4.8	$FeCr_2O_4$	2
	~5.0	Oxides of Cr with Fe and Mn	3
	[c]	Chromium phosphates	1
	[c]	$Cr(OH)_3$	1
Fe	4.9-5.2	Hematite Fe_2O_3, Magnetite Fe_3O_4	13
	4.3	Goethite FeOOH	11
	4.8	Fe_2MnO_4 [g]	3
	[c]	Compounds of Fe combined with Bi, Pb, or Cr	17
	~3.0	Iron phosphates	4
	~3.0	$Fe(OH)_3$	6
	2.3	Iron oxalates	[d]
	4.5-5.0	Ilmenite $FeTiO_3$ [e]	1
Hg	[c]	(Ag,Hg) oxide	1
La	[c]	$La_4(P_2O_7)_3$	1

Table 4-4. Density and Mineralogy by Element and Number of Tanks (2 pages)

Element	Mineral Density (g/mL) [a]	Observed Phases	# Tanks with Phase Observed [b]
Mn	[c]	Other oxides and oxyhydroxides of Mn with Fe	7
	5.0	Mn_2CrO_4, $Mn_3Cr_3O_8$	1
	5.0	MnO_2	[d]
	5.0	Mn_2MnO_4	1
Ni	4.0	$Ni_3O_2(OH)_4$	2
	[c]	Oxides or Phosphates of Ni with Al, Cr, Fe, Mn	2
Pb	[c]	Phosphates or oxides of Pb with Fe, Mn, Ni, Al	1
	7.2	$Pb_5(PO_4)_3OH$	1
	[c]	Pb-Cl or Pb-O	1
Pu	8-11	PuO_2 [f]	1 [16 [f]]
	19	Pu metal [f]	[5 [f]]
Si	2.6	SiO_2	4
Sr	3.5	$SrCO_3$	[d]
	2.0	Nastrophite $NaSrPO_4 \cdot 9H_2O$	2
U	5.6	$Na_2U_2O_7$	16
	7.3-11.0	UO_2, UO_3, U_2O_7, U_3O_8	11
	6.4	$NaUO_2OOH$	3
	3.4-3.5	U and U-Al phosphates	3
	3.8	$Na_4UO_2(CO_3)_3$	2
	[c]	CaU_2O_7	1
Zr	5.7	ZrO_2	4
	[c]	Oxides of Zr with Fe, Mn	2

Notes:

a. Density is expressed to one decimal place at most, since this table is only to show the range of densities that have been observed. Some values are noted as estimates with the "~" symbol. Other values are derived from measured values.

b. Number of tanks with specific mineral phase counted from observations in RPP-RPT-46618.

c. Data are not available.

d. No tanks with this phase observed to date, as determined from RPP-RPT-46618.

e. Additional minerals added from RPP-RPT-46618. Density data obtained from SciFinder.

f. Additional information gathered from RPP-RPT-46618. The numerical values in brackets are the number of tanks that have a probability of containing this mineral.

g. These mineral phases could be included in multiple element "bins," but were only included once in this table to avoid repetition for the number of tanks with phase observed.

4.2.2 Mineralogy and Density Uncertainties

The main uncertainty in the data on primary particle mineralogy and densities in Table 4-4 is the lack of complete knowledge of the primary particles (minerals) that may appear in Hanford tank wastes. This lack of knowledge exists because there is limited mineralogy data; only 60 of 177 SSTs and DSTs have been sampled. Both the sampled and unsampled tanks may contain other minerals. Prior work has attempted to identify minerals that may exist even though they have not yet been observed in samples.

Some of the inorganic solid compounds in the HLW lack a clear crystalline structure. These phases are called 'amorphous'. Amorphous solids often show a solid-solution style of variation in chemical composition, because they lack a crystalline structure. In minerals, the crystalline structure helps constrain the type and amount of elemental substitutions that can take place. The presence of solid solutions and amorphous phases is one reason why it is difficult to provide definitive chemical compositions of some HLW insoluble solids.

Another reason for uncertainty in chemical composition of insoluble particulate is the lack of adequate characterization data. Many inorganic phases in HLW have been seen infrequently in small samples that are difficult to obtain and prepare for analysis. Additionally, the samples often undergo alteration after retrieval or during the sample preparation process.

Inorganic phases found in Hanford HLW waste are referred to generically as "minerals". Where they fit the strict definition of a mineral, they are identified by their mineral name. Where their chemical composition and crystalline structure are well known, they are identified by a balanced chemical formula and/or by their crystal structure. Amorphous compounds are identified as such and accompanied by a list of the elements present in order of decreasing concentration. Compounds of uncertain identity are identified as precisely as current data allows.

The densities of minerals are generally well known, sometimes to multiple decimal places, although densities have only been listed to one decimal place in Table 4-4. For some generally identified minerals listed in Table 4-4, the densities are estimated as a range.

4.2.3 Mineralogy and Density Variation

The density values for the primary particles (as shown in Table 4-4) range from 1.8 g/mL (aluminum phosphates) to 19 g/mL (Pu metal). Table 4-4 also shows the variation in types of primary particles and density values. Figure 4-1 shows a histogram of the mineral density values in Table 4-4, where the number of tanks in which a given primary particle with a given density was observed was used to determine the frequencies (y-axis) of the histogram. Because some entries in the table included ranges, the histogram in Figure 4-1 is for the maximum density values and maximum number of tanks. Also, because the data in Table4-4 are not from volume-based, representative samples of tanks with particle identities and densities, the histogram in Figure 4-1 does not show the actual distribution of densities of primary particles in Hanford waste tanks. Rather, Figure 4-1 serves to provide some information about the relative frequencies of density values based on the number of tanks in which the various primary particles have been observed.

Figure 4-1. Density Histogram of Particles Shown in Table 4-4 with the Frequency of a Given Primary Particle with a Given Density Determined by the Number of Tanks in which the Primary Particle was Observed
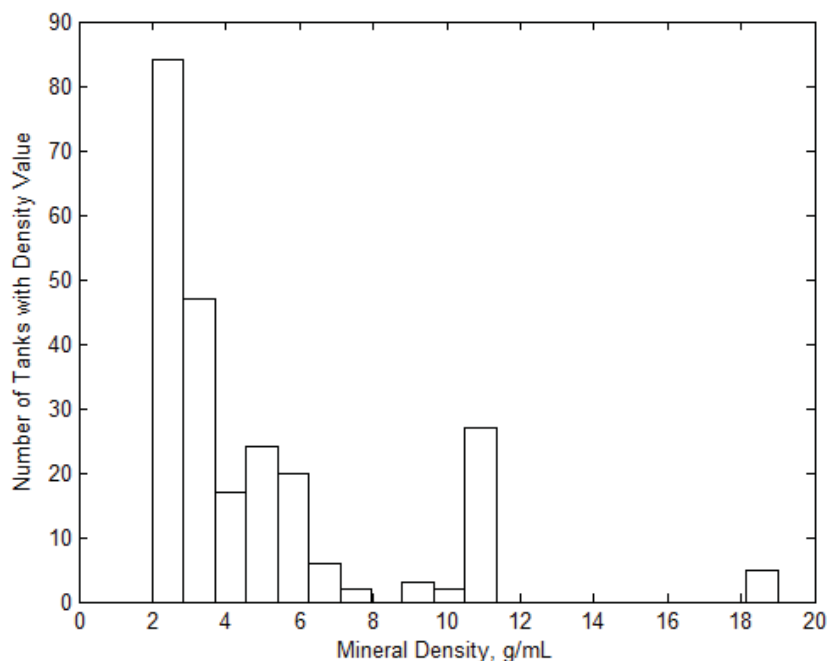
4.3 UNDISSOLVED SOLIDS PARTICLE SIZE AND SHAPE

The Hanford tanks listed in Table 4-1 are 20-feet diameter (i.e., 200 series SSTs) or 75-feet diameter (e.g., 100 series SSTs and DSTs) storage vessels buried below ground, with only a handful of riser locations available for sampling. Full depth core and auger solid samples obtained in the past were on the order of 1-inch diameter (WHC-SD-WM-TI-648, *Tank Characterization Reference Guide*). Heel samples, taken through the tank risers, have been obtained using a variety of techniques (e.g., a finger trap, clamshell sampler, or off-riser sample vehicle), but each total sample volume was on the order of 240 mL or less. Grab samples containing solids were typically obtained following retrieval, with their location near the settled solids/liquid interface in the receiving tank. Grab samples were obtained with wide or narrow mouth glass jars with internal volumes of 120 to 250 mL. Retrievals move waste from the source tank to the receiving tank through a transfer pump that is fit with a ⅜-inch screen to ensure the pump does not get clogged with larger particles.

The sampling methods and retrieval screen described above limit the maximum particle size that could be obtained for analysis, as well as the maximum particle size that could be transferred using the current systems in place, respectively. The maximum particle size that may have been obtained for most sampling would be smaller than 1-inch (25.4 mm) diameter for core samples or ⅜-inch (9.5 mm) diameter for grab samples. Some larger waste particles might be captured by clamshell or off-riser sampling techniques.

Large particles and agglomerates exist in the SSTs and DSTs. For example, Figure 4-2 shows the saltcake waste in SST A-103 and Figure 4-3 shows the sludge waste in SST B-111. These images show the surface of the large mass of solids in the tanks awaiting retrieval. These solids will need to be dissolved and/or broken apart and mobilized for eventual transfer to WTP. Depending on the technology used to break apart these solid masses, it is uncertain what will be the final PSD characterizing these solids.

Figure 4-2. December 28, 1988 Photo of SST A-103 Saltcake Solids

Figure 4-3. June 26, 1985 Photo of SST B-111 Sludge Solids
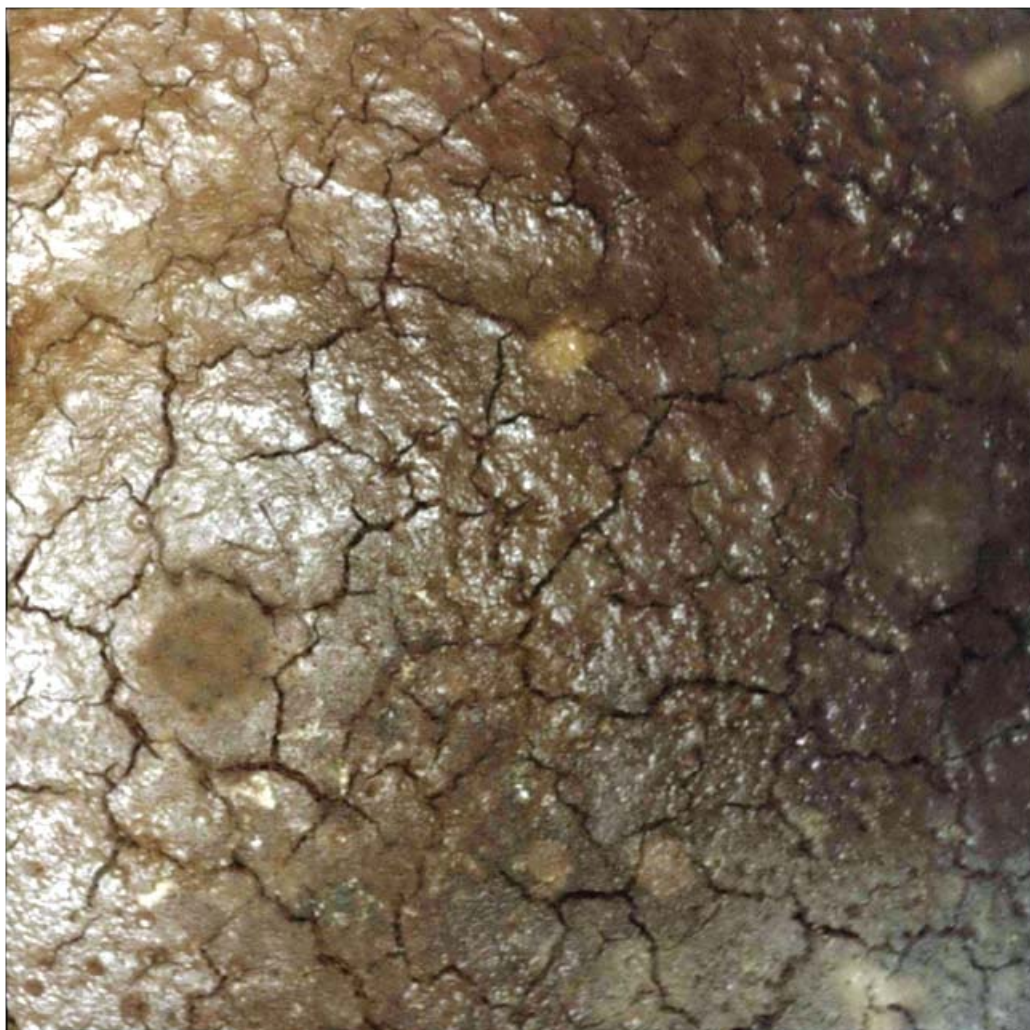
4.3.1   Particle Size and Shape Data

Most published data for Hanford tank waste particle shape and size were obtained using various analytical techniques on tank waste solid samples. The most common analytical techniques included SEM, TEM, PLM, sieve data, and a variety of PSD analyzers. The typical shape and maximum observed size of individual primary particles have been determined from images of the primary particles taken via SEM, TEM, and PLM. Detailed analyses of agglomerates have not typically been performed, because the primary focus has most commonly been on the individual mineral species present in tank waste. When measuring general particle size distributions, typically using PSD analyzers and more rarely using sieve data, the particles measured were combinations of small primary particles and those agglomerates that had not been broken apart during sampling and analysis. Therefore, when quantifying particle shape and size, the approach has been to focus on individual primary particle analysis.

In quantifying primary particle shape and size, images taken using TEM and SEM were the most commonly utilized methods. These techniques allowed for more focused images of the

individual particles and measurements of shape. The analyses performed in PNNL-20646 determined that TEM images enabled improved resolution of the smallest particle sizes and shapes in Hanford Tank Waste sludge when compared to other techniques, but not all solids were analyzed using TEM. In order to provide a large amount of data for comparison and analysis of the solids, a majority of the available data was utilized from PNNL-20646.

4.3.1.1 Primary Particles

Table 4-5 lists the shape and size data for many primary particle mineral compounds, which were compiled from the data in Table 3.14 of PNNL-20646. Data indicate that multiple shapes and sizes of primary particles were common. For example, gibbsite and boehmite were two of the most commonly observed aluminum phases in tank waste. Both of these minerals were observed to have at least three different particle shapes. Not all minerals had images available to distinguish particle shape and size. Therefore, in PNNL-20646, particle shape factors were determined from the limited set of tank waste sample images, surrogate images, and/or expert judgment.

All particles were assumed spherical to simplify calculations. Particle size was based on a sphere with an equivalent volume to that of the observed particle using automated analysis programs and expert judgment as described in Section 3.2.4 of PNNL-20646.

Table 4-5. Shape and Size Data for Primary Particles (2 pages)

Compound	Observed Particle Shape	Maximum Assumed Spherical Particle Size (µm)
Ag (zero valence)	---	2
Ag_2O	---	2
gibbsite $Al(OH)_3$	Thin, round hexagons; faceted lozenges; faceted plates and blocks	200
boehmite $AlOOH$	Rhombohedral platelets; fibrous or acicular; hexagonal plates	0.05
Bi_2O_3	Plates or cubes	3
$BiFeO_3$	---	0.1
Bismuth phosphates	Aggregates	---
$Ca_5OH(PO_4)_3$	---	9
$CaC_2O_4 \cdot H_2O$	---	9
$CaCO_3$	---	55
Chromium Aluminosilicates	Rounded particles	---
$CrOOH$	Rounded particles	0.4
Hematite Fe_2O_3	Rose pellet precipitates	---
$FePO_4 \cdot 2H_2O$	---	0.02
$FeOOH$	---	0.02
HgO	---	2
$KAlSiO_4$	---	8
$LaPO_4 \cdot 2H_2 0$	---	3
$Na(UO_2)_2(PO_4)_2 \cdot 2H_2O$	---	5
$Na_2U_2O_7$	---	5
$NaAlCO_3(OH)_2$	---	4.2

Table 4-5. Shape and Size Data for Primary Particles (2 pages)

Compound	Observed Particle Shape	Maximum Assumed Spherical Particle Size (μm)
$NaAlSiO_4$	---	8
$Ni(OH)_2$	---	0.5
Lead-Iron oxides	Aggregates	---
$Pu(OH)_4$ (co-precipitate on Fe phase)	---	0.02
Pu (zero valence)	---	100
PuO_2	---	40
SiO_2	---	100
Strontium phosphates	Elongated rods	---
ZrO_2	---	50
$Na_2C_2O_4$	---	8
$Na_2CO_3 \bullet H_2O$	---	80
Na_2SO_4	---	112
Na_3FSO_4	---	176
$Na_3NO_3SO_4 \bullet H_2O$	---	80
$Na_3PO_4 \bullet 25NaOH \bullet 12H_2O$	---	440
$Na_3PO_4 \bullet 8H_2O$	---	2,200
$Na_6(SO_4)_2CO_3$	---	32
$Na_7F(PO_4)_2 \bullet 19H_2O$	---	2,100
NaF	---	12
$NaFe_{2-3}(PO_4)_{4-5}$	Plate-like	---
$NaHCO_3$	---	328
$NaNO_2$	---	2,200
$NaNO_3$	---	650
$Na[(UO_2)O(OH)](H_2O)_{0-1}$	Round and elongated	---
Uranium Phosphates	Rod shaped	---
ZrOOH	Rounded particles	---

4.3.1.2 *Agglomerates*

Most of the solid tank waste has been observed in the form of agglomerates, while mineral particle shape and size analyses have been performed on individual primary particles. Optical measurement techniques (e.g., PSD analyzers) have been utilized more frequently than sieving to determine distributions of particle sizes within tank waste slurries. However, these techniques do not distinguish between primary particles and agglomerates.

Agglomerate shapes are typically roundish or oblong combinations of primary particles attached together. Images showing some small agglomerates of primary particles can be observed in Section D.4 in Appendix D of PNNL-20646.

Various methods have been utilized with the PSD analyzers to obtain more detailed information concerning particle size distributions. The methods have included a flowing or stirred slurry vessel and either using the as-received sludge or sonicating it prior to analyses. Comparison of these methods in PNNL-20646 indicated that sonication did not break apart all agglomerate

particles, and the PSDs for the stirred (e.g., no-flow), unsonicated samples provided a broader range of particle sizes than any of the other methods. The no-flow, unsonicated PSD results are also typically larger than the results of the other methods and are thus used in this report to select bounding particle sizes.[5]

In using PSD analyzer data to determine the largest particle size observed in Hanford tank waste, data for the no-flow, unsonicated saltcake composite and no-flow, unsonicated sludge composite were provided in Table H.3 on pg. H.16 of PNNL-20646. The largest particle sizes are listed in Table 4-6. It is assumed that these large particles are agglomerates, but with only data from the PSD analyzer and without further analysis of the individual large particles, it is uncertain whether this assumption is indeed valid.

Table 4-6. Largest No-Flow, Unsonicated Particle Size for Saltcake and Sludge Waste

Method	Largest Particle Size (µm)
No-flow, unsonicated saltcake	1,796
No-flow, unsonicated sludge	1,441

As referenced in PNNL-20646, PSDs from the Horiba LA-910 and Microtrac X-100/UPA systems of settled material from laboratory tests failed to identify very many large particles despite their being visible during the settling tests (HNF-8862, *Particle Property Analyses of High-Level Waste Tank Sludges*). HNF-8862 also noted that, in comparison to sieving analysis of particle size, the light-scattering particle size analyzer was poor at finding particles above 500 µm in size. Thus, larger particles may be underrepresented by these instruments.

4.3.2 Particle Size and Shape Uncertainties

Uncertainty analysis of the various techniques used to measure particle shape and size of Hanford tank wastes has been thoroughly performed in Appendix G of PNNL-20646. This section qualitatively describes the uncertainties of the analytical techniques that have been used at the Hanford site. The qualitative uncertainty of the microscopy and optical techniques are discussed, since these are the most frequently used methods for particle analysis.

Primary particles and their shapes are most commonly classified using TEM and SEM. These techniques take images of the particles and provide a more exact method (than particle size analyzers) for primary particle shape and size analyses. Although microscopy is the preferred method to determine the shape of tank waste primary particles, sampling errors can be large when attempting to use this method to determine PSDs. Typically, the sample size is small and the sample is mounted on a slide in a different environment than that of the original tank waste. In changing the chemistry of the solution in contact with the solids, the size and shape of the particles may change from their original state leading to uncertainty in the measured results.

---

[5] It is concluded in PNNL-20637 (*Comparison of Waste Feed Delivery Small-Scale Mixing Demonstration Simulant to Hanford Waste)* that characterization of the Hanford waste particle size with the no-flow unsonicated PSD measurement method can represent in situ process data.

The more general approach to determine the range of particle sizes is to use PSD instrumentation. Although the PSD instruments can provide analysis of the range of particle sizes within the Hanford tank waste sample, there are several limitations that must be considered in using the PSD data. The most prominent limitations include the following:

- Measured sizes are for equivalent spherical particles having the same average cross-sectional area.

- All solid particles are characterized using the same refractive index, even though different mineral phases have different refractive indices. Further, only one optical property setting can be made on the machine for an analysis. If the setting is not optimal for all of the solids being analyzed, it can result in biased measurements.

- Some particles may not be suspended in the analytical device during measurements. If the particle is too dense or too large, it will not be included in the analysis.

- Minimum and maximum particle sizes measured are within the limitations of the analytical device.

These limitations restrict the information gathered for Hanford tank waste solid analyses. No other method has been developed to provide more representative data. The optical PSD measurements are used and characterized as "apparent" PSD results.

Other limitations of PSD analyzers include the following:

- The range of particle sizes that can be measured is limited. The largest PSD range for the devices used is 0.02 µm to 2,000-µm diameter (PNNL-20646).

- Bias is introduced by the measurement devices. If air bubbles were formed during mixing or flowing within the instrumentation, they may be recorded as a particle.

- Measurements may vary because of the measurement methodology. Whether the system is flowing or stirred can affect the particle size and potentially lead to agglomerate breakage. Sonication affects the particle size and can potentially lead to agglomerate breakage. The selection of carrier fluid can affect the measurements and can change the environment of the solids. This change in environment may lead to a new equilibrium state that is different than that of the original tank waste.

Limitations of PSD analytical methods lead to many uncertainties in the results. Uncertainties in the PSD results include the underestimation of large (>500 µm) and/or dense particles; an inability to distinguish between agglomerates and individual primary particles; limited particle shape information; particle agglomeration or breakage during solid suspension within the PSD equipment; and interpolation and extrapolation of percentiles making up a PSD.

The set of percentiles of interest selected for use in PNNL-20646 were P01, P05, P10, P20, P25, P30, P40, P50, P60, P70, P75, P80, P90, P95, P99 and P100, where Px denotes the particle size below which x% of the distribution (on a volume percent basis) falls. The particle size information generated for a sample from an individual tank did not include a P100 (largest determined particle size) value for any of the samples. Further, anywhere from a few, to many, to most of the percentiles were missing for the instrument results for some samples. When

needed and possible, interpolation or extrapolation methods were used to fill in percentiles that had no reported values. The method used to obtain estimates of P100 for the tank samples involved the use of the Gumbel probability distribution, as discussed in detail in Section 3.2.5.3 of PNNL-20646. For the M-12 groups the resulting PSDs included particle size percentiles for P0, P01, P05, P10, P15, P20, P25, P30, P40, P50, P60, P70, P75, P80, P90, P95, P99 and P100, where the ellipses mean that the percentiles increased by factors of 5. The percentiles in the M-12 data that were not included in the set of percentiles of interest (listed earlier) were dropped for further analysis purposes in PNNL-20646 because the number of percentiles generated for M-12 groups was greater than for samples from individual tanks. Note that the particle size assessments used for the M-12 data included a P100 estimate as part of the assessment output, so extrapolation using the Gumbel probability distribution was not needed for the M-12 data (PNNL-20646).

Sieve separation has been performed on some tank waste solids. For example, heel solids were collected using a clamshell sampler from tank S-112 in June 2007 (74A10-WSC-08-152, *Results of Testing Performed to Characterize Tank 241-S-112 Heel Solid*). Particle size analyses of these solids were initially performed through sieving the solids into two fractions; particles greater than 850 μm and particles less than 850 μm. Of the solids collected in the greater than 850-μm sieve, the distribution of particles was found to be: 1 large body about10 mm in diameter, about 10 particles 3 to 5 mm in diameter, 10 to 20 particles 1 to 2 mm in diameter and about 50 particles ≤ 1 mm in diameter (74A10-WSC-08-152).

Similarly, a few large particles were found in the AN-102 grab samples taken near the settled solids/supernatant interface. These particles were retained on the 2.38-mm sieve and could not be crushed with a glass stopper to pass through the screen. On page 3.1 of PNWD-3228, *Chemical and Physical Properties Testing of 241-AN-102 Tank Waste Blended with 241-C-104 Wash/Leachate Solutions*, these solids were characterized as being consistent with gravel. Further characterization was not performed and the particles were subsequently discarded. About 5,250 g of slurry passed through the sieve and 7.8 grams (dry basis) did not. In Figure 4-4, the size of the agglomerated particle (in the tweezers) looks to be on the order of 5 by 3 screen openings based upon the shadow reflected on the sieve. This would make the particle approximately 12 by 7 mm.

It is uncertain how common these larger agglomerate particles are or what their compositions are because they are not commonly documented in laboratory reports. Typically, PSDs are the only documented analyses for particle size in published reports. Optical TEM and SEM images are less commonly published, but have been used as an attempt to determine the primary particle size of minerals that make up the solid agglomerates.

Figure 4-4. Portion of Tank AN-102 Grab Sample Retained on a 2.38 mm Sieve

It is uncertain how common these larger agglomerated particles are or what their compositions are because they are not commonly documented in laboratory reports. Typically, PSDs are the only documented analyses for particle size in published reports. Optical TEM and SEM images are less commonly published, but have been used as an attempt to determine the primary particle size of minerals that make up the solid agglomerates.

4.3.3 Particle Size and Shape Variation

This section discusses the variation in PSDs over the Hanford tank wastes for which there are data. PSDs were presented and discussed in PNNL-20646 for various tanks, waste types and composites, based on data collected using different instruments that use different particle size measurement methods. General waste types of sludge, saltcake, and mix (combination of sludge and saltcake) were identified based on the relative concentrations of soluble and insoluble undissolved solids (UDS). As specified in RPP-10006, *Methodology and Calculations for the Assignment of Waste Groups for the Large Underground Waste Storage Tanks at the Hanford Site*, a tank is classified as sludge if at least 75 volume percent (vol%) is sludge solids (insoluble UDS), and similarly, saltcake if it is at least 75 vol% saltcake/salt slurry solids (soluble UDS). A mix tank does not meet either of these criteria.

For the current work, only those tanks and waste types that are primarily sludge are considered because retrieval activities can dissolve the soluble waste. The different measurement methods used to generate PSDs included 1) flowing sonicated, 2) flowing unsonicated and 3) no-flow unsonicated. Table 4-7 lists the number of tanks and sludge samples with PSDs measured using each of the three measurement methods. The data in Table 4-7 is based on information in Table 3.17 of PNNL-20646.

Table 4-7. Numbers of Tanks/Sludge Samples with PSD Data Collected Using Three Measurement Methods

Flowing Sonicated	Flowing Unsonicated	No-Flow Unsonicated
15/63	15/61	13/87

Particle size distribution data were generated for samples from M-12 groups (M-12 and the M-12 groups are explained in Section 6.1.1.2) as well as individual Hanford waste tanks. Figure 4-5 shows PSD traces for sludge samples from individual tanks and samples from M-12 groups. Included are data measured by all three PSD measurement methods (non-flow unsonicated, flowing unsonicated, and flowing sonicated). The PSD traces for the individual tank samples are black, whereas the traces for the M-12 samples are red. Figure 4-5 shows that particle sizes for the various samples ranged from less than 0.2 microns to over 1000 microns. Furthermore, it is clear that the range of particle sizes for the M-12 data are encompassed by the range of particle sizes for the data from individual tank samples. This is reasonable given that the M-12 groups were formed by mixing samples from multiple individual tanks.

Figure 4-5. Cumulative PSD Traces for Sludge Samples from Individual Tanks (black) and M-12 Group Samples (red), Obtained Using All Three Measurement Methods
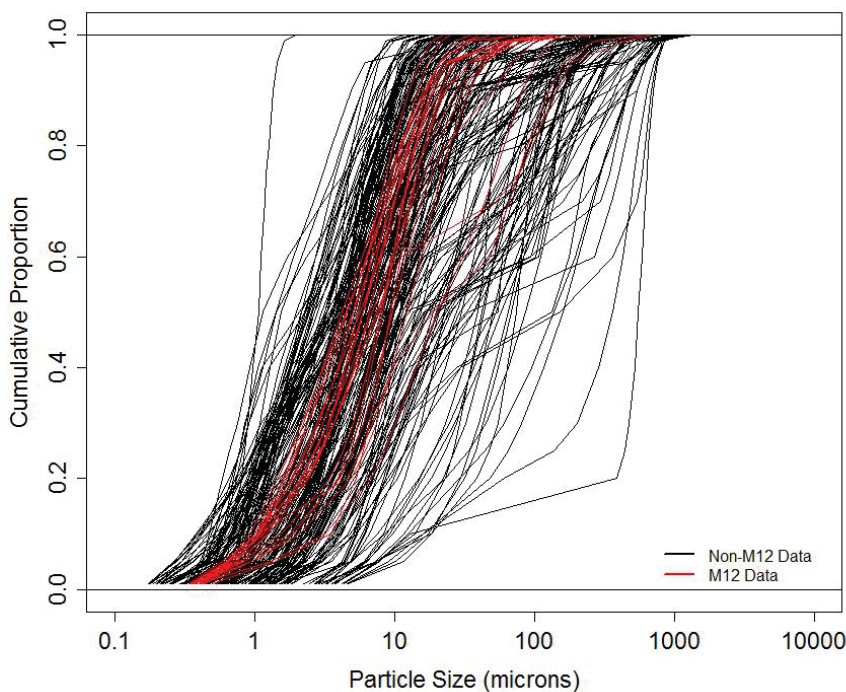
In this report, the description of particle sizes for waste that will be delivered from the tank farms to the WTP focuses on bounding cases with particular emphasis on the upper limits of particle size. Thus, it suffices to consider the PSDs for individual tank samples and exclude PSDs for the M-12 data. For complete details concerning PSDs as understood to date, the reader is directed to Section 3.2.5 of PNNL-20646.

PNNL-20646 reported minimum, median and maximum PSDs in an attempt to describe ranges in particle sizes for the different categories of waste and measurement methods. The reported

minimum and maximum PSDs provide estimates of likely extreme particle sizes for the different waste tanks, waste types, and composites. The reported median PSDs (50th percentiles) provide an estimate of "typical" particle sizes rather than potential extremes. In this section, we consider minimum, median and maximum PSDs over the available samples for a given tank.

Figure 4-6 through Figure 4-8 present the minimum, median and maximum PSDs over sludge samples within each tank, with different colors representing the PSD traces for the three different PSD measurement methods. Note that different samples had PSDs measured with different methods, so it is necessary to consider the PSDs over all three measurement methods in order to see the variation over all sludge samples from individual waste tanks. However, the primary purpose of Figure 4-6 through Figure 4-8 is to compare the variation of PSDs for the three measurement methods. PNNL-20646 concluded that the no-flow, unsonicated method for measuring PSD resulted in generally larger particle sizes than other measurement methods represented in the data (flowing unsonicated and flowing sonicated). Still, the no-flow, unsonicated data also included smaller particle sizes, comparable to the smaller particle sizes seen for the other two measurement methods. That is, the range of particle sizes for the no-flow, unsonicated data nearly encompasses the range of particle sizes for the tank sample data with the flowing-sonicated and flowing-unsonicated methods, except for the smallest particle sizes. This is true for the reported minimum, median and maximum PSDs for sludge samples as illustrated in Figure 4-6 through Figure 4-8.

For the reasons given in the previous discussion, it was decided to focus on variation in PSDs for sludge samples using the no-flow, unsonicated measurement method. The difference in coverage at the lower end of the particle size ranges is not a concern for this report because, as mentioned previously, the primary interest is on the larger particle sizes.

The remaining discussion of variation of PSDs focuses on the sludge samples measured using the no-flow, unsonicated method. There were 87 such samples from 13 tanks. Figure 4-9 shows the minimum, median, and maximum PSD traces from those samples. The PSD median trace for tank C-103 has all particle sizes less than ~ 5 μm (data for that tank is discussed more in the following paragraph). Overall, Figure 4-9 shows that particle sizes range from approximately 0.30 to over 1000 μm.

Figure 4-6. Cumulative PSD Traces, Minimums over Sludge Samples from Individual Tanks Using Three Measurement Methods
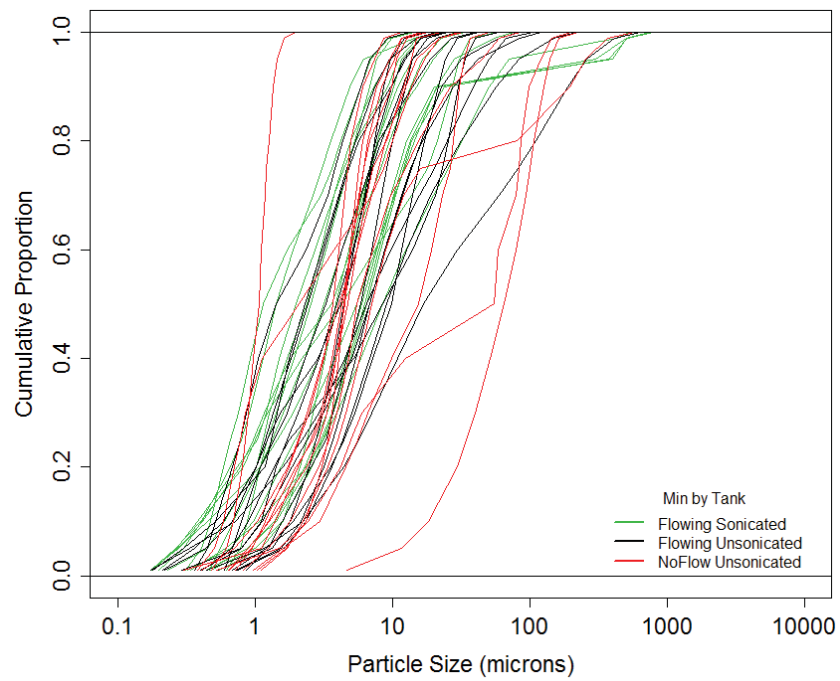
Figure 4-7. Cumulative PSD Traces, Medians over Sludge Samples from Individual Tanks Using Three Measurement Methods
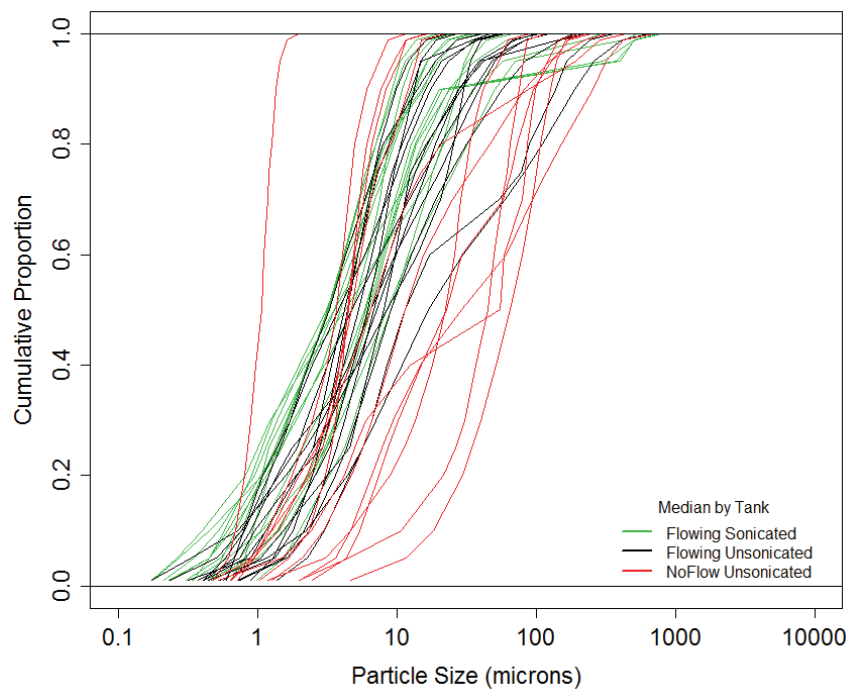
Figure 4-8. Cumulative PSD Traces, Maximums over Sludge Samples from Individual Tanks Using Three Measurement Methods
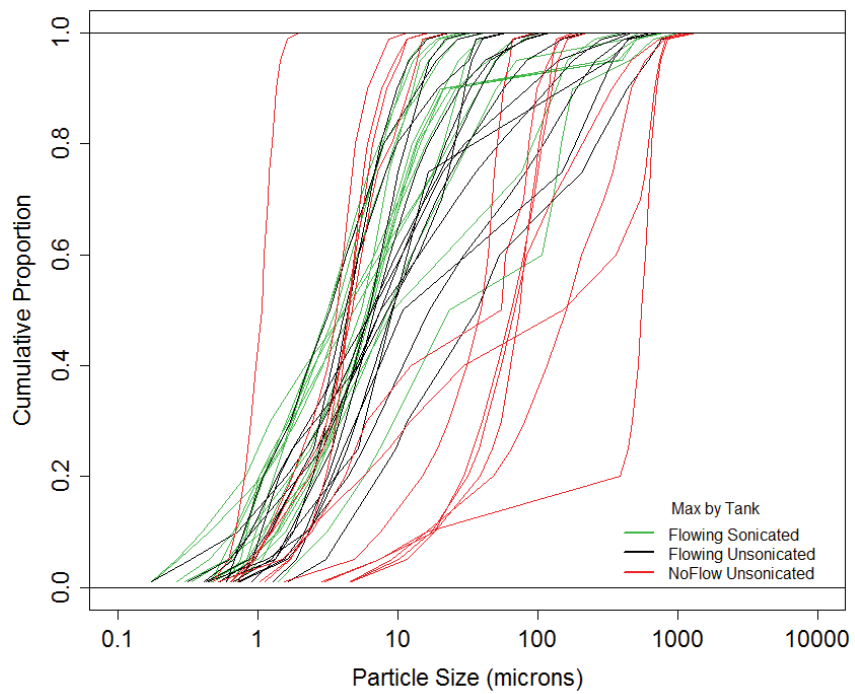
Figure 4-9. Cumulative PSD Traces, Minimums, Medians, and Maximums over Sludge Samples from Individual Tanks for the No-Flow, Unsonicated Measurement Method
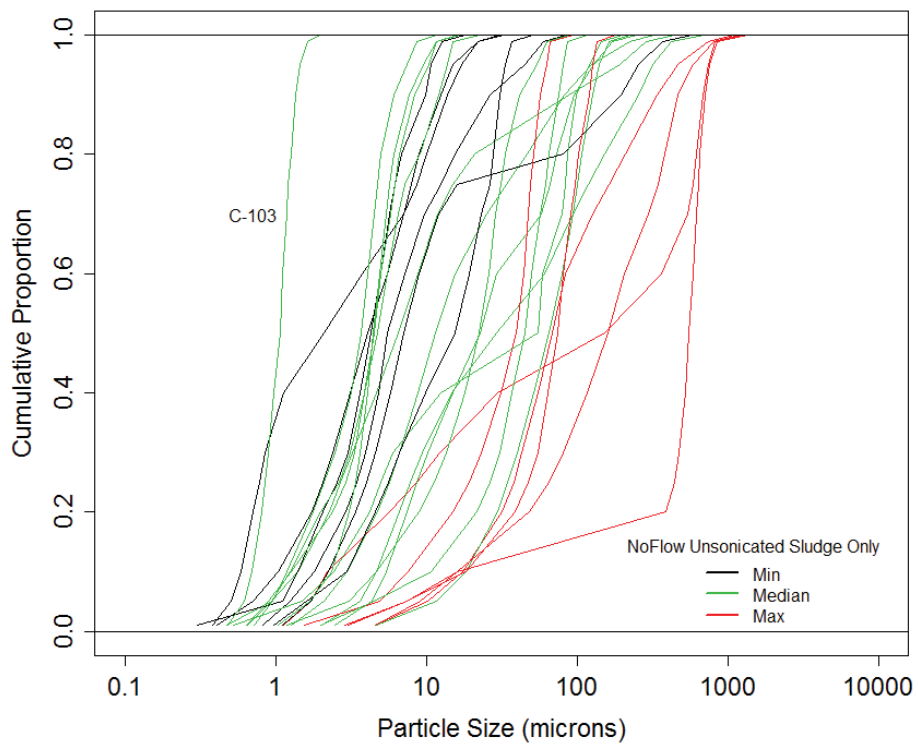
Table 4-8 provides the PSD data depicted in Figure 4-9. From P40 up to P100, the minimum particle sizes are the same for the minimum, median, and maximum PSDs. Also, for P05 up to P30, the minimum particle sizes are the same for the Median and Maximum PSDs. These equal values occur because one of the tanks (C-103) had only one sample for the no-flow, unsonicated sludge conditions. So for this sample, the minimum, median and maximum particle sizes were all the same at each of the percentiles reported. Furthermore, this particular sample had smaller particle sizes from P40 to P100 than other sludge samples measured with the no-flow, unsonicated method. The PSD trace for Tank C-103 is identified in Fig 4-9. For this trace, the median PSD was plotted last and therefore over plots the minimum and maximum PSDs for this tank.

Table 4-8. Minimums and Maximums of Minimum, Median, and Maximum PSDs Over Sludge Samples from Individual Tanks

*	P01	P05	P10	P20	P25	P30	P40	P50
Minimum PSDs								
Minimum	0.301	0.510	0.586	0.709	0.780	0.853	0.972	1.070
Maximum	4.65	11.72	18.25	29.78	34.51	39.83	51.37	64.98
Median PSDs								
Minimum	0.476	0.620	0.693	0.815	0.856	0.896	0.972	1.070
Maximum	4.65	11.72	18.25	29.78	34.51	39.83	51.37	64.98
Maximum PSDs								
Minimum	0.484	0.620	0.693	0.815	0.856	0.896	0.972	1.070
Maximum	4.65	11.72	18.40	386.80	444.92	472.69	521.16	552.93
*	P60	P70	P75	P80	P90	P95	P99	P100
Minimum PSDs								
Minimum	1.113	1.179	1.213	1.261	1.354	1.449	1.624	1.950
Maximum	79.25	93.48	101.01	108.18	196.84	258.00	369.11	584.52
Median PSDs								
Minimum	1.113	1.179	1.213	1.261	1.354	1.449	1.624	1.950
Maximum	79.25	94.82	119.50	152.44	254.88	316.00	424.19	701.93
Maximum PSDs								
Minimum	1.113	1.179	1.213	1.261	1.354	1.449	1.624	1.950
Maximum	586.57	620.51	638.02	656.06	711.92	756.52	858.48	1347.58

Notes: *Pxx denotes the particle size below which xx% of the particle sizes fall.

Figure 4-10 shows separate PSDs for each of the 87 sludge samples measured by the no-flow, unsonicated method. This plot does not illustrate the PSDs within tanks and their ranges over tanks as do Figure 4-7 through Figure 4-9. However, Figure 4-10 provides for easier comparison of the variation of PSDs over the 87 sludge samples from the 13 tanks without the need for minimum, median, and maximum PSDs determined over the samples from each tank.

Figure 4-10. Cumulative PSD Traces of 87 Sludge Samples from Individual Tanks for the No-Flow, Unsonicated Measurement Method
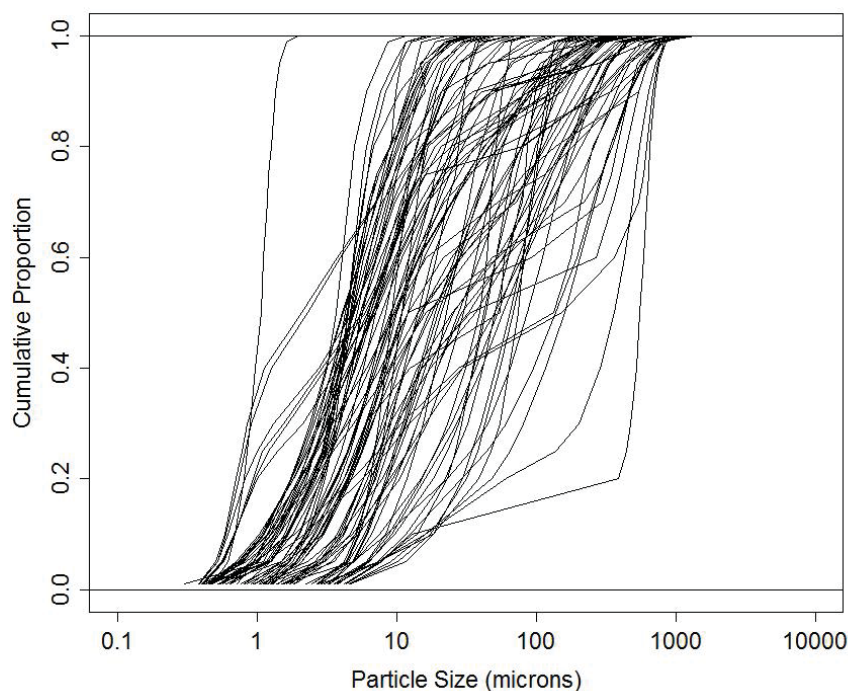
4.4   LARGE AND/OR DENSE PARTICLE ESTIMATES

Data provided in Sections 4.2 and 4.3 were analyzed to determine the particle size and density values. This section provides density/particle size combinations that are used in the Section 7.0 calculations. The estimates include the following:

- The densest primary particle and its largest size.

- The largest primary particle and its density based on SEM.

- The largest particle observed, coupled with the highest crystal density observed in AY-102 waste.

- The largest agglomerate and its density based on PSD results.

- The largest particle observed, coupled with the highest crystal density observed in AZ-101 waste.

- The hypothetical largest agglomerate and its density based on transfer equipment limitations (i.e., pump screen mesh size).

The densest particle that might be in the Hanford tank waste solids is plutonium (Pu) metal, with a density of 19 g/mL, and its largest estimated particle size is 100 μm (RPP-RPT-50941). This largest particle size was an estimated upper limit determined by several subject-matter experts on Pu processing.

In determining the mass of Pu solid material sent to the tank farms, several bounding assumptions were also included in the evaluation performed by the subject-matter experts. Some of the more prominent bounding assumptions were the following:

- The fraction of material unaccounted for associated with the liquid waste streams from the Plutonium Finishing Plant (PFP) from 1973 to 2004 was multiplied by a factor of 2.

- The most conservative values from the PSDs were used for the PFP source material.

- Plutonium metal fines were assumed to persist in the Hanford Tank waste, even though they are not thermodynamically stable in the highly caustic environment and may not have survived the extended storage time.

From Table 4-3, the largest low-solubility solid was gibbsite. The other solids that were larger, including sodium phosphates, sodium fluorophosphates, sodium nitrite, etc., are high solubility salts. Therefore, gibbsite is the logical choice for the largest undissolved solid mineral phase. The density of the mineral gibbsite is 2.4 g/mL. The largest observed particle size for gibbsite was 200 μm. Assuming that the 200 μm gibbsite particles form agglomerates with a fractal dimension of 2.25, the density is the following:

$$\rho = \left(\frac{200\ \mu m}{R}\right)^{3-2.25} \left(2.4\frac{g}{mL} - \rho_L\right) + \rho_L \qquad\qquad (4-2)$$

where ρ = agglomerate density (g/mL)

        R = agglomerate size (μm)

        ρ_L = density of the liquid or gas filling the pore space (g/mL)

Gibbsite agglomerate densities can be calculated using the bounding liquid density (1.37 g/mL) and bounding particle sizes (1,441 and 9,525 μm). Table 4-9 lists the particle size and density combinations that are used in Section 7.

Table 4-9. Particle Size and Density Combinations to Use in Limits of Technology Calculations

Particle	Diameter (μm)	Density (g/mL)
Most dense primary particle (Pu)	100	19
Largest primary particle observed by SEM (gibbsite)	200	2.4
Largest Particle hypothetically combined with highest density (Bi_2O_3) in AY-102	1,268	8.9
Agglomerate based on PSD limit (gibbsite)	1,441	1.6
Largest Particle hypothetically combined with highest density (Ag_2O) in AZ-101	1,441	7.14
Largest agglomerate based on pump screen mesh (gibbsite)	9,525*	1.43

Notes: *9,525 μm = ⅜-inch.

4.5 PRELIMINARY ASSESSMENT OF TRANSFER OPERATIONS AND STORAGE EFFECT ON PARTICLES

4.5.1 Effect of Single-Shell Tank Retrievals on Particles

Limited sampling and in-tank visual observations suggest that some large waste agglomerates remain behind in the SSTs and that retrievals have had some effect on waste PSDs. Examination of SST heel solids confirm that large agglomerates exist and that the bounding ⅜-inch agglomerate postulated earlier is reasonable. Staged DST waste feed is unlikely to resemble SST heels; however, the SST heel data suggest that some large particles might be present. Solid phase characterization was performed on heel solids samples from the majority of retrieved tanks, but PSDs within heel solids are only currently available for tanks S-112 and C-108.

4.5.1.1 *Tank Heel Particle Sizes*

The S-112 heel solids were first separated into greater than 850 μm and less than 850 μm fractions by wet sieving with a U.S. Standard No. 20 sieve. The greater than 850 μm fraction was subsequently dried and weighed. Several large particles ranging from 1-mm to 5-mm in diameter and one large body with diameter approximately 10-mm were observed in this sieve fraction. Particle size measurements were performed on the greater than 850-μm fraction using a light-scattering-based technique. Sieve and light-scattering results were combined and the overall PSD within the S-112 heel solids is provided in Table 4-10.

Table 4-10. Tank S-112 Heel Solids Particle Size Distribution

< 2 μm	2-50 μm	50-250 μm	250-850 μm	> 850 μm
0.9 wt%	13.7 wt%	61.9 wt%	13.2 wt%	10.3 wt%

X-ray diffraction analysis of tank S-112 heel solids revealed that a majority of the samples were composed of gibbsite, $Al(OH)_3$. Trace amounts of sodium carbonate monohydrate, $Na_2CO_3 \cdot H_2O$ (thermonatrite) were also identified. Polarized light microscopy and SEM-EDS analyses also confirmed that the solids were dominated by coarse gibbsite crystals (Figure 4-11).

Figure 4-11. Gibbsite Particles in S-112 Heel Solids
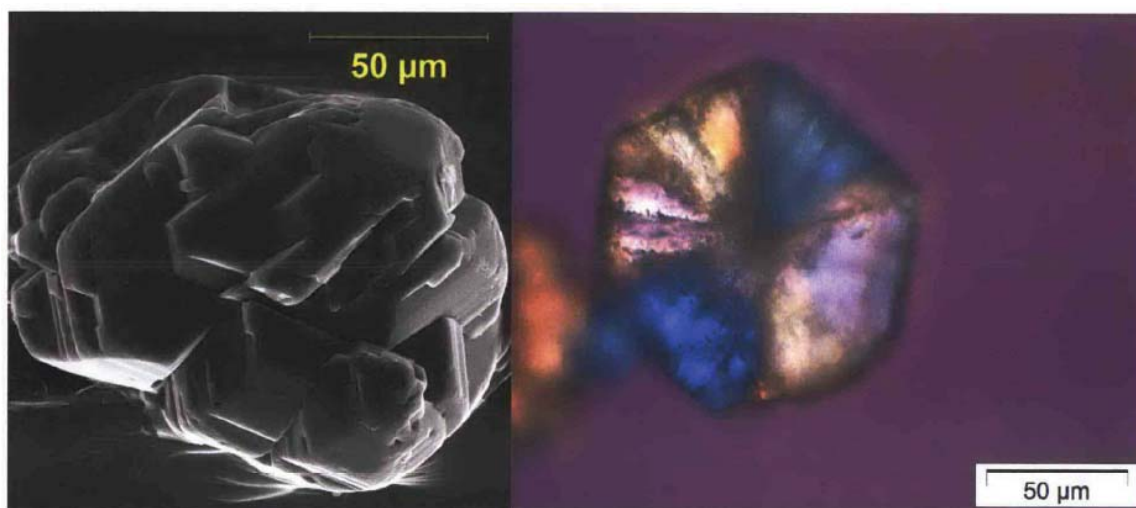
Tank C-108 heel solids were also analyzed for PSD and solid phase characterization. Heel solids were initially separated into greater than ¼-inch and less than ¼-inch fractions using coarse sieves (Figure 4-12). The greater than ¼-inch fraction made up 18.6 wt% of the composite sample, with the less than ¼-inch fraction making up the remainder. The smaller fraction solids were again separated into a greater than 600 μm fraction by wet sieving. The greater than 600 μm fraction accounted for 19.9 wt% of the initial composite sample.

Figure 4-12. Tank C-108 Heel Solids

Visual observation of the C-109 heel solids indicated a large variability in the physical characteristics. Six of the eight samples were selected for the initial characterization. Gibbsite was the dominant mineral phase identified in the crushed cobbles subsamples (LAB-RPT-11-00009, *Final Report for the Initial Solid Phase Characterization of the 2011 Grab Samples and Composite for the C-109 Hard Heel Study*). X-ray diffraction analysis

indicated gibbsite was the only crystallized phase in the crushed cobbles. Scanning electron microscopy examination results indicated that the crushed cobbles consisted primarily of agglomerated gibbsite crystals ranging from 20 to 100 μm in size. Figure 4-13 shows an example of gibbsite heel samples.

Figure 4-13. Scanning Electron Microscopy Images of Tank C-109 Heel Sample
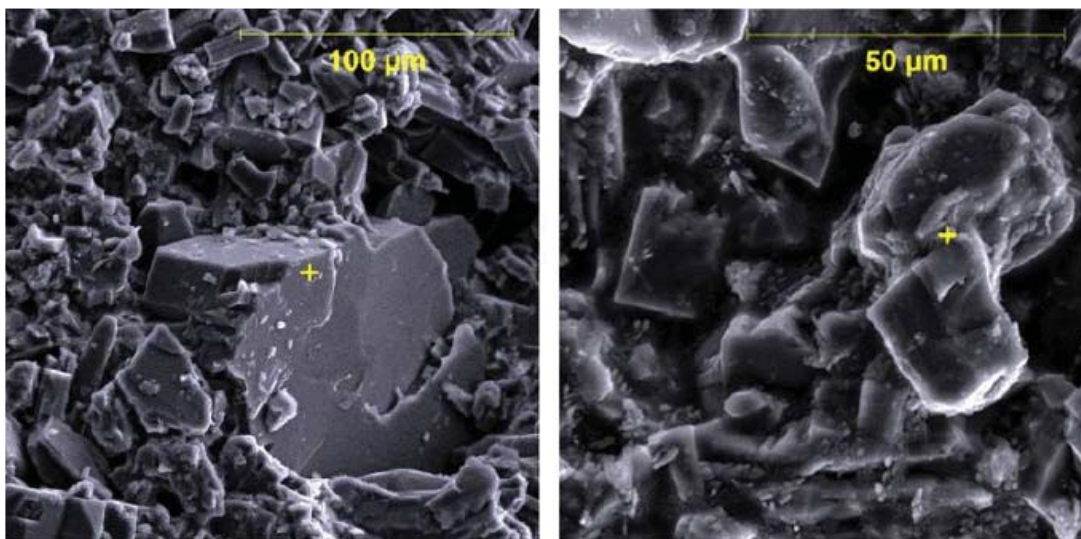
Similar to C-109 heel solids, composites of C-110 heel solids were characterized for solid phases (see Figure 4-14). The left image shows large solids surrounded by fine-grained whitish to pale yellow materials. The right image shows a mixture of coarse-to-fine-grained sand-sized materials. X-ray diffraction analysis detected natrophosphate as the only solid mineral phase. Polarized light microscopy and SEM analyses indicated the minor presence of gibbsite, sodium aluminosilicate, sodium diuranate, and nastrophite (LAB-RPT-11-00008, *Solid Phase Characterization of Heel Samples from Tank 241-C-110*).

Figure 4-14. Images of As-Received C-110 Heel Solids
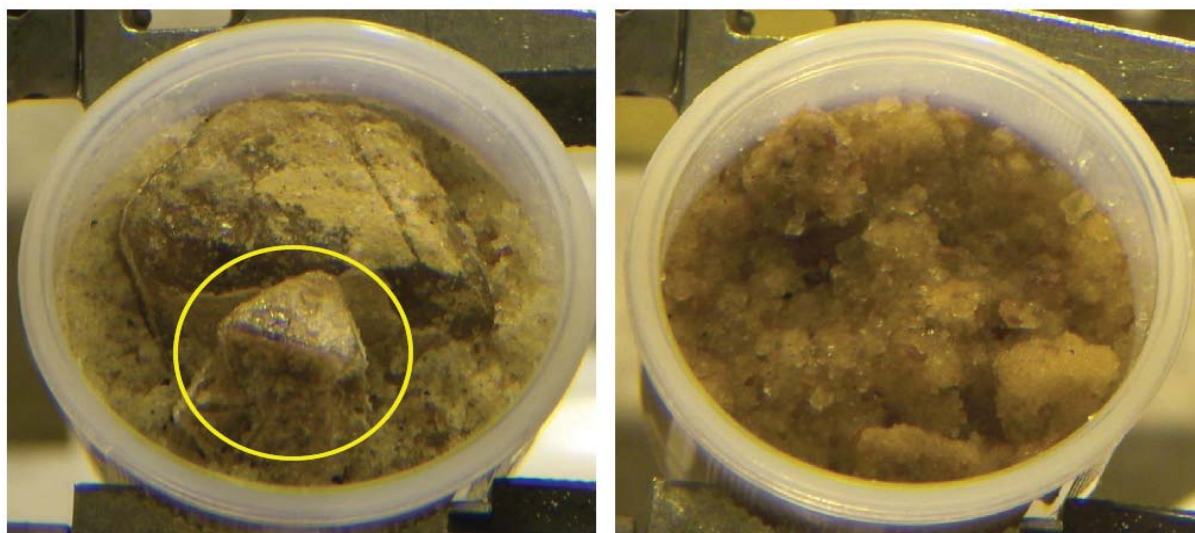
4.5.1.2 *Tank Heel Particle Densities*

Bulk density of the S-112 heel was 1.91 g/cm^3 (at 28^{0}C). Using a similar method, the bulk density of the tank C-108 heel was 1.88 g/cm^3. See LAB-RPT-10-00001, *Results of Physicochemical Characterization, and Caustic Dissolution Tests on Tank 241-C-108 Heel Solids*. The average particle density of the heel solids composite was estimated by removing the weight and volume of the interstitial liquid in the composite from the bulk density calculation. Assuming that all water in the composite was associated with interstitial liquid, the solids particle density was directly calculated with inputs from a measured interstitial liquid density and the fractions of water in the wet sample and in the interstitial liquid. The average particle density of tank S-112 heel solid composite was estimated as 2.53 g/cm^3.

It was more complicated to estimate the tank C-108 particle density due to the nature of the heel. The majority of the water in the C-108 heel composite was not associated with interstitial liquid. No free liquid was present, thus, no interstitial liquid composition analysis could be performed. Furthermore, the major portion of the C-108 heel solids was water soluble. For those reasons, an alternative approach was applied to estimate particle density of C-108 heel solids. At the completion of the bulk density measurement, the composite had been through a *de facto* water wash of 0.45 parts water to 1 part composite (weight-based) and the calculated weight of the remaining heel solids was 404.78 g. The calculated dry density of the remaining solids was reported as 1.933 g/cm^3 (LAB-RPT-10-00001).

4.5.2 Effect of Long-Term Storage on Particles

An understanding of the waste evolution during storage is important because most of the waste will not be delivered for many years and there is an opportunity for the waste physical properties to change during storage.

The sludge in tank AZ-101 has been stored with a liquid surface since the tank was filled. Particle size analyses on year 2000 core samples were performed and the PSD is reproduced in Figure 4-15. [6] A mean particle size diameter of 5.4 µm was determined (PNWD-3206, *Filtration, Washing, and Caustic Leaching of Hanford Tank AZ-101 Sludge*). The AZ-101 sludge sample was run through a laboratory scale cell-unit filter (CUF) simulating the WTP ultra filtration process. After running through the CUF, the mean particle size was 1.6 µm indicating that the agglomerated particles were broken up during transport in the filter. These results suggest that the AZ-101 slurry undergoes substantial agglomeration. HNF-8862 showed a relationship between energy input into a slurry and PSD. Increased impeller speed, pump speed, and sonication in the PSD instrument led to decreased particle sizes.

The PSD analyzers can be operated using various methods to mobilize the sample and these methods can affect particle agglomerates. Comparison of the PSD data for AZ-101 as reported in PNNL-20646 illustrates this influence. The median particle size for the no-flow, unsonicated PSDs is 18.7 µm, while for the flowing sonicated samples it is 3.2 µm, indicating that agglomerated particles were broken up by the flow or sonication, or both. Similar effect is observed in other wastes (PNNL-20646) and increased agitation in the PSD analyzer has also been shown to reduce particle size for multiple tank wastes (e.g., HNF-8862) again indicating the breakup of agglomerated particles.

Figure 4-16 shows Scanning Electron Microscope images of particles in the AZ-101 sludge sample. These images show that the particles in AZ-101 are agglomerates of much smaller particles. Other tanks would also be expected to undergo agglomeration. The factors that affect agglomeration are well-understood (Elimilech et al., 1995), but are not necessarily easily quantified for Hanford waste in a predictive manner. What can be concluded is that the extent of agglomeration may change over time if the conditions of the Hanford waste change over time. PNL-7758, *Characterization of the first core sample of neutralized current acid waste from double-shell tank 101-AZ*, reported the PSD of Tank AZ-101 samples from 1989 and reported a mean particle size of 5 µm, which is not appreciably different from the 5.4 µm report for the sample taken in 2000. The PSD measurement technique of PNL-7758 is not known, and thus it is indeterminate if this comparison between the data of PNL-7758 and PNWD-3206 is meaningful.[7] Within the limitations of the data, however, the extent of agglomeration did not change appreciably after more than 10 years of storage. This may provide indication that the physical properties of tank samples available now will still be representative of waste behavior at the time the WTP is operational.

---

[6] The difference between the PSD results of Figure 4-15 and Figures 7-8 through 7-10 can be attributed to 1) the samples for the data of Figure 4-15 were agitated with a dual-bladed impeller in a laboratory "homogenization vessel" for approximately 2 hours, and 2) the data of Figure 4-15 is from the flowing unsonicated PSD measurement technique, while that of Figures 7-8 through 7-10 is from the no-flowing unsonicated PSD measurement technique (see Section 4.3.3).

[7] As noted with respect to the data of Figure 4-15 and Figures 7-8 through 7-10, sample handling and PSD measurement technique can influence PSD results.

Single-shell tanks have not been stored with a wet surface, which has allowed some waste to dry out. An evaluation of the surfaces of several C-farm tanks has shown that some C-farm waste develops a hard surface that requires substantial force to break apart (RPP-RPT-52196, *Methods for Heel Retrieval for Tanks C-101, C-102, and C-111*). It is not clear how these hard surfaces will evolve over time.

Figure 4-15. Particle Size Distribution for CY 2000 AZ-101 Core Sample
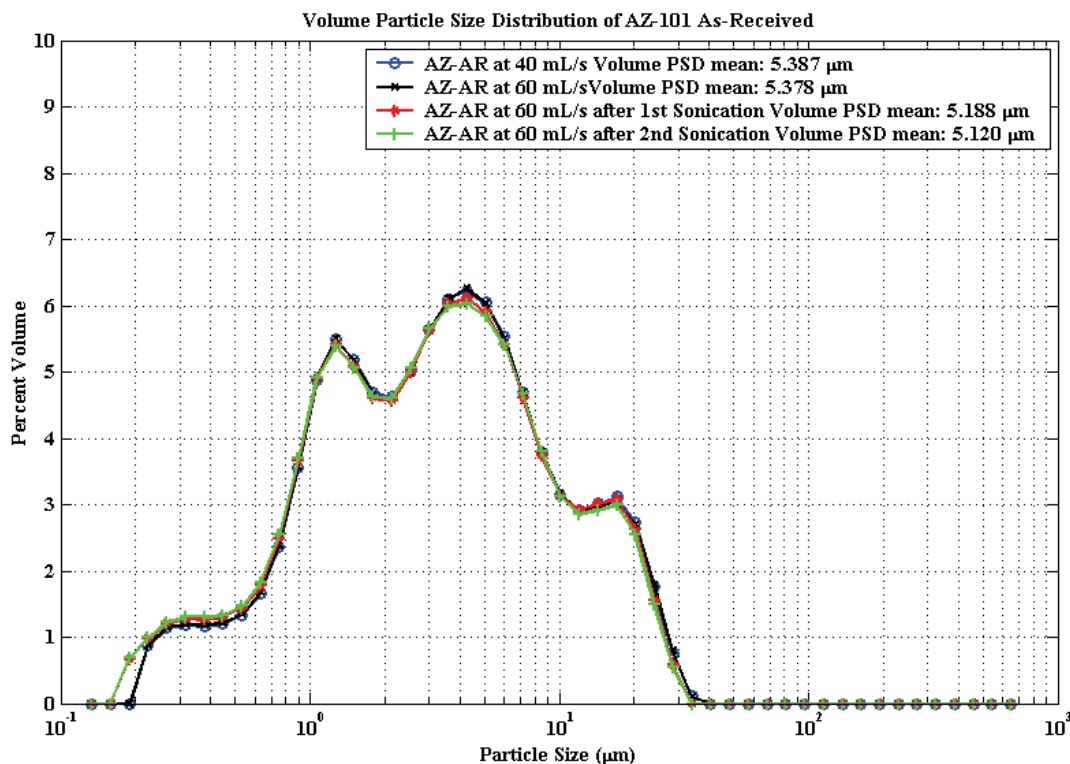
Figure 4-16. Images of Large Agglomerates in AZ-101 Waste
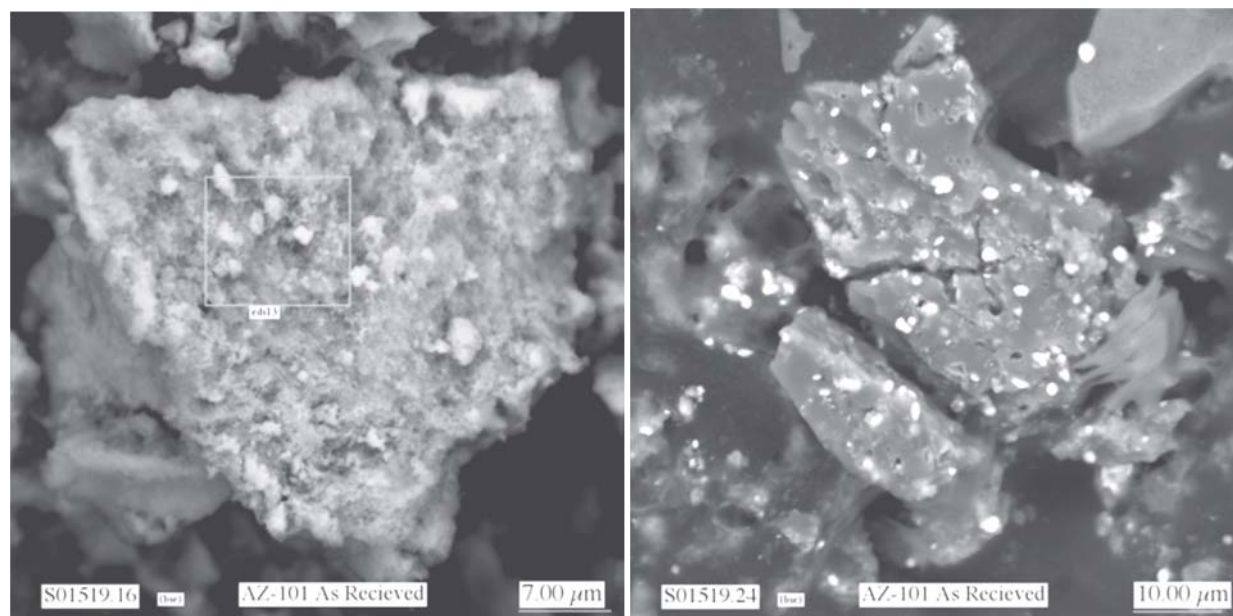
4.5.3   Effect of Waste Feed Delivery on Particles

Ultimately, what is of interest for particles that will be fed to WTP is the distribution of solid particle size, shape, and density in the waste slurry delivery batches. Because the plans for retrieval, mixing and WFD of tank wastes to WTP are not complete, it is difficult to provide accurate, quantitative estimates of the distributions of particle size, shape, and density. However, expertise and experience provides for making some qualitative or semi-quantitative judgments.

It is believed that delivered particle size is limited by the transfer pump inlet screen (e.g., ⅜-inch or 9,525 µm) or transfer pump pipe openings and that typical particle shape is an agglomerate of roughly spherical shape. Any rods or sharp edges might be broken and/or worn as the solids are agitated during retrievals, transfers and in preparation for feeding waste to WTP. Some break up of agglomerates might occur when slurry is cycled through the mixer pumps and transfer pumps, but these WFD operations by themselves are not likely to eliminate large agglomerates.

As described in more detail in Section 7.1.2, jet mixer pumps were used in the AZ-101 baseline configuration mixer pump test reported in RPP-6548, *Test Report, 241-AZ-101 Mixer Pump Test*. The PSD data from an AZ-101 core sample taken approximately 5 months prior to the mixer pump operation is compared to PSD data from suspended solids samples taken within nominally 10 to 100 minutes after 2.5 days of mixer pump operation was stopped in Figure 7-8, Section 7.1.3. The similarities of the PSDs, depending on sample location, suggest that either agglomerate particles were not broken up by the mixer pump operation or the particles rapidly re-agglomerated upon cessation of the mixer pump operation. With respect to the latter possibility, note that the particle concentration of the material suspended by the mixer pump was approximately 1% by mass (PNNL-18327, *Estimate of the Distribution of Solids Within Mixed Hanford Double-Shell Tank AZ-101: Implications for AY-102*), indicating that agglomeration occurred rapidly in a very dilute suspension.

5.0   LIQUID WASTE DATA, UNCERTAINTIES AND VARIATION

Available data on specific gravity and viscosity of the liquid phase of Hanford tank wastes, as well as the relevant uncertainties and variation[8], are presented and discussed. Sections 5.1 and 5.2 discuss the density (or specific gravity) of liquid waste for samples of Hanford tank wastes and batches of feed to the WTP. Sections 5.3 and 5.4 discuss viscosity of liquid waste for the same two data sets. Section 5.5 discusses the preliminary assessment of what effect storage and transfer operations will have on Hanford wastes.

5.1   LIQUID WASTE SPECIFIC GRAVITY

Data on liquid phase samples of Hanford tank waste with measured SpG and analyzed compositions of dissolved solids were extracted from the TWINS database. These data were used to quantify the uncertainty in measuring SpG and assess the assumptions and performance of the liquid-density model incorporated in HTWOS [RPP-17152, *Hanford Tank Waste Operations Simulation (HTWOS) Version 6.6.1 Model Design Document*], discussed subsequently in Section 5.2.

Section 5.1.1 summarizes the SpG data for liquid phase samples from Hanford waste tanks, as retrieved from the TWINS database. Section 5.1.2 discusses measurement uncertainty in the SpG data.

5.1.1   Specific Gravity Data

At the time of this work, the TWINS database contained measured SpG data for 1,343 liquid-phase samples from 93 Hanford SSTs and DSTs. Some of these waste tanks have multiple liquid-phase samples, while other tanks have only one liquid-phase sample. For some samples in some tanks, there were multiple (two to four) measurements of SpG. These multiple SpG values were generally similar and were used to quantify measurement uncertainty (see Section 5.1.2). For subsequent investigations and figures, only one SpG value per sample was used (either a single value if there was only one or the average of multiple measurements). Table 5-1 summarizes the 93 tanks as well as the number of liquid-phase samples and range of SpG values for each tank.

Some of the liquid-phase samples with SpG values were either not analyzed for composition or were incompletely analyzed for composition. A subset of the data discussed above, 559 samples from 53 tanks, had composition data for the components used in the HTWOS liquid-density model discussed in Section 5.2.

---

[8] See the definitions of "uncertainty" and "variation" in the Terms section at the start of the report.

Table 5-1. Hanford SSTs and DSTs Which have Measured Liquid SpG Data, With the Number of Samples, and SpG Range for Each Tank

Tank	No.	Range SpG	Tank	No.	Range SpG	Tank	No.	Range SpG	Tank	No.	Range SpG
A-101	15	1.34-1.51	AY-102	121	0.97-1.22	C-105	1	1.25-1.25	T-103	1	1.25-1.25
AN-101	26	1.03-1.42	AZ-101	38	1.16-1.26	C-106	8	1.02-1.25	T-104	1	1.10-1.10
AN-102	35	1.37-1.58	AZ-102	29	1.09-1.24	C-107	6	1.16-1.19	T-105	5	1.05-1.20
AN-103	20	1.34-1.54	B-106	1	1.28-1.28	C-110	3	1.00-1.19	T-107	3	1.02-1.21
AN-104	27	1.34-1.51	B-107	6	1.00-1.37	S-101	6	1.34-1.48	T-110	1	1.11-1.11
AN-105	33	1.34-1.53	B-108	1	1.37-1.39	S-102	17	1.27-1.55	T-112	2	1.10-1.11
AN-106	39	1.02-1.27	B-203	4	1.03-1.06	S-103	3	1.43-1.50	T-201	5	1.05-1.07
AN-107	35	1.11-1.49	B-204	3	1.03-1.06	S-104	3	1.36-1.39	T-203	1	1.08-1.09
AP-101	19	0.98-1.37	BX-103	1	1.19-1.19	S-106	12	1.38-1.53	TX-104	6	1.40-1.58
AP-102	19	1.19-1.38	BX-109	1	1.26-1.27	S-107	6	1.21-1.36	TX-116	2	1.35-1.36
AP-103	22	0.99-1.38	BX-110	6	1.36-1.58	S-109	4	1.36-1.52	U-101	4	1.13-1.17
AP-104	10	1.00-1.29	BX-111	1	1.43-1.47	S-110	4	1.40-1.45	U-102	5	1.34-1.51
AP-105	38	1.22-1.49	BY-102	1	1.46-1.46	S-111	8	1.34-1.46	U-103	11	1.34-1.50
AP-106	19	0.99-1.22	BY-103	3	1.19-1.30	S-112	9	1.16-1.48	U-105	4	0.99-1.50
AP-107	34	0.98-1.37	BY-105	25	1.08-1.48	SX-101	9	1.46-1.52	U-106	5	1.32-1.40
AP-108	47	0.98-1.47	BY-106	3	1.24-1.42	SX-102	4	1.44-1.52	U-107	22	1.03-1.49
AW-101	37	1.34-1.53	BY-107	10	1.40-1.49	SX-103	12	1.44-1.51	U-108	4	1.37-1.45
AW-102	21	1.02-1.20	BY-109	2	1.48-1.52	SX-104	2	1.46-1.49	U-109	1	1.46-1.49
AW-103	15	0.96-1.42	BY-110	7	1.04-1.50	SX-105	18	1.39-1.52	U-111	3	1.38-1.43
AW-104	26	1.00-1.49	BY-111	3	1.41-1.44	SX-106	9	1.29-1.50	U-201	1	1.25-1.26
AW-105	28	1.00-1.17	BY-112	2	1.46-1.48	SY-101	32	1.13-1.46	U-202	1	1.27-1.29
AW-106	32	1.01-1.47	C-103	7	0.84-1.09	SY-102	114	1.02-1.40	U-203	1	1.27-1.28
AX-101	16	1.34-1.57	C-104	2	1.09-1.15	SY-103	7	1.47-1.53	U-204	1	1.11-1.11
AY-101	66	1.02-1.31	---	---	---	---	---	---	---	---	---

Notes: *Some tanks with only one sample have a range of values because multiple analyses (two to four) were performed.

For these 559 samples, Figure 5-1 shows a scatterplot matrix of the composition components (molarities) used in the HTWOS liquid-density model. A scatterplot matrix is a matrix of scatterplots of pairs of composition components plotted one against another. The plots above the diagonal are mirror images of the plots below the diagonal. By looking at the plots in a given row or column, one can see the pairwise distributions of one component (corresponding to the row or column) versus all of the other components. Figure 5-1 shows two pairs of components $[(Al^{+3}/Al(OH)_4^-$, $Cl^-)$ and $(NO_2^-$, $Cl^-)]$ have relatively strong positive correlations. Several pairs of components, such as $(Cl^-$, $CO_3^{-2})$ and $(Cl^-$, $F^-)$, are such that both components cannot be at their maximum molarities at the same time. Scatterplots involving Fe^{+3} show relatively few samples having larger values.

Figure 5-1. Scatterplot Matrix Graph Showing Molarities of Components Used in the HTWOS Model for Liquid Density

5.1.2   Specific Gravity Uncertainties

The only source of uncertainty in the measured SpG values is measurement uncertainty. For 328 of the 1,343 tank samples, two to four (generally two) measurements of SpG were made on the same sample within a short period. For those samples with multiple SpG measurements, means and SD were calculated. Given that the means and SDs are calculated only from two to four SpG values, they are subject to considerable uncertainty. However, such means and SDs suffice for investigating whether the SDs appear to (1) have a relationship with the mean values, or (2) differ significantly for some Hanford tanks.

Figure 5-2 shows the SDs of multiple SpG measurements plotted versus the mean values for the 328 samples with multiple SpG measurements. There is no apparent relationship between the SDs and the means. All of the SDs are below 0.09, while all but four are below 0.05. The majority of the SDs are below 0.01. Hence, as would be expected, the measurement uncertainty (i.e., SD) from repeat SpG measurements is small. A pooled (i.e., combined) estimate of the SpG measurement SD is 0.0146, which was estimated with 347 degrees of freedom.

Figure 5-2. Plot of Standard Deviations (SD) versus Means Calculated from Multiple Specific Gravity (SpG) Measurements of Samples from Hanford Waste Tanks
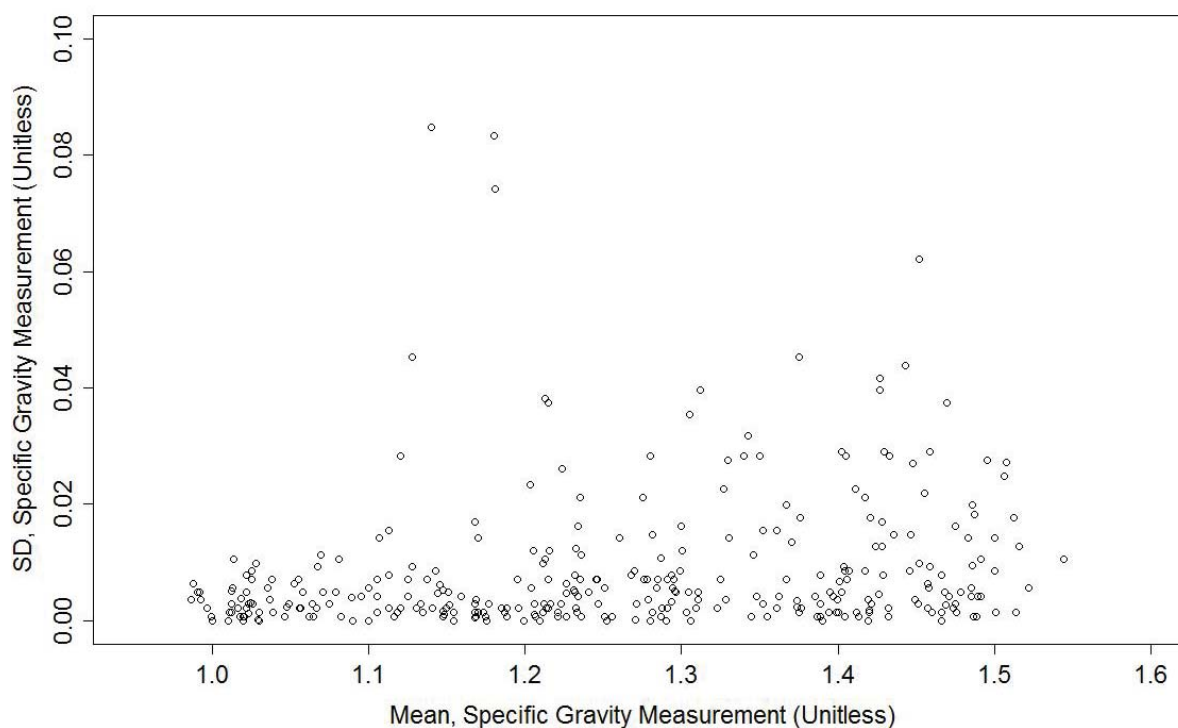
An interval estimate for the true, unknown SpG value corresponding to a specific measured value is given by the statistical method referred to as a 95% prediction interval (95% PI)[9].

---

[9] A 95% PI contains the true unknown value with 95% confidence. This confidence is interpreted as follows. A specific 95% PI for a given SpG measurement either will or will not contain the true, unknown value. However, if

Because the measurement SD was estimated with a large number of degrees of freedom, it is acceptable to use the normal (Gaussian) distribution rather than the t-distribution to calculate 95% PIs on SpG values. For this situation, the formula for a 95% PI on a SpG value is given by the following:

$$95\% \text{ PI SpG} = \text{SpG} \pm 1.96(0.0146) = \text{SpG} \pm 0.0286 \qquad (5-1)$$

where   SpG = measured specific gravity
        ±1.96 = standard normal distribution[10] values that contain 95% of the distribution.

To illustrate the use of this formula, consider that a measured SpG value is 1.23. Then, a 95% PI would be $1.23 \pm 0.0286 = (1.2014, 1.2586)$.

5.1.3   Specific Gravity Variation

It was decided not to investigate the variation of SpG values over the data described in Section 5.1.1. The data include many sources of within tank variation of SpG, including results for diluted and undiluted samples and variation over many years. Some of these sources of variation were considered inappropriate or not applicable relative to variation in waste feed batches to the WTP. Hence, the tank-to-tank and within tank variation of SpG for this data set were not evaluated.

5.2   LIQUID WASTE DENSITY PREDICTIONS

Section 5.2.1 summarizes the development and assumptions of the model used in HTWOS to predict the density of liquid waste. The details of the model development and assumptions are presented in Section A.1 of Appendix A. Section 5.2.3 discusses the uncertainties in model-predicted liquid densities. Section 5.2.4 discusses a performance assessment of the HTWOS liquid-density model for data from Hanford waste tank samples. Section 5.2.5, discusses variation of the HTWOS-predicted liquid densities over the course of waste transfers to the WTP.

5.2.1   Liquid Waste Density Prediction Model

Several related model forms to calculate the SpG or density of the liquid phase of Hanford tank wastes and waste feed batches to the WTP are discussed in Section A.1 of Appendix A. The different models have different mathematical forms depending on 1) whether SpG or liquid density is calculated and 2) the input variables required to perform the model calculations. Table 5-2 summarizes several model forms discussed in Section A.1. Although not listed explicitly in Section A.1, the models for SpG in Equations A-1, A-4 and A-5 could be converted to models for liquid density by multiplying both sides of those equations by the density of water.

---

the process of estimating the measurement SD and calculating the specific 95% PI were conceptually repeated a large number of times, the 95% PI would include the true, unknown value 95% of the times.

[10] A standard normal distribution has mean 0 and standard deviation 1.

That is how Equation A-8 was obtained from Equation A-7. All of the model forms listed in Table 5-2 use component density coefficients (denoted γ_i) developed as discussed in Section A.2 of Appendix A. The coefficients were originally developed for liquid densities expressed in units of g/L, so the model in Equation A-8 calculates liquid density in those units. Because HTWOS expresses liquid density in units of kg/L, Equation A-9 is the re-expression of Equation A-8 to predict liquid density in kg/L units.

Table 5-2. Model Forms for Specific Gravity and Density of the Liquid Phase of Tank Waste

Modeled Variable	Inputs	Equation No.
SpG	γ_i, M_i	A-1
SpG	m_i, V_t	A-4
SpG	c_i	A-5
SpG	m_i, m_t, $\rho_W^{g/L}$	A-7
$\rho_L^{g/L}$	m_i, m_t, $\rho_W^{g/L}$	A-8
$\rho_L^{kg/L}$	m_i, m_t, $\rho_W^{g/L}$	A-9
$\rho_L^{kg/L}$	m_i, m_t, $\rho_W^{g/L} = \frac{1kg}{L}$ at 30°C	A-10, 5-2

Notes: SpG= $\rho_L^{g/L}/\rho_W^{g/L}$ = specific gravity of liquid waste, dimensionless

$\rho_L^{g/L}$= density of liquid, g/L

$\rho_W^{g/L}$= density of water, g/L

γ_i= density coefficient of the ith component, L/g-mol

M_i= molarity of the ith component, g-mol/L

m_i= mass of the ith component dissolved in liquid waste, kg

V_t= total volume of the liquid waste

c_i= concentration of the ith component dissolved in liquid waste, kg/L

m_t= total mass of the liquid waste, kg

$\rho_L^{kg/L}$= density of liquid waste, kg/L

$\rho_W^{kg/L}$= density of water, kg/L

The liquid-density models in Equations A-7 and A-8 are functions of $\rho_W^{kg/L}$, which in turn are functions of temperature, as given in Equation A-2 of Appendix A. The model in Equation A-9 is a function of $\rho_W^{kg/L}$, which in turn is also a function of temperature, as given in Equation A-3. The model actually used by HTWOS to calculate liquid density is given by Equation A-10 in Appendix A. The HTWOS model in Equation A-10 was obtained from Equation A-9 by (incorrectly) assuming that $\rho_W^{kg/L}$ (30°C) = 1.0 kg/L. For convenience, the model in Equation A-10 is repeated here

$$\rho_L^{kg/L} = \frac{m_t}{m_t - 1000 \sum_i \frac{\gamma_i m_i}{mw_i}}$$
(5 − 2)

where m_i = mass of the ith component dissolved in the liquid waste, kg
         m_t = total mass of the liquid waste, kg
         mw_i = molecular weight of the ith component, g/g-mol

The coefficients γ_i are listed in the last column of Table A-2 in Appendix A. Development of Equation A-10 in Appendix A makes clear how units of kg/L are obtained for $\rho_W^{kg/L}$, which is not immediately obvious from the terms in Equation 5-2 and their units as expressed in Table 5-2.

5.2.2   Predictions of Liquid Density for Waste Feed

The liquid-density model in Equation 5-2 was applied to predict liquid densities for the waste transfer batches calculated by HTWOS for 10 cases in ORP-11242. The 10 cases include the Baseline Case and nine other cases discussed in ORP-11242. The results are discussed in Section 5.2.5.

5.2.3   Liquid Density Prediction Uncertainties

Predictions of liquid density by HTWOS using the model in Equation 5-2 are subject to several uncertainties, as discussed in the following subsections.

5.2.3.1   *Systematic Uncertainty in the Model Form for Liquid Density*

The HTWOS model in Equation 5-2 (and Equation A-10 in Appendix A) was developed from the model in Equation A-1. When the component density coefficients (γ_i) are constants, as in the case of the HTWOS model, the model in Equation A-1 assumes the effects of dissolved components on liquid density and SpG are additive in terms of component molarities. That is, the HTWOS model does not allow curvilinear or interactive effects of the dissolved components, nor does it allow those effects to depend on temperature. This is not rigorously correct, because the HTWOS model is a simplification of a model with "variable density coefficients" (discussed in Section A.2.1) that do involve curvature and interactive effects of dissolved components and a temperature effect. However, RPP-14767 showed that the liquid-density model in Equation A-9 with $\rho_W^{kg/L}(30°C) = 0.9956$ did not have noticeable bias in predictions. While an incorrect model form nominally causes systematic errors, such errors can lead to over-predictions of density for some compositions and under-predictions for others, such that the prediction errors appear random with respect to the magnitude of the density. In the end, however, all models will depend on composition and composition accuracy. Precision is judged a bigger issue than the HTWOS model currently used to calculate liquid density.

5.2.3.2 *Systematic Uncertainty (Bias) as a Result of Simplifying the Liquid-Density Model*

As discussed in Section 5.2.1, the HTWOS model in Equation A-10 was obtained from Equation A-9 by substituting $\rho_W^{kg/L}(30°C) = 1.0$ kg/L (HNF-SD-WM-SP-012, RPP-17152). However, that substitution conflicts with the dependence of $\rho_W^{kg/L}$ on temperature given in Equation A-3, which calculates $\rho_W^{kg/L}(30°C) = 0.9956$. As discussed in Section A-2, the γ_i coefficients used in the HTWOS model for liquid density in Equation A-9 were derived from empirical models that incorporated the temperature dependence of $\rho_W^{kg/L}$. Hence, the HTWOS simplification from Equation A-9 to Equation A-10 introduces a bias (systematic uncertainty) in calculated values of liquid density. Specifically, the HTWOS model slightly over-predicts liquid density at 30°C by a factor of (1/0.9956 = 1.0044). To the extent that the temperature of the liquid-phase waste differs from 30°C, the bias in HTWOS model predictions would change according to Equation A-3.

5.2.3.3 *Liquid-Density Model Coefficient Uncertainties*

Because the liquid-density model coefficients in Table A-1 were obtained by least-squares-regression fits to empirical data (Novotny and Sohnel 1988), they are subject to regression estimation uncertainty. The choice of constant component density coefficients (Table A-2 of Appendix A) to represent a small range of concentration-dependent coefficients introduces additional uncertainty. However, RPP-14767 found that this source of uncertainty had little impact on liquid-density predictions. Work discussed in Section 5.3.4 using the tank sample data from Section 5.1.1 confirmed this conclusion.

5.2.3.4 *Uncertainties in the Estimates of Component Masses Used as Input Variables to the Liquid-Density Model*

Inputs to the liquid-density model used in HTWOS are measured compositions when applied to experimental data, while the inputs are calculated compositions when applied in HTWOS simulations. If the estimated (measured or calculated) component compositions are biased, especially for the most influential components in the model [nitrate, nitrite, hydroxide, CO_3^{-2} and Al^{+3} or $Al(OH)_4^-$], then the model-predicted liquid densities can be significantly biased. If an HTWOS liquid density appears suspicious (noticeably too low or too high), it is more likely related to a biased estimate of composition than to a problem with the model form or coefficients.

Measured estimates of component compositions are subject to random measurement uncertainty, which will contribute to the random uncertainty of liquid densities calculated by the HTWOS model. Composition estimates generated in HTWOS simulations may be subject to random uncertainty if measured compositions of tank samples are the basis for simulation calculations. However, it was beyond the scope of this work to quantify random measurement uncertainty for measured compositions. It was assumed for purposes of this work that HTWOS-calculated compositions of waste feed batches are unbiased and not subject to random uncertainty.

5.2.4 Performance Assessment of the HTWOS Liquid-Density Model for Data from Hanford Waste Tank Samples

As part of the uncertainty assessment of the HTWOS liquid-density model in Equation 5-2, the model was applied to a set of data from the TWINS database that includes measured compositions and measured SpG values for 559 liquid-phase samples from 53 Hanford tanks. This was the subset of data that was previously discussed in Section 5.1.1. Because measured values of SpG are available in the database, the HTWOS model for liquid density would have to be re-expressed as a model for SpG. While doing that is possible, the model form in Equation 5-2 is not consistent with the form of the composition data in the TWINS database. The composition data are concentrations c_i in units of kg/L, which is consistent with the model in Equation A-5. However, the model for SpG in Equation A-5 can be immediately re-expressed as the model for SpG in Equation A-1. The SpG model in Equation A-1 is mathematically equivalent to the liquid-density model in Equation A-9, as discussed in Section A.1 of Appendix A.

As discussed previously, the current HTWOS model in Equation 5-2 over-predicts liquid density at 30°C by a factor of 1.0044. Hence, that model would also lead to over-predicting SpG at 30°C by a factor of 1.0044 if the correct density of water at 30°C were used to convert from liquid density to SpG. However, if the incorrect density of water at 30°C = 1.0 is used to convert Equation A-10 to a model for SpG, then the effects of the water density being incorrect cancel. Hence, the model for SpG in Equation A-1 is not affected by the HTWOS model in Equation A-10 having assumed an incorrect value of 1.0 for the density of water at 30°C.

Figure 5-3 compares measured SpG values (x-axis) to the predicted SpG values (y-axis) obtained using the model in Equation A-1. The diagonal line in the figure corresponds to perfect model prediction (i.e., predicted values = measured values). The tanks with data used in RPP-14767 in the model validation work have open circle plotting symbols, whereas solid square plotting symbols are used for data from all other tanks. Outlying sample results are marked in Figure 5-3 with the tank number from which the sample was collected.

Figure 5-3 shows a tendency of the HTWOS model to over-predict SpG below ~ 1.08, over-predict between ~ 1.34 – 1.54 and under-predict above 1.54. However, there are limited data below 1.08 and above 1.54, so these observations may or may not correspond to actual systematic uncertainty (bias) in model predictions. Also, the data set of SpG values for 559 samples from 53 Hanford tanks was constructed by screening out a substantial portion of the original data set (SpG values for 1,343 samples from 93 Hanford tanks, see Section 5.2.1). This screening eliminated many data points with incomplete composition data for which the model significantly under-predicted. Hence, it is possible that some of the perceived tendencies from Figure 5-3 that the HTWOS SpG model over-predicts could be a result of screening out under-predictions. Another possible explanation for over-predictions in Figure 5-3 is outlying composition determinations for the key components affecting predictions of SpG. An investigation of the highest, over-predicted results in Figure 5-3 showed that none of them had significantly outlying composition components one-at-a-time or two-at-a-time. While it is possible that some composition components could be outlying three-or-more-at-a-time, it is

probably more reasonable to conclude that the HTWOS SpG model over-predicts more in some cases than others.

Figure 5-3. Plot of Predicted- versus Measured Specific Gravity Values for 559 Liquid-Phase Samples from 53 Hanford Waste Tanks
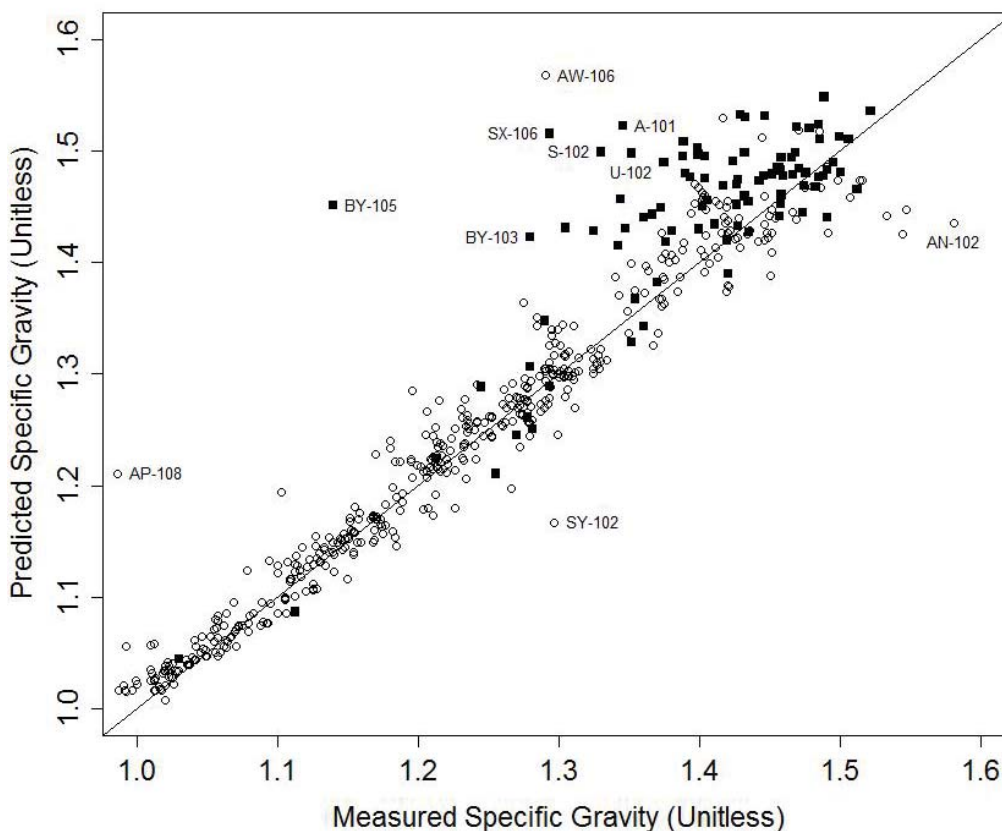
The uncertainties of liquid densities predicted by the model can be quantified using the prediction errors (predicted – measured) for the points plotted in Figure 5-3. These prediction errors include contributions from the uncertainty of the model coefficients as well as the uncertainties in compositions used as inputs to the model. The figure clearly shows that the prediction errors are more variable above SpG ~ 1.27. Table 5-3 summarizes the statistical analyses of the prediction errors of the liquid-density/SpG model for the data from 559 liquid-phase samples from 53 Hanford waste tanks. Table 5-3 shows that for SpG ≤ 1.27 there are 288 prediction errors having a mean of 0.0089 and a SD of 0.0293. For SpG > 1.27, there are 271 prediction errors having a mean of 0.0153 and a SD of 0.0489. Both mean values are statistically greater than zero (p-value < 0.0001). However, these statistical significances may be a result of the large number of data points and the mean prediction errors (0.0089 for SpG ≤ 1.27, 0.0153 for SpG > 1.27) may not be of practical significance. Table 5-3 also lists the ±Uncertainty values for the two cases (SpG ≤ 1.27, SpG > 1.27). When the ±Uncertainty values are added to predicted liquid densities from the model, 95% PIs are obtained. The 95% PIs on predicted liquid densities obtained in this way account for the uncertainty in the model form and coefficients, as well as the uncertainty in measured liquid densities.

Table 5-3. Statistical Analysis Results of Prediction Error for the Specific Gravity Model

Statistic	Specific Gravity ≤1.27	Specific Gravity > 1.27
Number of samples (n)	288	271
Mean	0.0089	0.0153
Standard deviation (SD)	0.0293	0.0489
Standard error (SE)[a]	0.00173	0.00297
p-value[b]	5.4E-7	4.8E-7
z_{95}[c]	1.96	1.96
± Uncertainty[d]	0.0574	0.0958

Notes:

a. Standard error is $SD/\sqrt{n}$

b. Probability of incorrectly declaring that the Mean is statistically different from zero.

c. The value z_{95} such that the interval $(-z_{95}, z_{95})$ includes 95% of the central portion of a standard normal distribution (i.e., with mean = 0 and SD = 1).

d. Uncertainty = z_{95}*SD, which when added to model-predicted liquid-density/SpG values provides 95% prediction intervals.

It is of interest to compare Figure 5-3 to Figure 5-2 (presented in RPP-14767) to summarize the validation of the HTWOS SpG model in use at that time. Figure 2 in RPP-14767 is reproduced here as Figure 5-4. Figure 5-3 includes SpG data for 559 samples from 59 tanks, much greater than the RPP-14767 data for 28 Hanford tanks in Figure 5-4. Also, the data points in Figure 5-3 are significantly more scattered about the "predicted = measured line" than are the data points in Figure 5-4. The larger scatter of points in Figure 5-3 suggests the current HTWOS model for SpG may be subject to more uncertainty than the earlier HTWOS model used in RPP-14767 to produce Figure 5-4. Or, there may be something about the smaller data set RPP-14767 used that resulted in less scatter in Figure 5-4. In the following paragraphs, several possible explanations are discussed for the differences between Figures 5-3 and 5-4.

The SpG predictions in Figures 5-3 and 5-4 were produced using the model in Equation A-1 and the only difference is in the γ_i density coefficients used. RPP-14767 listed the same γ_i density coefficients in its Table 2 as are listed in Table B.2 of this document. However, RPP-14767 used slightly different values of some coefficients to be consistent with the coefficients being used in HTWOS at that time (~ 2003). To assess whether the coefficients used in RPP-14767 account for the greater scatter in Figure 5-3 compared to Figure 5-4, a new version of Figure 5-3 was produced using the same coefficients as used in RPP-14767. This figure (not included in this report) showed a similar scatter as Figure 5-3. Hence, the fact that some coefficients were slightly different in the work of RPP-14767 does not explain the differences between Figures 5-3 and 5-4.

Figure 5-4. Figure from RPP-14767 Comparing SpG Predictions with Measured Values

Figure 2
Calc SpG vs. TWINS SpG
(including Cl, CrO4, PO4)

$y = 0.9966x$
$R^2 = 0.9536$

Red line – diagonal represents a perfect correlation of TWINS SpG with Calc SpG
Black line – regressed trend line forced through the point 0,0
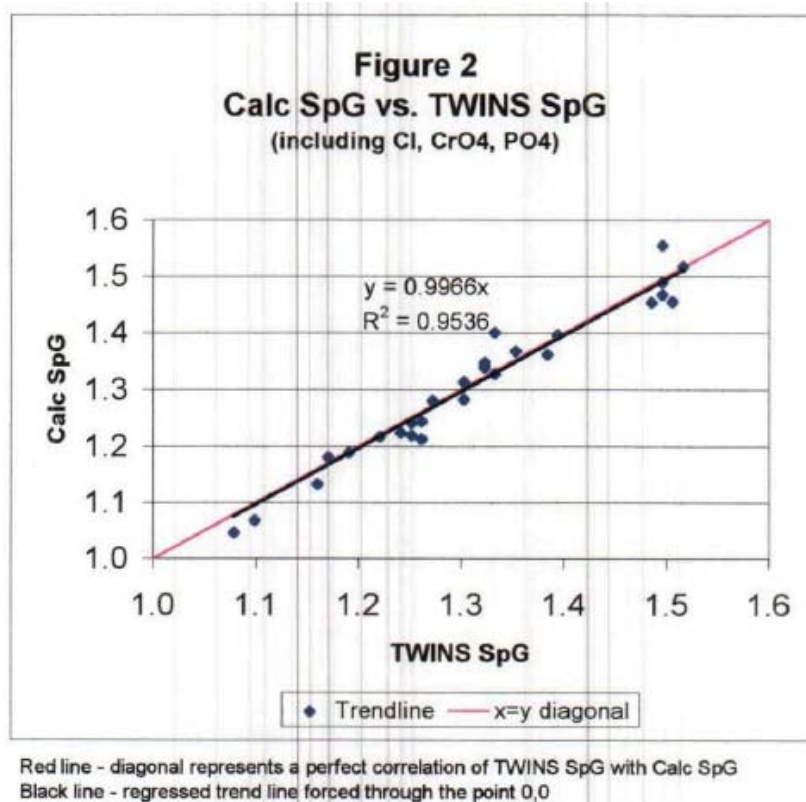
The remaining possible explanations for the smaller scatter in Figure 5-4 could relate to the smaller set of composition data used in RPP-14767. Table 3 in RPP-14767 listed only single compositions for each of the 28 tanks represented in Figure 5-4, whereas the data used to produce Figure 5-3 contains multiple samples (and hence multiple composition analyses) from many tanks. RPP-14767 did not describe the procedure used to obtain the compositions listed in his Table 3. One possibility is that the average of analyzed compositions and measured SpG values from multiple samples within each of the 28 tanks may have been used. If so, this would reduce the scatter of predicted-measured points around the predicted = measured line, as occurred in Figure 5-4. The data in Figure 5-3 corresponding to the 28 tanks considered in RPP-14767 are marked with open circle plotting symbols, while data for other tanks are marked by solid squares. The open circle plotting symbols in Figure 5-3 show smaller scatter in SpG values than for the solid squares. However, even the open circles in Figure 5-3 show more scatter than does Figure 5-4.

In summary, HTWOS uses a model for liquid density that predicts in units of kg/L. That model slightly over-predicts liquid density at 30°C by a factor of 1.0044 because of assuming an incorrect value of 1.0 for the density of water at 30°C. If the same incorrect value is used to convert HTWOS liquid-density predictions to liquid SpG predictions, then the SpG predictions are not biased. Based on a comparison of Figures 5-3 and 5-4, we conclude that the HTWOS model for liquid density/SpG makes predictions that have more uncertainty than indicated in RPP-14767. Table 5-3 lists the ±Uncertainty values of 0.0574 when SpG ≤ 1.27 and 0.0958

when SpG > 1.27. These ±Uncertainty values can be added to model-predicted liquid densities to give 95% PIs on the true, unknown values.

5.2.5   Variation of Liquid-Density Predictions for Waste Feed

For various retrieval, blending, and operating scenarios, HTWOS can simulate the compositions of waste feed batches to the WTP over the course of the feed transfer and vitrification mission. HTWOS uses the liquid-density model discussed in Section 5.2.1 to predict the liquid density of each waste feed batch. The density of liquid waste can be controlled by adding water (dilution) or removing water (evaporation), or by blending wastes with different liquid densities.

In this section, we investigate the variation in HTWOS predictions of liquid density for the projected waste feed batches in 10 cases for System Plan Rev. 6 (ORP-11242). The 10 cases include the Baseline Case and nine other cases discussed in ORP-11242. HTWOS projects liquid density for both HLW and LAW feed batches, but only HLW batches are considered here.

The Baseline Case includes the HTWOS-predicted liquid densities for 600 HLW feed batches dated 5/31/2018 to 2/18/2043. Figures 5-5 and 5-6, respectively, present a histogram and a cumulative distribution function of these liquid-density predictions. Figures 5-5 and 5-6 show that the predicted liquid densities range from 1.11 to 1.60 kg/L, with about 95% of values falling in the 1.14 to 1.37 kg/L range.

Study of the Baseline Case in Figure 5-5 shows that there are 10 HLW batches (from 11/29/2041 to 8/11/2042) that have liquid densities of 1.60 kg/L. Those 10 batches are within the end-of-mission activities projected to begin on 9/8/2039 in the Baseline Case. End-of-mission activities include consolidating the remaining waste in the DSTs into the last several HLW and LAW feed campaigns and cleaning out the remaining DST heels. The HTWOS uses a simplified set of model controls during end-of-mission activities that are not reflective of how those last campaigns would be prepared and delivered. Work is underway to include a refined set of end-of-mission controls in the HTWOS model to remedy this issue for the next revision of the System Plan and the corresponding Integrated Waste Feed Delivery Plan.

Figures 5-7 and 5-8, respectively, present a histogram and a cumulative distribution function of the HTWOS-predicted liquid densities for HLW feed batches in the Baseline Case prior to the end-of-mission activities starting on 9/8/2039. This subset of the data has 505 HLW feed batches dated from 5/31/2018 to 4/24/2039 with predicted liquid densities ranging from 1.14 to 1.37 kg/L. Figure 5-7 shows a roughly symmetric, unimodal distribution of predicted liquid densities prior to the end-of-mission activities.

Figure 5-5. Histogram of HTWOS-Predicted Liquid Densities for 600 HLW Feed Batches from 5/31/2018 to 2/18/2043 for the Baseline Case of System Plan Rev. 6
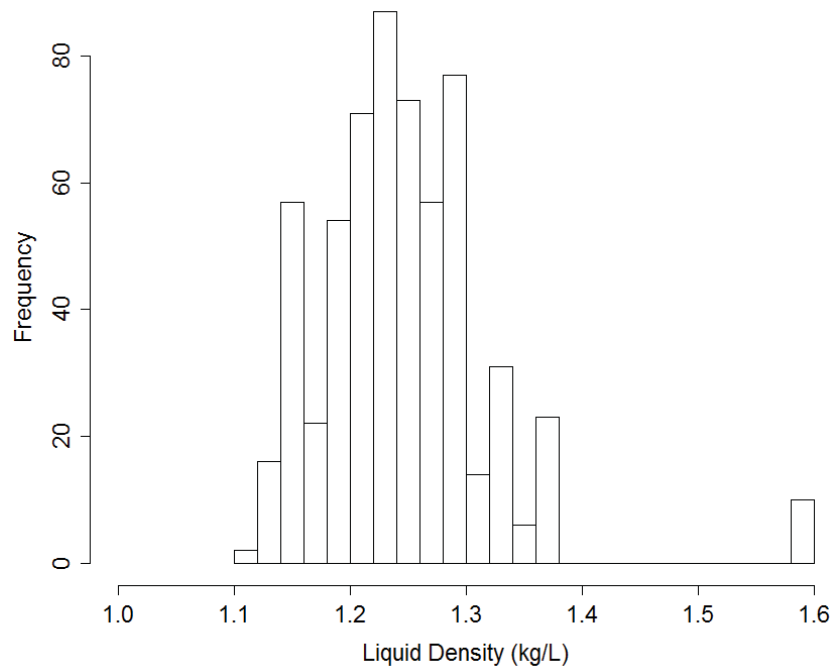
Figure 5-6. Cumulative Distribution Function of HTWOS-Predicted Liquid Densities for 600 HLW Feed Batches from 5/31/2018 to 2/18/2043 for the Baseline Case of System Plan Rev. 6
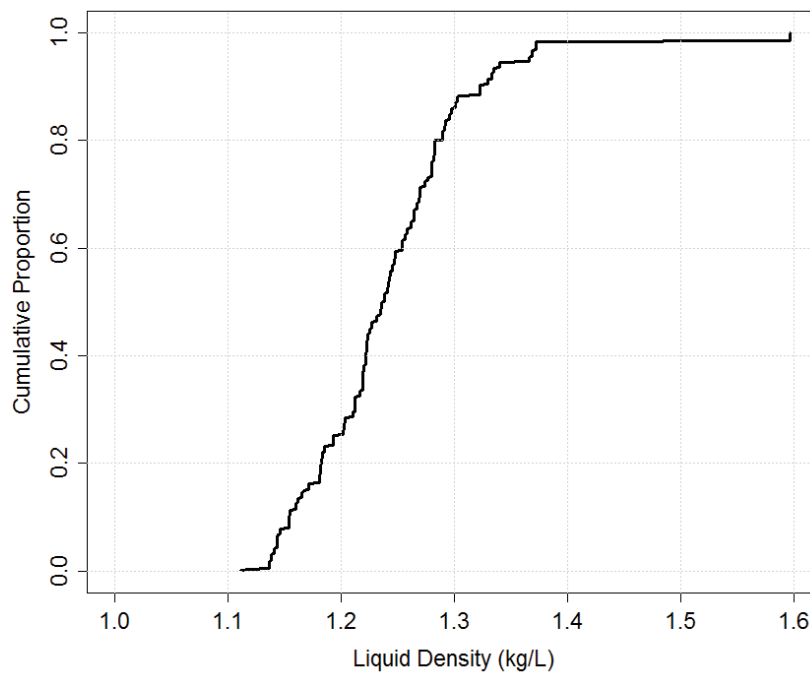
Figure 5-7. Histogram of HTWOS-Predicted Liquid Densities for 505 HLW Feed Batches from 5/31/2018 to 4/24/2039 for the Baseline Case of System Plan Rev. 6
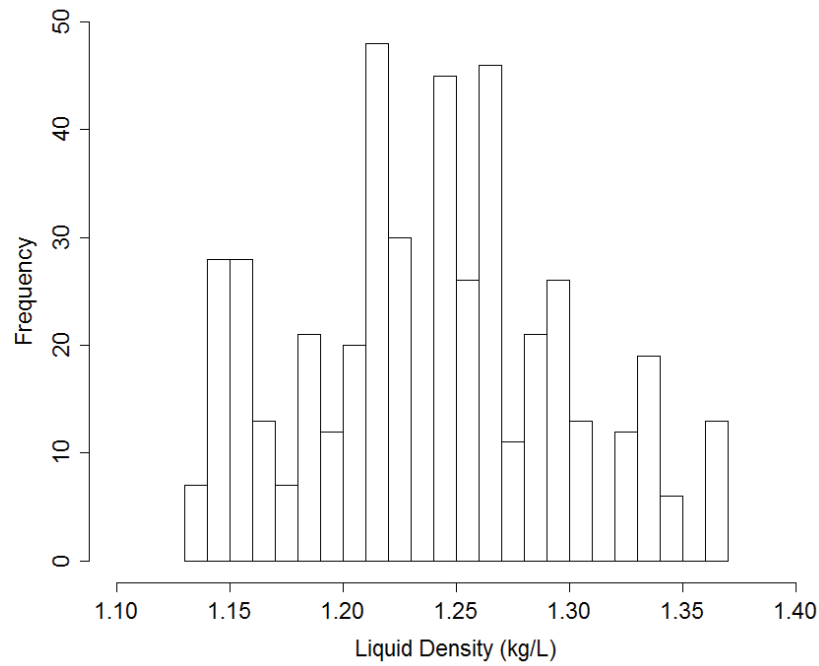
Figure 5-8. Cumulative Distribution Function of HTWOS-Predicted Liquid Densities for 505 HLW Feed Batches from 5/31/2018 to 4/24/2039 for the Baseline Case of System Plan Rev. 6
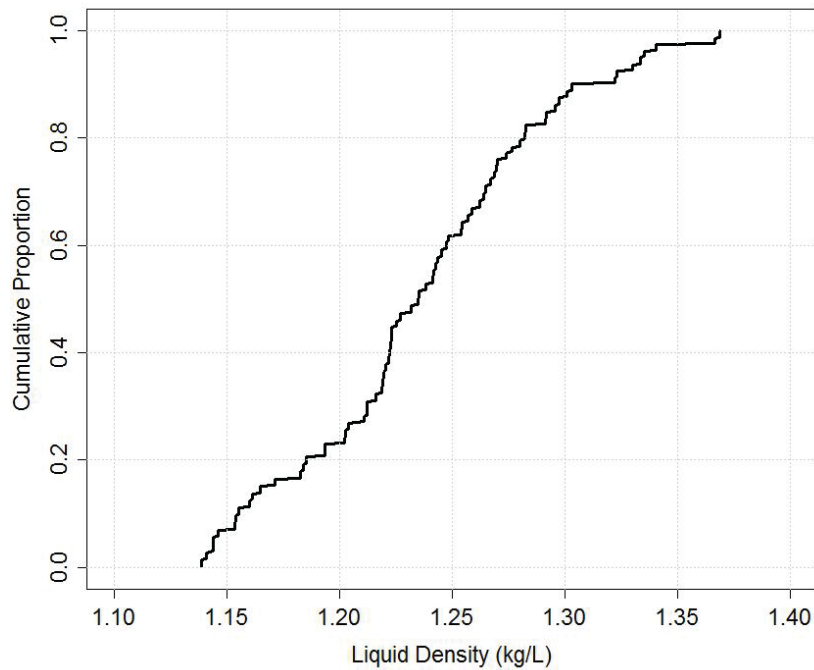
Figure 5-9 is similar to Figure 5-8, except that cumulative distribution functions of liquid density for all 10 cases evaluated in System Plan, Rev. 6 are displayed together. Figure 5-9 uses the HLW batches from the 10 cases dated up to 9/9/2037. The date 9/9/2037 is the earliest date for which any of the 10 cases begin end-of-mission activities and was chosen for consistency in comparing the results of all 10 cases. Figure 5-9 illustrates that the kinds of assumptions and parameters that were changed among the 10 cases (ORP-11242) have a relatively small effect on the range of liquid densities of the HLW batches throughout the mission. For just the Baseline Case, the liquid densities range from 1.139 to 1.369. Across all 10 cases, the liquid densities range from 1.105 to 1.476. For all 10 cases, 99.6% of the HLW batches have predicted liquid densities falling between 1.1 to 1.4 kg/L.

Figure 5-9. Cumulative Distribution Function of HTWOS-Predicted Liquid Densities for HLW Feed Batches Dated Up to 9/9/2037 for the Baseline Case (black line) and Nine Other Cases (gray lines) of System Plan Rev. 6
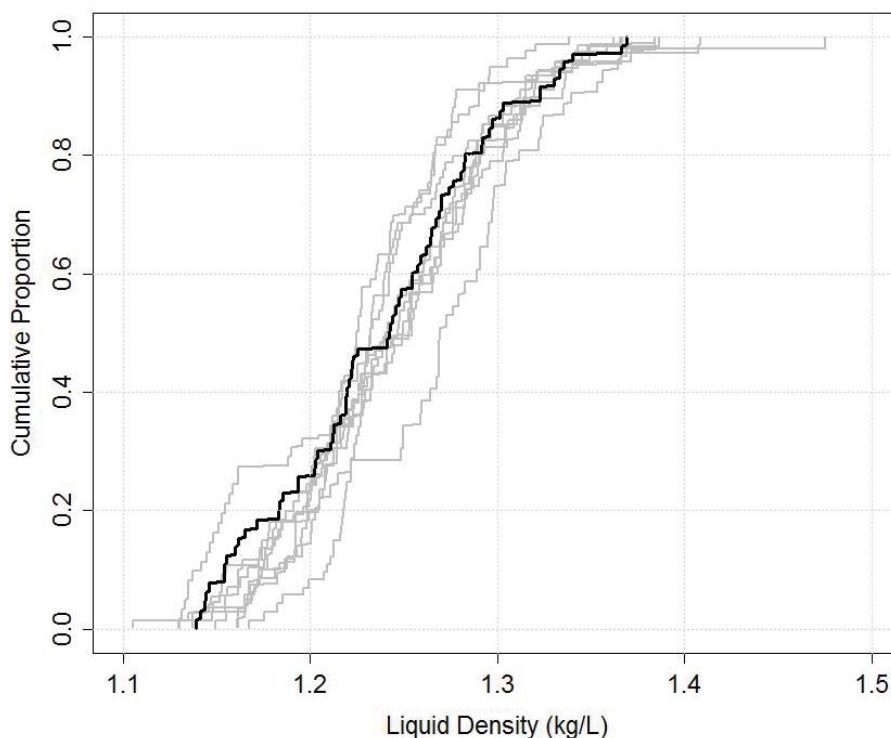
The variations in liquid densities projected by HTWOS for HLW batches in the Baseline Case and the nine other cases (from ORP-11242) prior to the end-of-mission period are affected by uncertainties discussed in Sections 5.2.3 and 5.2.4. Specifically, there are two uncertainties in HTWOS model predictions of liquid density that are not accounted for in the variations displayed in Figures 5-4 to 5-8.

- The model used in HTWOS to calculate liquid density is subject to systematic uncertainty (bias) in that it over-predicts liquid density at 30°C (the assumed temperature of liquid waste) by a factor of 1.0044. This is because of the assumption in developing the HTWOS liquid-density model that the density of water at 30°C equals 1.0 kg/L,

rather than the value 0.9956 kg/L used in developing the model's component coefficients. This is discussed in Section 5.2.3.

- The predicted liquid densities from the HTWOS model are subject to the random uncertainties discussed in Sections 5.2.3 and 5.2.4. These uncertainties are quantified by the ± Uncertainty values (in Table 5-3) corresponding to 95% PIs.

- Because the over-prediction bias in the HTWOS liquid-density model is small and conservative, the HTWOS-predicted values were not adjusted. In this effort, we quantified how the uncertainties of predictions from the liquid-density model (represented by 95% PIs) increase the ranges of liquid densities for the Baseline Case and all 10 cases in System Plan Rev. 6. In both cases, only the period prior to the end-of-mission activities is considered.

- Baseline Case (whole mission): The HTWOS-predicted, liquid densities for the Baseline Case (including the end-of-mission activities) range from 1.112 to 1.596. Expanding this range using the ±Uncertainty values in (which corresponds to 95% PIs) yields 1.112 – 0.057 = 1.055 as the lower limit and 1.596 + 0.096 = 1.692 as the upper limit.

- Baseline Case (prior to end of mission activities): The HTWOS-predicted, liquid densities for the Baseline Case (prior to the end-of-mission activities) range from 1.139 to 1.369. Expanding this range using the ±Uncertainty values in (which corresponds to 95% PIs) yields 1.139 – 0.057 = 1.082 as the lower limit and 1.369 + 0.096 = 1.465 as the upper limit.

- All 10 Cases: The HTWOS-predicted, liquid densities for the 10 cases from ORP-11242 (prior to the end-of-mission period) range from 1.105 to 1.476. Expanding this range using the ±Uncertainty values in Table 5-3 (which correspond to 95% PIs), yields 1.105 – 0.057 = 1.048 as the lower limit and 1.476 + 0.096 = 1.572 as the upper limit.

- The most conservative range of HTWOS-predicted liquid-densities from System Plan Rev. 6 runs is the range over all 10 cases, namely 1.048 to 1.572. Less conservative would be the range for the Baseline Case, namely 1.082 to 1.465. Table 5-4 summarizes the variation and uncertainties in liquid-density and SpG values from the HTWOS System Plan Rev. 6 projections of waste feed batches.

Table 5-4. Variation in HTWOS-Predicted Liquid Densities Without and With Uncertainties for System Plan Rev. 6 HLW Feed Batches

Data Set	Without Uncertainties		With Uncertainties	
	Min	Max	Min	Max
Predicted liquid density, HTWOS baseline case (end of mission)[a]	1.112	1.596	1.055	1.692
Predicted liquid density, HTWOS baseline case (no end of mission)[b]	1.139	1.369	1.082	1.465
Predicted liquid density, HTWOS 10 cases[c]	1.105	1.476	1.048	1.572

Notes:

a. For WFD batches of the Baseline Case, including the end-of-mission activities (from 5/31/2018 to 2/18/2043).

b. For WFD batches of the Baseline Case, prior to end-of-mission activities (from 5/31/2018 to 4/24/2039).

c. For waste feed batches of the 10 cases for System Plan Rev. 6, prior to the end-of-mission activities (up to 9/9/2037).

5.3   LIQUID WASTE VISCOSITY PREDICTIONS

Liquid viscosity has seldom been measured on samples of liquid-phase waste from Hanford tanks. The measured viscosity data that does exist was used in PNNL-20646 (Section 3.2.2) to develop a model to predict liquid viscosity as a function of temperature and liquid density. It would be better to develop a model for liquid viscosity as a function of the temperature and composition of the liquid-phase wastes, because liquid density cannot completely represent all of the effects of dissolved solids in liquid waste. However, developing a liquid-viscosity model as a function of temperature and composition was not possible because the data used to develop the model did not have sufficient compositional analyses.

Section 5.3.1 presents the liquid-viscosity model developed for use in this report. Section 5.3.2 summarizes the model-predicted viscosities of liquid phase samples from Hanford waste tanks. This data set and its measured SpG values (from the TWINS database) were discussed in Section 5.1.1. The uncertainties and variation of the predicted liquid viscosities are summarized in Sections 5.3.3 and 5.3.4, respectively. Although the predicted liquid viscosities are for "as is" samples in Hanford waste tanks (as opposed to the liquid phase of waste expected to be delivered to the WTP), it is useful to summarize the results.

Model for Predicting Liquid Viscosity as a Function of Temperature and Density

A liquid-viscosity model based on the model in Section 3.2.2 of PNNL-20646, but with several improvements, was developed as discussed in Appendix B. The model is given by the following:

$$\mu_L = e^{[a(\rho_L - f)_+ + b(\rho_L - 1) + (c(\rho_L - 1) + d)/T]} \begin{cases} (\rho_L - f)_+ = (\rho_L - f) & (\rho_L - f) \geq 0 \\ \\ (\rho_L - f)_+ = 0 & (\rho_L - f) < 0 \end{cases} \tag{5-3}$$

where
μ_L = liquid viscosity, cP
ρ_L = liquid density, g/mL
T = temperature, K
a,b = coefficients for effect of liquid density on liquid viscosity, mL/g
c = coefficient for interactive effect of liquid density and temperature on liquid viscosity, K·mL/g
d = coefficient for the effect of temperature on liquid viscosity, K
f = coefficient where the linear liquid-density effect on liquid viscosity changes

The model in Equation 5-3 was fit to the data in Table B.1 with a generalized linear model (Myers et al. 2002) using Matlab (2007). The resulting estimates of the five coefficients (a, b, c, d and f) are listed in Table 5-5 along with their SEs and p-values.

Table 5-5. Coefficients, Standard Errors (SE) and p-Values of Liquid Viscosity Model

Coefficient	Value	Standard Error	p-Value[a]
a	5.29	2.23	0.02
b	-18.29	3.04	<0.001
c	7,103.79	964	<0.001
d	54.36	74.20	0.46[b]
f	1.42	NA[c]	NA

Notes: [c]

   a.   A p-value is the probability of incorrectly concluding the estimated coefficient is significantly different from zero. Values below 0.001 indicate highly statistically significant coefficient estimates.

   b.   This value is not statistically significant but it is kept in the equation to maintain model hierarchy.

   c.   This parameter was optimized via a separate process and not as part of the generalized linear model fitting process. Therefore it does not have a standard error or p-value associated with it.

The liquid-viscosity model in Equation 5-3 assumes that (1) the Arrhenius equation ($Ae^{B/T}$) represents the temperature effects on liquid viscosity and (2) liquid density has a linear effect on the coefficients (A and B) of the Arrhenius equation. Generally, the Arrhenius equation well represents the effect of temperature on liquid viscosity over small ranges of temperature, such as applies for the transfer of Hanford tank wastes. Further, the liquid-viscosity model assumes that the linear effect of liquid density on the A coefficient changes at liquid density of 1.42 g/mL. PNNL-20646 (Section 3.2.2) discusses why a change in the effect of liquid density is appropriate. An assessment of the linear effect of liquid density on liquid-viscosity model coefficients is presented in Section B.1 of Appendix B.

The model in Equation 5-3 has a similar form to the model discussed in PNNL-20646 (Section 3.2.2), but there are several improvements. Whereas the PNNL-20646 model was discontinuous in liquid density and applied an ad-hoc correction to resolve the discontinuity, the model in Equation 5-3 is continuous in both the liquid density and temperature domains[11]. Further, the model had more coefficients than it needed, which increases the uncertainty of model predictions. The model in Equation 5-3 has only five coefficients compared to the nine coefficients of the model. Three of the four coefficients in Equation 5-3 calculated using a generalized linear model are statistically significant at the 95% confidence level, with the exception being "d" that was kept in the model to maintain model hierarchy. The model in Equation 5-3 has $R^2 = 0.796$, whereas the model in PNNL-20646 has $R^2 = 0.767$. A higher value would be desirable, but liquid density is an imperfect representative of the effect of composition of dissolved solids in liquid waste.

---

[11] Comparing the predicted-versus measured plots for the model in Equation 5-3 (Figure 5.9) and the PNNL-20646 model (Figure 3.4) shows that the PNNL-20646 model better predicts the two AP-104 points that are over-predicted by the model in Equation 5-3. This was determined to be a result of the discontinuous nature of the PNNL-20646 model. Given the relatively poor fit of both models, it was decided a model continuous in liquid density was preferable for this work.

Figure 5-10 shows a predicted-versus-measured plot for the data set used to fit the coefficients in Table 5-5. The diagonal line represents ideal prediction performance (predicted = measured), with points falling above that line denoting over-prediction and points falling under the line denoting under-prediction. Figure 5-10 shows that the model has a tendency to over-predict liquid viscosity below ~ 5 cP, especially when $\rho_L \leq 1.42$ g/mL. The model also significantly under predicts for three data points, namely (AN-104, ρ_L = 1.4, 25°C, μ_L = 16.9), (AN-104, ρ_L = 1.3, 25°C, μ_L = 17.5) and (AN-103, ρ_L = 1.48, 29°C, μ_L = 27.4), although the reason for this is not clear given the limited amount of data for μ_L > ~13 cP. The model also over-predicts for one point (AP-104, ρ_L = 1.41, 25°C, μ_L = 3.6). Otherwise the model is subject to considerable "random" uncertainty, although that may be substantially a result of liquid density being an inadequate stand-in for the effects of dissolved components on liquid viscosity.

Figure 5-10. Predicted versus Measured Plot for the Data Used to Fit the Liquid-Viscosity Model in Equation 5-3
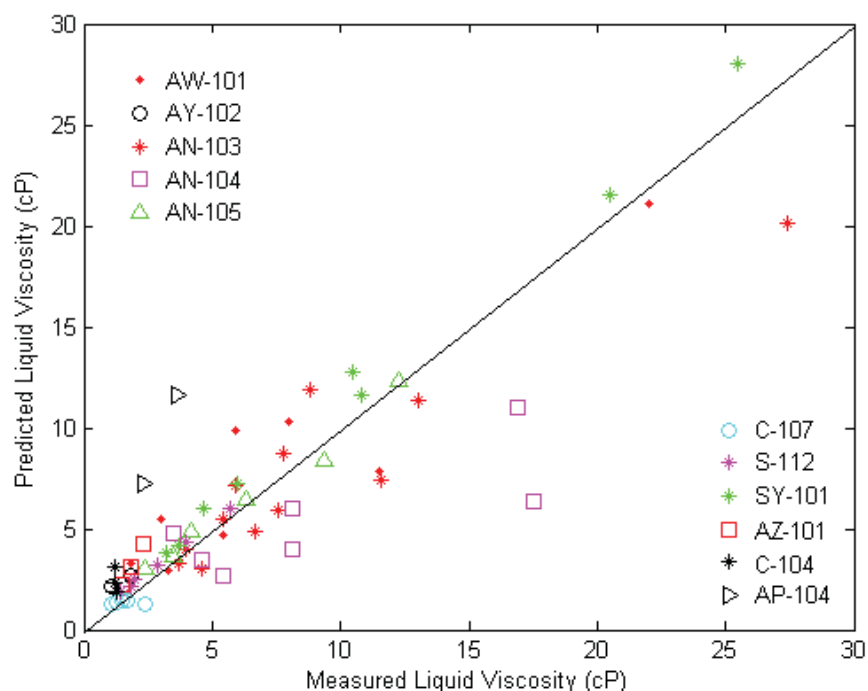
Confidence and PIs on the viscosity predictions made with Equation 5-3 can also be obtained. In a subsequent section, 95% PIs are used to quantify the uncertainty in predictions made with the liquid-viscosity model. Figure 5-11 shows the lower and upper limits of the 95% PIs for the data used to fit the liquid-viscosity model in Equation 5-3.

Figure 5-11. Lower and Upper Limits of 95% Prediction Intervals for the Data Points Used to Fit the Liquid-Viscosity Model
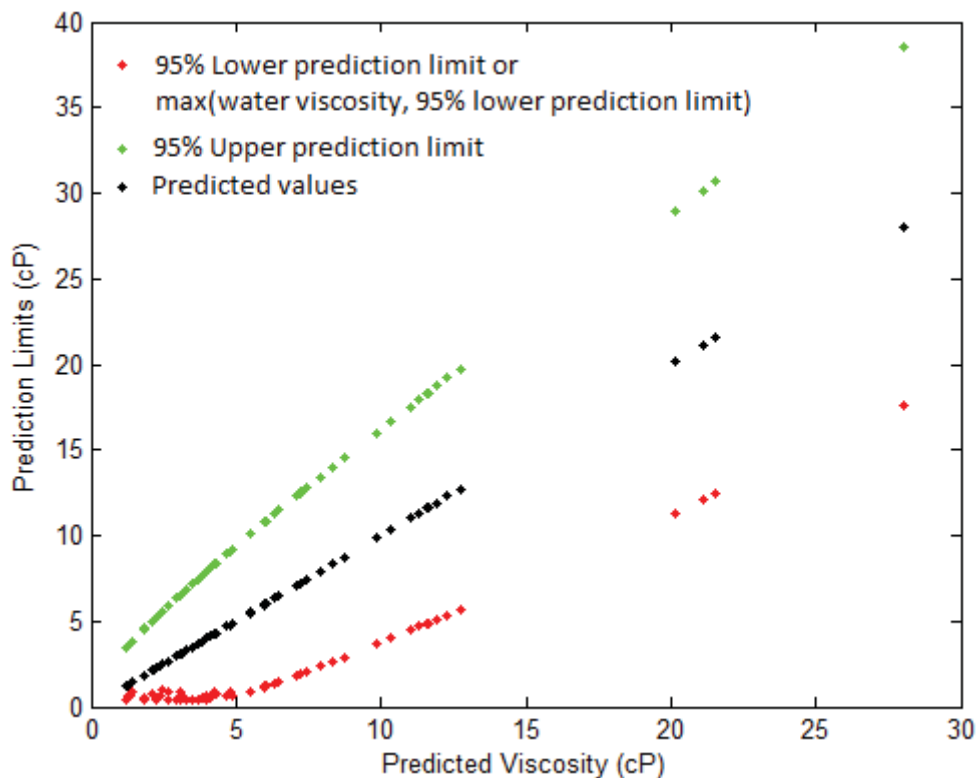
The generalized linear model methodology used to develop the liquid-viscosity model discussed in this subsection does not ensure that physically valid predictions are obtained. Extrapolations (liquid-viscosity predictions for density and temperature values outside the region of data used to build the model) should generally be avoided, although minor extrapolations could be used with caution. Because of the empirical nature of Equation (5-3), 95% lower prediction limits can result in zero or negative values for the dataset used to build the model. They can also result in lower limit values that are positive but less than the viscosity of water. For this reason, 95% lower prediction limits with values less than the viscosity of water at the same temperature were substituted with the viscosity of water at the appropriate temperature and plotted in Figure 5-11.

5.3.1 Model-Predicted Liquid Viscosities for Samples of Hanford Waste Tanks

Liquid viscosities were calculated for the two data sets described in Section 5.1.1:

- 1343 samples from 93 Hanford SSTs and DSTs
- 559 samples from 53 Hanford SSTs and DSTs.

The second data set is a subset of the first data set that had composition data for the major dissolved solids that affect SpG. In Section 5.2.4 it was necessary to use the second data set for assessing the performance of the HTWOS liquid-density model, which depends on having composition data. However, because the liquid-viscosity model in Section 5.3.1 is a function of liquid density rather than composition, the full data set as well as the subset can be used to generate predicted liquid viscosities. Table 5-6 summarizes the 93 tanks in the full data set as

well as the number of liquid-phase samples and range of predicted- liquid viscosities for each tank.

Table 5-6. Viscosities for Liquid-Phase Samples from 93 Hanford SSTs and DSTs

Tank	No.	μL Range (cP)	Tank	No.	μL Range (cP)	Tank	No.	μL Range (cP)	Tank	No.	μL Range (cP)
A-101	15	6.81-25.48	AY-102	121	1.01-3.65	C-105	1	4.26-4.26	T-103	1	4.29-4.29
AN-101	26	1.42-10.33	AZ-101	38	2.73-4.58	C-106	8	1.34-4.24	T-104	1	2.00-2.00
AN-102	35	8.03-55.74	AZ-102	29	1.94-4.11	C-107	6	2.66-3.23	T-105	5	1.55-3.42
AN-103	20	6.99-36.71	B-106	1	4.98-4.98	C-110	3	1.20-3.18	T-107	3	1.33-3.52
AN-104	27	6.84-27.99	B-107	6	1.20-8.07	S-101	6	6.95-19.83	T-110	1	2.07-2.14
AN-105	33	6.95-34.13	B-108	1	8.19-8.76	S-102	17	4.81-39.91	T-112	2	2.01-2.10
AN-106	39	1.33-4.85	B-203	4	1.40-1.66	S-103	3	11.65-22.95	T-201	5	1.55-1.72
AN-107	35	2.10-20.46	B-204	3	1.40-1.63	S-104	3	7.63-8.90	T-203	1	1.84-1.87
AP-101	19	1.09-8.03	BX-103	1	3.13-3.13	S-106	12	8.67-31.39	TX-104	6	9.18-54.02
AP-102	19	3.18-8.28	BX-109	1	4.68-4.85	S-107	6	3.44-7.70	TX-116	2	7.21-7.43
AP-103	22	1.15-8.52	BX-110	6	7.47-56.32	S-109	4	7.63-30.74	U-101	4	2.37-2.87
AP-104	10	1.17-5.29	BX-111	1	11.65-18.05	S-110	4	9.61-14.81	U-102	5	6.92-27.99
AP-105	38	3.76-22.01	BY-102	1	14.96-15.76	S-111	8	7.06-15.93	U-103	11	6.99-23.93
AP-106	19	1.12-3.79	BY-103	3	3.16-5.60	S-112	9	2.67-18.82	U-105	4	1.11-23.68
AP-107	34	1.10-8.09	BY-105	25	1.81-20.25	SX-101	9	15.12-31.07	U-106	5	6.21-9.27
AP-108	47	1.06-17.68	BY-106	3	4.11-10.38	SX-102	4	12.14-29.49	U-107	22	1.40-22.48
AW-101	37	6.77-31.39	BY-107	10	9.18-21.56	SX-103	12	12.14-26.29	U-108	4	8.07-13.91
AW-102	21	1.33-3.35	BY-109	2	20.04-30.74	SX-104	2	15.28-22.01	U-109	1	15.28-21.56
AW-103	15	0.97-10.49	BY-110	7	1.47-23.93	SX-105	18	8.94-31.07	U-111	3	8.24-11.17
AW-104	26	1.21-22.48	BY-111	3	10.07-12.14	SX-106	9	5.32-22.95	U-201	1	4.44-4.47
AW-105	28	1.19-2.93	BY-112	2	16.10-19.02	SY-101	32	2.38-15.76	U-202	1	4.82-5.37
AW-106	32	1.26-17.32	C-103	7	0.80-1.90	SY-102	114	1.33-9.42	U-203	1	4.92-5.10
AX-101	16	6.99-50.74	C-104	2	1.90-2.54	SY-103	7	16.78-33.77	U-204	1	2.12-2.15
AY-101	66	1.30-5.84	---	---	---	---	---	---	---	---	---

Note: The "No." columns indicate the number of liquid samples available in a given tank. Some tanks with only one sample have a range of liquid viscosities because there were multiple (two to four) measurements of liquid density for the one sample. This allowed applying the liquid-viscosity model to predict multiple liquid viscosities for samples with multiple SpG measurements.

5.3.2 Uncertainties of Predicted Liquid Viscosities for Samples of Tank Waste

Predictions of liquid viscosity at 30°C for the liquid-phase samples of Hanford waste tanks were made using the model discussed in Section 5.3.1 with measured liquid densities of the samples used as inputs to the model. These liquid-viscosity predictions are subject to several uncertainties, as discussed in the following subsections.

### 5.3.2.1 *Systematic Uncertainty in Liquid-Viscosity Model Form*

The liquid-viscosity model discussed in Section 5.3.1 assumes that (1) the Arrhenius equation $(Ae^{B/T})$ represents the temperature effects on liquid viscosity and (2) liquid density has a linear effect on the coefficients (A and B) of the Arrhenius equation. The Arrhenius equation is expected to represent adequately the effect of temperature over the relatively small range of temperatures applicable for the transfer of Hanford tank wastes. The assessment of assumption (2) is discussed in Appendix B. The conclusion there is that the linear dependencies of the Arrhenius coefficients on liquid density are weak, with considerable random uncertainty. Further, retaining or removing some potentially outlying data points significantly impacts the linear relationships. Hence, the liquid-viscosity model discussed in Section 5.3.1 may be subject to systematic uncertainty. However, it is impossible to quantify without additional data (which, if available, would be used to improve the liquid-viscosity model and remove the systematic uncertainty).

5.3.2.2 *Uncertainties of Liquid-Viscosity Model Coefficients*

Because the liquid-viscosity model coefficients in Table 5-5 were obtained by generalized linear model fits to empirical data, they are subject to regression estimation uncertainty. For reasons discussed in the previous subsection, the weak linear dependence of liquid viscosity on liquid density makes the liquid-viscosity model coefficients (and hence predictions) subject to considerable uncertainty. The generalized linear model methodology (Myers et al. 2002) provides for calculating 95% PIs to represent the uncertainty in liquid-viscosity predictions resulting from uncertainty in the model coefficients. The application of this methodology is discussed subsequently.

5.3.2.3 *Uncertainties in Liquid-Viscosity Model Predictions Resulting from Uncertainties in Liquid Densities*

Liquid densities measured for liquid-phase samples of Hanford tanks wastes were used as inputs to the liquid-viscosity model. The measured liquid densities are subject to measurement uncertainty, as discussed and quantified in Section 5.1.2. In that section, some samples had multiple (two to four) measurements of liquid density, which provided a basis to quantify the measurement uncertainty (SD). For this section, the multiple liquid-density measurements were used as inputs to the liquid-viscosity model to obtain multiple predicted liquid viscosities. These multiple values per sample were then used to calculate means and SDs, which are subject to considerable uncertainty being calculated only from two to four values. However, such means and SDs suffice for investigating whether the SDs appear to have a relationship with the mean values, or differ significantly for some Hanford tanks.

Figure 5-12 shows the SDs of multiple predicted liquid viscosities plotted versus the mean values for the 328 samples with multiple SpG measurements. The magnitude of the SDs increase with increasing means of predicted liquid viscosities. A plot of percent relative standard deviations (%RSD) versus the means (not included) showed the %RSD values were relatively constant with the magnitude of the mean. All of the %RSDs are below 60, while all but eight are below 30. A substantial fraction of the %RSDs are below 10. A pooled estimate of the %RSD for predicted liquid viscosities is 10.2, which was estimated with 347 degrees of freedom.

Figure 5-12. Standard Deviations versus Means Calculated from Predicted Liquid-Viscosities for Replicate Specific Gravity Measurements on Hanford Waste Samples
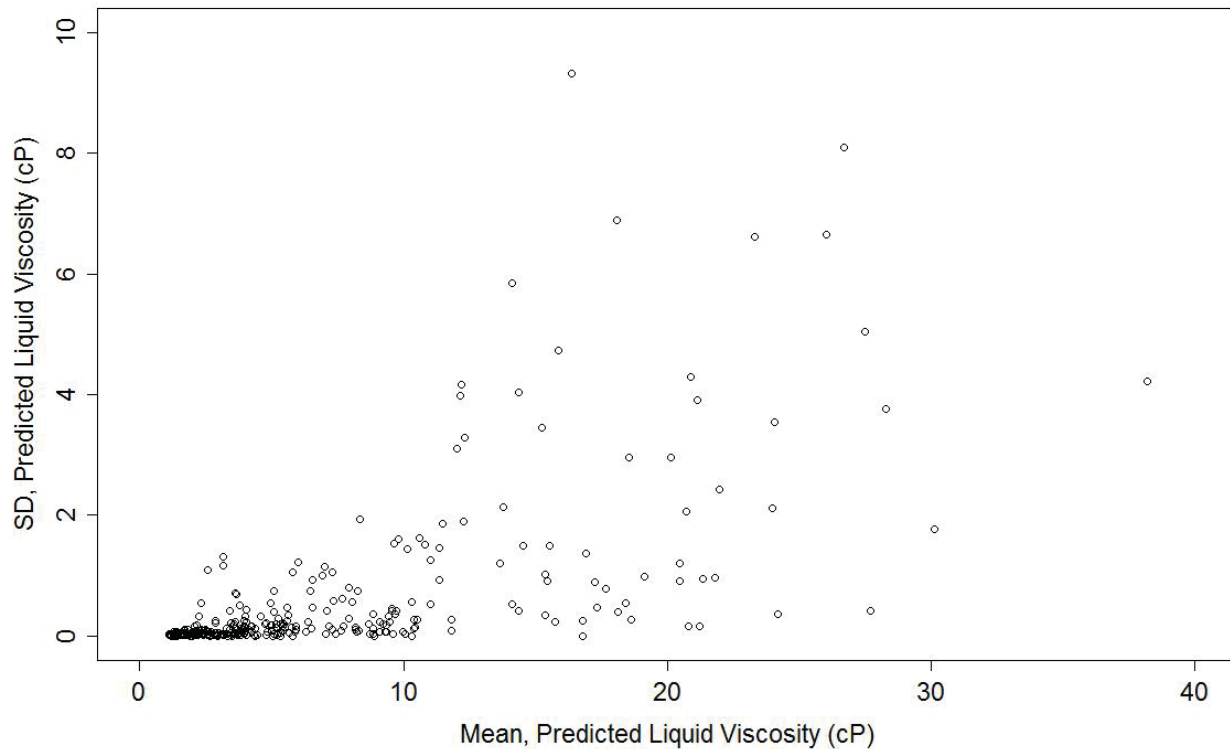
5.3.3   Variation of Predicted Liquid Viscosities for Hanford Waste Samples

For the reasons given in Section 5.1.3, the variation in predicted liquid viscosities corresponding to variation in the measured SpG values from the Hanford waste tank samples were not evaluated.

5.4   PREDICTIONS OF LIQUID VISCOSITY FOR WASTE FEED

Section 5.4.2 summarizes the results of predicted liquid viscosities obtained by applying the viscosity model (discussed in Section 5.3.1) to the waste feed batches from System Plan Rev. 6 (ORP-11242). Sections 5.4.2 and 5.4.3, respectively, discuss uncertainties and variation of the predicted liquid viscosities over the course of waste transfers to the WTP.

5.4.1   Liquid-Viscosity Predictions for Waste Feed

The liquid-viscosity model discussed in Section 5.3.1 was applied to predict liquid viscosities at 30°C for the waste feed batches calculated by HTWOS for 10 cases in System Plan Rev. 6 (ORP-11242). The 10 cases include the Baseline Case and nine other cases discussed in (ORP-11242). The HTWOS software calculates liquid densities using the model discussed in

Section 5.2.1. Those calculated liquid densities then are used as inputs to calculate the viscosity of the liquid phase of each waste feed batch. The results are discussed in Section 5.4.3.

5.4.2   Uncertainties in Liquid-Viscosity Predictions for Waste Feed

Predictions of liquid viscosity at 30°C for waste feed batches to WTP were made using the model discussed in Section 5.3.1 with liquid-density input values predicted by the model in Equation 5-2. These liquid-viscosity predictions are subject to several uncertainties, as discussed previously in Section 5.3.3, except for one difference. In that section, measured liquid densities were used as inputs to the liquid-viscosity model. In this section, the liquid densities were predicted by the model discussed in Section 5.2.1, which is a function of component compositions. In the situation covered in this section, the component compositions calculated by HTWOS may or may not be subject to uncertainty. For simplicity, the composition estimates made by HTWOS were treated as being without uncertainty. Any uncertainties in component compositions would induce uncertainties in model-predicted liquid densities, which in turn would induce uncertainties in model-predicted liquid viscosities.

5.4.3   Variation of Liquid Viscosity Model Predictions for Waste Feed

For various retrieval, blending, and operating scenarios, HTWOS can simulate the compositions of waste feed batches to the WTP over the course of the feed transfer and vitrification mission. HTWOS does not include a liquid-viscosity model, but the liquid-viscosity model discussed in Section 5.3.1 can be used in conjunction with the HTWOS model for liquid density (discussed in Section 5.2.1) to predict liquid viscosities for each waste feed batch. The viscosity of liquid-phase waste can be controlled by adding water (dilution) or removing water (evaporation), or by blending wastes with different liquid-phase densities.

In this section, we investigate the variation in model-predicted values of liquid viscosity for the projected waste feed batches in the 10 cases of System Plan Rev. 6 (ORP-11242). The 10 cases include the Baseline Case and nine other cases discussed in ORP-11242. HTWOS makes calculations for both HLW and LAW feed batches, but only HLW batches are considered here (as was done in Section 5.2.5).

The Baseline Case includes the HTWOS-predicted, liquid densities for 600 HLW feed batches dated 5/31/2018 to 2/18/2043. The liquid-viscosity model from Section 5.3.1 was used to predict the liquid viscosity at 30°C using these HTWOS-predicted, liquid densities for each of the 600 HLW feed batches. Figures 5-13 and 5-14, respectively, present a histogram and a cumulative distribution function of these liquid-viscosity predictions. These figures show that the predicted liquid viscosities range from 2.12 to 65.50 cP. The distributions have obvious outlying data, as discussed following.

Figure 5-13. Histogram of Model-Predicted Liquid Viscosities 600 HLW Feed Batches from 5/31/2018 to 2/18/2043 for the Baseline Case of System Plan Rev. 6
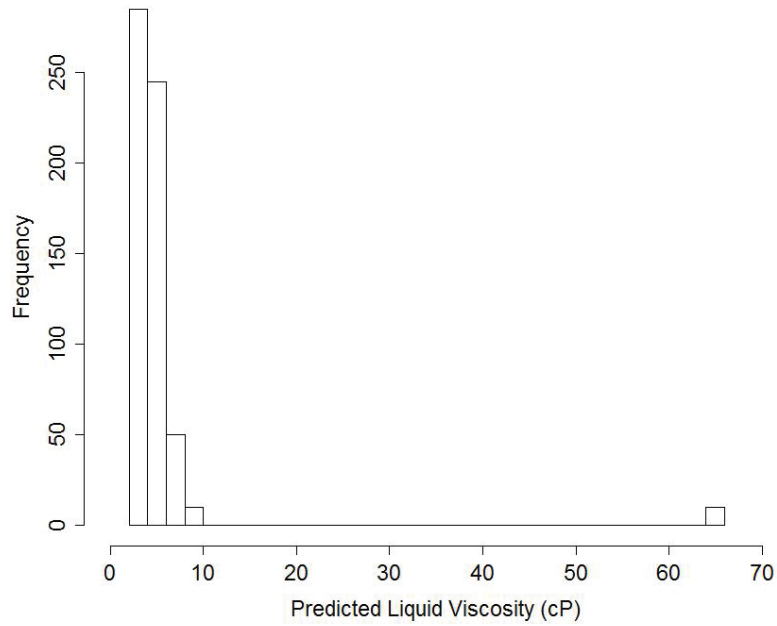
Figure 5-14. Cumulative Distribution Function of Model-Predicted Liquid Viscosities for 600 HLW Feed Batches from 5/31/2018 to 2/18/2043 for the Baseline Case of System Plan Rev. 6
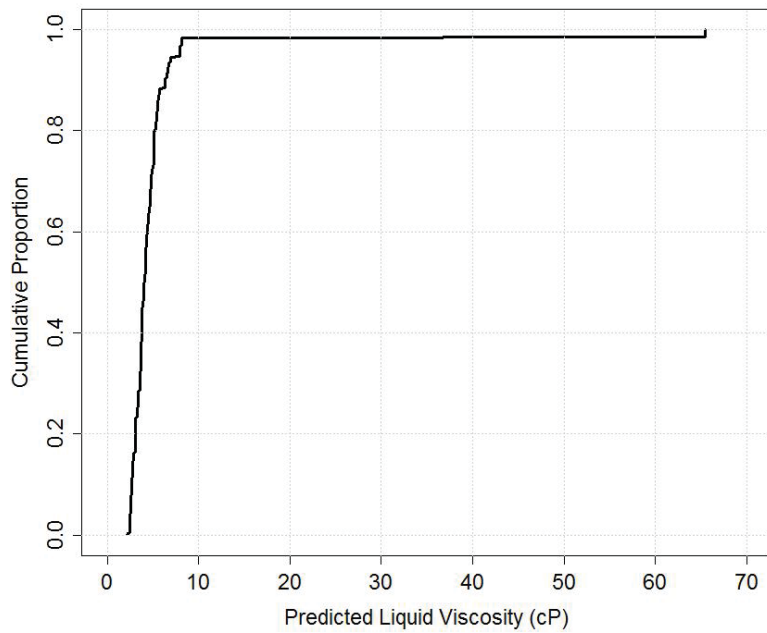
As noted previously, there are 10 HLW batches (from 11/29/2041 to 8/11/2042) that have liquid densities of 1.60 kg/L. The predicted liquid viscosities for those 10 batches are 65.50 cP, which are clear outliers in Figure 5-13. Those 10 batches are within the end-of-mission activities projected to begin on 9/8/2039 in the Baseline Case. End-of-mission activities include consolidating the remaining waste in the DSTs into the last several HLW and LAW feed campaigns and cleaning out the remaining DST heels. The HTWOS uses a simplified set of model controls during end-of-mission activities that are not reflective of how those last campaigns would be prepared and delivered. Work is underway to include a refined set of end-of-mission controls in the HTWOS model to remedy this issue for the next revision of the System Plan and the corresponding Integrated Waste Feed Delivery Plan.

Figures 5-15 and 5-16, respectively, present a histogram and a cumulative distribution function of the model-predicted, liquid viscosities for HLW feed batches in the Baseline Case prior to the end-of-mission activities starting on 9/8/2039. This subset of the data has 505 HLW feed batches dated from 5/31/2018 to 4/24/2039 with predicted, liquid viscosities ranging from 2.44 to 8.00 cP. Figure 5-15 shows a distribution of predicted, liquid viscosities that is unimodal and slightly skewed to the right. Figure 5-16 shows that roughly 95% of the predicted liquid viscosities fall within the 2.5 to 7.5 cP range.

Figure 5-15. Histogram of Model-Predicted Liquid Viscosities for 505 HLW Feed Batches from 5/31/2018 to 4/24/2039 for the Baseline Case of System Plan Rev. 6
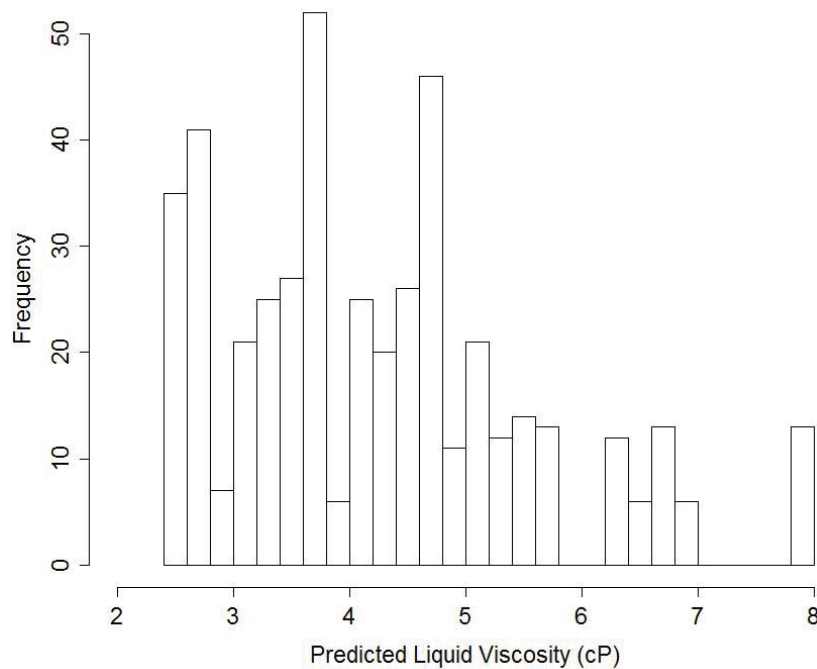
Figure 5-16. Cumulative Distribution Function of Model-Predicted Liquid Viscosities for 505 HLW Feed Batches from 5/31/2018 to 4/24/2039 for the Baseline Case of System Plan Rev. 6
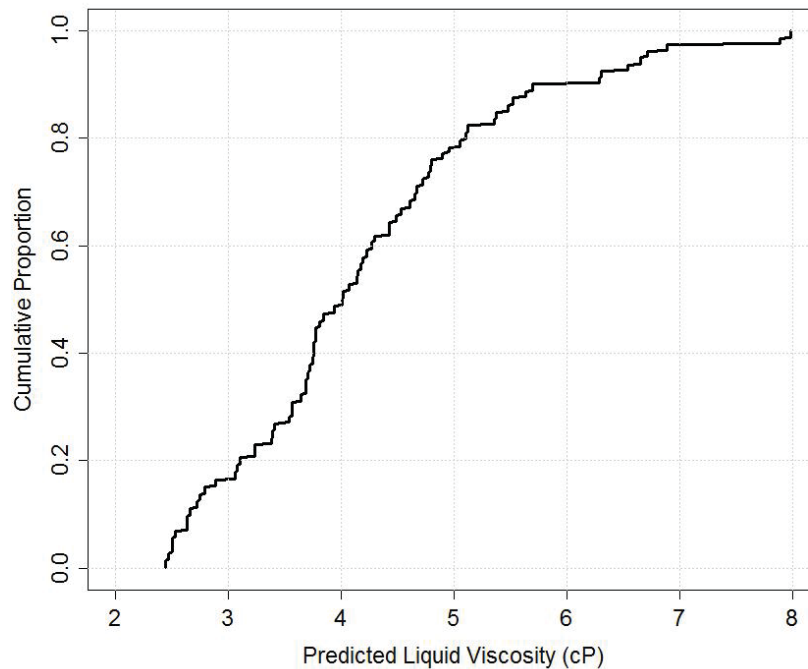
Figure 5-17 is similar to Figure 5-16, except that cumulative distribution functions of liquid viscosity for all 10 cases evaluated in System Plan Rev. 6 (ORP-11242) are displayed together. Figure 5-17 uses the HLW batches from the 10 cases dated up to 9/9/2037. The date 9/9/2037 is the earliest date for which any of the 10 cases begin end-of-mission activities and was chosen for consistency in comparing the results of all 10 cases. Figure 5-17 illustrates that the kinds of assumptions and parameters that changed among the 10 cases have only a small effect on the range of liquid viscosities of the HLW batches up to the start of end-of-mission activities. For just the Baseline Case, the predicted liquid viscosities range from 2.44 to 8.00, as noted previously. Across all 10 cases, the predicted liquid viscosities range from 2.05 to 18.53. For all 10 cases, approximately 95% of all the HLW batches have predicted, liquid viscosities falling between 2.5 to 7.5 cP. Ninety-five percent of the predicted values fall between 2.5 to 7.5 cP for both the Baseline Case and all 10 cases.

Figure 5-17. Cumulative Distribution Functions of Model-Predicted Liquid Viscosities for HLW Feed Batches Dated Up to 9/9/2037 for the Baseline Case (black line) and Nine Other Cases (gray lines) of System Plan Rev. 6
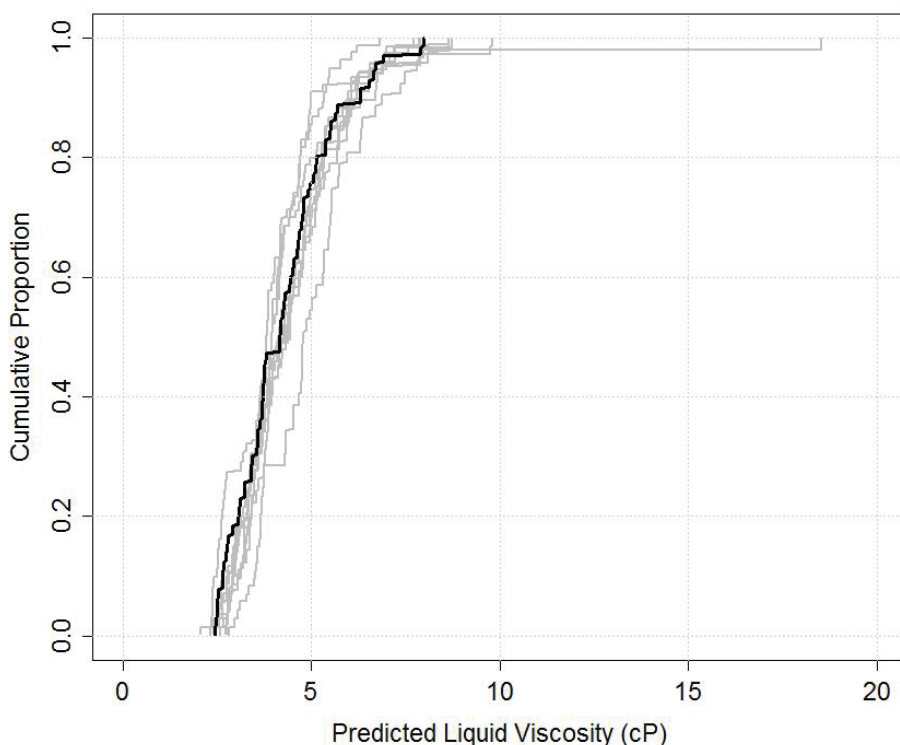
Finally, we discuss and quantify how the variations in predicted liquid viscosities for HLW batches in the Baseline Case and the nine other cases (from System Plan Rev. 6) prior to the end-of-mission period are affected by the uncertainties discussed in Section 5.4.2. These uncertainties include systematic and random uncertainties in liquid-viscosity predictions resulting from the liquid-viscosity model form, the fit of the liquid-viscosity model to experimental data, the HTWOS model predictions of liquid densities used as input variables to the liquid-viscosity model and the fit of the liquid-density model to experimental data.

As noted in Section 5.3.4, there are insufficient data to quantify systematic uncertainty resulting from the form and fit of the liquid-viscosity model. Also, the liquid-density model yields predicted values that are over-predicted by a factor of 1.0044 (as discussed in Section 5.2.3). The propagation of systematic and random uncertainties in the liquid-density model is not investigated. The resulting bias in liquid viscosities is expected to be relatively small compared to random uncertainty in liquid-viscosity model predictions. However, the random uncertainty in liquid-density predictions could contribute non-negligible uncertainty to liquid-viscosity model predictions. Investigating how liquid-density model uncertainties affect liquid-viscosity model uncertainties is left to a future effort.

In this effort, we quantified how the uncertainties in liquid-viscosity predictions (represented by 95% PIs) increase the ranges of predicted liquid viscosities for the Baseline Case of System Plan Rev. 6 (ORP-11242). Figures 5-18 and 5-19 display cumulative distribution functions for the lower and upper limits of 95% PIs on liquid viscosities for HLW feed batches. Figure 5-18 is for

the full WTP mission (5/31/2018 to 2/18/2043), while Figure 5-19 is for the period 5/31/2018 to 4/24/2039 prior to the end-of-mission (as discussed in Section 5.2.5). Liquid viscosities, with model prediction uncertainties, range from 0.80 to 81.90 cP in Figure 5-18 and from 0.80 to 13.54 cP in Figure 5-19.

The 95% PIs shown in Figures 5-18 and 5-19 were obtained using asymptotic results (Myers and Montgomery 2002) and the fitted, liquid-viscosity model has significant uncertainty. The lower limits from the methodology were actually negative values in many cases, but it is not physically possible to have negative liquid viscosities. It was decided that a reasonable practical lower limit for the 95% PIs was given by the viscosity of water at 30ºC. Hence, in Figures 5-18 and 5-19 the lower limits of the 95% PIs that were less than the viscosity of water at 30ºC (including negative values) were replaced by that value (0.7975). The 95% PIs in Figure 5-19 look much wider than the 95% PIs in Figure 5-18. However, Figure 5-18 has predicted liquid viscosities ranging up to more than 80 cP, whereas the values in Figure 5-19 range up to only 8 cP. The narrower range makes the widths of the 95% PIs look wider in Figure 5-19 than in Figure 5-18.

Figure 5-18. Cumulative Distribution Functions of Predicted Liquid Viscosities (black) and Lower and Upper Limits of 95% Prediction Intervals (gray) for HLW Feed Batches from 5/31/2018 to 2/18/2043 (Full Mission) for the Baseline Case of System Plan Rev. 6
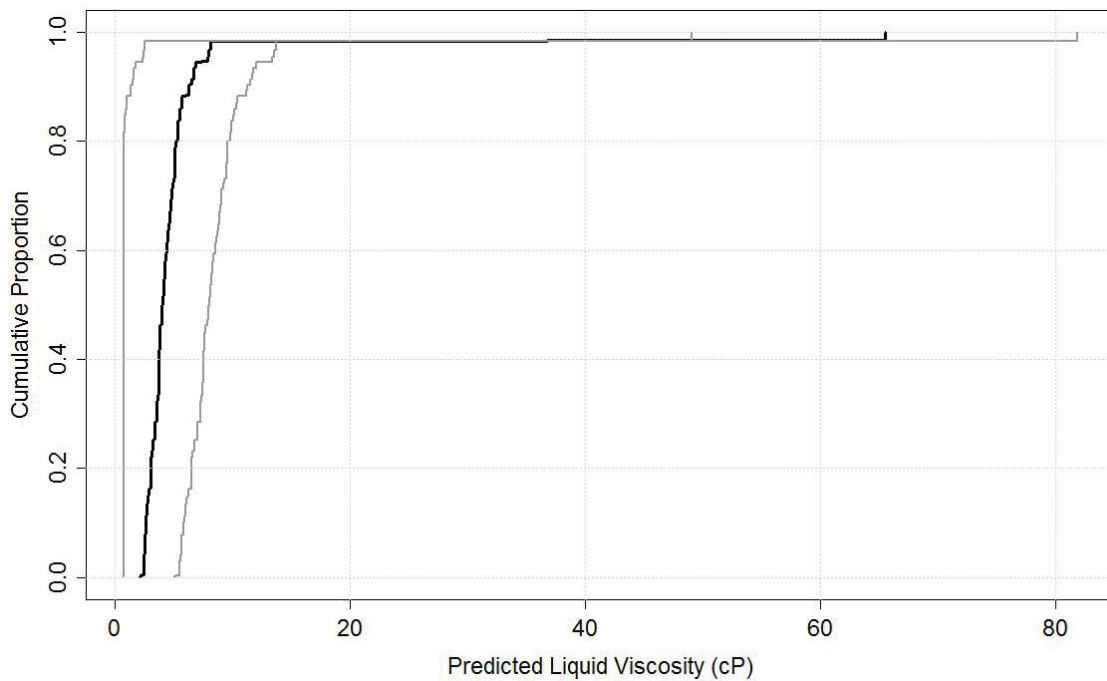
Figure 5-19. Cumulative Distribution Functions of Predicted Liquid Viscosities (black) and Lower and Upper Limits of 95% Prediction Intervals (gray) for HLW Feed Batches from 5/31/2018 to 4/24/2039 (Before End-of-Mission) for the Baseline Case in System Plan Rev. 6
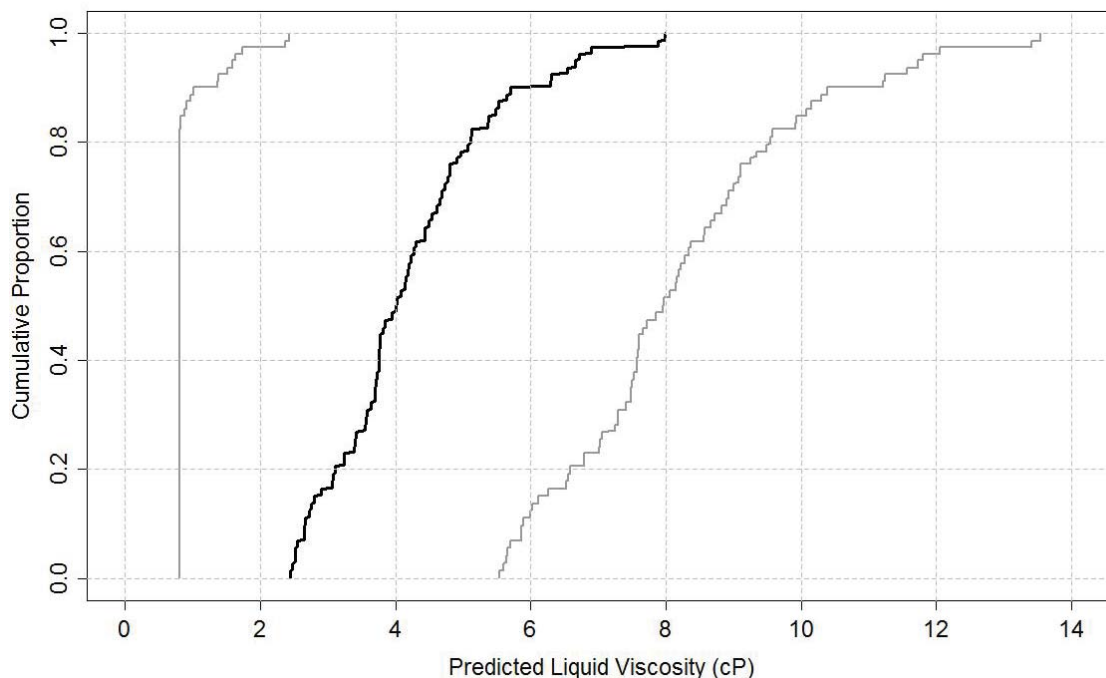
Table 5-7 summarizes the variation and uncertainties in model-predicted liquid viscosities for the HTWOS System Plan Rev. 6 projections of waste feed batches.

Table 5-7. Variation in Model-Predicted Liquid Viscosities Without and With Uncertainties for HLW Feed Batches from System Plan Rev. 6

Data Set	Without Uncertainties		With Uncertainties	
	Min, cP	Max, cP	Min, cP	Max, cP
Liquid viscosity, HTWOS baseline case[a]	2.12	65.50[d]	0.80[e]	81.90[d]
Liquid viscosity, HTWOS baseline case[b]	2.44	8.00[f]	0.80[e]	13.54[f]
Liquid Viscosity, HTWOS 10 cases[c]	2.05	18.53	—[g]	—[g]

Notes:

a. For waste feed batches from 5/31/2018 to 2/18/2043, the whole mission for the Baseline Case.

b. For waste feed batches from 5/31/2018 to 4/24/2039, prior to the end-of-mission activities for the Baseline Case.

c. For waste feed batches up to 9/9/2037, prior to the end-of-mission activities for all 10 cases in System Plan Rev. 6.

d. Maximum viscosities without and with uncertainties were obtained using a maximum liquid density value without uncertainty of 1.596 (from Table 5-4)

e. The calculated lower limits of 95% PIs were lower than, and hence replaced by, the viscosity of water at 30ºC, which is equal to 0.7975 and was rounded to 0.80 for this table

f. These maximum viscosities without and with uncertainties were obtained using a maximum liquid density value without uncertainty of 1.369 (from Table 5-4).

g. Case 4 of the 10 cases has a much higher maximum value of predicted liquid viscosity than the other nine cases and accounting for model-prediction uncertainties would yield an even larger maximum "prediction plus uncertainty" value for Case 4. Hence, these calculations were not performed.

5.5   PRELIMINARY ASSESSMENT OF STORAGE AND TRANSFER OPERATIONS EFFECT ON LIQUID PROPERTIES

Most storage and transfer operations affect liquid densities and viscosities. The DSTs are actively ventilated and simple storage in the absence of other activities results in concentration of supernatant. For example, the supernatant in AY-102 is most likely going to require some dilution before LAW commissioning. In addition, liquid properties are often adjusted by in-line dilution during waste transfers and the 242-A Evaporator will be routinely used to concentrate liquid waste during WFD (ORP-11242).

Long-term liquid densities and viscosities have high uncertainties because simple storage and nearly all operations will affect density and viscosity. Fortunately, liquid densities and viscosities are relatively easy to manipulate through blending, dilution and concentration (i.e., evaporation).

6.0   SLURRY RHEOLOGY DATA, UNCERTAINTIES AND VARIATION

Rheology data for slurries of liquids (with dissolved solids) and undissolved solids for Hanford tank wastes are presented and discussed in Section 6.1. Rheology predictions at 10 wt% solids are presented in Section 6.2. Preliminary assessments of WFD operations effect on rheological properties are presented in Section 6.3.

6.1   SLURRY VISCOSITY AND YIELD STRESS

Rheology data are available for slurry samples of a limited number of Hanford tanks. The majority of the rheology data were obtained from laboratory measurements of samples retrieved from the tanks. These samples were retrieved using push- and rotary-mode core samples, auger samples and grab samples. A limited set of data is available from in situ measurements. Slurry rheological properties include Bingham yield stress (yield stress) and the Bingham consistency (viscosity). A discussion of rheological characterization and measurement techniques is provided in PNNL-16857, *Estimate of Hanford Waste Rheology and Settling Behavior*.

Yield stress and viscosity are common terms used to describe a material's rheological properties, which are measured indirectly. Yield stress and viscosity measurements are available for concentrated slurries from 29 individual tanks and eight composite groups (PNNL-20646). Rheological properties depend on the characteristics of the system, including undissolved solids (UDS) concentration, PSD, particle shape, pH, quiescent time, elevation within the sediment, retained gas content and temperature. This is discussed in detail in PNNL-20646.

In this section the rheological properties of slurries from tank samples, or blends of tank samples, of the Hanford tank waste are evaluated to investigate the WFD rheological characteristics. Temperature, agitation and blending effects on the slurries are also discussed subsequently.

6.1.1   Slurry Viscosity and Yield Stress Data

6.1.1.1   *Data from Tank Samples*

Figures 6-1 and 6-2 are Figures 3.110 and 3.111 from PNNL-20646. Sludge and saltcake waste as indicated by the primary waste type in the respective tanks are shown separately. The complicated dependence of the Bingham parameters on UDS concentration makes it difficult to apply a single, simple model to these parameters as a function of UDS concentration. However, even for the disparate data set, a trend of increasing Bingham parameter values with increasing UDS concentration is apparent. At a given mass fraction the Bingham parameters vary by about two orders of magnitude. Analyses were performed between 20 and 90ºC which accounts for some of the range of data at a given UDS mass fraction. A portion of each property's distribution over the tanks is above the ICD-19 acceptance criteria for HLW feed of 1 Pa Bingham yield stress and 10 cP Bingham viscosity at 10 wt% UDS and less. The saltcake data

points in these figures are of less significance to the current evaluation because it is likely that a good portion, if not all, of the saltcake solids will be dissolved during SST retrievals or WFD.

Figure 6-1. Measured Yield Stress as a Function of Solids Concentrations for Sludge and Saltcake Wastes in 23 Tanks
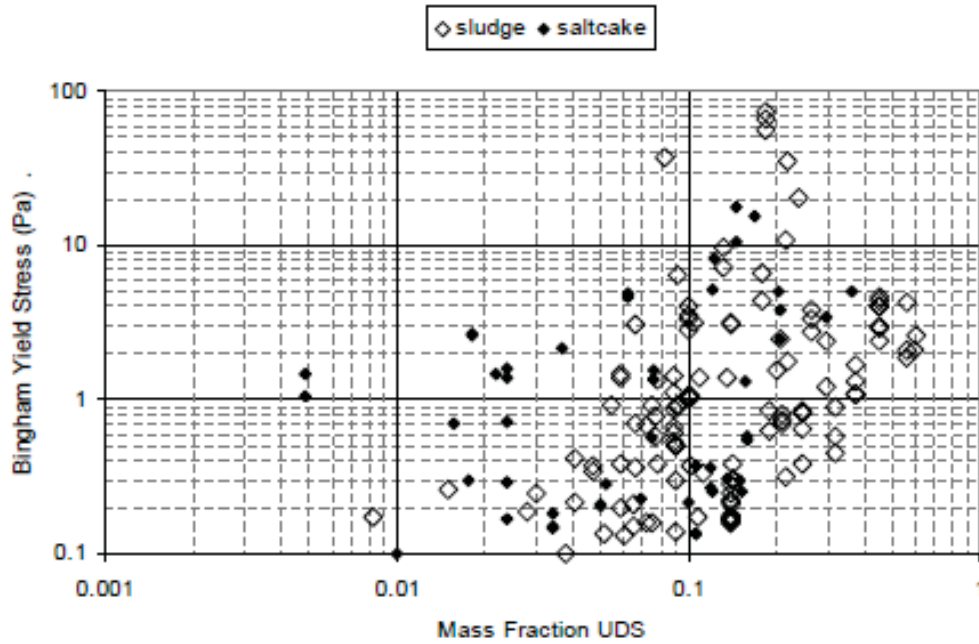
Figure 6-2. Measured Viscosity as a Function of Solids Concentration for Sludge and Saltcake Wastes in 23 Hanford Tanks
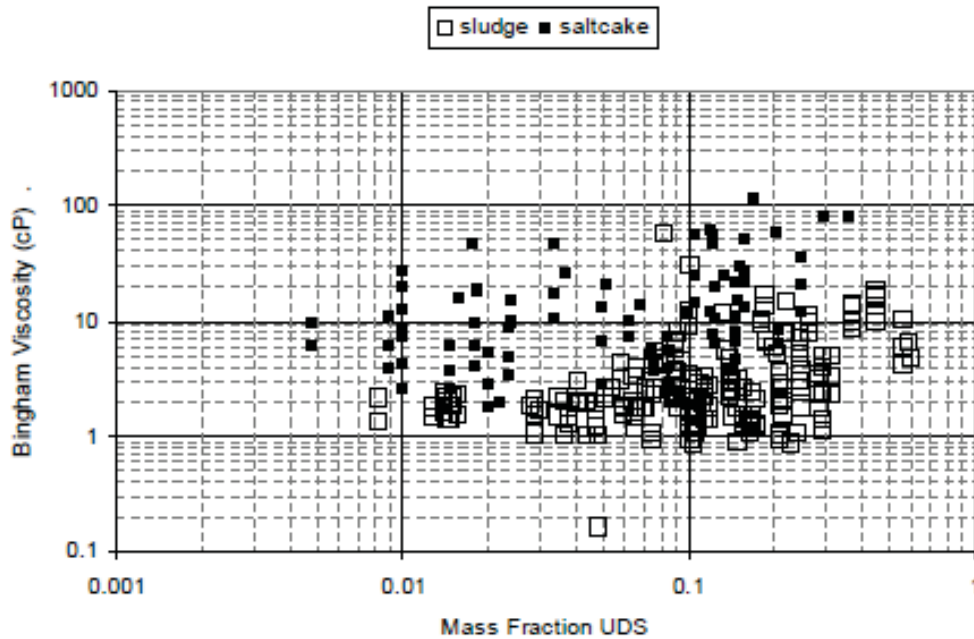
Rheological data for each tank are presented in Figure 6-3 through Figure 6-26. The figures plot yield stress and viscosity data as a function of UDS concentration. Rheological data were collected at various temperatures for each of the tanks. The data for some tanks were taken at just one temperature, while the data for other tanks were taken at several temperatures. For better comparisons, individual curves were fitted to the data in temperature increments.

Yield stress has a power law dependence, given by the following (PNNL-20646):

$$\tau_y = Ex^F \tag{6-1}$$

where τ_y = yield stress (Pa)
x = mass fraction of solids in the slurry (dimensionless)
E = fitting parameter (Pa)
F = fitting parameter (dimensionless)

Yield stress was fitted in the form shown by Equation 6-1 using Excel's power-law fitting function.

Viscosity follows an exponential curve (PNNL-20646):

$$\mu_B = Ge^{Hx} \tag{6-2}$$

where μ_B = viscosity (cP)
x = mass fraction of solids in the slurry (dimensionless)
G = fitting parameter (cP)
H = fitting parameter (dimensionless)

Viscosity data were fitted using Excel's exponential fitting function in the form shown by Equation 6-2.

PNNL-16857 described the rheological changes due solely to UDS concentration change as mechanically dominated. Mechanically dominated behavior was postulated to occur when the values of rheological properties increase with increasing UDS concentration. Chemically-dominated behavior was postulated to occur when the rheological properties increase to a maximum value with water dilution. Examples that show this type of behavior include Figure 6-10 for tank B-201 and Figure 6-14 for tank C-104. At the bottom of Figures 6-3 to 6-23 are the empirical curve fits for shear stress and viscosity.

Figure 6-3. Rheology Data for AN-103 Waste (A2 Saltcake)
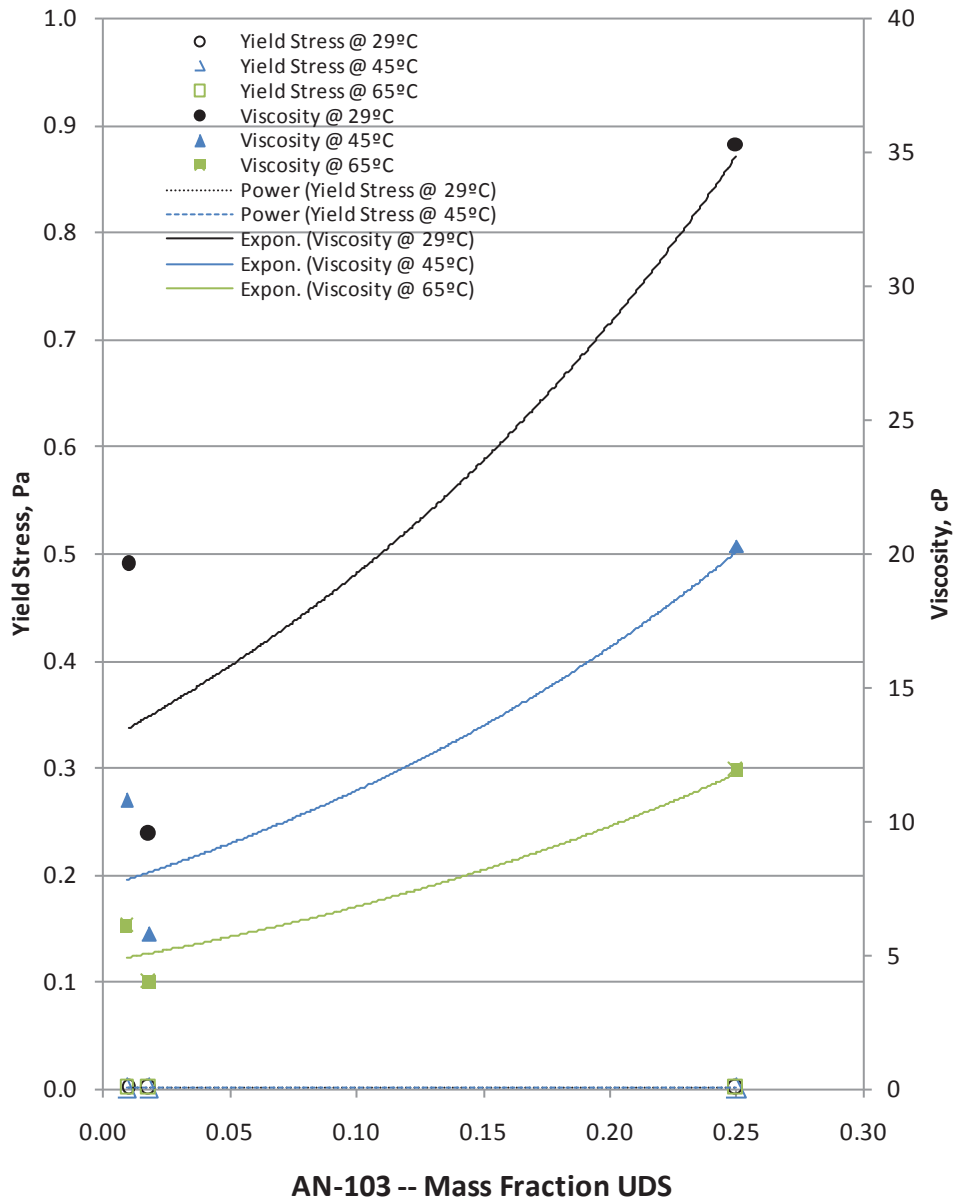
	Yield Stress Curve Fits		Viscosity Curve Fits	
29ºC	$\tau_y = 0.0$	R^2 = n/a	$\mu_B = 12.99e^{3.946x}$	R^2=0.669
45ºC	$\tau_y = 0.0$	R^2 = n/a	$\mu_B = 7.555e^{3.903x}$	R^2=0.724
65ºC	$\tau_y = 0.0$	R^2 = n/a	$\mu_B = 4.721e^{5.662x}$	R^2=0.828

Figure 6-4. Rheology Data for AN-104 Waste (A2 Saltcake)
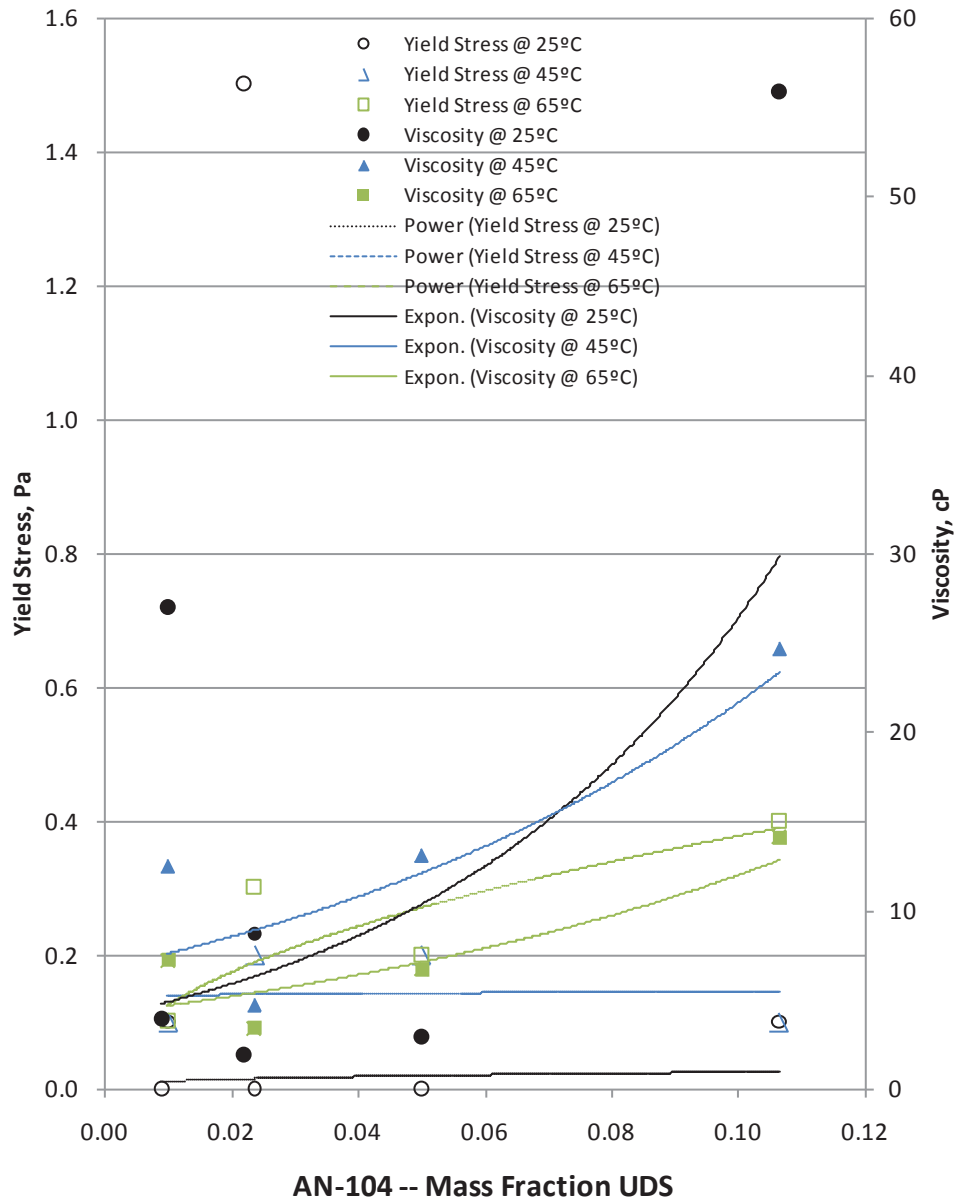
	Yield Stress Curve Fits		Viscosity Curve Fits	
25ºC	$\tau_y = 0.052x^{0.325}$	$R^2=0.009$	$\mu_B = 4.056e^{18.75x}$	$R^2=0.273$
45ºC	$\tau_y = 0.148x^{0.011}$	$R^2=0.001$	$\mu_B = 6.748e^{11.64x}$	$R^2=0.526$
65ºC	$\tau_y = 1.156x^{0.673}$	$R^2=0.536$	$\mu_B = 4.208e^{10.50x}$	$R^2=0.593$

Figure 6-5. Rheology Data for AN-105 Waste (A2 Saltcake)
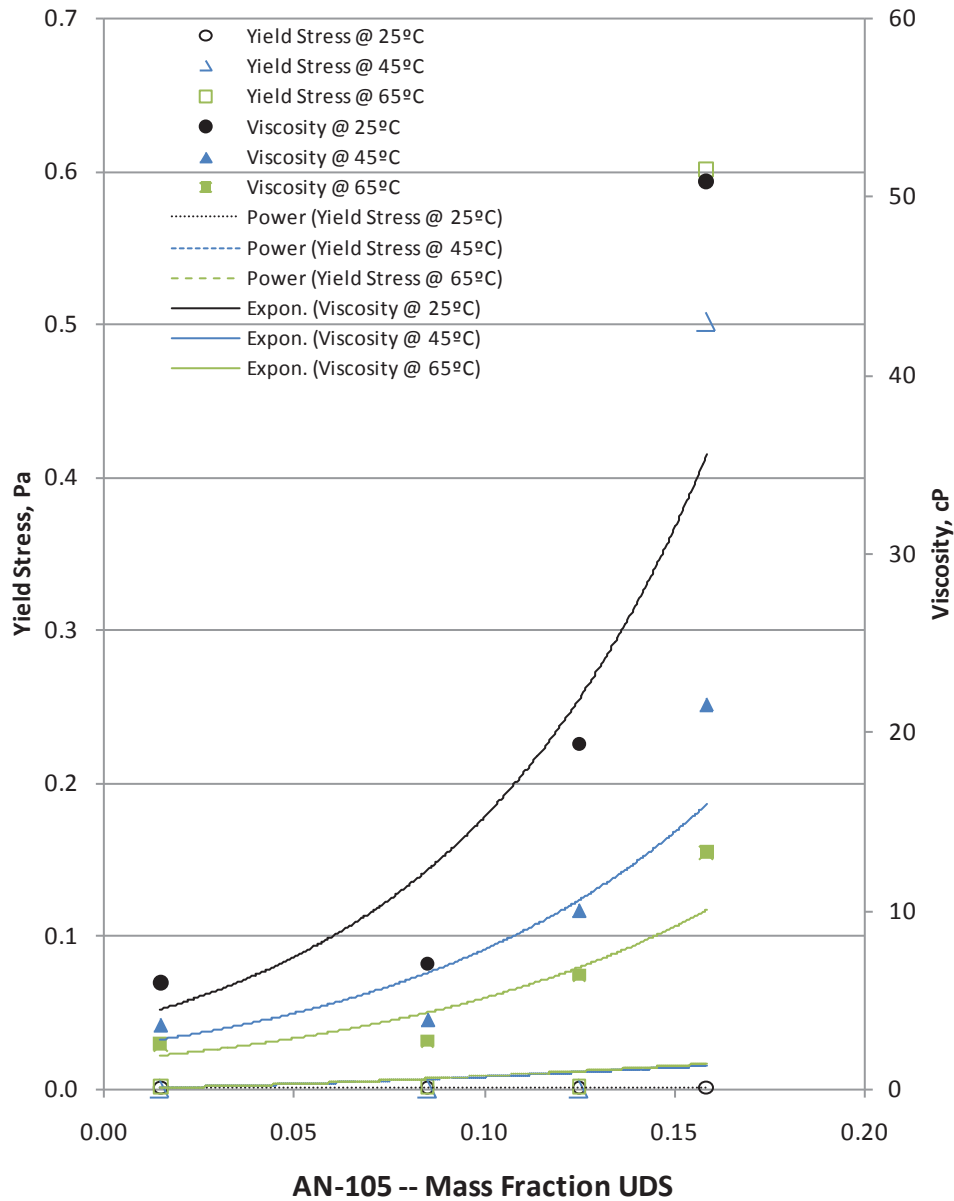
	Yield Stress Curve Fits		Viscosity Curve Fits	
25ºC	$\tau_y = 0.0$	R^2= n/a	$\mu_B = 3.567e^{14.51x}$	R^2=0.818
45ºC	$\tau_y = 0.219x^{1.447}$	R^2=0.25	$\mu_B = 2.284e^{12.29x}$	R^2=0.802
65ºC	$\tau_y = 0.257x^{1.489}$	R^2=0.251	$\mu_B = 1.634e^{11.45x}$	R^2=0.801

Figure 6-6. Rheology Data for AW-101 Waste (A2 Saltcake)
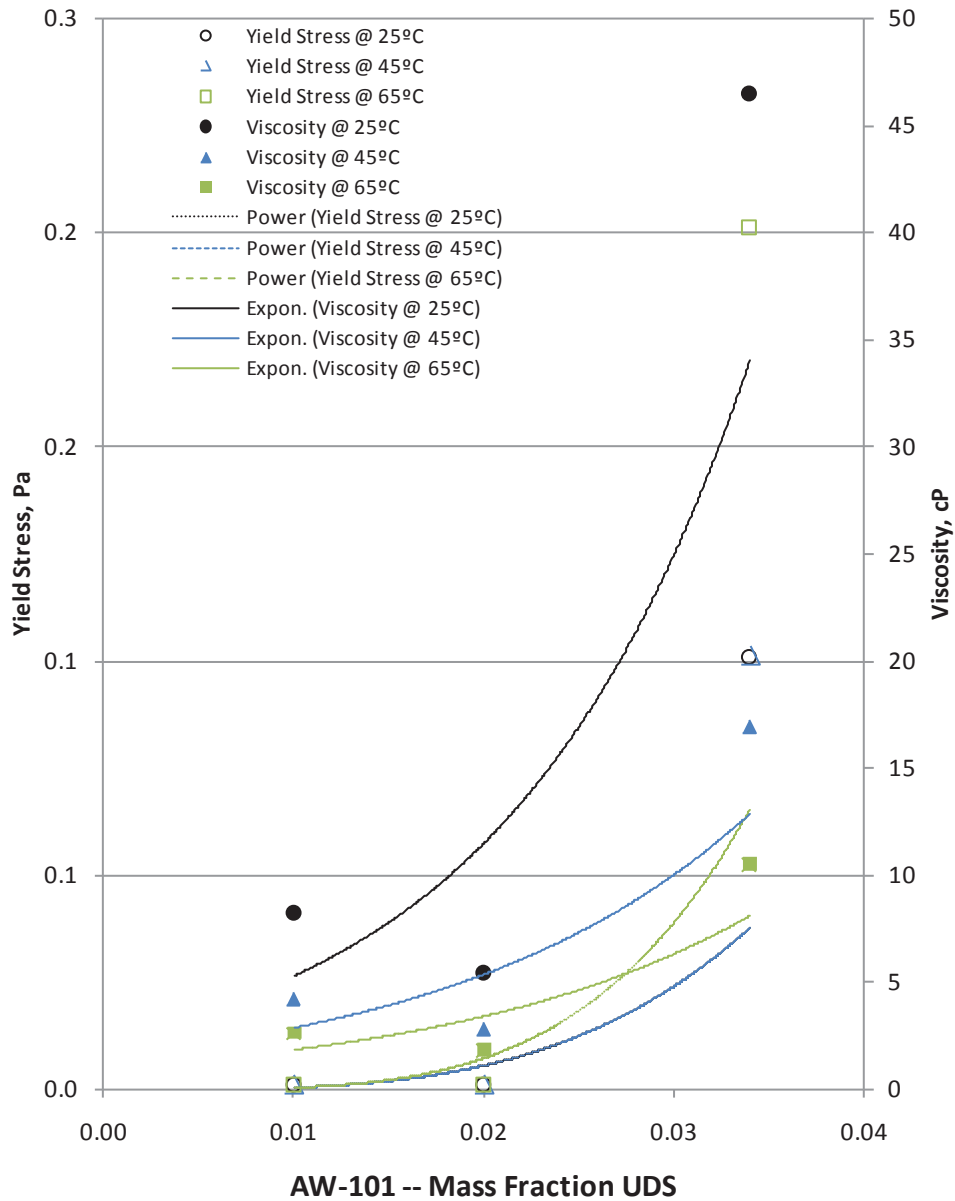
	Yield Stress Curve Fits		Viscosity Curve Fits	
25ºC	$\tau_y = 6921x^{3.583}$	$R^2=0.692$	$\mu_B = 2.433e^{77.53x}$	$R^2=0.670$
45ºC	$\tau_y = 6921x^{3.583}$	$R^2=0.692$	$\mu_B = 6.353e^{-11.4x}$	$R^2=0.681$
65ºC	$\tau_y = 72468x^{4.117}$	$R^2=0.681$	$\mu_B = 0.965e^{62.51x}$	$R^2=0.656$

Figure 6-7. Rheology Data for AY-102 Waste (BL Sludge)
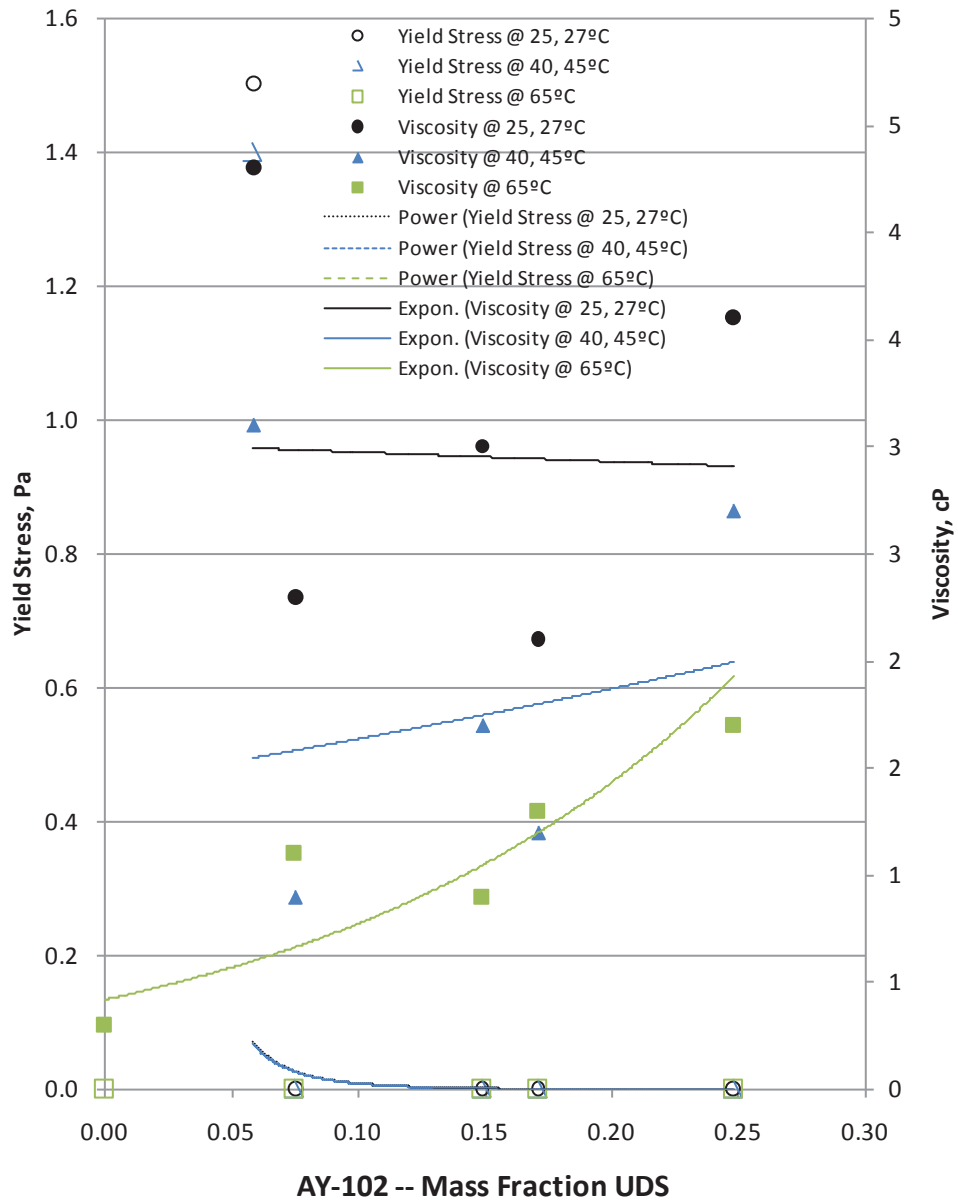
Yield Stress Curve Fits			Viscosity Curve Fits	
20, 27ºC	$\tau_y = 2\text{E-}06x^{-3.77}$	$R^2=0.477$	$\mu_B = 3.012e^{-0.14x}$	$R^2=0.001$
40, 45ºC	$\tau_y = 2\text{E-}06x^{-3.73}$	$R^2=0.477$	$\mu_B = 1.431e^{1.377x}$	$R^2=0.038$
65ºC	$\tau_y = 0.0$	$R^2= n/a$	$\mu_B = 0.779e^{2.765x}$	$R^2=0.535$

Figure 6-8. Rheology Data for AZ-101 Waste (P3 Sludge)
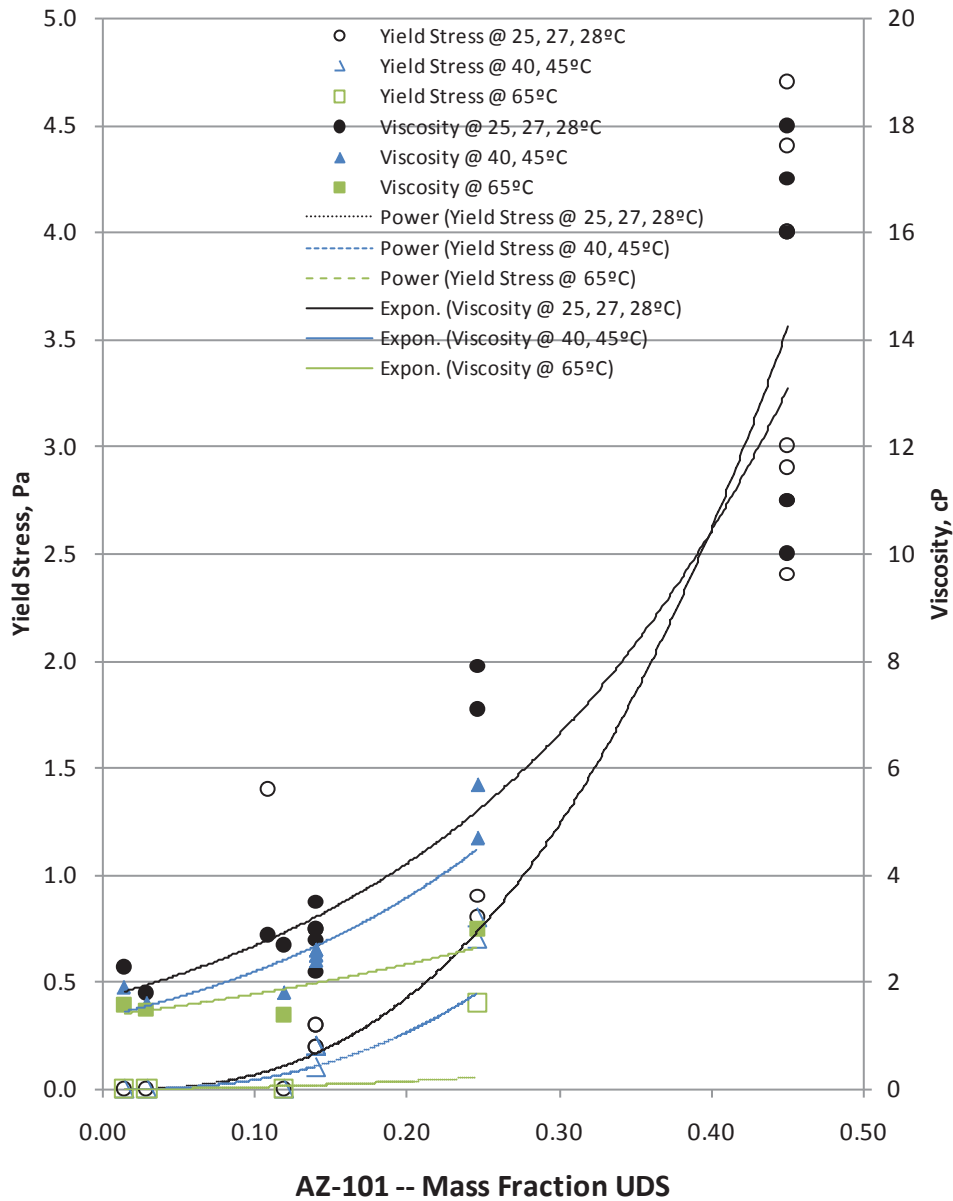
	Yield Stress Curve Fits		Viscosity Curve Fits	
25, 27, 28ºC	$\tau_y = 28.4134x^{2.602}$	$R^2 = 0.783$	$\mu_B = 1.709e^{4.523x}$	$R^2 = 0.921$
40, 45ºC	$\tau_y = 15.055x^{2.504}$	$R^2 = 0.703$	$\mu_B = 1.350e^{4.857x}$	$R^2 = 0.831$
65ºC	$\tau_y = 0.5274x^{1.6823}$	$R^2 = 0.536$	$\mu_B = 1.709e^{4.523x}$	$R^2 = 0.683$

Figure 6-9. Rheology Data for AZ-102 Waste (P3 Sludge)
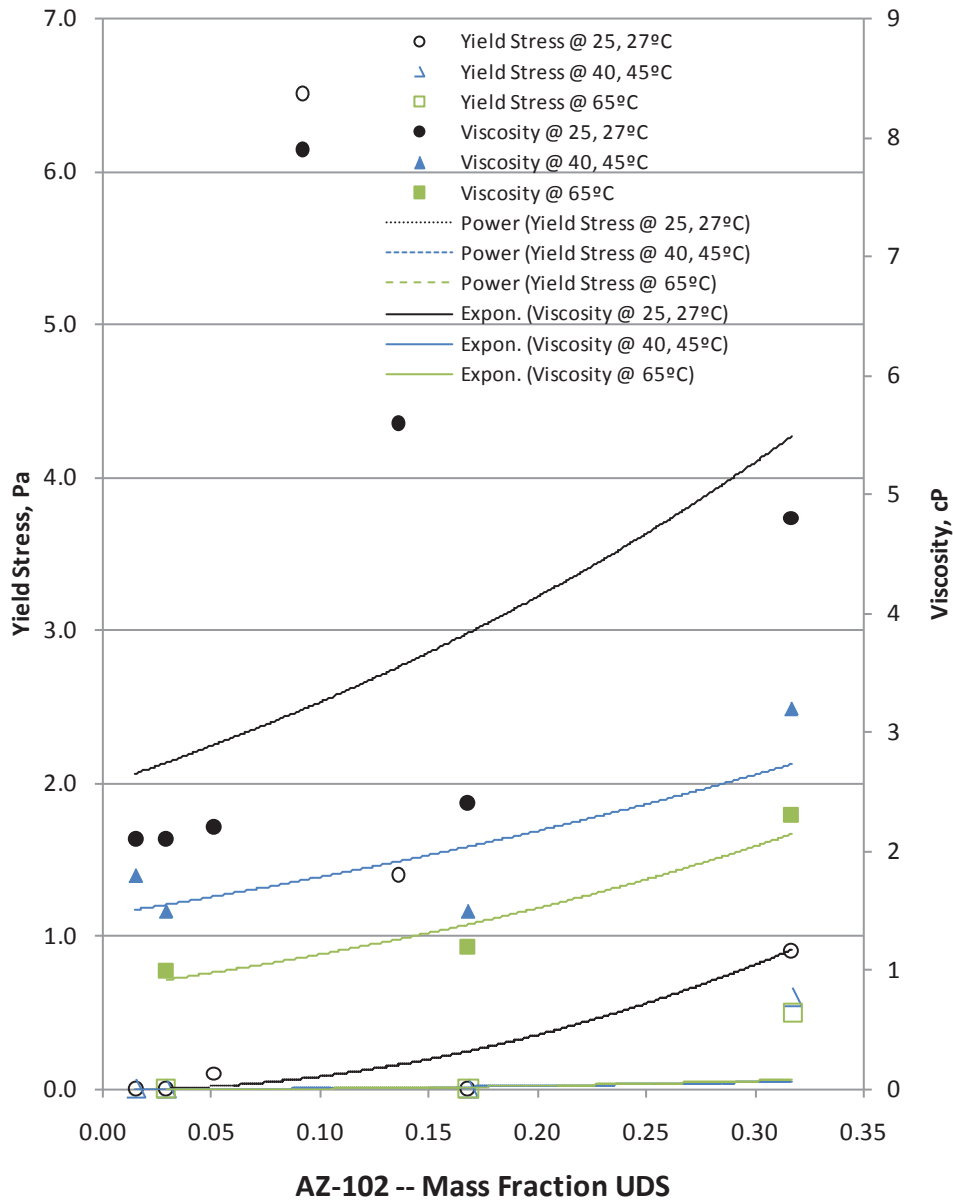
	Yield Stress Curve Fits		Viscosity Curve Fits	
25, 27ºC	$\tau_y = 9.4078x^{2.0301}$	$R^2=0.311$	$\mu_B = 1.709e^{4.523x}$	$R^2=0.921$
40, 45ºC	$\tau_y = 0.3255x^{1.5688}$	$R^2=0.497$	$\mu_B = 1.459e^{1.982x}$	$R^2=0.608$
65ºC	$\tau_y = 0.6524x^{2.0431}$	$R^2=0.497$	$\mu_B = 0.852e^{2.909x}$	$R^2=0.916$

Figure 6-10. Rheology Data for B-201 Waste (Pre-1949 Sludge)

Yield Stress Curve Fits   Viscosity Curve Fits
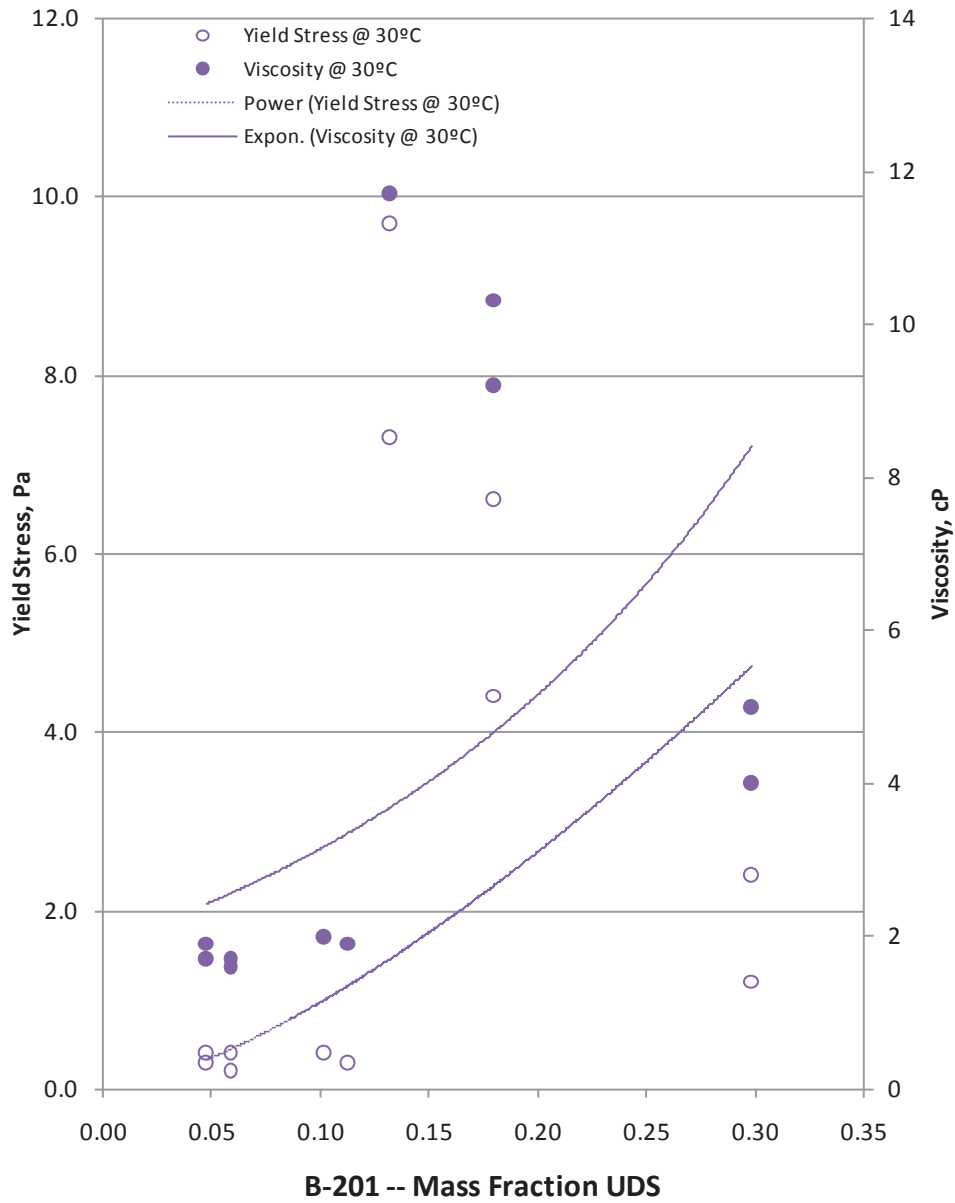
30 ºC $\tau_y = 27.113x^{-1.4396}$ $R^2 = 0.422$ $\mu_B = 1.919e^{4.957x}$ $R^2 = 0.111$

Figure 6-11. Rheology Data for B-202 Waste (Pre-1949 Sludge)
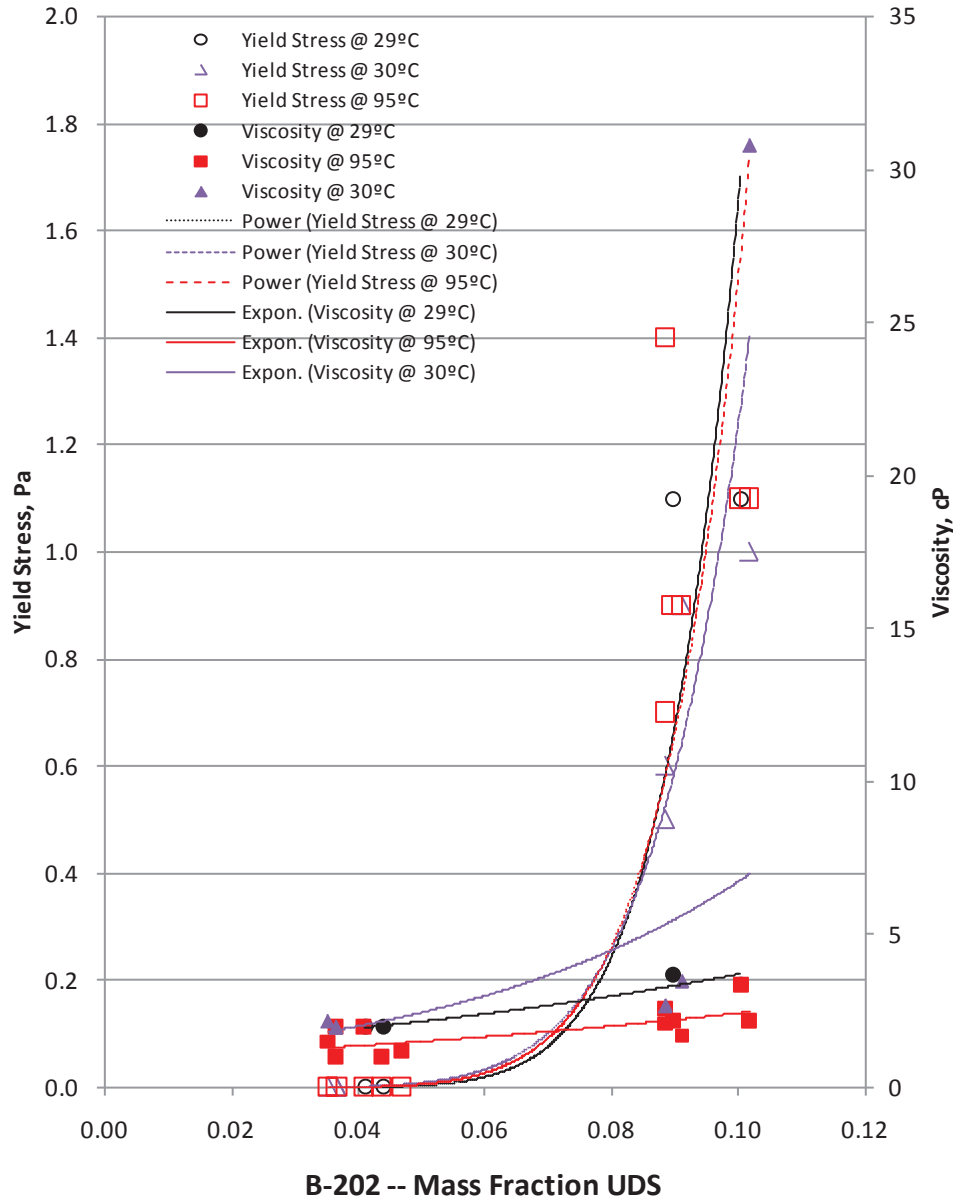
	Yield Stress Curve Fits		Viscosity Curve Fits	
29 °C	$\tau_y = 6.267E08x^{8.578}$ $R^2=0.987$		$\mu_B = 1.295e^{10.49x}$ $R^2=0.939$	
30 °C	$\tau_y = 1.241E07x^{6.997}$ $R^2=0.996$		$\mu_B = 0.879e^{20.36x}$ $R^2=0.403$	
95 °C	$\tau_y = 1.018\ E08x^{7.824}$ $R^2=0.962$		$\mu_B = 0.963e^{9.317x}$ $R^2=0.490$	

Figure 6-12. Rheology Data for B-203 Waste (Pre-1949 Sludge)
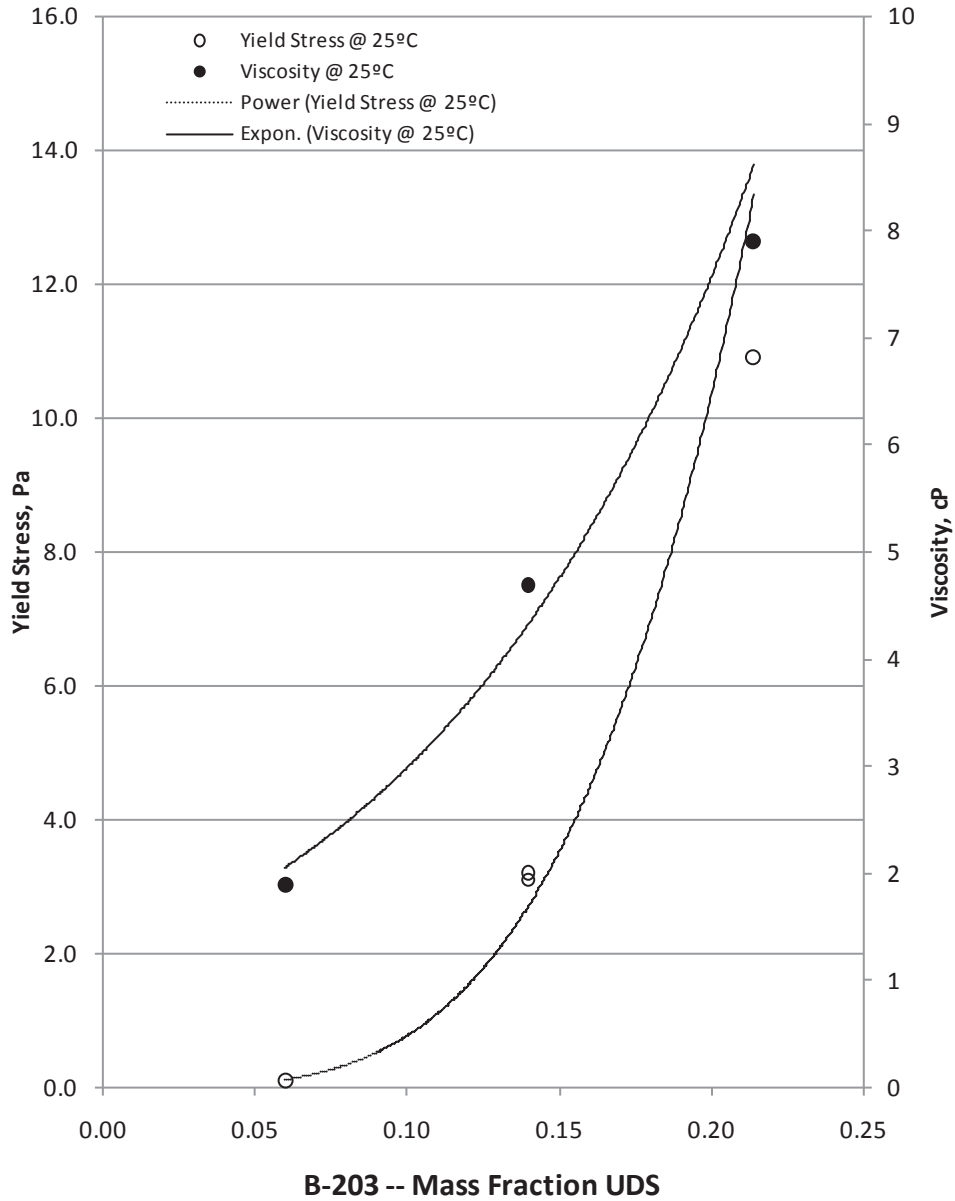
	Yield Stress Curve Fits	Viscosity Curve Fits
25 ºC	$\tau_y = 4469x^{3.769}$ $R^2=0.991$	$\mu_B = 1.177e^{9.295x}$ $R^2=0.974$

Figure 6-13. Rheology Data for BX-107 Waste (IC Sludge)
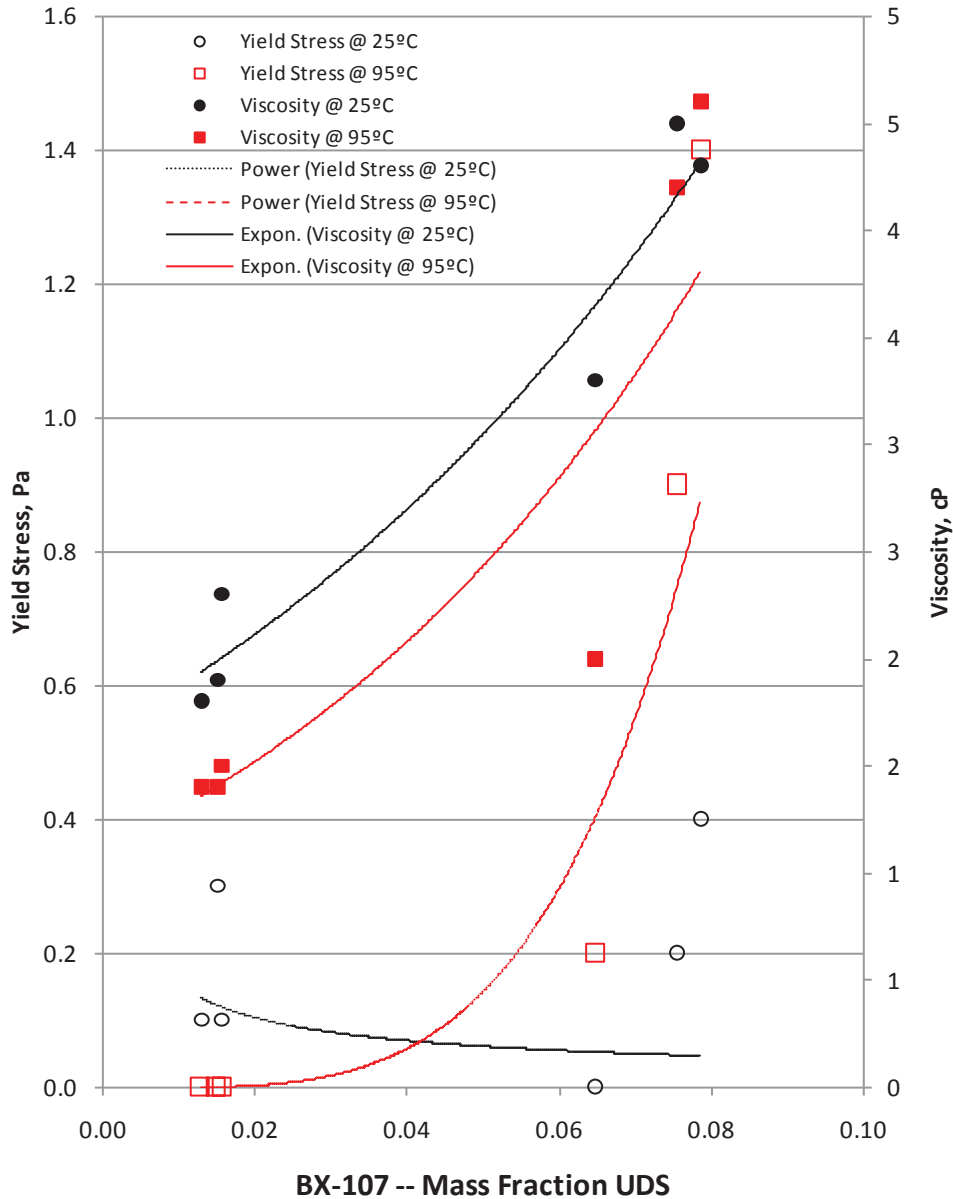
	Yield Stress Curve Fits		Viscosity Curve Fits	
25 ºC	$\tau_y = 0.011x^{-0.56}$	$R^2=0.051$	$\mu_B = 1.655e^{12.19x}$	$R^2=0.947$
95 ºC	$\tau_y = 22{,}835x^{3.997}$	$R^2=0.983$	$\mu_B = 1.110e^{15.66x}$	$R^2=0.840$

Figure 6-14. Rheology Data for C-104 Waste (CWP1 Sludge)
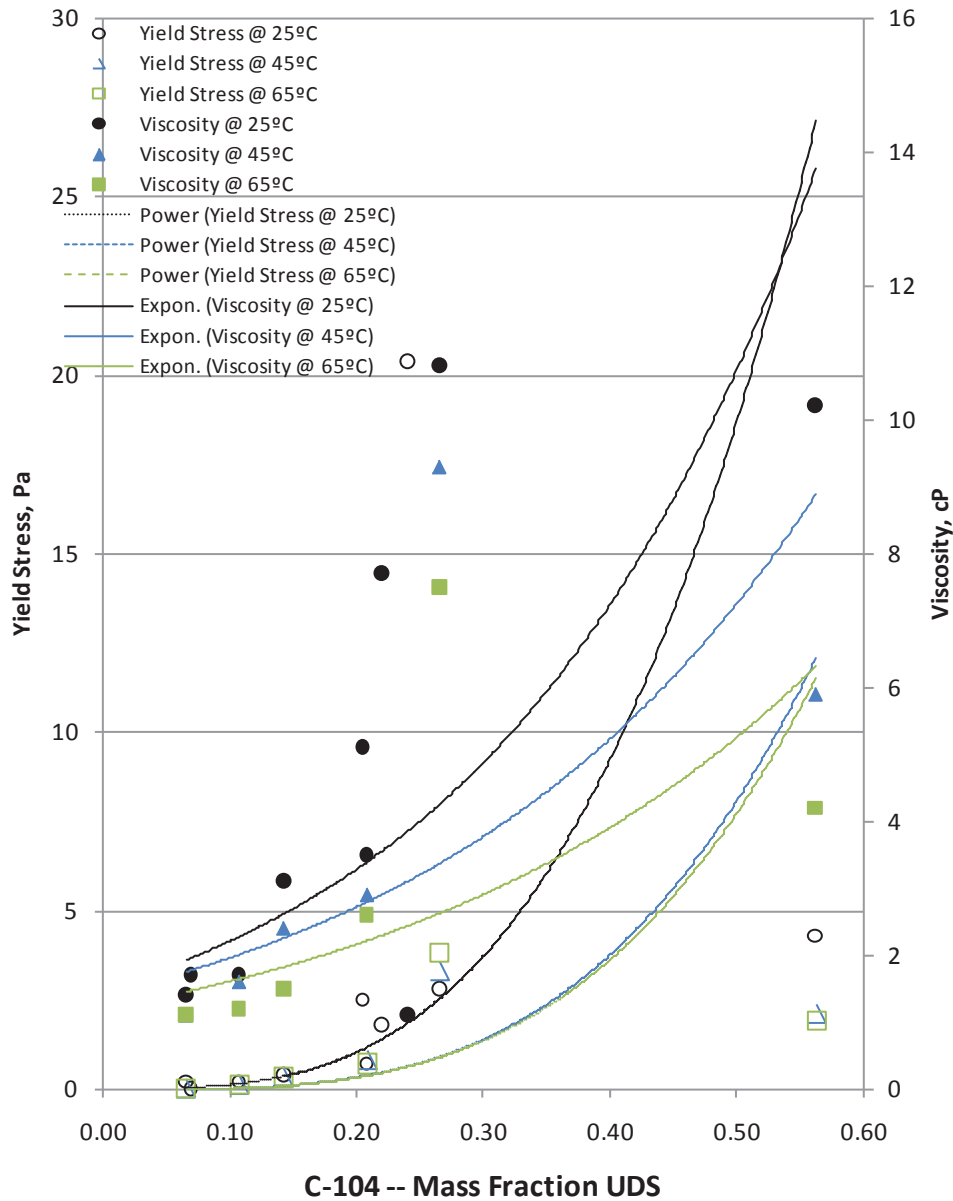
	Yield Stress Curve Fits		Viscosity Curve Fits	
25 ºC	$\tau_y = 167.3821x^{3.1589}$ $R^2=0.597$		$\mu_B = 1.495e^{3.947x}$	$R^2=0.447$
45 ºC	$\tau_y = 85.82363x^{3.40558}$ $R^2=0.748$		$\mu_B = 1.423e^{3.255x}$	$R^2=0.537$
65 ºC	$\tau_y = 80.45995x^{3.37721}$ $R^2=0.735$		$\mu_B = 1.201e^{2.955x}$	$R^2=0.486$

Figure 6-15. Rheology Data for C-107 Waste (IC Sludge)

Legend:
- ○ Yield Stress @ 20, 25ºC
- ⊿ Yield Stress @ 45ºC
- ☐ Yield Stress @ 65ºC
- ● Viscosity @ 20, 25ºC
- ▲ Viscosity @ 45ºC
- ■ Viscosity @ 65ºC
- ·········· Power (Yield Stress @ 20, 25ºC)
- – – – Power (Yield Stress @ 45ºC)
- – – – Power (Yield Stress @ 65ºC)
- —— Expon. (Viscosity @ 20, 25ºC)
- —— Expon. (Viscosity @ 45ºC)
- —— Expon. (Viscosity @ 65ºC)

Y-axis (left): Yield Stress, Pa
Y-axis (right): Viscosity, cP
X-axis: C-107 -- Mass Fraction UDS
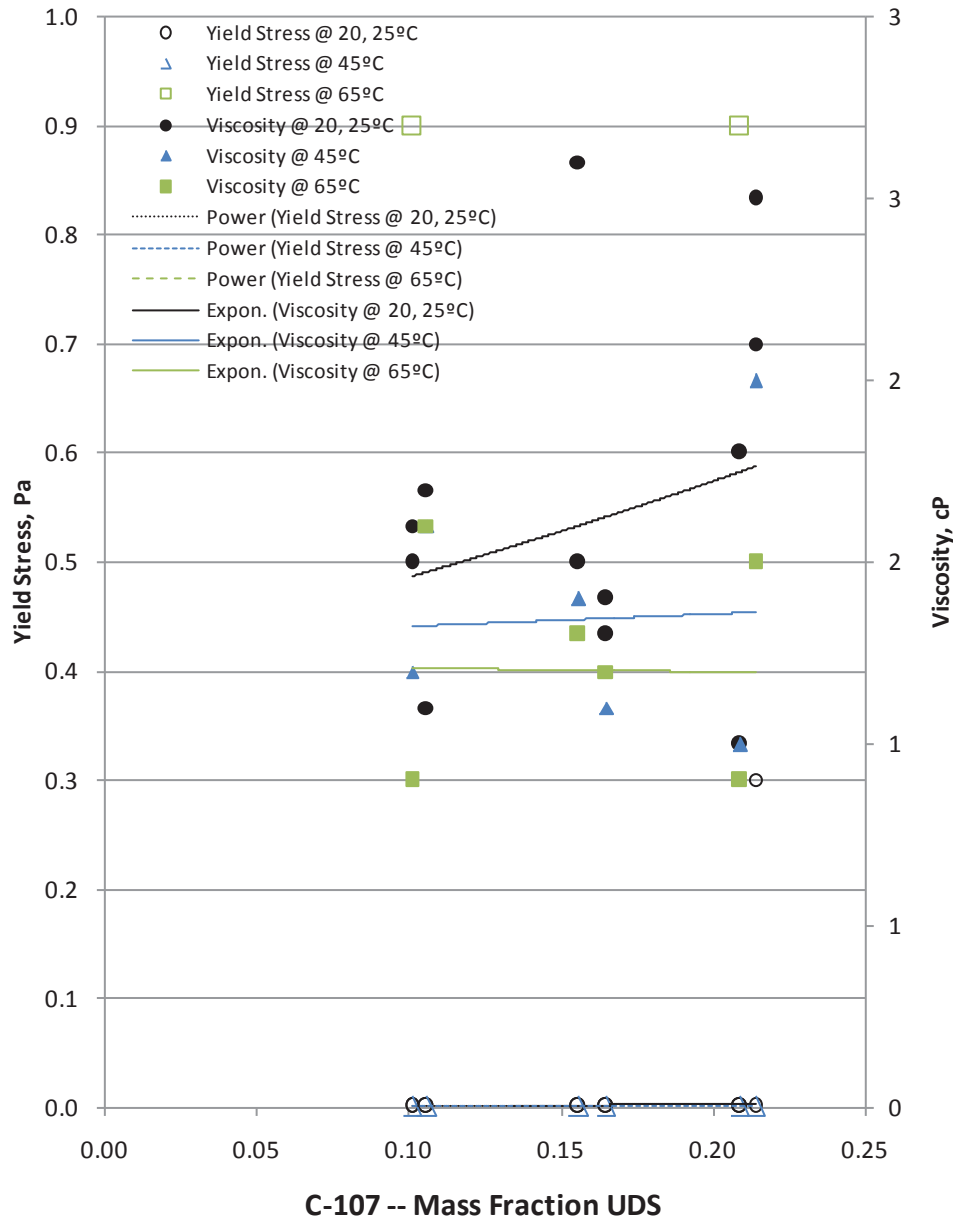
	Yield Stress Curve Fits		Viscosity Curve Fits	
20, 25ºC	$\tau_y = 0.0543x^{1.868}$	$R^2 = 0.122$	$\mu_B = 1.236e^{1.660x}$	$R^2 = 0.067$
45ºC	$\tau_y = 0.0$	$R^2 = n/a$	$\mu_B = 1.289e^{0.263x}$	$R^2 = 0.002$
65ºC	$\tau_y = 0.0$	$R^2 = n/a$	$\mu_B = 1.217e^{-0.07x}$	$R^2 = 0.000$

Figure 6-16. Rheology Data for C-109 Waste (FeCN Sludge)
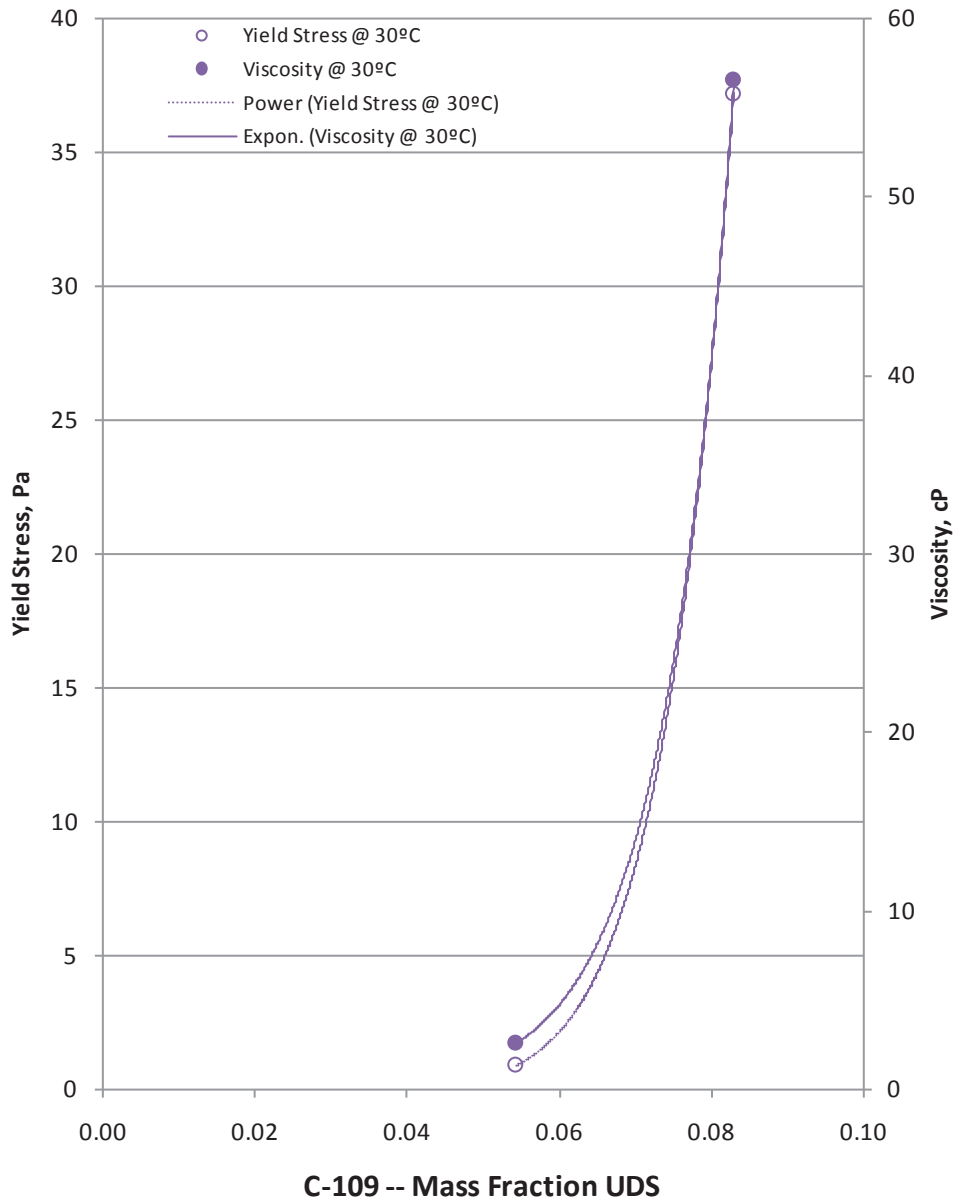
Yield Stress Curve Fits

30ºC $\tau_y = 1.050E+11x^{8.742}$ R^2=1.00

Viscosity Curve Fits

$\mu_B = 0.0078e^{107.0491x}$ R^2=1.000

Figure 6-17. Rheology Data for C-110 Waste (1C Sludge)
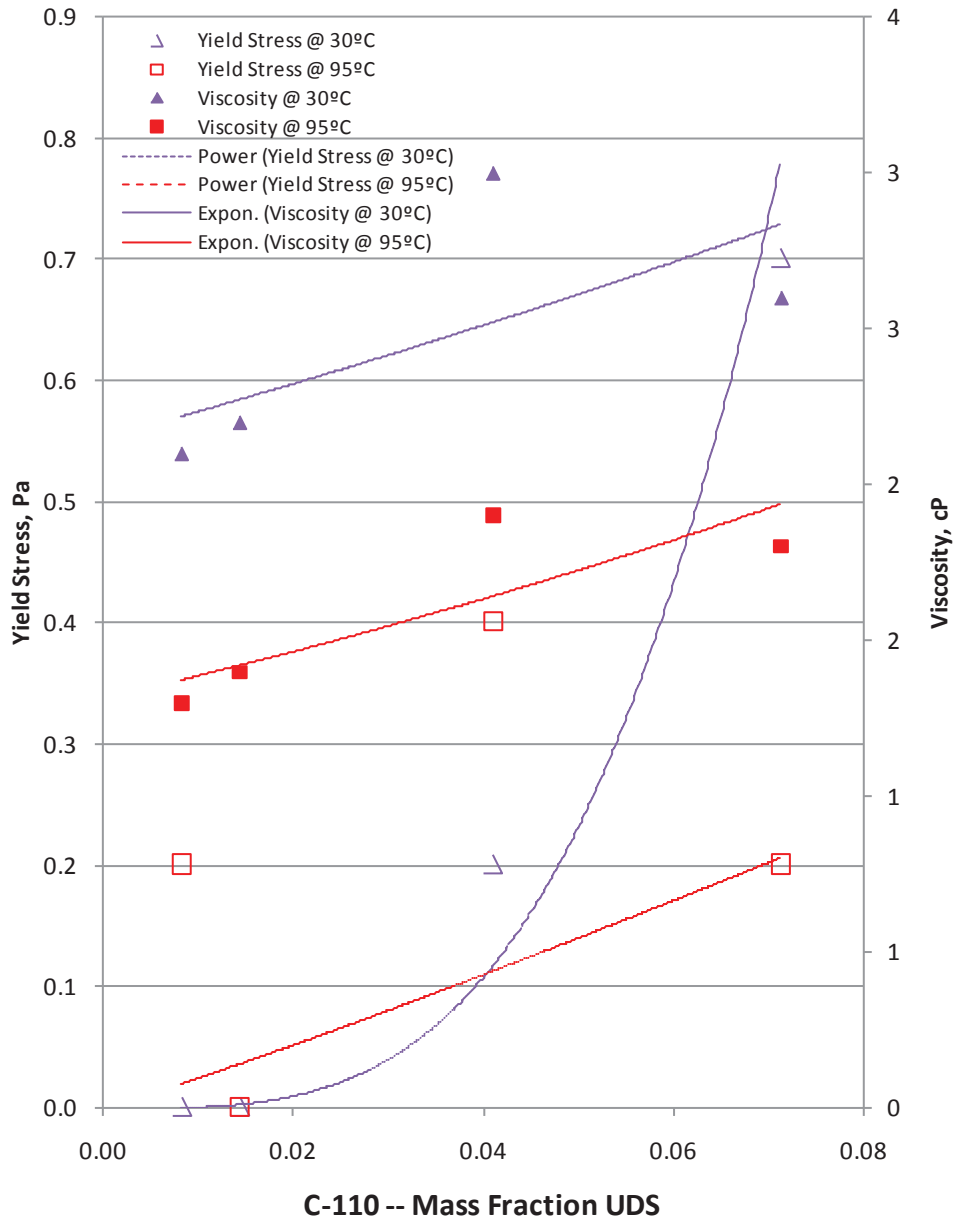
Yield Stress Curve Fits		Viscosity Curve Fits	
30ºC	$\tau_y = 6{,}689x^{3.430}$ $R^2=0.939$	$\mu_B = 2.147e^{3.906x}$ $R^2=0.474$	
95ºC	$\tau_y = 3.71205x^{1.09457}$ $R^2=0.147$	$\mu_B = 1.314e^{5.448x}$ $R^2=0.711$	

Figure 6-18. Rheology Data for S-104 Waste (1C Sludge)
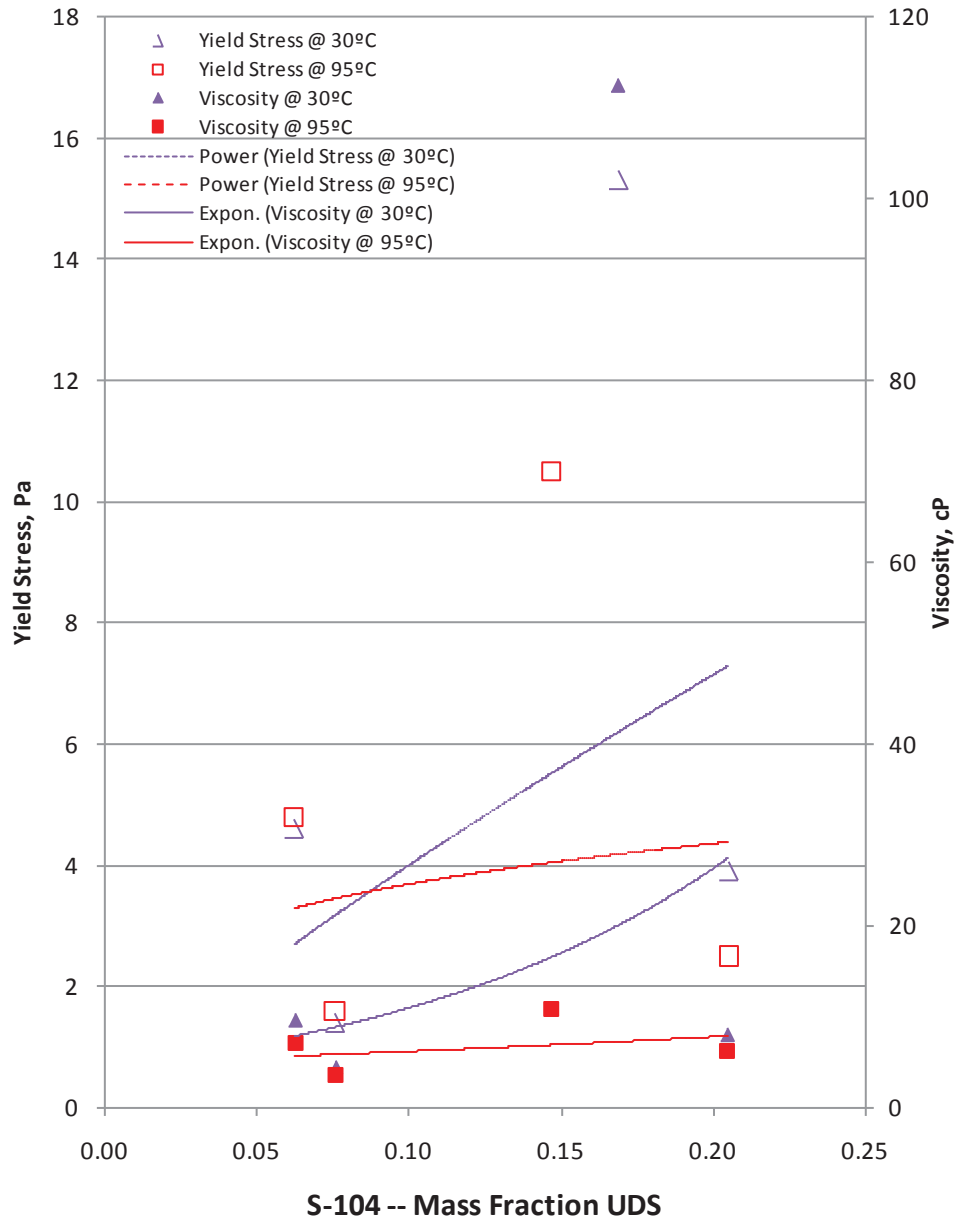
	Yield Stress Curve Fits		Viscosity Curve Fits	
30ºC	$\tau_y = 27.41246x^{0.83643}$	$R^2 = 0.249$	$\mu_B = 4.673e^{8.640x}$	$R^2 = 0.179$
95ºC	$\tau_y = 6.39654x^{0.23884}$	$R^2 = 0.026$	$\mu_B = 4.901e^{2.386x}$	$R^2 = 0.126$

Figure 6-19. Rheology (Yield Stress) Data for SY-101 Waste (S2 Saltcake)
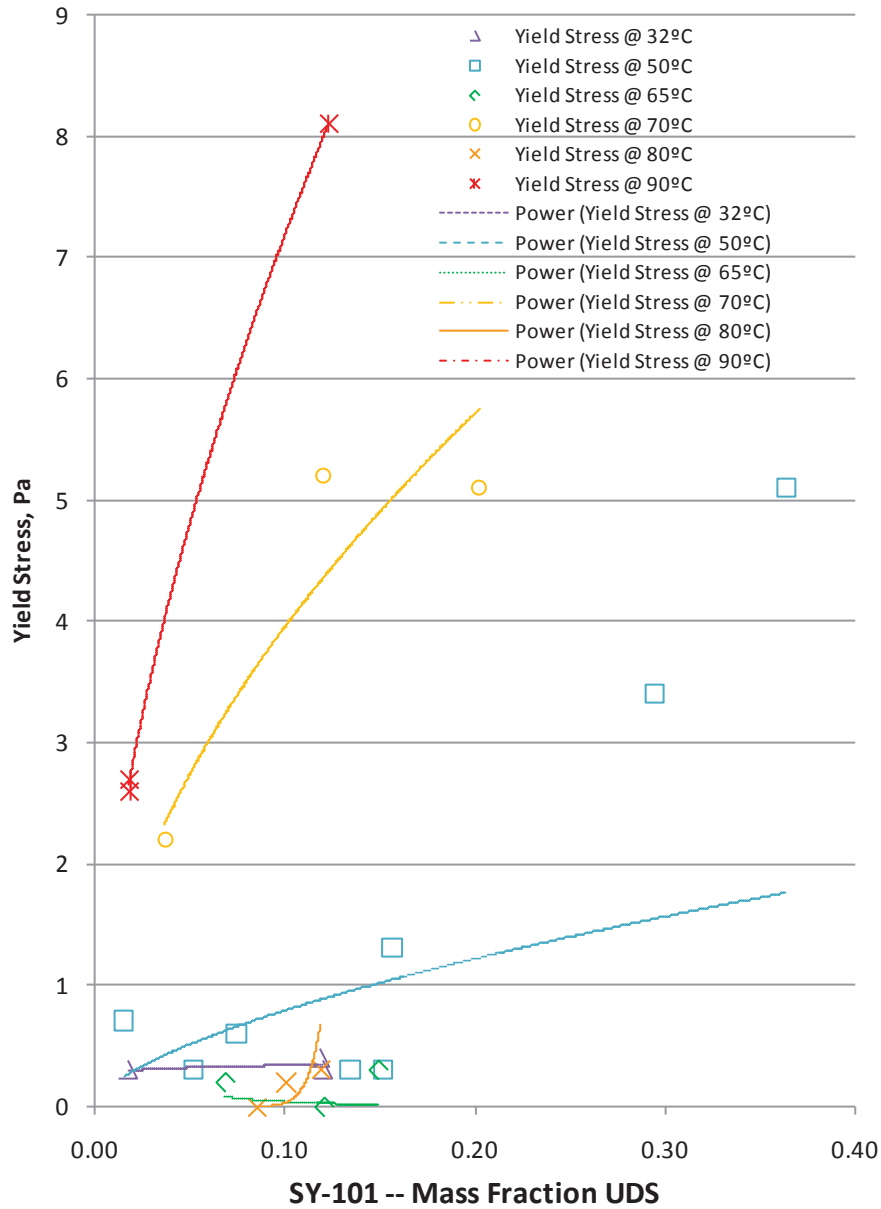
Yield Stress Curve Fits

32ºC	$\tau_y = 0.406x^{0.074}$	$R^2 = 0.244$
50ºC	$\tau_y = 3.28433x^{0.61448}$	$R^2 = 0.311$
65ºC	$\tau_y = 0.0013x^{-1.5197}$	$R^2 = 0.037$
70ºC	$\tau_y = 13.48x^{0.532}$	$R^2 = 0.899$
80ºC	$\tau_y = 1E+16x^{17.52}$	$R^2 = 0.790$
90ºC	$\tau_y = 27.52x^{0.584}$	$R^2 = 0.999$

Figure 6-20. Rheology (Viscosity) Data for SY-101 Waste (S2 Saltcake)
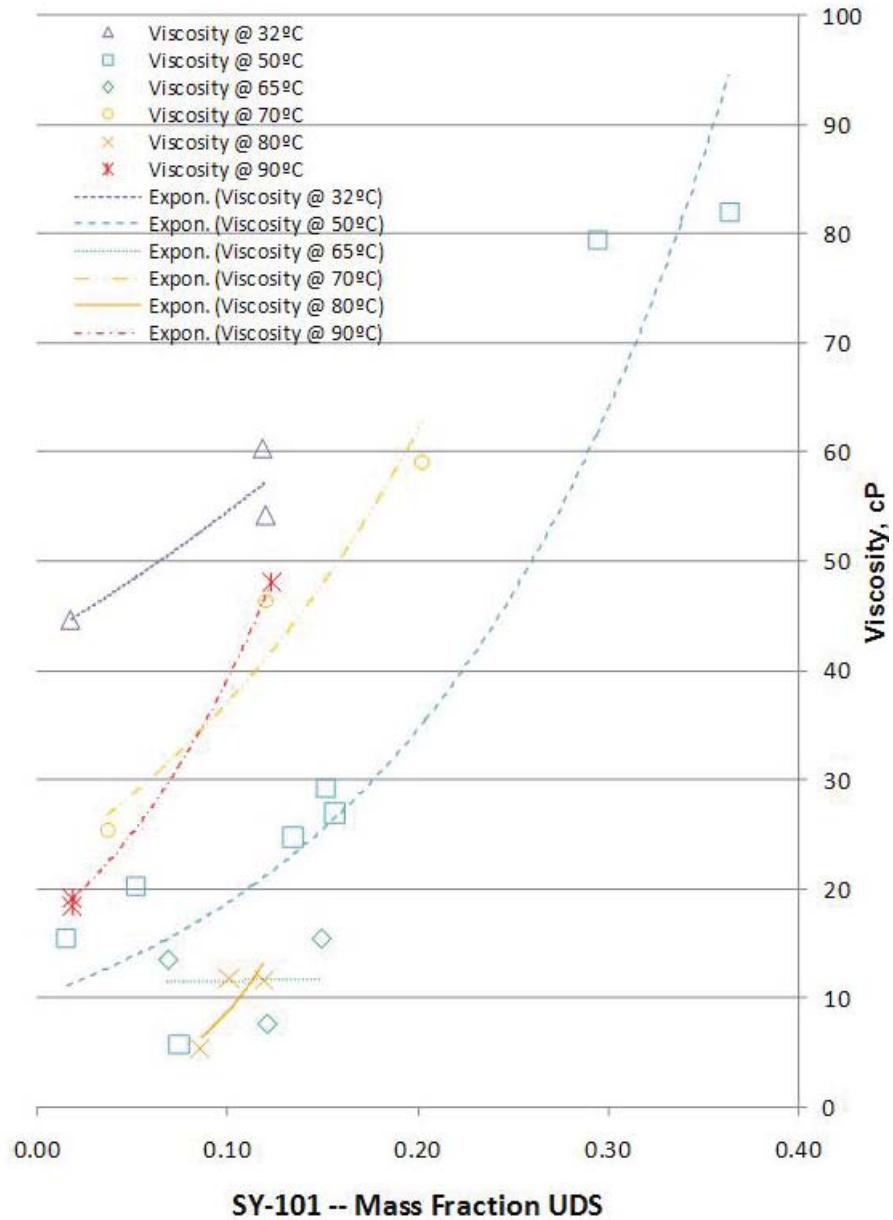
Viscosity Curve Fits

32ºC	$\mu_B = 42.86e^{2.422x}$	$R^2=0.869$
50ºC	$\mu_B = 10.10e^{6.152x}$	$R^2=0.732$
65ºC	$\mu_B = 11.54e^{0.114x}$	$R^2=0.000$
70ºC	$\mu_B = 22.22e^{5.130x}$	$R^2=0.994$
80ºC	$\mu_B = 0.986e^{21.84x}$	$R^2=0.676$
90ºC	$\mu_B = 16.02e^{8.897x}$	$R^2=0.998$

Figure 6-21. Rheology Data for SY-102 Waste (Unidentified Sludge)
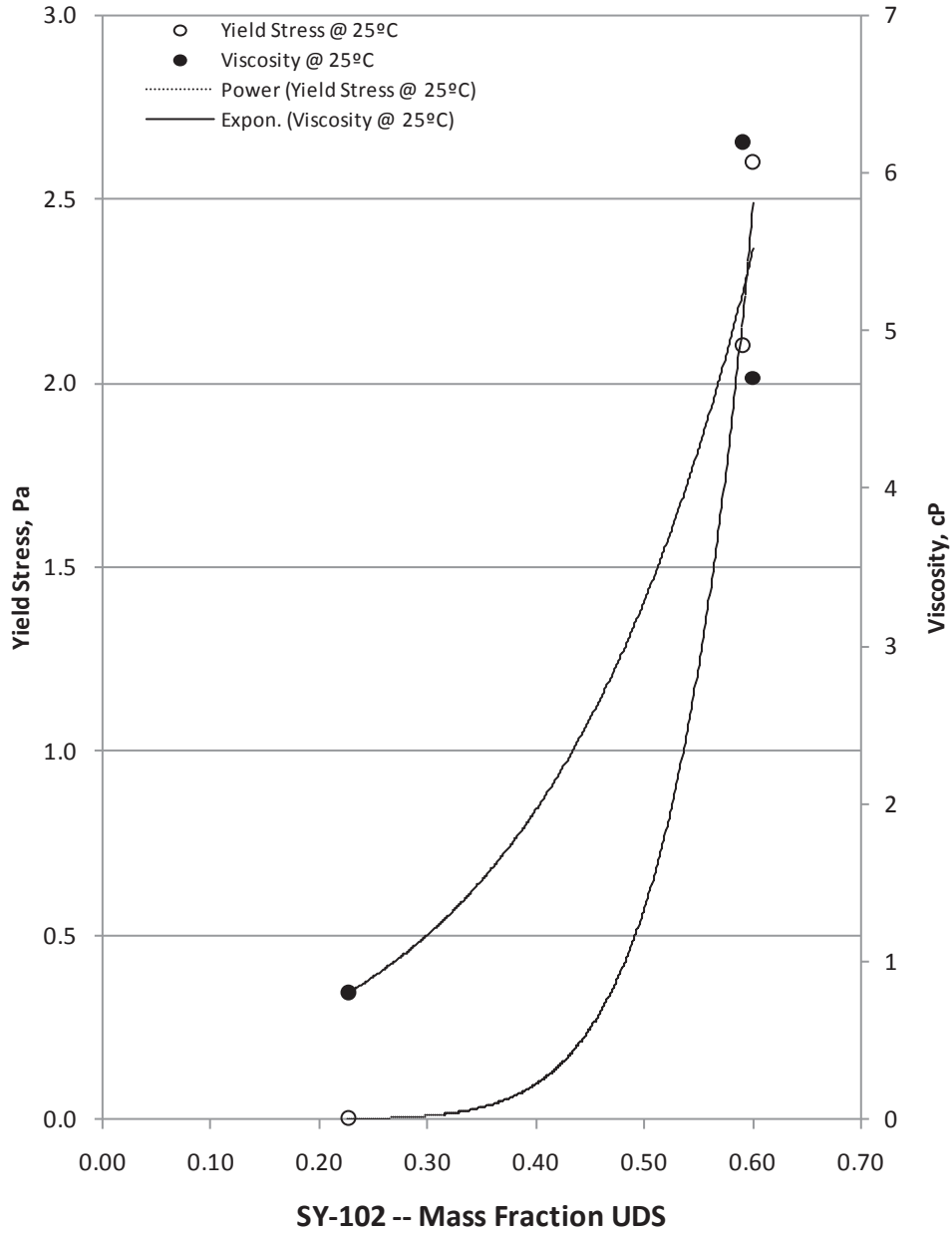
	Yield Stress Curve Fits		Viscosity Curve Fits	
25 °C	$\tau_y = 147.0x^{8.004}$	$R^2 = 0.999$	$\mu_B = 0.251e^{5.143x}$	$R^2 = 0.978$

Figure 6-22. Rheology Data for T-102 Waste (CWP2 Sludge)
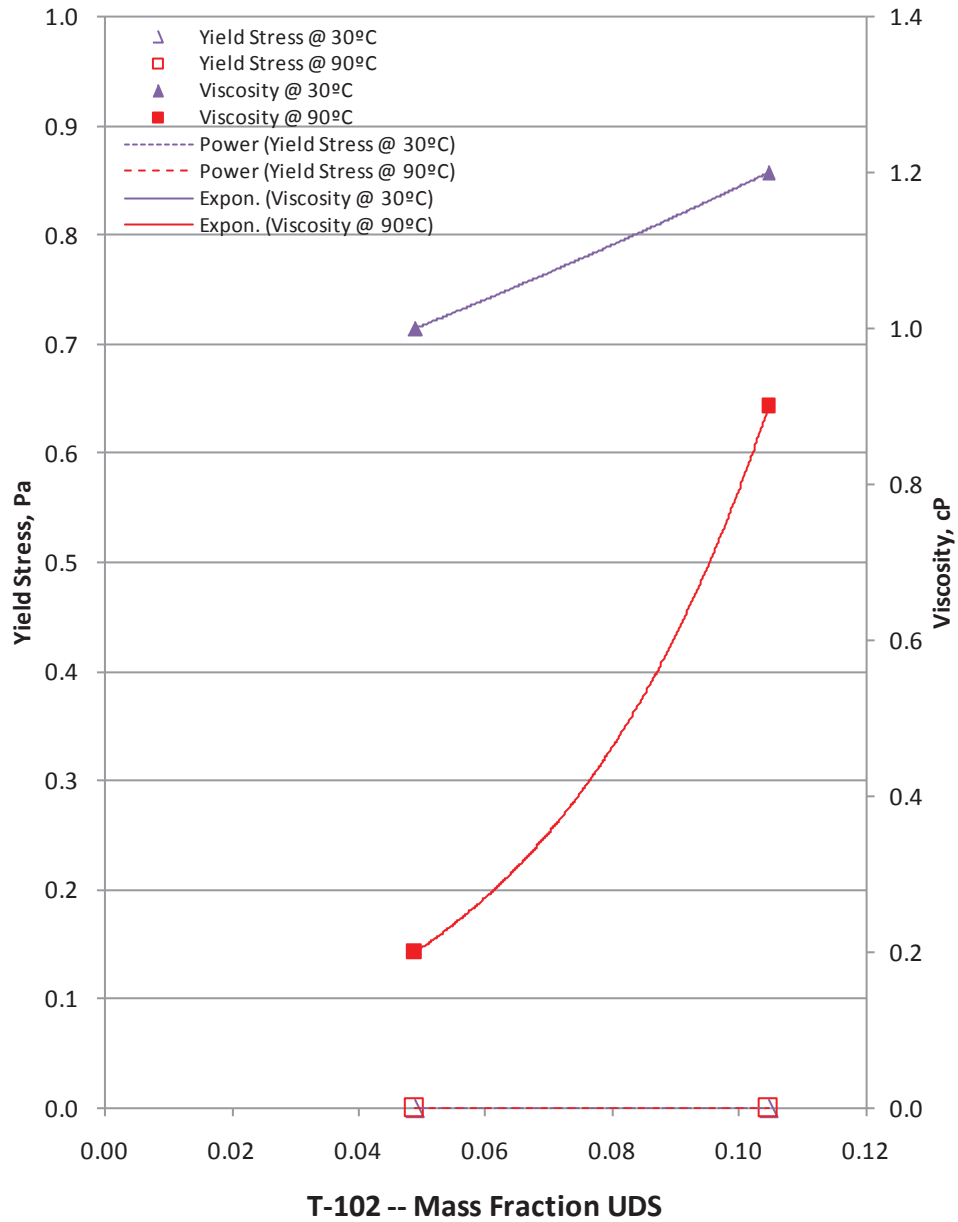
	Yield Stress Curve Fits		Viscosity Curve Fits	
30ºC	$\tau_y = 0.0$	$R^2 = $ n/a	$\mu_B = 0.851e^{3.277x}$	$R^2 = 1.000$
90ºC	$\tau_y = 0.0$	$R^2 = $ n/a	$\mu_B = 0.053e^{27.03x}$	$R^2 = 1.000$

Figure 6-23. Rheology Data for T-107 Waste (1C Sludge)
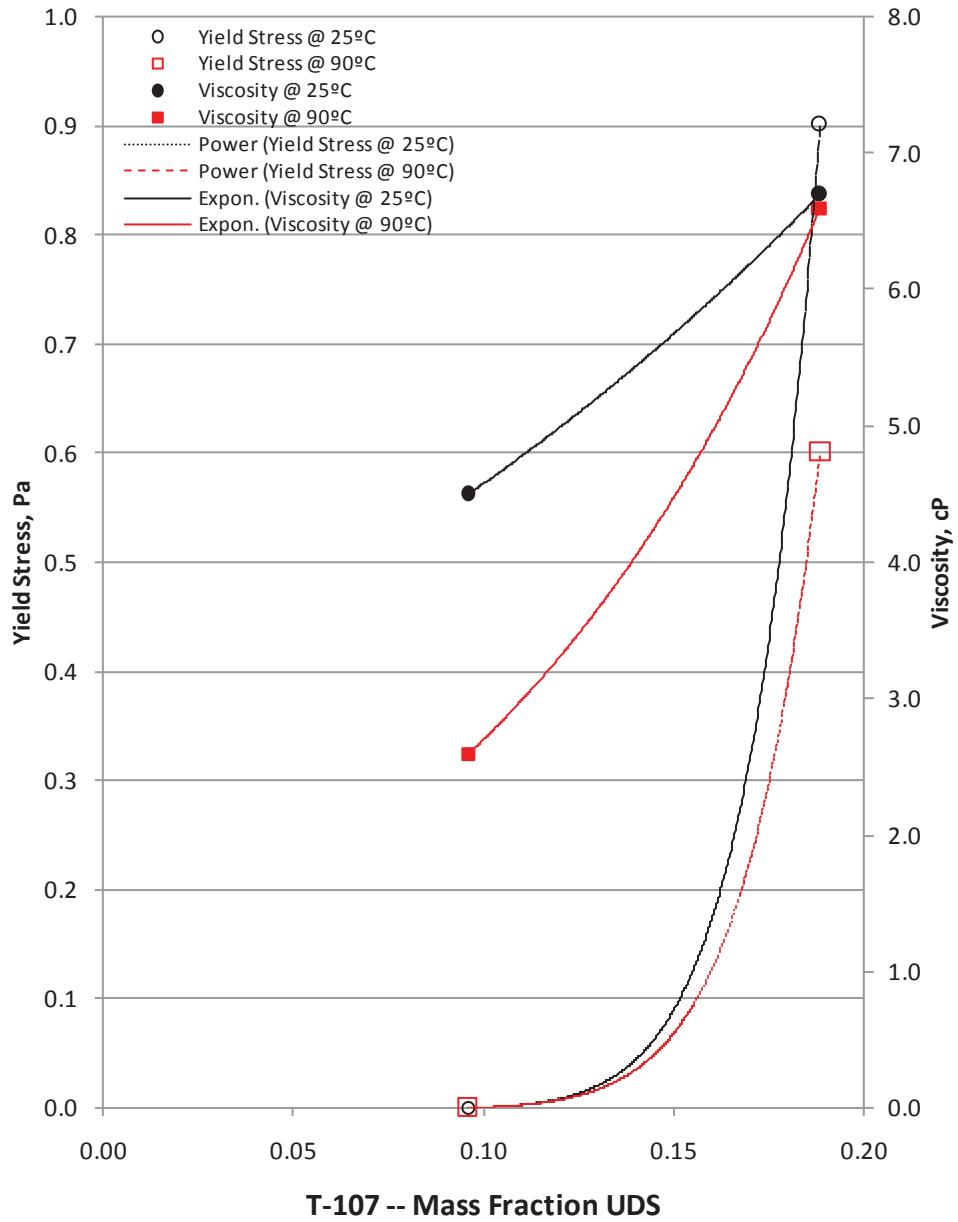
	Yield Stress Curve Fits		Viscosity Curve Fits	
25 ºC	$\tau_y = 1.68E+07x^{10.03}$	$R^2 = 1.000$	$\mu_B = 2.986e^{4.288x}$	$R^2 = 1.000$
90 ºC	$\tau_y = 4.14E+06x^{9.433}$	$R^2 = 1.000$	$\mu_B = 0.9957e^{10.037}$	$R^2 = 1.000$

Figure 6-24. Rheology Data for T-110 Waste (2C Sludge)

Legend:
- ○ Yield Stress @ 25 ºC
- ● Viscosity @ 25 ºC
- .... Power (Yield Stress @ 25 ºC)
- —— Expon. (Viscosity @ 25 ºC)

T-110 -- Mass Fraction UDS
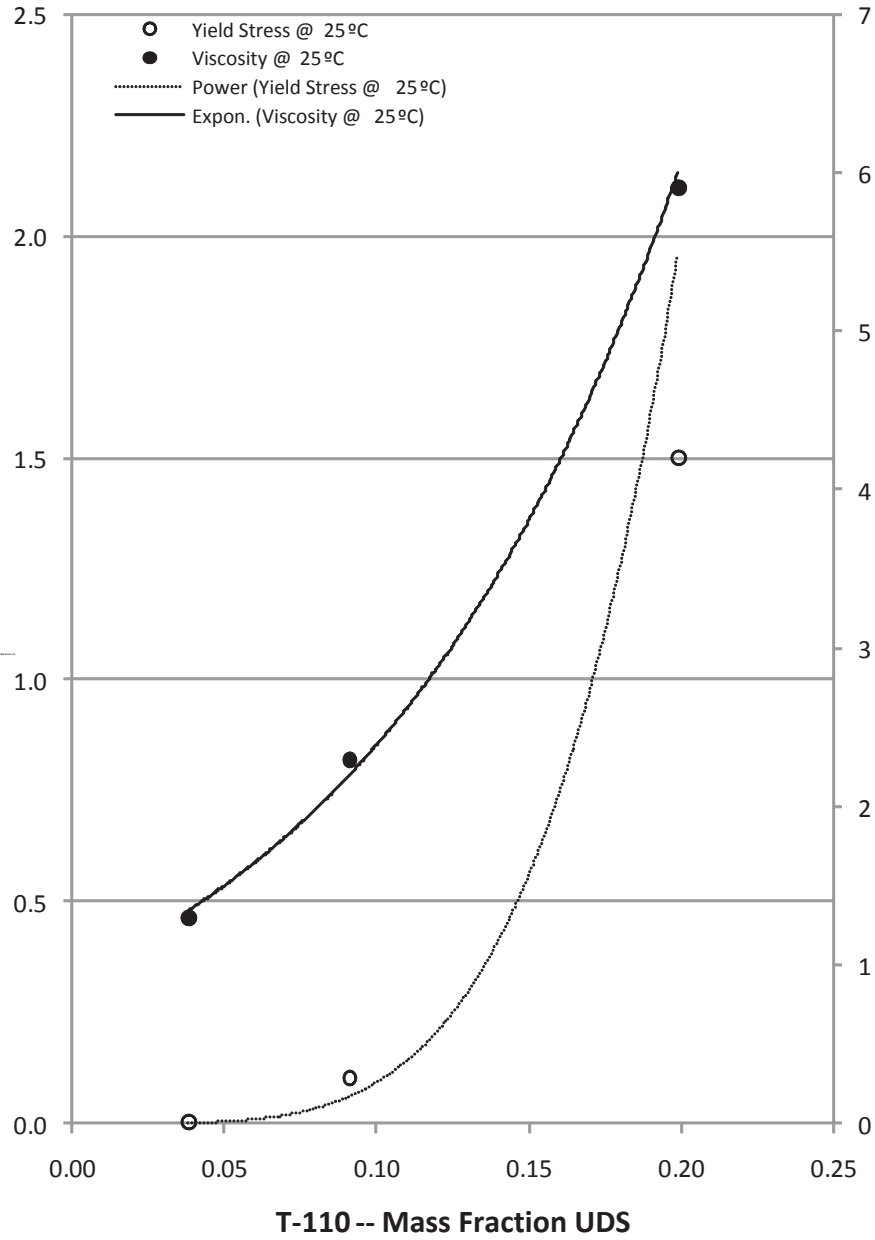
	Yield Stress Curve Fits	Viscosity Curve Fits
25ºC	$\tau_y = 2517x^{4.434}$ $R^2 = 0.986$	$\mu_B = 0.942e^{9.296x}$ $R^2 = 0.977$

Figure 6-25. Rheology Data for T-111 Waste (2C Sludge)
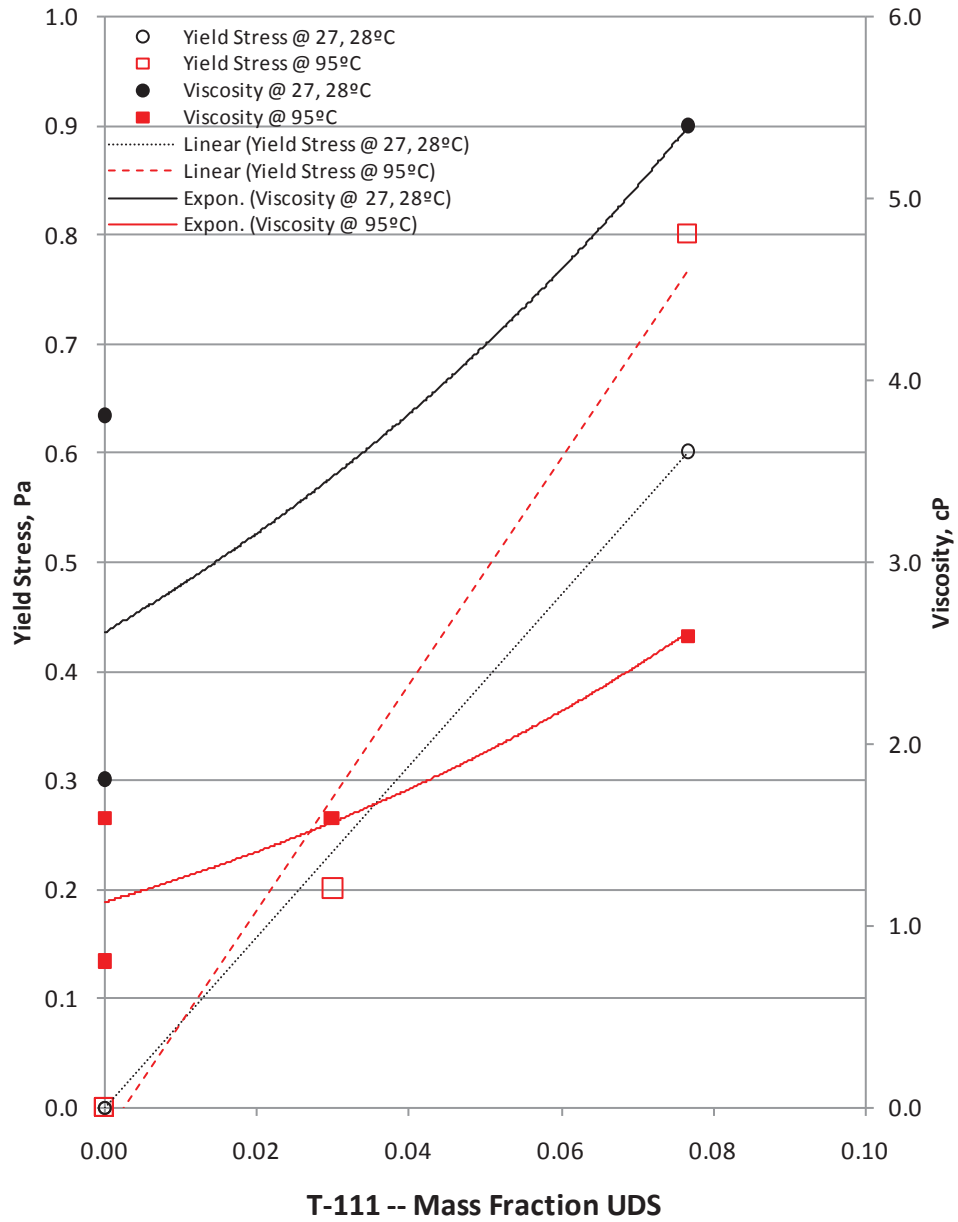
	Yield Stress Curve Fits		Viscosity Curve Fits	
27, 28ºC	$\tau_y = 7.826x + 0.001$	$R^2=1.00$	$\mu_B = 2.615e^{9.456x}$	$R^2=0.556$
95ºC	$\tau_y = 10.33x - 0.024$	$R^2=0.977$	$\mu_B = 1.136e^{10.87x}$	$R^2=0.659$

Figure 6-26. Rheology Data for T-203 Waste (Post 1949 Sludge)

Yield Stress Curve Fits   Viscosity Curve Fits
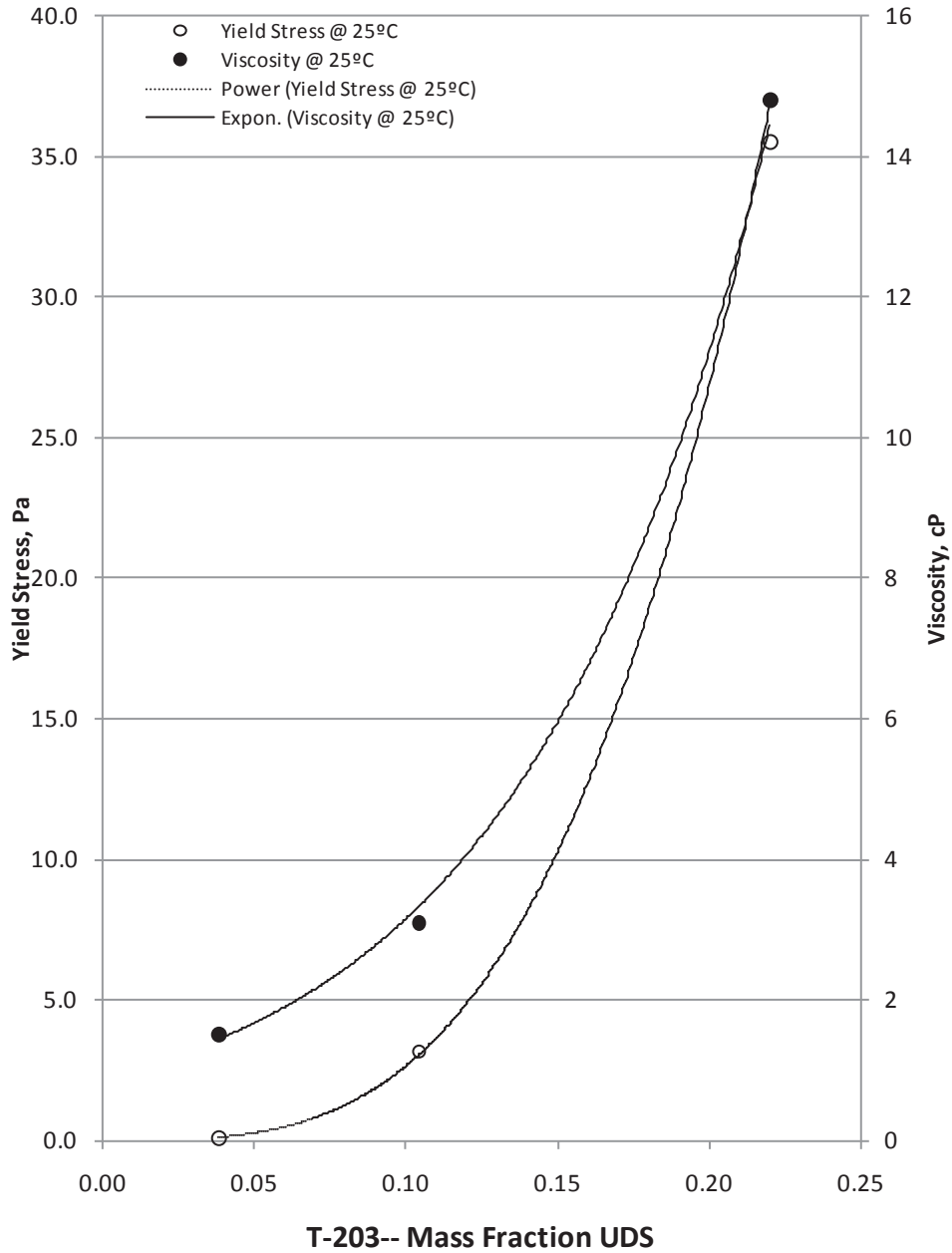
25ºC $\tau_y = 5815.x^{3.343}$ R^2=0.999 $\mu_B = 0.887e^{12.68x}$ R^2=0.997

Figure 6-27. Rheology Data for T-204 Waste (Post 1949 Sludge)

Yield Stress Curve Fits
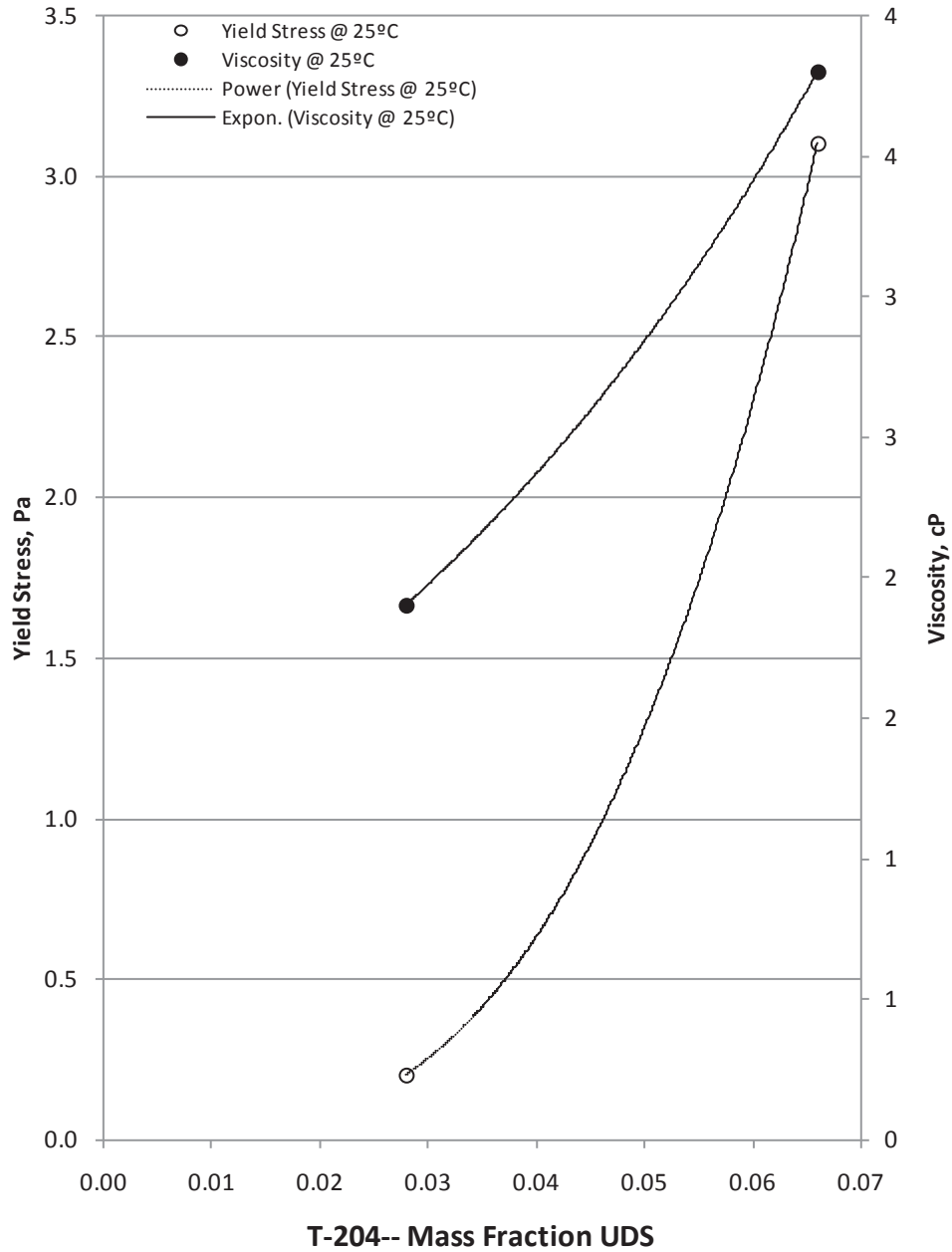
Viscosity Curve Fits

25ºC $\tau_y = 18{,}130x^{3.191}$ $R^2 = 1.000$ $\mu_B = 1.140e^{18.24x}$ $R^2 = 1.000$

6.1.1.2 *Data from M-12 Studies*

There are only 24 tanks with enough rheological data to produce rheology curves as a function of UDS and these tanks only represent an estimated 8.6 vol% of the current Hanford tank UDS waste inventory. Additional data are available from the M-12 studies. The External Flowsheet Review Team was assembled in October of 2005 to perform an in-depth review of the WTP process flowsheet of the WTP. The Engineering Flow Sheet Review Team (EFRT) identified 17 major issues, including M-12; neither the caustic leaching nor the oxidative leaching processes planned for the WTP Pretreatment Facility had been demonstrated at greater than bench scale.

To address M-12, the Office of River Protection (ORP) and WTP developed a pilot-scale leaching and ultrafiltration facility and demonstrated the effectiveness of the leaching and ultrafiltration processes (PNNL-18894, *Pretreatment Engineering Platform Phase 1 Final Test Report*). To support the pilot-scale demonstration of these leaching processes, eight waste types were identified, existing waste samples were selected and composited to obtain actual waste composites that would represent these eight waste groups and extensive laboratory testing was conducted on the composites.

The eight waste groups are: bismuth phosphate sludge waste (Group 1), bismuth phosphate saltcake (Group 2), PUREX cladding waste sludge (Group 3), Reduction-Oxidation (REDOX) cladding waste sludge (Group 4), REDOX sludge (Group 5), S-saltcake (Group 6), tri-butyl phosphate (TBP) waste sludge (Group 7) and ferrocyanide (FeCN) waste sludge (Group 8). These eight waste groups represented about 75% of the HLW mass expected to be processed through the WTP (PNNL-18120, *Characterization, Leaching, and Filtration 6.5Testing of Ferrocyanide Tank Sludge (Group 8) Actual Waste Composite*). Table 6-1 summarizes the groups with primary waste types and source tanks comprising each group (PNNL-20646).

Table 6-1. Eight Waste Groups for M-12 with Waste Types and Source Tanks

Group		Reference	Type	Source Tank(s)
1	Bismuth phosphate sludge	WTP-RPT-166	1C Sludge	B-104, BX-112, T-104
			2C Sludge	B-104
2	Bismuth phosphate saltcake	WTP-RPT-166	BY Saltcake	BX-110, BX-111, BY-104, BY-105, BY-107, BY-108, BY-109, BY-110, BY-112
			T1 Saltcake	T-108, T-109
			T2 Saltcake	TX-104, TX-113
3	PUREX cladding sludge	WTP-RPT-167	CWP1 Sludge	C-103, C-105, C-104
			CWP2 Sludge	B-109, B-108, C-104, BY-109
4	REDOX cladding sludge	WTP-RPT-167	CWR1 Sludge	U-203, U-105, U-201, U-202, U-204
5	REDOX sludge	WTP-RPT-172	R1 (boiling) Sludge	S-101, S-107, S-110, SX-103
6	S-Saltcake	WTP-RPT-172	S1 Saltcake	S-106, S-111, SX-102, SX-105, SX-106, U-103, U-108
			S2 Saltcake	SX-102, SX-106, SY-103, U-103, U-108
7	TBP sludge	WTP-RPT-169	TBP Sludge	B-106, BX-109
8	FeCN sludge	WTP-RPT-170	FeCN Sludge	BY-104, BY-105, BY-106, BY-108, BY-110

The rheological data for homogenized samples and filtered samples are given for each group in Table 6-2.

Table 6-2. M-12 Studies Yield Stress and Viscosity Data

Group	Description	Solids (wt%)	Yield Stress (Pa)[a]	Viscosity (cP)	Reference
1	Homogenized source	9.0	0.3	6.7	WTP-RPT-166
2	Homogenized source	37.4	1.7	14	WTP-RPT-166
1/2	Low solids (prior to filtering)	7.2	[b]	5.0	WTP-RPT-166
1/2	High solids (concentrated/filtered)	14	3.2	13	WTP-RPT-166
3	Homogenized source	28.8	[b]	3.4	WTP-RPT-167
4	Homogenized source	29.7	[b]	2.4	WTP-RPT-167
5	Homogenized source	18.5	57	13	WTP-RPT-172
5	Low solids (prior to filtering)	4.3	2.2	4.6	WTP-RPT-172
5	High solids (concentrated/filtered)	16	74	14	WTP-RPT-172
6	Homogenized source	14.7	[b]	8.0	WTP-RPT-172
5/6	Homogenized source	13.2	6.1	13	WTP-RPT-172
5/6	Low solids (prior to filtering)	3	4.1	6	WTP-RPT-172
5/6	High solids (concentrated/filtered)	13	1.3	14	WTP-RPT-172
7	Homogenized source[c]	10	[b]	12	WTP-RPT-169
7	Low solids (prior to filtering)	4.3	1.3	3.1	WTP-RPT-169
8	Homogenized source	11.4	[b]	3.3	WTP-RPT-170
8	Low solids (prior to filtering)	5.9	[b]	3.0	WTP-RPT-170
8	High solids (concentrated/filtered)	13	0.8	5.1	WTP-RPT-170

Notes:
a. Values are for 25°C and are the maximum reported values.
b. Newtonian.
c. Slurry demonstrated hysteresis with different results on up and down viscometer ramps. Down ramp value shown.

6.1.2 Slurry Viscosity and Yield Stress Data Discussion

Tank rheology data shown in Figures 6-3 through 6-26 indicate that rheology property values decrease with decreasing UDS. Common experiences suggest that rheology property values decrease with increasing temperature. For example, honey and molasses become thinner (less viscous) when heated. For a slurry, this relationship is more complex because the primary dependence on temperature is with respect to the liquid phase of the slurry unless solids are dissolving or precipitating in and out of the liquid, thereby changing the solid concentration, composition, etc.

A decrease in rheological property values with increasing temperature generally appears to happen with Hanford waste slurries as well. Figures 6-3 through 6-26 show the rheological properties for several tank waste slurries. The level of individual curves generally falls with increasing temperature. The rheology for Tank C-104 (Figure 6-14) is a good example of this, however, there are exceptions. In general it is hard to tell if the exceptions are artifacts (reality) or if they are a result of the limited data set and/or measurement uncertainty. In some instances, however, there appears to be more going on than just poor measurements. An example of this is Tank AN-104 (Figure 6-4) where the property values for this tank tend to increase with temperature. Viscosity increasing with temperature is likely a result of physical or chemical

changes as more of the highly soluble saltcake waste dissolves as temperature increases. Higher sodium concentration in the liquid phase tends to make the slurry more viscous.

Figure 6-28 shows rheology plots not shown in the other figures because there were not enough data points for UDS plots. However, there were enough data to plot the rheology properties as a function of temperature. Notice that the curves slope down, which means that the rheology properties are decreasing with increasing temperature as expected. The black curves are for Tank AN-102 A2 Saltcake. The blue curves are for Tank C-112 FeCN Sludge. The red curves are for M-12 Group 7 TBP Sludge.

Figure 6-28. Rheology Properties as a Function of Temperature
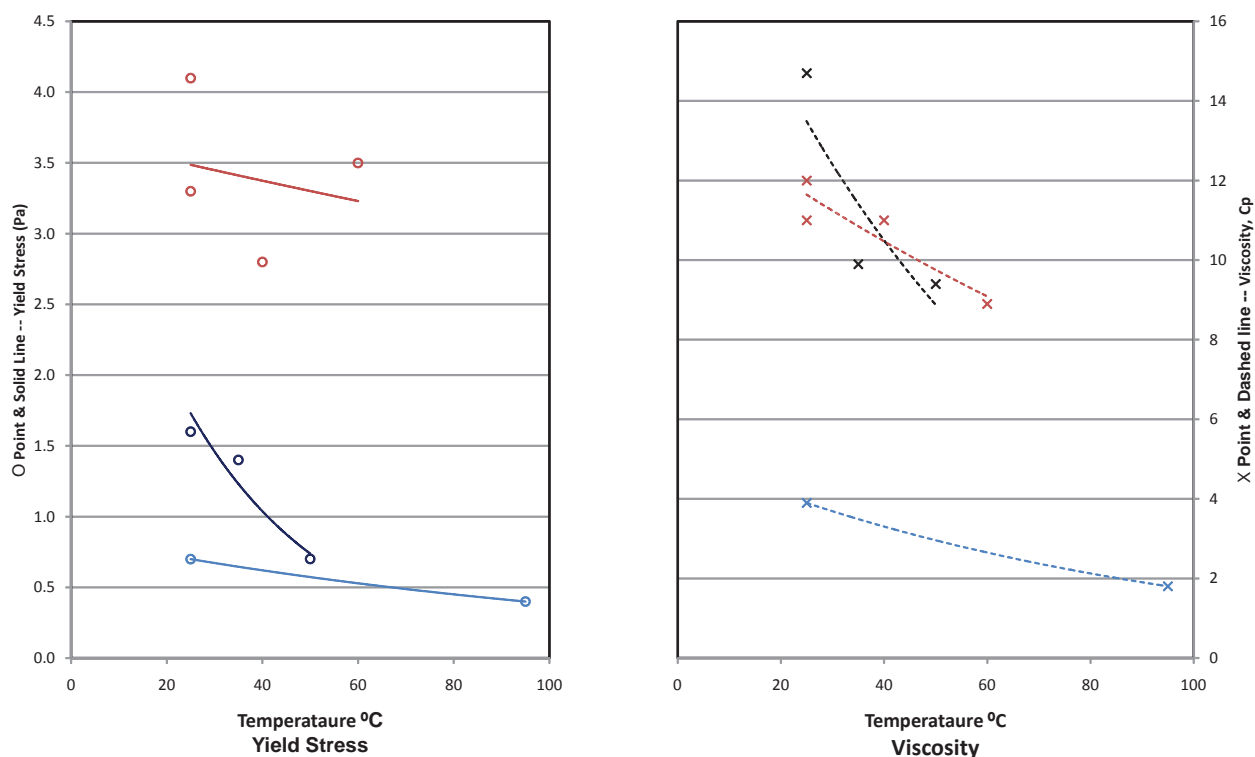
6.1.2.1   *Uncertainties in Slurry Viscosity and Yield Stress*

The largest source of uncertainty relevant to this section is the limited amount of rheological property data available. The limited number of samples from a limited number of individual tanks is unlikely to yield property values that span the true range of those properties for Hanford tank wastes. Including data from M-12 groups increases the volume percentage of Hanford tank inventory represented by the data. However, the M-12 data are for grouped samples that may tend to yield more "average" properties than would have individual samples from the tanks represented in group samples.

The sources of slurry viscosity and yield stress data used for this report did not provide information on the uncertainties typical in measuring these properties. Viscosity and yield stress are not direct measurements, but are determined from a plot of shear stress as a function of shear

rate (see discussion in PNNL-16857). Typically the uncertainties in such a process for indirectly determining property values would be quantified by replicating the measurement process on a sufficient number of samples. Then, the replicate results would be used to calculate the SD or percent relative standard deviation (as appropriate) to quantify the uncertainty in the measurement process. However, it is unknown whether the waste tank samples provided sufficient material to do this. In any case, the uncertainties in the indirectly measured viscosity and yield stress values for tank samples were not reported in the data sources.

6.1.2.2 *Variation in Slurry Viscosity and Yield Stress*

Viscosity and yield stress data for samples from individual waste tanks and M-12 groups have a significant spread. Focusing on only the sludge data, viscosity ranged from near 1 cP at 0.1 wt% solids to slightly more than 100 cP at 18 wt% solids. Yield stress data ranged from near 0.1 Pa at 1 wt% solids to near 80 Pa at 18 wt% solids. Measuring Bingham yield stress below about 1 Pa is difficult, so values smaller than this number are subject to additional uncertainty. Further, because only a limited amount of data were available and some of the data is for group samples, it is likely that the ranges of yield stress and viscosity over all of the Hanford waste tank inventory will be greater than the data ranges listed here.

6.2 SLURRY VISCOSITY AND YIELD STRESS PREDICTIONS

6.2.1 Slurry Viscosity and Yield Stress Prediction Model

Table 6-3 shows the weight percent solids estimated in the about 600 HLW feed batches (SVF-2115, *WTP_SPEC_7_Update for SP6 Baseline Case_V8.xlsm, Version 8*) planned during the WFD mission. The HLW feed batches range from a low of 0.7 wt% solids to a high of 9.6 wt% solids. These data suggest that 10 wt% solids may be a limiting case.

Table 6-4 shows predictions of yield stress and viscosity at 10 wt% solids using Equations 6-1 and 6-2 for the sludge data from individual waste tanks presented in Section 6-1. Because Equations 6-1 and 6-2 were fit to data groups, the temperature value or values (if data were grouped) are included in Table 6-4. Predicted values of yield stress and viscosity are listed for each group of temperature data used to fit the equations.

Table 6-3. Percent Solids in the HLW Feed Batches (2 pages)

Date	Solids (%)	Date	Solids (%)	Date	Solids (%)	Date	Solids (%)	Date	Solids (%)	Date	Solids (%)
5/31/2018	9.6	6/4/2026	7.6	8/17/2029	7.5	11/4/2032	7.3	1/14/2036	5.7	3/12/2039	7.6
6/5/2018	9.6	6/17/2026	7.6	8/27/2029	8.0	11/13/2032	7.3	1/28/2036	5.7	3/27/2039	7.6
6/10/2018	9.6	6/30/2026	7.6	9/7/2029	8.0	11/23/2032	8.2	2/8/2036	5.7	4/5/2039	7.6
7/31/2019	9.6	7/12/2026	7.6	9/18/2029	8.0	12/2/2032	8.2	2/19/2036	5.7	4/14/2039	7.6
2/2/2020	9.6	7/25/2026	7.6	9/30/2029	8.0	12/14/2032	8.2	3/5/2036	5.7	4/24/2039	7.6
4/4/2020	7.8	8/5/2026	7.6	10/12/2029	8.0	12/25/2032	8.2	3/19/2036	5.7	10/30/2039	8.4
6/9/2020	7.8	8/25/2026	7.4	10/23/2029	8.0	1/5/2033	8.2	4/6/2036	5.7	11/6/2039	8.4
9/5/2020	7.8	9/7/2026	7.4	11/3/2029	7.7	1/20/2033	8.2	4/19/2036	7.2	11/18/2039	8.4
11/29/2020	7.8	9/19/2026	7.4	11/13/2029	7.7	2/3/2033	8.2	4/27/2036	7.2	12/6/2039	8.4
2/3/2021	7.8	9/29/2026	7.4	11/23/2029	7.7	2/16/2033	8.1	5/11/2036	7.2	12/17/2039	9.3
4/1/2021	7.8	10/10/2026	7.4	12/4/2029	7.7	2/28/2033	8.1	5/17/2036	7.2	12/27/2039	8.1
5/15/2021	7.8	10/18/2026	7.4	12/15/2029	7.7	3/13/2033	8.1	5/25/2036	7.2	1/25/2040	8.1
6/30/2021	6.1	10/30/2026	6.0	12/25/2029	7.7	3/27/2033	8.1	6/1/2036	7.2	2/10/2040	8.0
8/11/2021	6.1	11/6/2026	6.0	1/3/2030	7.7	4/10/2033	8.1	6/9/2036	7.2	2/24/2040	9.1
9/14/2021	6.1	11/16/2026	6.0	1/18/2030	7.8	4/24/2033	8.1	6/22/2036	7.8	3/6/2040	9.1
10/13/2021	6.1	11/25/2026	6.0	1/28/2030	7.8	5/4/2033	8.1	7/3/2036	7.8	3/15/2040	9.1
11/9/2021	6.1	12/3/2026	6.0	2/7/2030	7.8	5/13/2033	8.1	7/14/2036	7.8	3/23/2040	9.1
12/4/2021	6.1	12/13/2026	6.0	2/19/2030	7.8	5/25/2033	8.1	7/26/2036	7.8	3/31/2040	9.1
12/30/2021	8.2	1/11/2027	6.5	3/1/2030	7.8	6/5/2033	8.1	8/5/2036	7.8	4/13/2040	9.1
1/26/2022	8.2	1/21/2027	6.5	3/12/2030	7.8	6/15/2033	8.1	8/20/2036	7.8	4/22/2040	9.1
3/2/2022	8.2	1/31/2027	6.5	3/25/2030	7.8	6/25/2033	8.1	8/30/2036	7.8	5/11/2040	9.1
4/8/2022	8.2	2/6/2027	6.5	4/9/2030	7.7	7/1/2033	8.1	9/9/2036	7.7	5/27/2040	9.1
5/20/2022	8.2	2/13/2027	6.5	4/19/2030	7.7	7/10/2033	8.1	9/22/2036	7.7	6/6/2040	9.0
6/29/2022	8.2	2/24/2027	6.5	4/30/2030	7.7	7/20/2033	8.0	10/4/2036	7.7	6/22/2040	8.6
8/16/2022	7.8	3/3/2027	6.5	5/12/2030	7.7	8/1/2033	8.0	10/13/2036	7.7	7/2/2040	8.6
9/22/2022	7.8	3/29/2027	7.5	5/21/2030	7.7	8/8/2033	8.0	10/22/2036	7.7	7/11/2040	8.2
10/11/2022	7.8	4/11/2027	7.5	6/4/2030	7.7	8/17/2033	8.0	11/3/2036	7.7	7/22/2040	8.2
11/7/2022	7.8	4/19/2027	7.5	6/14/2030	7.7	8/29/2033	8.0	11/16/2036	7.7	7/31/2040	8.2
11/29/2022	7.8	4/28/2027	7.5	6/25/2030	7.9	9/4/2033	8.0	12/19/2036	7.6	8/9/2040	8.2
12/19/2022	7.8	5/10/2027	7.5	7/4/2030	7.9	9/11/2033	8.0	1/5/2037	7.6	8/19/2040	8.2
1/13/2023	7.8	5/18/2027	7.5	7/15/2030	7.9	9/21/2033	8.5	1/20/2037	7.6	8/28/2040	8.2
2/6/2023	8.1	6/18/2027	7.5	7/24/2030	7.9	9/30/2033	8.5	2/1/2037	7.6	9/8/2040	8.2
3/4/2023	8.1	6/30/2027	7.5	8/3/2030	7.9	10/10/2033	8.5	2/10/2037	7.6	9/17/2040	8.2
4/2/2023	8.1	7/9/2027	7.5	8/11/2030	7.9	10/21/2033	8.5	2/18/2037	7.6	9/27/2040	8.2
4/27/2023	8.1	7/21/2027	7.5	8/29/2030	7.7	10/28/2033	8.5	3/2/2037	7.6	10/7/2040	8.2
5/23/2023	8.1	7/31/2027	7.5	9/12/2030	7.7	11/5/2033	8.5	3/11/2037	5.8	10/12/2040	7.6
6/19/2023	8.1	8/8/2027	7.5	9/28/2030	7.7	11/11/2033	8.5	3/18/2037	5.8	10/25/2040	7.6
7/17/2023	8.5	8/18/2027	6.9	10/12/2030	7.7	12/23/2033	8.2	3/28/2037	5.8	11/17/2040	7.6
8/14/2023	8.5	8/25/2027	6.9	10/24/2030	7.7	1/19/2034	8.2	4/4/2037	5.8	12/2/2040	7.8
9/14/2023	8.5	9/4/2027	6.9	11/4/2030	7.7	1/30/2034	8.2	4/10/2037	5.8	12/28/2040	7.8
10/13/2023	8.5	9/14/2027	6.9	11/15/2030	7.7	2/9/2034	8.2	4/18/2037	5.8	1/7/2041	7.8
11/7/2023	8.5	9/22/2027	6.9	11/29/2030	7.9	2/16/2034	8.2	4/28/2037	5.8	1/18/2041	7.8
12/2/2023	8.5	9/30/2027	6.9	12/10/2030	7.9	2/23/2034	8.2	5/4/2037	7.9	1/29/2041	7.8
12/30/2023	7.4	11/8/2027	5.6	12/23/2030	7.9	3/1/2034	8.2	5/12/2037	7.9	2/7/2041	7.8
1/24/2024	7.4	11/19/2027	5.6	1/4/2031	7.9	3/10/2034	8.4	5/22/2037	7.9	2/17/2041	7.8
2/22/2024	7.4	11/28/2027	5.6	1/14/2031	7.9	3/17/2034	8.4	6/3/2037	7.9	3/2/2041	7.8
3/14/2024	7.4	12/9/2027	5.6	1/27/2031	7.9	3/25/2034	8.4	6/13/2037	7.9	3/16/2041	7.8
4/12/2024	7.4	12/16/2027	5.6	2/5/2031	7.9	4/2/2034	8.4	6/24/2037	7.9	3/26/2041	7.8
5/13/2024	7.4	12/27/2027	5.6	2/16/2031	8.0	4/14/2034	8.4	7/20/2037	7.9	4/2/2041	8.8
6/5/2024	7.4	1/2/2028	5.6	2/27/2031	8.0	4/26/2034	8.4	8/9/2037	7.9	4/16/2041	8.8
7/3/2024	7.9	1/29/2028	6.3	3/9/2031	8.0	5/9/2034	8.4	8/24/2037	7.9	4/27/2041	8.8
8/5/2024	7.9	2/6/2028	6.3	3/20/2031	8.0	5/14/2034	8.1	9/5/2037	7.9	5/13/2041	8.8
9/7/2024	7.9	2/15/2028	6.3	3/29/2031	8.0	5/27/2034	8.1	9/16/2037	7.9	5/26/2041	8.8

Table 6-3. Percent Solids in the HLW Feed Batches (2 pages)

Date	Solids (%)	Date	Solids (%)	Date	Solids (%)	Date	Solids (%)	Date	Solids (%)	Date	Solids (%)
10/12/2024	7.9	2/23/2028	6.3	4/9/2031	8.0	6/11/2034	8.1	9/30/2037	7.9	6/14/2041	8.8
11/15/2024	7.9	3/3/2028	6.3	4/28/2031	8.0	6/24/2034	8.1	10/11/2037	7.9	7/9/2041	8.8
12/20/2024	7.9	3/16/2028	6.3	5/10/2031	7.7	7/10/2034	8.1	10/21/2037	7.9	7/30/2041	8.8
1/9/2025	8.1	3/24/2028	7.1	5/22/2031	7.7	7/25/2034	8.1	11/1/2037	8.2	8/12/2041	8.8
1/20/2025	8.1	4/1/2028	7.1	6/3/2031	7.7	7/31/2034	8.1	11/12/2037	8.2	8/24/2041	8.8
2/2/2025	8.1	4/8/2028	7.1	6/11/2031	7.7	8/13/2034	8.0	11/23/2037	8.2	9/7/2041	8.8
2/11/2025	8.1	4/18/2028	7.1	6/19/2031	7.7	8/26/2034	8.0	12/2/2037	8.2	9/18/2041	1.5
2/22/2025	8.1	4/27/2028	7.1	6/30/2031	7.7	9/13/2034	8.0	12/13/2037	8.2	9/25/2041	1.5
3/4/2025	8.1	5/7/2028	7.1	7/13/2031	8.2	9/24/2034	8.0	12/22/2037	8.2	10/1/2041	1.5
3/14/2025	8.3	6/15/2028	8.2	7/26/2031	8.2	10/11/2034	8.0	12/31/2037	8.2	10/11/2041	1.5
3/24/2025	8.3	6/28/2028	8.2	8/6/2031	8.2	10/26/2034	8.0	1/10/2038	7.6	10/17/2041	1.5
4/3/2025	8.3	7/10/2028	8.2	8/17/2031	8.2	11/10/2034	8.0	1/18/2038	7.6	10/24/2041	1.5
4/19/2025	8.3	7/21/2028	8.2	8/27/2031	8.2	11/24/2034	8.0	1/27/2038	7.6	10/30/2041	1.5
5/12/2025	8.3	8/5/2028	8.2	9/7/2031	8.2	12/11/2034	8.0	2/7/2038	7.6	11/6/2041	1.5
5/29/2025	8.3	8/18/2028	8.2	9/16/2031	8.2	12/26/2034	8.0	3/4/2038	7.6	11/13/2041	1.5
6/6/2025	5.8	8/29/2028	6.6	10/1/2031	8.2	1/12/2035	8.0	3/31/2038	7.6	11/23/2041	1.5
6/17/2025	5.8	9/9/2028	6.6	10/14/2031	8.2	1/20/2035	8.0	4/13/2038	7.6	11/29/2041	4.4
6/27/2025	5.8	9/18/2028	6.6	10/27/2031	8.2	2/5/2035	8.0	4/28/2038	8.1	12/13/2041	4.4
7/10/2025	5.8	9/27/2028	6.6	11/9/2031	8.2	2/17/2035	8.0	5/7/2038	8.1	12/23/2041	4.4
7/20/2025	5.8	10/6/2028	6.6	11/22/2031	8.2	3/1/2035	7.8	5/14/2038	8.1	1/7/2042	4.4
7/29/2025	5.8	10/22/2028	6.6	12/8/2031	8.2	3/14/2035	7.8	5/24/2038	8.1	3/7/2042	4.4
8/8/2025	5.8	11/1/2028	6.6	12/20/2031	8.2	3/26/2035	7.8	6/1/2038	8.1	4/16/2042	4.4
8/20/2025	8.1	11/11/2028	7.2	1/4/2032	8.1	4/13/2035	7.8	6/10/2038	8.1	5/13/2042	4.4
8/28/2025	8.1	11/22/2028	7.2	1/19/2032	8.1	4/22/2035	7.8	6/18/2038	8.1	6/3/2042	4.4
9/12/2025	8.1	12/2/2028	7.2	2/2/2032	8.1	5/3/2035	7.8	7/2/2038	7.9	6/29/2042	4.4
9/24/2025	8.1	12/12/2028	7.2	2/18/2032	8.1	5/13/2035	7.8	7/11/2038	7.9	8/11/2042	4.4
10/6/2025	8.1	12/24/2028	7.2	3/2/2032	8.1	5/23/2035	5.6	7/21/2038	7.9	8/18/2042	0.7
10/17/2025	8.1	1/5/2029	7.2	3/16/2032	8.1	6/12/2035	5.6	7/30/2038	7.9	9/17/2042	0.7
10/31/2025	8.0	1/15/2029	7.8	3/23/2032	8.1	6/27/2035	5.6	8/10/2038	7.9	9/22/2042	0.7
11/11/2025	8.0	1/24/2029	7.8	4/12/2032	7.5	7/6/2035	5.6	8/18/2038	7.9	10/16/2042	0.7
11/23/2025	8.0	2/3/2029	7.8	4/21/2032	7.5	7/15/2035	5.6	8/26/2038	7.9	11/1/2042	0.7
12/7/2025	8.0	2/14/2029	7.8	5/2/2032	7.5	7/22/2035	5.6	9/4/2038	7.7	11/16/2042	0.7
12/21/2025	8.0	3/1/2029	7.8	5/14/2032	7.5	7/29/2035	5.6	9/14/2038	7.7	11/27/2042	0.7
1/2/2026	8.0	3/13/2029	7.8	5/26/2032	7.5	8/7/2035	8.2	9/30/2038	7.7	12/6/2042	0.7
1/13/2026	7.6	3/26/2029	7.3	6/3/2032	7.5	8/13/2035	8.2	10/25/2038	7.7	12/11/2042	0.7
1/20/2026	7.6	4/4/2029	7.3	6/16/2032	8.3	8/22/2035	8.2	11/17/2038	7.7	12/17/2042	0.7
1/31/2026	7.6	4/17/2029	7.3	6/29/2032	8.3	9/3/2035	8.2	11/28/2038	7.7	12/20/2042	4.5
2/8/2026	7.6	4/27/2029	7.3	7/23/2032	8.3	9/10/2035	8.2	12/8/2038	7.7	12/27/2042	3.6
2/21/2026	7.6	5/9/2029	7.3	8/4/2032	8.3	9/24/2035	8.2	12/18/2038	7.6	1/1/2043	3.6
3/5/2026	7.6	5/21/2029	7.3	8/16/2032	8.3	10/4/2035	8.2	12/30/2038	7.6	1/6/2043	3.6
4/6/2026	5.8	6/3/2029	7.3	8/26/2032	8.3	11/2/2035	7.8	1/10/2039	7.6	1/13/2043	3.6
4/12/2026	5.8	6/12/2029	7.5	9/6/2032	8.3	11/9/2035	7.8	1/20/2039	7.6	1/19/2043	3.6
4/18/2026	5.8	6/24/2029	7.5	9/14/2032	7.3	11/20/2035	7.8	1/28/2039	7.6	1/25/2043	3.6
4/27/2026	5.8	7/6/2029	7.5	9/26/2032	7.3	12/1/2035	7.8	2/7/2039	7.6	1/31/2043	3.6
5/3/2026	5.8	7/16/2029	7.5	10/4/2032	7.3	12/9/2035	7.8	2/15/2039	7.6	2/6/2043	3.6
5/13/2026	5.8	7/25/2029	7.5	10/15/2032	7.3	12/23/2035	7.8	2/25/2039	7.6	2/12/2043	3.6
5/19/2026	5.8	8/5/2029	7.5	10/26/2032	7.3	1/8/2036	7.8	3/5/2039	7.6	2/18/2043	3.6

**Table 6-4. Interpolation and/or Extrapolation of Yield Stress and Viscosity
for 10% Solids Feed**

Sample	Temperature(s) (°C)	Yield Stress at 10% Solids (Pa)	Viscosity at 10% Solids (cP)
AY-102 BL Sludge	25,27	0.01	3.0
AY-102 BL Sludge	40,45	0.01	1.6
AY-102 BL Sludge	65	< 0.01	1.0
AZ-101 P3 Sludge	25,27,28	0.07	2.7
AZ-101 P3 Sludge	40,45	0.05	2.2
AZ-101 P3 Sludge	65	0.01	1.8
AZ-102 P3 Sludge	25,27	0.09	3.2
AZ-102 P3 Sludge	45	0.01	1.8
AZ-102 P3 Sludge	65	0.01	1.1
B-201 Pre-1949 Sludge	30	0.03	2.2
B-202 Pre-1949 Sludge	29	1.7	3.7
B-202 Pre-1949 Sludge	30	1.2	6.7
B-202 Pre-1949 Sludge	95	1.5	2.4
B-203 Pre-1949 Sludge	25	0.8	3.0
BX-107 IC Sludge	25	0.04	5.6
BX-107 IC Sludge	95	2.3	5.3
C-104 CWP1	25	0.12	2.2
C-104 CWP1	45	0.03	2.0
C-104 CWP1	65	0.03	1.6
C-107 IC Sludge	20,25	< 0.01	1.5
C-107 IC Sludge	45	< 0.01	1.3
C-107 IC Sludge	65	< 0.01	1.2
C-109 FeCN Sludge	30	190 [a]	348 [b]
C-110 1C Sludge	30	2.5	3.2
C-110 1C Sludge	95	0.30	2.3
SY-102 Unidentified Sludge	25	< 0.01	0.42
T-102 CWP Sludge	30	< 0.01	1.2
T-102 CWP Sludge	90	< 0.01	0.79
T-107 IC Sludge	25	< 0.01	4.6
T-107 IC Sludge	90	< 0.01	0.79
T-110 2C Sludge	25	< 0.01	2.4
T-111 2C Sludge	27,28	0.78	6.7
T-111 2C Sludge	95	1.0	3.4
T-203 Post-1949 Sludge	25	2.6	3.2
T-204 Post-1949 Sludge	25	12	7.1

Notes:

a. Extrapolated yield stress from a curve fit of two data points. Measurement far exceeds the highest measured value of 80 Pa and is most likely an outlier.

b. Extrapolated viscosity from a curve fit of two data points. Measurement far exceeds the highest measured value of about 100 cP and is most likely an outlier.

6.2.2 Slurry Viscosity and Yield Stress Prediction Uncertainties

The empirical curve fits of yield stress (Equation 6-1) and viscosity (Equation 6-2), as functions of mass fractions of UDS (denoted x), were performed using Ordinary Least Squares (OLS) fitting capabilities (i.e., regression) in Excel. Because yield stress and viscosity are functions of temperature as well as x, the data were grouped into temperature ranges before fitting Equations 6-1 and 6-2 to the data. The resulting equation fits are subject to uncertainty because of using temperatures that are close but not equal, as well as uncertainty in the measured rheological properties and temperatures.

An alternative approach would have been to fit yield stress and viscosity data to an equation that captures the functional dependence of both x and temperature. This approach would have provided larger data sets that would have been less subject to outlying data when fitting the equation. Also, larger data sets would have provided (1) a better basis for assessing the goodness of fit of the data to the equation, and (2) a basis for quantifying the uncertainty in predicted values of yield stress and viscosity. However, given the uncertainties associated with the effects of mixing and blending (see Section 6.3), this effort was deferred.

Another possible source of uncertainty in the fits of Equations 6-1 and 6-2 to data (the results of which are listed at the ends of Figures 6-3 to 6-26) relates to the validity of the assumptions for using OLS regression. These assumptions are as follows.

1. The uncertainties in the measured response (yield stress or viscosity) are independently distributed, which means the response values cannot be correlated across data points.

2. The uncertainties in measuring the response variable (yield stress or viscosity) are identically distributed. Identically distributed means the uncertainties in measuring the response variables must have the same mean and same SD for every data point. This assumption is violated if the uncertainty in the response variable changes with the magnitudes of the response variable and/or predictor variable.

3. The predictor variable (mass fraction of UDS) must be known without uncertainty. In practice, OLS tends to perform well as long as the uncertainty in the predictor variable is small (e.g., less than 10% of the uncertainty in the response variable after propagating the predictor variable uncertainty to response variable units).

The PNNL-20646 and PNNL-16857 reports from which the yield stress and viscosity data were collected did not describe the measurement process for yield stress and viscosity. However, practicality constraints with measuring these properties for samples with different x and temperature values can result in correlations for subsets of the data, which would violate Assumption 1. Further, because values of yield stress and viscosity have ranges greater than an order of magnitude (i.e., power of 10), that can result in large uncertainties for large values of yield stress or viscosity. In such a case, Assumption 2 would be violated. Finally, the approach of using grouped temperatures violates Assumption 3. Violations of Assumptions 1 to 3 can lead

to the fitted equations yielding biased predictions of the properties, and/or to incorrect uncertainties of the predicted values calculated using formulas based on OLS theory.

The predictions of yield stress and viscosity in Table 6-4 are subject to other uncertainties than those already mentioned, even if Assumptions 1 to 3 are valid.

- Uncertainties of rheology property predictions at 10 wt% solids depend on where this value falls with respect to the data for a given tank. There are tanks for which the 10 wt% solids value is in the middle of the data range. (e.g., Tank AZ-102 in Figure 6-9), on the low or high end of the data range (e.g., Tank C-104 in Figure 6-14 and Tanks B-202 in Figure 6-14), and outside the data range (e.g., Tank BX-107 in Figure 6-13 and Tank SY-102 in Figure 6-20). Extrapolating beyond the range of data is generally subject to large uncertainty, especially when the equations were fit to relatively few numbers of data points.

- Predictions of the rheology properties are not made at the same temperature values (or range of temperature values), which makes it difficult to compare results. Fitting equations that are functions of temperature and x, as discussed previously, would enable predicting rheology property values at the same temperature value. However, depending on the temperature value, this could involve interpolating or extrapolating to various extents depending on the range of temperature values investigated for a given tank.

- Some of the equation fits involve only two values of wt% solids (i.e., Figure 6-16, Figure 6-20, Figure 6-21, and Figure 6-26). In these cases the equations fit the data exactly, and thus are sensitive to outlying data points.

- Even for equation fits performed with more than two wt% values, the number of values is limited. This increases the potential for biased predictions or predictions with larger uncertainty.

For some tanks with enough data, it would be possible to apply OLS formulas for calculating uncertainties (e.g., SD or PIs) assuming that Assumptions 1 to 3 are valid and that the equations fit the data well enough. There was insufficient time to investigate all of these issues, so uncertainties of the predicted yield stress and viscosity values in Table 6-3 were not calculated. It should be kept in mind that the predicted property values in Table 6-3 are subject to varying degrees of uncertainty, which is likely substantial in some cases.

6.2.3   Slurry Viscosity and Yield Stress Prediction Model Variation

Viscosity and yield stress predictions (at 10 wt% solids) listed in Table 6-3 have moderate spreads. The outlying values for C-109 FeCN Sludge were excluded from the following summaries. Irrespective of temperature, viscosity ranged from 0.42 to 6.7 cP, while yield stress ranged from < 0.01 to 12 Pa. Note that these are ranges in equation-predicted values, with no attempt to account for the effect of prediction uncertainties, as discussed in Section 6.2.2. Because of the limited number of tanks represented along with what could be large uncertainties in predictions, it is likely that the ranges of yield stress and viscosity at 10 wt% solids over all of the Hanford waste tanks will be greater than the data ranges listed here.

6.3   PRELIMINARY ASSESSMENT OF WFD OPERATIONS EFFECT ON RHEOLOGY

6.3.1   Need for Waste Feed Blending

One of the key challenges in supporting the RPP mission includes the incidental and intentional blending between the tanks (RPP-40149-VOL1). Incidental blending may occur throughout retrieval, staging, and delivery of the wastes. Intentional blending occurs based on available space within the DSTs and a need to improve waste processability and to meet waste acceptance criteria. Feed blending can also reduce the total amount of immobilized high-level waste (IHLW) produced, by increasing the overall waste oxide loading. As an example for intentional blending, Table 6-5 shows a list of the associated waste transfers for Campaign HLW-3 (RPP-40149).

Table 6-5. Campaign HLW-3 Associated Waste Transfers

Source tank	Receipt tank	Transfer date	Liquid Volume (gal)	Solids Volume (gal)
AZ-102	AW-102	6/8/2012	371,300	0
AZ-102	AW-102	6/18/2012	371,300	0
AZ-101	AZ-102	10/15/2012	823,647	343
AZ-102	AP-103	11/14/2014	863,994	356
AX-103	AZ-102	1/1/2016	863,155	1,331
AZ-102	AW-102	3/31/2016	855,791	0
AX-103	AZ-102	4/25/2016	312,166	482
AX-104	AZ-102	5/31/2016	291,655	2,065
AX-102	AZ-102	1/5/2017	246,933	171
AZ-102	AW-102	2/8/2017	838,183	0
AX-102	AZ-102	3/4/2017	607,588	421
AX-101	AZ-102	5/21/2017	229,886	288
AZ-102	AW-102	8/25/2017	831,335	0
AX-101	AZ-102	9/18/2017	830,294	1,041
AZ-102	AW-102	3/8/2018	825,424	0
AX-101	AZ-102	4/1/2018	824,391	1,034
AZ-102	AW-102	8/11/2018	693,627	0
AX-101	AZ-102	9/3/2018	603,437	757
AP-107	AZ-102	10/19/2018	89,433	0

Additional examples for intentional blending include blending high-zirconium waste in Tanks AW-103 and AW-105 and blending of the high concentration of fissile ^{233}U in Tank C-104 (RPP-40149-VOL1). Furthermore, it is known that tank wastes of the Group 5 (S-101, S-107, S-110 and SX-103) are highly blended and involved in many batch transfers (ranging from 14 to 40 batches transfer) [SVF-2117, *WTP_TRACEBACK_4MINTIMESTEP(6MELTERS)-MMR-11-031-6.5-8.3R1-2011-03-18-AT-01-31-58_V8.XLSM]*.

6.3.2   Physicochemical Perspective on Waste Feed Blending

Waste feed blending inherently involves changes in various physicochemical characteristics, in comparison to original wastes. Important physicochemical characteristics include pH, chemical compositions of particles and salts, concentrations of particles and salts, PSD, and density and shape of particles among others. Changes of such physicochemical characteristics may be coupled with each other. A good example is the subsequent changes that occur when pH changes. When the waste feed blending alters pH, the surface charge density, and surface potential of solid oxides/hydroxides change (Hunter 2001). Each solid oxide/hydroxide possesses different amphoteric dissociations in surface functional groups represented by the isoelectric point (IEP) or zero point of charge (ZPC). These differences depend on the chemical composition of particles (Parks 1964). Furthermore, a recent study showed that the IEPs of rutile and hematite significantly differ over a range of high-salt concentrations (up to ~1M of salts) but the amount of change depends on the chemical composition of particles (Kosmulski et al. 2002). Therefore, the changes in pH, chemical composition of particles, surface charges/potential, and concentration of salts are strongly correlated. This example illustrates how a simple pH change from the blending can result in a complicated interplay between various physicochemical characteristics.

Rheological properties of waste feed are affected by the delicate balance between repulsive and attractive particle interactions, influenced by the physicochemical characteristics (Russel et al. 1989, Hunter 2001). For example, the yield stress in shear of a slurry (one of the most important rheological properties) is the stress required to initiate a slurry flow. To re-state, it is the minimum stress required to cause the fluid to flow like a viscous material with a finite viscosity, and can thus be regarded as a material property denoting a transition between solid-like and liquid-like behavior (Dzuy and Boger, 1983). It corresponds to the maximum force per unit area that the floc or microstructure in slurry can withstand before rupturing at a low shear rate; it originates from the elastic nature of floc or microstructure. Therefore, a yield stress is closely related to the characteristics of floc in the slurry. The number of nearest particles in the floc depends on the strength of the attractive van der Waals interactions, balancing with repulsive electrostatic (and/or steric) interactions. For the pH variation discussed above, the change in pH resulting from waste-feed blending can lead to different surface potentials of particles. This alters a previous balance between repulsive and attractive particle interactions that existed in original wastes before waste feed blending.

Flocs form when the attractive van der Waals interactions dominate over the repulsive interactions (i.e., decrease in the surface potential). Subsequently, the yield stress increases. In contrast, when the particles become more stable because of an increase in surface potential, the yield stress decreases. Similarly, changes in the particle size (and distribution), particle density and shape of particles from waste feed blending can also alter the balance between repulsive and attractive particle interactions. Therefore, the waste feed blending can significantly alter the rheological properties, which may significantly challenge waste transport.

Scales et al. (1998) and Zhou et al. (2011) reported a quantitative model between the interactions and rheological properties for a simple case. Based on the assumption that particles are chemically identical and spherical with the same size, the authors showed the following relation

between yield stress and repulsive electrostatic and attractive van der Waals interactions, as well as the particle volume fraction, Φ, for flocculated particle systems:

$$\tau_y = \frac{\Phi K(\Phi)}{24\,\pi d}\left(\frac{A}{H_s^2} - \frac{24\pi\varepsilon_0\varepsilon\kappa\zeta^2}{1+e^{\kappa H}}\right) \tag{6-3}$$

where $K(\Phi)$ = mean coordination number as a function of the particle volume fraction

A = Hamaker constant
ε_0 = permittivity of vacuum
ε = dielectric constant of the suspending medium
κ = inverse Debye length
ζ = zeta potential
H_s = separation between particles
d = particle diameter

The first and second terms on the right hand side correspond to contributions from attractive van der Waals and repulsive electrostatic interactions, respectively. Equation 6-3 clearly connects a yield stress with physicochemical characteristics such as the zeta potential, Hamaker constant (a function of dielectric properties of particle and suspending medium) and particle volume fraction. However, it may not be practically valuable for many applications since it is rare to have a mono-dispersed case. Nevertheless, the 'scaling' of yield stress as a function of physicochemical characteristics might be informative if changes of physicochemical characteristics from waste-feed blending can be identified.

As a result, tank wastes are very unique and far from such an ideal case. Tank wastes exhibit very complicated and wide ranges of physicochemical characteristics (PNNL-16857, PNNL-20646). They contain high concentrations of various dissolved salts and metal hydroxide/oxide particles as major components in solid particles. They possess a wide chemical composition of particles (e.g., compounds associated with Ag, Ni, Pu, Pb, and Sr, Al, and salts) with broad density distribution (2 - 11 g/cm^3). The PSD of the tank wastes is also broad, typically ranging from 0.1 to 100 µm. Furthermore, many particles would be non-spherical, either elongated or plates. The tank wastes are generally basic; many of the tank wastes have pH ~ 13-14 with some exceptions having pH ~ 8-10.

Tank waste rheological properties are extremely complicated so that a simple model such as Equation 6-3 cannot be applied. In fact, the rheological properties of tank wastes vary from Newtonian to non-Newtonian, generally depending on the UDS concentration of the waste. For example, the maximum measured Bingham yield stress of sludge waste types ranges from 0.3 to 80 Pa, whereas that of saltcake waste types ranges from 0.2 to 20 Pa (PNNL-20646). Because of such wide ranges of physicochemical characteristics in the wastes, blended wastes are likely to show unexpected changes of physicochemical characteristics (and thus rheological properties) which cannot be simply deduced from a fractional contribution from each waste in the blending. Therefore, estimating rheological properties of blended wastes is a formidable challenge, and empirical measurements are necessary.

6.3.3 Possible Waste Feed Blending Effects on Rheological Properties

A previous subsection briefly discussed physical insights on waste feed blending and how blending can change rheological properties. This subsection illustrates possible effects of waste feed blending on rheological properties, based on various previous studies. First, more detailed discussions of the relationship between individual key physicochemical characteristics (physical and surface chemistry aspects) and rheological properties are provided to gain better insights on the possible effects of the physicochemical characteristics on rheological properties, which would help understand the effects of waste blending accordingly. Next, the effects of blending on rheological properties are illustrated using both simple systems and actual composite wastes samples (Group 5/6, Group 1/2, Group 3/4, and Group 7/AY-102).

6.3.3.1 *UDS Concentration, Particle Size Distribution, and Particle Shape*

Waste feed blending obviously changes the UDS concentration and PSD. As expected, UDS concentration (equivalently, particle volume fraction) mainly affects the van der Waals interaction simply by changing an average separation between particles. An average separation between particles scales as $a\Phi^{-1/3}$, where a is the representative particle radius. To relate the study results to the actual waste sample data described previously, note that weight fraction of particles (i.e., UDS concentration) can be converted to particle volume fraction (as shown in PNNL-17707, *An Approach to Understanding Cohesive Slurry Setting, Mobilization, and Hydrogen Gas Retention in Pulsed Jet Mixed Vessels*):

$$\Phi = \frac{x(\rho_L/\rho_s)}{1 + x[(\rho_L/\rho_s) - 1]} \qquad (6-4)$$

where
x = particle mass fraction
ρ_L = suspending medium liquid density
ρ_s = particle density

The particle size changes electrostatic and van der Waals interactions (Russel et al. 1989, Hunter 2001) so that rheological properties are expected to be changed from waste feed blending. Leong et al. (1995) demonstrated the effects of UDS concentration and PSD in ZrO_2 suspensions. At pH ~ 7 (IEP of ZrO_2), varying the particle volume fraction from 0.12 to 0.24 showed the maximum increase in yield stress from 100 to 1,325 Pa. Similar increases with respect to the UDS concentration were shown with polystyrene latex, attapulgite clay and bentonite suspensions (Buscall et al. 1987). However, in Leong et al.'s study, such differences with respect to the UDS concentration decrease as pH deviates from 7 because of the increase in the surface potential of particle, which implies a coupling between UDS concentration and surface potential for resultant rheological properties. Qualitatively similar behaviors were observed in other studies with alumina suspensions (Channell and Zukoski 1997, Zhou et al. 2001), titania suspensions (Zhou et al. 2001) and three different coal suspensions (Turian et al. 2002). It is noteworthy that the yield stresses in Leong et al. (1995) were measured by the vane method. For slurries with low and intermediate UDS concentrations (relevant to all examples in this section), previous studies clearly showed that the vane method can provide similar Bingham

yield stresses as obtained by the shear stress measurement with varying shear rate, called the flow curve measurement (Dzuy and Boger 1985, Chun et al. 2010, PNNL-20646).

In addition, the yield stress significantly varies with d_{50} (50th percentile diameter of the PSD) for the same ZrO_2 suspension (Leong et al. 1995). With 57 wt% of ZrO_2 suspension, the one with $d_{50} = 0.25$ μm showed ~ 400 Pa of yield stress whereas the other with $d_{50} = 0.66$ μm showed ~ 250 Pa of yield stress at pH ~ 7.5. Although the difference in yield stress varies with pH, a clear difference was observed in the pH range from 5 to 10. While the UDS effect is expected, the d_{50} dependence on yield stress is not quite convincing since the study used a relatively narrow PSD. Recently, Chun et al. (2011) studied similar PSD effects on rheological properties by using nuclear waste simulants having broad particle size distributions. Using three LAW simulants, it was shown that the yield stress varies significantly (from Newtonian to 9 Pa) in spite of very similar d_{50} values (~ 17 μm). The study concluded that the increase in yield stress is more a function of the percentage (or relative amount) of particles with diameter smaller than about 5 μm rather than d_{50}.

The importance of particle size on the relative contributions of hydrodynamic and colloidal interactions (or forces) can be explained by two dimensionless numbers: shear-repulsion number (N_{SR}) and shear-attraction number (N_{SA}) (Probstein 1994). These dimensionless numbers are defined as the following:

$$N_{SR} = \frac{\mu a^2 \dot{\gamma}}{\varepsilon \zeta^2} ; N_{SA} = \frac{\mu a^3 \dot{\gamma}}{A} \qquad (6-5)$$

where
ζ = zeta potential of particle
μ = viscosity of the medium
ε = Permittivity of the medium
$\dot{\gamma}$ = shear rate
A = Hamaker constant, an order-of-magnitude measure of van der Waals interactions

Under very high-salt concentration, which is applicable to the waste simulants and actual wastes, $N_{SR} >> O(1)$, irrespective of particle size, since the zeta potential of the particle is likely to be negligible. Therefore, only the shear-attraction number is of interest. The shear-attraction number scales as a^3, which implies that the relative importance of van der Waals interactions becomes rapidly negligible as the particle size increases. For aqueous slurries with particles of 5 μm diameter and a typical Hamaker constant (~ 10-20 J), $N_{SA} \sim C\dot{\gamma}$ where C is an $O(1)$ constant, which suggest that hydrodynamic and colloidal forces are comparable at shear rates of $O(1)$.

Therefore the role of attractive van der Waals interactions on rheological properties of slurries is significant for particles less than 5 μm. It is worth noting that the importance of the relative amount of small particles is indeed dependent on surface chemistry-related characteristics such as pH and salt concentration. Chun et al. (2011) showed that, under low ionic strength (~ 0.01M of sodium nitrate), gibbsite slurries even with a high percentage of small particles (> 50%) surprisingly exhibit smaller yield stresses (~ 5-7 Pa) than what are expected solely from the relative amount of small particles. The point of zero change (PZC) of gibbsite is about 5 (Parks

1964) and the pH of the slurries is about 11 so that electrostatic repulsion between particles is not negligible (i.e., $N_{SR} \sim O(1)$ or less for particles < 5 μm). In this case, increasing the number of small particles did not give rise to appreciably higher yield stress in the slurries.

No clear example was identified for the effect of particle shape. However, the van der Waals interaction scales as $1/H^2$ for spherical particles but it diminishes faster or slower than $1/H^2$ for rod-like particles, depending on their orientation and separation (Russel et al. 1989). It is not difficult to expect a change in the particle interaction and thus one can deduce the addition of different shape of particles due to waste feed blending will lead to a change in yield stress. This is especially true considering that a yield stress is correlated to the maximum force per unit area. The addition of rod-like particles is expected to increase the yield stress under the same condition, compared to spherical particles.

6.3.3.2 *IEP, Salts, and pH Surface Chemistry Aspects*

It is expected that waste feed blending can change the concentration of salts and pH. This results in changes in electrostatic repulsion between particles, depending on the composition of particles (i.e., IEP). The DLVO (Derjaguin-Landau-Verwey-Overbeek) theory may be a useful framework to understand such changes (Russel et al. 1989, Hunter 2001). Leong and Boger (1989) clearly showed the relation between rheological properties and surface properties. It was observed that a yield stress of the Morwell coal suspension (40% of particles less than 10 μm) disappears around pH=4 above which an electrophoretic mobility of the particle sufficiently provides a deflocculation. While Leong and Boger limited the study for pH above the IEP of Morwell coal (pH ~ 2), a further study with ZrO_2 suspension by Leong et al. (1995) varied the pH sufficiently including its IEP (i.e., IEP ± 2). The latter study showed that the variation of yield stress is approximately symmetric around the IEP of the particles (~ pH=7), although the range of yield stress variation depends on the particle volume fraction. Maximum yield stress was achieved near the IEP and nearly zero yield stress was observed around pH = 5 and 10.

Leong and Boger (1989) showed that the yield stress for the Morwell coal suspension increases as the salt concentration increases. More importantly, the increase in yield stress depends on the valence of salt (e.g., Na^+ vs. Ca^{2+}) and no further increase in yield stress takes place after a certain threshold concentration (~ 0.75M) of salt for both Na^+ and Ca^{2+}. While a similar threshold salt concentration for yield stress is observed, bentonite suspension exhibited the opposite trend (Goh et al. 2011); the yield stress decreases as the (phosphate) salt concentration increases. This peculiar behavior originates from the chemical composition of bentonite. Bentonite is 2:1 smectite clay comprised mainly of montmorillonite. It consists of an alumina octahedral sheet being sandwiched by two tetrahedral silica sheets. Therefore, it possesses alumina-like edges and silica-like planar surfaces or faces. Because of two different IEPs (i.e., pH ~ 2 for the silica-like faces and pH ~ 8-9 for the alumina-like edges) (Parks 1964), edges and faces are oppositely charged in a typically range of pH. Therefore, bentonite naturally forms a very strong card-house structure (see Figure 6-29) which exhibits a very high yield stress even with 5 to 7 wt% of the particles. As the concentration of salt increases, a weaker card-house structure is formed due to the shielding of electrical double layer, which reduces the yield stress. Owing to the same reason, no symmetry trend for the variation of yield stress with respect to pH was observed. The difference between the Morwell coal and bentonite suspension clearly

suggests that the chemical composition of particles and resultant surface characteristics are important to understand the rheological properties.

Figure 6-29. Illustration of Card-House Structure (adapted from Goh et al. 2011)
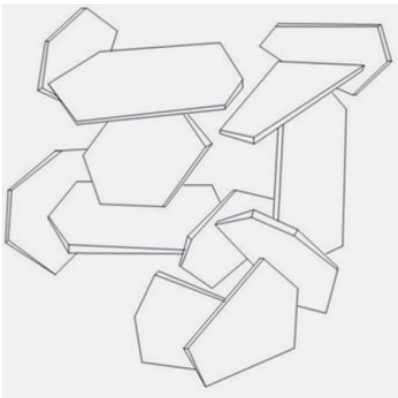
6.3.3.3 *Simple Systems Blending Examples*

Subbanna et al. (1998) studied the rheological behavior of a mixture of alumina and zirconia suspension having relatively narrow PSDs. As expected, both alumina and zirconia suspensions showed the maximum yield stresses around their IEPs (pH ~ 8 for alumina and pH ~ 6-7 for zirconia). Additionally, the symmetry of changes in yield stress was observed around their IEPs. For various particle volume fractions (0.1 to 0.4) and pH range (from 2 to 10), the yield stress of blended mixture lies between those of two sources. In fact, it appears that a common fractional contribution from each suspension can be applicable to estimate the yield stress of the blended mixture. This outcome may be a result of the relative similarity of the two sources. As for surface chemistry aspects, their IEPs are quite similar so there is no abrupt change of the interaction between alumina and zirconia particles over the pH range. It appears that there are some differences from physical aspects, such as a specific surface mean diameter, PSD, and solid density of particle. However, the concentration of salt is very low (~ 10^{-2} M) so that for most cases (except near IEPs), electrostatic repulsion is likely to dominate over van der Waals interaction. Therefore, the effects from such differences could not be appreciable.

PNNL-14333 performed rheological characterization for a kaolin, bentonite, and kaolin/bentonite (80/20) mixture to investigate the physical and liquid chemical simulant formulations for transuranic (TRU) wastes. Table 6-6 summarizes the rheological behavior of the sources and two mixtures. Note that the rheological properties of bentonite are not available in PNNL-14333. Available data for 7-wt% bentonite suspension (Goh et al. 2011) is presented assuming that pH ~ 7 for the PNNL-14333 testing.

Table 6-6. Rheological Behavior of Kaolin, Bentonite and Two Mixtures of Kaolin/ Bentonite (80/20) at 25°C (reproduced from PNNL-14333 and Goh et al. 2011)

Description	Solids Concentration (wt%)	Rheology	Yield Stress (Pa)
Kaolin #1	30.0	Non-Newtonian	6.02
Kaolin #2	20.0	Non-Newtonian	1.25
Bentonite	7.0	Non-Newtonian	~ 20
Kaolin/Bentonite (80/20) mixture #1	21.2	Non-Newtonian	5.43
Kaolin/Bentonite (80/20) mixture #2	14.2	Non-Newtonian	0.93

Both kaolin and bentonite show non-Newtonian rheological characteristics. Between the two sources, bentonite exhibits much more significant non-Newtonian characteristics and higher yield stress. Kaolin clay, composed of the mineral kaolinite, has two oppositely charged surfaces (i.e., alumina-like and silica-like planar surfaces), whereas bentonite has alumina-like edges and silica-like planar surfaces. Both have roughly the same particle density (~ 2.65 g/cm^3). Bentonite clay is typically composed of very thin (0.001 to 0.01 μm) and small-sized surface (0.1 to 1 μm) particles, yielding a huge surface area per unit mass. Kaolin clay has thicker (0.03 to 1 μm) and larger (0.3 to 3 μm) plate-shaped particles (PNNL-11685, *Retrieval Process Development and Enhancements Waste Simulant Compositions and Defensibility*). More importantly, bentonite exhibits a card-house structure due to the opposite charges in edges and surfaces; kaolin clay does not. Therefore, a combination of the order-of-magnitude difference in contacts and charge distribution would result in the difference in their yield stresses. The increased yield stress of the bentonite, relative to the kaolin, was observed at similar concentrations (PNNL-20646). As shown in Table 6-6, both mixtures of kaolin/bentonite are based on 80/20 (mass) blending so that rheological properties are expected to be similar to that of kaolin.

The discussion on kaolin and bentonite is closely correlated with a difference between cohesive and non-cohesive slurry in clay/water systems (and/or other systems). The face-to-edge contacts indeed correspond to more cohesive forces between the bentonite particles. For a slurry under a plastic state (i.e., the slurry undergoes a permanent deformation when subjected to an applied stress greater than its yield stress), its liquid content must be sufficient for the particles to slide freely past each other but the magnitude of the net force between particles must be enough to maintain cohesive nature between them. A plasticity index may give a good indication of the "degree" of plasticity of cohesive slurry (Bain 1971). Plasticity is defined by the difference between the liquid limit and the plastic limit, which can be evaluated from the Atterberg limits (ASTM D 4318 - 10). As shown in Bain (1971), plasticity indices up to 550 to 600 have been obtained for bentonite, while some kaolinites are virtually non-plastic with plasticity indices less than 10. Plastic kaolinites may have plasticity indexes of 40 to 50.

6.3.3.4 *Actual Waste Blending Examples*

In contrast to simple systems, each actual waste contains complicated salts and particles as shown in previous studies (e.g., PNNL-16857, PNNL-20646). Since all physicochemical characteristics are coupled with each other, it is extremely difficult to understand the effects of waste feed blending on rheological properties. Previous studies (e.g., PNNL-16857,

PNNL-20646) indicated that high pH and high salt concentrations are common in most of tank wastes. Using the shear-repulsion number (N_{SR}) and shear-attraction number (N_{SA}) shown in section 6.3.3.1, it can be deduced that $N_{SR} >> O(1)$ for most of tank wastes, which can imply that the contribution from electrostatic interactions are negligible and thus characteristics related to surface chemistry aspects such as IEP, salt concentrations, pH may not be decisive factors to interpret the effects of feed waste blending on rheological properties. Instead, changes in physical characteristics from blending are expected to be more important to interpret rheological properties. However, it is important to note that the interpretation and analysis are solely based on existing/available characterization for the blending tests. It would be possible that the surface chemistry related parameters can become more important or an additional factor plays a role in the rheological behavior of actual waste blending in case the characterization does not reflect all aspects of the samples.

Rheological data of actual wastes representing the effect of blending (i.e., before and after blending) have been searched. Identified examples of blending between different groups of composite M-12 samples (i.e., obtained from different tanks within the same group) are shown in this section. While tanks represent in such M-12 samples were considered, there are no M-12 groups wherein rheological properties are known for all (or even majority) of the individual tank waste components. However, such limited blending testing can provide valuable insights on how to apply current knowledge from simple systems to understand such complex systems. Note that only rheological data at 25°C are shown here for simpler interpretation, although some rheological data at higher temperatures (40°C and 60°C) is available. Table 6-7 shows the projected distribution of water-insoluble components to help chemically identify different waste groups (PNNL-17368).

Table 6-7. Projected Distribution of Water-Insoluble Components in the Tank Waste Groups (reproduced from PNNL-17368)

Group	Type	Al* (wt%)	Cr* (wt%)	F* (wt%)	Fe* (wt%)	Oxalate* (wt%)	Phosphate* (wt%)	Sulfate* (wt%)
1	Bi Phosphate sludge	4	4	22	22	0.5	36	7
2	Bi Phosphate saltcake (BY, T)	13	18	24	8	37	23	42
3	CWP, PUREX Cladding Waste sludge	17	1	1.3	5	1	2	0.4
4	CWR, REDOX Cladding Waste sludge	10	1	< 0.1	1	0.4	0.1	< 0.1
5	REDOX sludge	29	6	0.1	4	3	1	0.4
6	S-Saltcake (S)	8	46	0.6	4	27	4	14
7	TBP Waste sludge	1	0.4	0.5	7	0.1	17	3
8	FeCN Waste sludge	1	1	0.4	7	1	6	1
---	Balance	17	24	51	41	30	10	32

Notes: *Component values were rounded off: therefore, the sums may not add to exactly 100-wt%. CWP=PUREX cladding waste; CWR=REDOX cladding waste; FeCN=Ferrocyanide, PUREX=Plutonium-Uranium Extraction; TBP=tri-butyl phosphate

PNNL-17965 performed filtration and leach testing for the REDOX sludge and S-saltcake. As shown in Table 6-7, the REDOX sludge is categorized as Group 5 waste which is anticipated to be high in boehmite (~ 29% of Al). The S-saltcake is Group 6 waste which contains a significant fraction of water-insoluble chromium. During the testing, rheological properties were characterized for Group 5 source, Group 6 source, and the Group 5/6 mixture. Table 6-8 summarizes the results. The rheological data shown in Table 6-8 are for 25°C.

Table 6-8. Rheological Behavior of Group 5, 6 and Group 5/6 mixture at 25°C (reproduced from PNNL-17965)

Description	Solids concentration UDS (wt%)	Rheology	Yield Stress (Pa)	Viscosity (cP)
Group 5 Source	18.5	Non-Newtonian	57	13
Group 6 Source	14.7	Newtonian	negligible	8.0
Group 5/6 Mixture	13.2	Non-Newtonian	7.4	13

As shown in Table 6-8, the two source waste groups show drastically different rheological characteristics, even considering the ~ 4-wt% difference in solids concentration. Group 5 is highly non-Newtonian, showing a yield stress of 57 Pa and a viscosity of 13 cP. In contrast, Group 6 is Newtonian and has a viscosity of 8 cP, which is slightly less than the Group 5 source material's viscosity. The Group 5/6 mixture is non-Newtonian with a yield stress of 7.4 Pa and a viscosity of 13 cP. Like most of other tank wastes, Group 5 and 6 wastes have pH ~ 14 and contain large amounts of salts (PNNL-17965, PNNL-20646), which suggest that the electrostatic repulsion between the particles is likely to be negligible. Under this situation, the yield stress could be proportional to the relative amount of small particles (less than about 5 μm), according to Chun et al. (2011). However, the particle size analyses indicated that the relative amount of small particles for Group 6 (~ 60%) is comparable to that for Group 5 (~ 50%).

Interestingly, solid densities for Groups 5 and 6 are quite different; 1.507 g/cm^3 for Group 5 and 4.720 g/cm^3 for Group 6 (PNNL-17368). Supernatants for both wastes are aqueous solutions with dissolved solids (most likely salts); the density of the supernatant would not be significantly different from that of water. Therefore, the higher density for Group 6 can create an appreciable settling of particles under the relatively small solid concentration (14.7 wt%). Note that the expected difference in settling can be supported by actual settling tests: ~ 3.5 mm/hr of "fast" interface velocity (a measure of settling) for Group 6 but no settling for Group 5 (PNNL-20646). The densities estimated from solid phase compositions for Group 5 and Group 6 are 3.5 g/cm^3 and 2.6 g/cm^3 respectively (PNNL-20646). However, it can be postulated that measured solid densities in this case are more reasonable because other factors that affect the settling (e.g., PSD) are comparable. The difference in settling can mitigate the effective formation of floc or microstructure over the entire slurry. A continuous and volume spanning network of the floc, rather than a collection of discrete flocs, corresponds to a higher yield stress so that such mitigation would, in turn, give rise to Newtonian nature.

The rheological properties of the Group 5/6 mixture can be understood similarly. Although the mass ratio of Group 5 to Group 6 is about 2 in the waste blending (PNNL-17965), the rheological properties of the mixture are expected to be more similar to those of Group 5 due to their significant density difference (e.g., much more particles from Group 5). However, the yield

stress of the 13.2 wt% mixture is much lower than that observed in Group 5 of similar concentration. This implies that even a small number of high-density particles from Group 6 may hinder the effective formation of floc and reduces the yield stress, whereas there is no noticeable effect on viscosity.

The second example of actual waste blending includes Group 1 and Group 2 wastes, reported in PNNL-17992. Similar to the previous example, the testing was conducted to perform the characterization, leaching, and filtration testing for bismuth phosphate sludge and bismuth phosphate saltcake. As shown in Table 6-7, the bismuth phosphate sludge waste (Group 1) is anticipated to be high in phosphorus. It is implicitly assumed present as $BiPO_4$ although results presented in PNNL-17992 indicated that phosphate in Group 1 is actually present as amorphous iron (III) phosphate. The bismuth phosphate saltcake (Group 2) is anticipated to be high in phosphorus but would contain a mixture of gibbsite, sodium phosphate and aluminum phosphate owing to the relatively low bismuth content and higher aluminum content indicated in Table 6-7. During the testing, rheological properties were measured for Group 1 source, Group 2 source, dilute Group 1/2 mixture, and concentrated Group 1/2 mixture. Table 6-9 summarizes the results.

Table 6-9. Rheological Behavior of Group 1, 2 and Two Group 1/2 Mixtures at 25°C (reproduced from PNNL-17992)

Description	Solids Concentration (wt%)	Rheology	Yield Stress (Pa)	Viscosity (cP)
Group 1 Source	9.0	Non-Newtonian	0.3	6.7
Group 2 Source	37.4	Non-Newtonian	1.1	13
Dilute Group 1/2 Mixture	8.2	Newtonian	negligible	5.0
Concentrated Group 1/2 Mixture	16.0	Non-Newtonian	3.0	12

As shown in Table 6-9, both source wastes show slightly non-Newtonian rheological characteristics with yield stresses close to the instrument limit of detection. Among the two source materials, Group 2 shows a higher yield stress, which can be reasonably deduced from its much higher solids concentration (37.4 wt% USD) and higher relative amount (~ 65%) of small particles (i.e., less than about 5 µm), in comparison to those of Group 1 (9.0 wt% UDS and ~ 40% of smaller particles). Note that solid densities of Group 1 (5.155 g/cm^3) and Group 2 (4.130 g/cm^3) are high but comparable to each other (similar to that of Group 6 in the previous example). A similar small difference in density can be also observed in the densities based on solid phase compositions (~ 3.6 g/cm^3 for Group 1 and ~ 2.8 g/cm^3 for Group 2) (PNNL-20646). Although Group 2 has appreciably high relative amounts of small particles and UDS concentration, it may be postulated that the high solid density for Group 2 would trigger the small yield stress.

The dilute Group 1/2 mixture has an UDS concentration of 8.2 wt%, which is similar to that of Group 1. Based on the similar solids concentration, it is not surprising that the dilute slurry mixture has similar yield stress (zero) and viscosity (5.0 cP). However, surprisingly, concentrating the slurry changes the rheology from Newtonian to non-Newtonian, with a yield stress of 3.0 Pa and a viscosity of 12 cP. This is an unexpected increase, especially considering that the concentrated group mixture has about a half of UDS concentration (16 wt%), compared to that of Group 2. Such an increase can be understood from changes in PSD after blending.

According to the particle size analysis, the blending gives rise to ~ 75% of relative amounts of small particles, which can be responsible for the increase in yield stress.

The third example of actual waste blending is between Group 3 and Group 4 wastes (PNNL-18048). The blending was intended for filtration and leach testing. As shown in Table 6-7, Group 3 is the PUREX cladding waste sludge and Group 4 is the REDOX cladding waste sludge. Both Groups 3 and 4 have solids consisting of > 85% gibbsite. During the testing, rheological properties were measured for dilute Group 3/4 mixture and concentrated Group 3/4 mixture. Rheological properties of Group 3 and Group 4 sources were reported in PNNL-18054. Table 6-10 summarizes the rheological behavior of the sources and mixtures. Note that two measurements are shown for yield stress and viscosity.

Table 6-10. Rheological Behavior of Group 3, 4 and Two Group 3/4 Mixtures at 25°C (reproduced from PNNL-18054 and PNNL-18048)

Description	Solids Concentration (wt%)	Rheology	Yield Stress [Pa]	Viscosity [cP]
Group 3 Source	~ 29	Newtonian	negligible	2.3/2.4
Group 4 Source	~ 30	Newtonian	negligible	3.2/3.4
Dilute Group 3/4 Mixture	6.0	Newtonian	negligible	2.0/2.0
Concentrated Group 3/4 Mixture	13.0	Non-Newtonian	3.1/3.4	7.1/7.6

As shown in Table 6-10, both source wastes show Newtonian rheological characteristics with very low viscosities (about 2-3 cP); Group 4 source has a slightly higher viscosity than Group 3. A possible reason for the Newtonian characteristics, even with high UDS concentrations, can be related to settling behaviors. While ~ 40% and ~ 25% of particles are less than 5 μm for Group 3 and Group 4 respectively, very significant settling rates (~ 40 mm/hr for Group 3 and ~ 53 mm/hr for Group 4) were observed for both cases (PNNL-20646). These relatively high settling values can significantly reduce the effective formation of floc or microstructure over the entire slurry, even with high UDS concentrations.

The dilute Group 3/4 mixture shows a similar viscosity to those of Group 3 and Group 4 even with very small UDS concentration of 6.0 wt%. More interestingly, the concentrated Group 3/4 mixture exhibits non-Newtonian behavior with a yield stress of ~ 3.3 Pa and a viscosity of ~ 7.4 cP, although UDS concentration is still low (13.0 wt%). The particle size analyses (PNNL-18054, PNNL-18048) indicated that the relative amount of small particles for Group 3/4 mixture becomes ~ 50% after the blending, which is higher than that from either of two sources. Therefore, while a detailed reason is unknown, such onset of non-Newtonian behavior may be related to changes in PSDs from the blending.

The last example of actual waste blending is between Group 7 and AY-102 wastes, described in PNNL-18119. Tank AY-102 waste samples were blended with the Group 7 waste composite because of insufficient quantity of Group 7 waste composite during the characterization, leaching, and filtration testing. As shown in Table 6-7, Group 7 is the TBP waste sludge that contains high concentrations of phosphate and aluminum (primarily as gibbsite), but a relatively low concentration of chromium. Table 6-11 summarizes the rheological behavior of the sources and mixture. Note that two measurements are shown for yield stress and viscosity.

**Table 6-11. Rheological Behavior of Group 7, AY-102 and the Mixture at 25°C
(reproduced from PNNL-18119 with consulting PNNL-20646)**

Description	Solids Concentration (wt%)	Rheology	Yield Stress (Pa)	Viscosity (cP)
Group 7 Source	11.7[a]	Non-Newtonian	4.1/3.3	11/12
AY-102 Source	~ 6[b]	Newtonian	negligible	3.9/4.1
Concentrated Group 7/AY-102 Mixture	26	Non-Newtonian	5.2/4.6	10/10

Notes:

a. Averaged value after eliminating one outlier value (6.7 wt%).

b. Estimated value from the available data in PNNL-20646 but the range of the UDS concentration is noticeably broad (from 6 to 25 wt%) with the similar viscosity.

As shown in Table 6-11, the two source wastes show different rheological characteristics. Group 7 is non-Newtonian, showing a yield stress of 3-4 Pa and a viscosity of 12 cP. In contrast, AY-102 is Newtonian and has a viscosity of 4.0 cP, which is about one-third of the Group 7 source material's viscosity. A possible difference between Group 7 and AY-102 sources would come from different UDS concentrations but no clear statement can be made due to the broad range of the UDS reported for the AY-102. The concentrated Group 7/AY-102 mixture exhibits non-Newtonian behavior with a yield stress of ~ 5 Pa and a viscosity of 10 cP, which is similar to those of Group 7. This result may be expected considering that the UDS concentration of the concentrated Group 7/AY-102 mixture is more than two times that of Group 7. In spite of no available data for PSD of the Group7/AY-102 mixture, the effect of the AY-102 source is expected to be more significant to determine the rheological properties of the mixture. Based on previous examples, it can be deduced that the relative amount of small particles would decrease due to the blending, compared to that of Group 7.

6.3.4 Summary on Waste Blending Effects on Rheology

Incidental and intentional blending between the tanks is inevitable for the tank farm operation to accomplish the RPP mission. Such blending affects rheological properties through changes in various physicochemical characteristics such as pH, chemical composition of particles and salts, concentrations of particles and salts, PSD and density and shape of particles. An additional challenge to understand the effect of blending on rheology is that those characteristics are strongly coupled in a complex fashion. Tank wastes contain a wide variety of materials, pH, UDS concentrations, particle size and density distributions and shapes. Therefore, it is difficult or impossible with the current data to draw deterministic conclusions on the effect of tank waste blending on rheology. In fact, it is case-by-case as noted from the examples of actual waste blending. Measurements on actual blended waste feed are needed and are planned for flow loop samples (see Section 3.2).

Considering that high pH and high-salt concentrations are common in most tank wastes, the changes in physical characteristics from blending are expected to be more important than characteristics related to surface chemistry, unless an external modification on tank wastes (e.g., the addition of rheological modifiers) takes place. Therefore, changes of UDS concentration, PSD, particle density, and particle shape should be more carefully analyzed in order to gain some insights on the effect of the waste feed blending on slurry rheology.

7.0   RETRIEVAL AND TRANSFER SYSTEM CAPABILITIES

As previously described in Section 3, the Hanford DST system provides the staging location for WFD to the WTP. The current baseline mixing system employs two jet mixer pumps to mix and mobilize the waste, and a transfer pump to transfer the mobilized waste vertically out of the DST and through a horizontal pipeline to the WTP. The capabilities of the WFD system to transfer large and/or dense particulate are considered. The limits of performance of the WFD system with respect to UDS particle size and density that can be transported are evaluated using simple models. Where possible, the simple model approach is compared to full-scale process data and scaled test data.

Each component of the WFD system for particulate transport is considered sequentially:

- Jet mobilization and transport of particles to the transfer pump

- Particle entrainment into the transfer pump

- Particle motion in the vertical transfer pipeline

- Particle transfer in the horizontal pipeline

The limits of performance of each WFD system component are compared to the "upstream" component capabilities as well as to the bounding waste properties of Sections 4, 5, and 6. The mixer-pump capabilities are evaluated in Section 7.1, and the vertical and horizontal sections of the transfer line are evaluated in Sections 7.2 and 7.3, respectively. A summary of the determined WFD system capabilities is provided in Section 7.4. Future full-scale experimental studies are summarized in Section 7.5.

7.1   MIXER PUMP CAPABILITIES

Mixer pumps are utilized to mix waste in DSTs. This section evaluates the limits of performance of the current baseline mixing system, with respect to the UDS particle size and density. Particle mobilization and the trajectory of the mobilized particles are two key mechanisms whereby the jet mixer pumps can transport UDS particulate such that it can be ingested into the transfer line. Because this study addresses the limits of performance of the system, the limiting particle (the largest, most dense particle available for transfer) is of interest. The probability that the limiting particle is available (with respect to actual waste concentration, initial particle location in the vessel, etc.) is not evaluated.

The models describing the flow resulting from the jet mixer pumps are developed in Section 7.1.1. Results of this modeling approach are compared to prototypic and small-scale test results in Section 7.1.2. The models are applied to estimate the limiting particles in Section 7.1.3.

7.1.1 Mixer Pump Jet Model

A fluid jet from the feed delivery jet pumps can be described as an axisymmetric, circular offset jet.[12] After the flow emerges from the nozzle, the jet entrains fluid from the surrounding area as it expands. If the jet is sufficiently close to a solid wall, in this case the tank bottom, this entrainment pulls the jet down to the wall until it forms a wall jet (e.g., Rajaratnam 1976), which has a different velocity profile.

If it is assumed that a particle enters the jet pump inlet, the distance that the particle will travel after leaving the jet pump nozzle can be estimated. Estimating this distance includes (1) the longitudinal distance traveled as a suspended particle based on the velocity distribution of the jet and the terminal falling velocity of the particle, and (2) transport along the bottom of the vessel based on the wall shear stress generated by the jet.

The longitudinal distance can be estimated based on the following assumptions:

- The fluid jet is neutrally buoyant and Newtonian
- The initial location of the particle is in the jet at the top edge of the jet nozzle
- The particle terminal velocity is not affected by jet turbulence
- The particle travels at the same velocity as the jet at any location without slippage
- The particle remains in the vertical center plane of the jet
- The radial velocity components associated with jet development are neglected

The terminal falling velocity of a spherical particle can be calculated via Camanen (2007)

$$v_T = \frac{\mu}{\rho_L d}\left(\sqrt{15 + \sqrt{\frac{Ar}{0.3}}} - \sqrt{15}\right)^2 \qquad (7-1)$$

where v_T = settling velocity
Ar = Archimedes number

---

[12] A circular axisymmetric offset jet refers to a fluid jet exiting a circular nozzle with an axisymmetric velocity profile. This assumes that the flow path inside the jet pump does not skew the exiting velocity. The offset refers to the fact that the jet is parallel to the bottom of the tank and the jet centerline is offset from the bottom by a specified distance.

The Archimedes number is defined by the following:

$$Ar = \frac{\left(\frac{\rho_s}{\rho_L} - 1\right) g d^3}{\left(\frac{\mu}{\rho_L}\right)^2} \tag{7-2}$$

where D = particle diameter
ρ_s = particle density
ρ_L = liquid density
μ = dynamic viscosity
g = gravitational constant

If the centerline of the nozzle is located a distance H from the bottom of the vessel, the maximum particle height, z_{max}, is therefore the following:

$$z_{max} = H + \frac{D_0}{2} \tag{7-3}$$

where D_0 = nozzle diameter

The total particle falling time, t, is given by

$$t = \frac{z_{max}}{v_t} \tag{7-4}$$

The total distance travelled, L, from the nozzle exit is determined using the integral equation

$$L = \int_0^t u(z,x)dt = \int_0^t u(z_{max} - v_t t, x)dt \tag{7-5}$$

where u = jet velocity
z = particle elevation
x = longitudinal radial distance from the nozzle exit

The solution of this equation requires knowledge of the fluid jet velocity as a function of location. The fluid jet evolves through two different phases after leaving the jet pump nozzle:

- The fluid leaving the nozzle forms a circular jet that expands until it interacts with the vessel bottom

- The jet transforms into a wall jet that continues to expand along the bottom of the vessel

7.1.1.1 *Circular Jet*

A circular jet emerges from the nozzle with an average velocity U_0 and expands as it travels away from the nozzle. The total momentum exiting the nozzle, M_0, is assumed to be conserved so that at any longitudinal distance x from the nozzle

$$M_0 = \frac{\pi}{4}\rho D_0^2 U_0^2 = \pi\rho \int_0^\infty ru^2(r,x)dr \tag{7-6}$$

where U_0 = average fluid exit velocity at the nozzle

Momentum diffusion causes the jet to expand and the surrounding fluid is entrained to satisfy continuity. As the jet expands, the radial velocity profile broadens and the maximum velocity at the jet centerline, u_m, decreases inversely proportional to the distance x,

$$u_{m0} \propto \frac{1}{x}; \quad \frac{u_m}{U_0} = \frac{C_1}{x/D_0} \tag{7 - 7}$$

The Tollmein solution, developed in Rajaratnam (1976), results in the relative velocity, u/u_m, being expressed as a function of the dimensionless radial distance

$$\varphi = \frac{r}{ax} \tag{7 - 8}$$

where a is an empirically determined coefficient. The maximum velocity for this solution is given by

$$\frac{u_m}{U_0} = \frac{0.965}{ax/(D_0/2)} \tag{7 - 9}$$

The relative velocities are given in Table 2-I of Rajaratnam (1976). Experimental results indicate that values of a are in the range of 0.066 to 0.076. Rajaratnam (1976) provides the suggested expression for maximum velocity as

$$\frac{u_m}{U_0} = \frac{6.3}{x/D_0} \tag{7 - 10}$$

The radial velocity expansion may be expressed by the normal distribution of Weigel (1966) as

$$u_r = u_m e^{-77\left(\frac{r}{x}\right)^2} \tag{7 - 11}$$

7.1.1.2 *Transition*

The transition from the offset jet to a wall jet has been studied by a variety of groups, including Yoon et al. (1995), Gu (1996), Gao and Ewing (2007), Bhuiyan et al. (2011) and Agelin-Chaab and Tachie (2011). A difference between these studies and the DST jet pump geometry is that, for the jet studies, the jet usually enters from a vertical wall that doesn't allow convection under the nozzle, whereas in the DST the nozzle is over open liquid with a jet inlet nearby. For simplification, it is assumed that the effect of this difference will be negligible.

The reattachment length is expressed in terms of the offset height and is relatively insensitive to jet velocity. Examples of plots showing the reattachment length for offset slot jets are Figure 2 in Yoon et al. (1995) and Figs. 6 and 7 in Gu (1996). Fig. 1(a) of Agelin-Chaab and Tachie (2011) provides an example of the reattachment for an offset circular jet. For a circular jet at $H/D_0 = 3$ (feed delivery jet mixer pumps $H = 18$ inches, $D_0 = 6$ inches, see Section 3), the data of Agelin-Chaab and Tachie (2011) indicate that the jet can be described as a circular free jet until $x/D_0 \sim 40$ and a wall jet after $x/D_0 \sim 50$. For the current work, a linear combination of the free and wall jet center-line and z-direction respectively is made for $40 < x/D_0 \le 50$.

7.1.1.3 *Wall Jet*

The circular jet expands until it begins to interact with the vessel bottom, at which point the fluid entrainment pulls the jet down to the wall. The velocity profile of the jet shifts until it is transformed into a wall jet. The characteristics of the wall jet are different from the circular free jet in that the jet expansion rates in the transverse (y-direction) and elevation (z-direction) are different.

There is a substantial body of work considering attaching wall jets from slot jets and square, rectangular and circular bluff jets (e.g., Verhoff 1963, Sforza and Herbst 1970, Rajaratnam 1976, Pani and Dash 1983, Gu 1996). The maximum velocity decreases slightly faster than inversely proportional to the longitudinal distance, as in the circular free jet. The exponent for the velocity decrease with x has been determined from other studies to vary in the range of 1.0-1.29, Law and Herlina (2002). From the circular off-set jet data of Agelin-Chaab and Tachie (2011), the center-line velocity decay can be written as

$$\frac{u_m}{U_0} = 9.6 \left(\frac{x}{D_0}\right)^{-1.185} \tag{7-12}$$

for $H/D_0 \sim 3$. The z-direction velocity profile along the centerline plane can be described by Verhoff's (1963) empirical equation

$$\frac{u_m}{U_0} = 1.48 \left(\frac{z}{z_{m/2}}\right)^{\frac{1}{7}} \left[1 - \text{erf}\left(0.68 \frac{z}{z_{m/2}}\right)\right] \tag{7-13}$$

where $z_{m/2}$ is the velocity half-height. At $H/D_0 \sim 3$ from Agelin-Chaab and Tachie (2011), the velocity half-height can be written as

$$\frac{z_{m/2}}{D_0} = 0.056 \frac{x}{D_0} + 1.024 \tag{7-14}$$

The wall jet creates a wall shear stress that decays inverse to the longitudinal distance squared

$$\tau_{0m} \propto \frac{1}{x^2} \tag{7-15}$$

where the subscript 0 indicates the stress along the center plane (Rajaratnam 1976). Law and Herlina (2002) calculated a skin friction coefficient of 0.01 for circular wall jets, so the wall stress can be written as

$$\frac{\tau_{0m}}{\frac{1}{2}\rho_L u_m^2} = 0.01 = c_f \tag{7-16}$$

This result for a circular wall jet is slightly higher than the generally reported value of 0.0065 for the skin friction coefficient (e.g., Rajaratnam and Pani 1972).

7.1.2   Mixer Pump Jet Model Comparison to Erosion Test Data

Estimates of the feed delivery mixer pump jet performance are compared to representative prototypic and small-scale test results in this section. The comparison is made for the erosion of sediment and particulate as effective cleaning radius (ECR) and the estimated wall stress. The test results include the prototypic scale AZ-101 baseline mixer pump tests (RPP-6548), small-scale tests of the baseline WFD system (SRNL-STI-2011-00278) and the development of ECR models (PNL-10582, PNL-10464 and PNNL-11686). The model results relative to test data for particulate suspension are discussed in Section 7.1.3.

7.1.2.1   *Prototypic Scale Effective Cleaning Radius Tests*

Jet mixer pumps as described in Section 3 were used in the AZ-101 baseline configuration mixer pump test as reported in RPP-6548. As summarized in PNNL-19245, the two 300-hp Lawrence centrifugal mixer pumps located at a tank radius of 22 feet ingested fluid in from approximately 12 inches above the tank bottom and discharged it horizontally from two opposed 6-inch diameter nozzles at nominally 18 inches above the tank bottom (i.e., as the feed delivery mixer pumps, Section 3). Mixer pump 1 was initially operated with the horizontal nozzle discharge at five fixed radial directions through a series of tests, typically incrementally increasing the pump discharge speeds of nominally 725, 1,000 and 1,150 rpm. The pump was operated at each speed for approximately 3 hours. The ECRs for these fixed position operations (which were limited by time of operation, not by reaching a steady state ECR) were approximately 26.4 to 29.4 feet at the completion of the fixed position tests.

Mixer pump 1 was then operated in oscillation mode (horizontal nozzle discharge, 180º pump rotation at 0.05 and 0.2 rpm) at each of the three nominal velocities totaling an operating period of almost 3.5 days. Mixer pumps 1 and 2 subsequently operated at equivalent rates, again ramping up at nominal values of 725, 1,000, and 1,150 rpm over a total operating period of approximately 11 days. The nominal operation rates approximately correspond to 7,100, 9,200, and 10,500 gallons per minute (gpm) total flow, or 12.3, 15.9, and 18.2 m/s for each nozzle (PNNL-18327).

The ECR in AZ-101 for the oscillatory mode mixer pump operations at the three nominal velocities are reported in RPP-6548 and summarized in Table 7-1. The sediment in AZ-101 at the time of the mixer pump operations was approximately 17.5 inches deep at 0.48 UDS mass fraction, and the liquid can be approximated at 1.22 g/mL and 2 cP (PNNL-18327). Three shear strength measurements using a shear vane instrument for AZ-101 sediment samples are 1,500, 1,769, and 4,190 Pa (PNNL-20646). RPP-6548 states "...the ECR for mixer pump 1 is significantly larger than for mixer pump 2...because the material [sediment] closer to mixer pump 1 had been disturbed during [prior] testing, and subsequent remobilization of that material was easier...". As is discussed for the SRNL-STI-2011-00278 small-scale test data below, it may be likely that larger ECRs would have been achieved had the mixer pumps operated at fixed positions for the test duration as opposed to the oscillatory operation. In addition, as with the prior-referenced fixed-direction operations, the ECRs were not determined at a steady-state condition. Rather, the ECRs were instead the observed distance at the end of the mixer pump operation time, and may thus be smaller than a final state.

The maximum velocity at the jet centerline, u_m, can be calculated from Equations 7-10 and 7-11, with the transition from free to all jets made as described in Section 7.1.1. The calculated jet centerline velocity and wall shear stress for the AZ-101 configuration, calculated using Equation 7-16, are shown in Figure 7-1 for $U_0 = 18.2$ m/s. The calculations are for fixed-direction jets. The calculation for the wall stress is started at $x/D_0 \geq 50$ for the wall jet (see Section 7.1.1). Also depicted are the distances from the mixer pump to the farthest vertical vessel wall with two mixer pumps (~ 43.5 ft) and with one mixer pump (~59.5 ft).

The measured relation of nozzle velocity and ECR (RPP-6548) from Table 7-1 is shown in Figure 7-2. Also shown in Figure 7-2 are ECR predictions made via rearrangement of Equation 7-16 with Equation 7-12 to express the radius as a function of the jet parameters and the applied stress. In this approach, it is assumed that the applied stress can be equated to the critical stress for erosion of the bed at the experimentally measured ECR of each test condition. A least squares regression is used to fit the measured ECR to Equation 7-16 where the fit is optimized by adjusting τ_{0m}, thus approximating the critical stress for erosion, τ_c, of the sediment as the wall stress. The rate of erosion is not considered in this approach, so this analysis does not consider whether the estimated critical stress is for surface or mass erosion or complete failure (e.g., see PNNL-18831). Reasonable agreement is achieved between the model and the measured data when a single value of critical stress is applied to the respective data sets. The estimated critical stress for erosion values listed in the figure legend, 6.4 Pa and 9 Pa for mixer pumps 1 and 2 respectively, are in close agreement.

As discussed above, the ECRs were not determined at a steady-state condition, and it may be likely that larger ECRs would have been achieved had the mixer pumps operated at fixed positions as opposed to the oscillatory operation. It may thus be possible that the estimated critical stresses for erosion are larger than the actual value. Comparisons of the estimated critical stress for erosion, calculated values for the sediment particulate, and the measured shear strength of the sediment are made below.

RPP-6548 concluded that by the end of the mixer pump test in AZ-101 that the sediment was mobilized for at least 95% of the area of the tank bottom, and inferred from the data that 100% was mobilized. It is therefore of interest to note from Figure 7-1 that the calculated wall stress at ~43.5 feet ($x/D_0 \sim 87$) is approximately 5.4 Pa. The potentially high estimates of the critical stress for erosion, 6.4 Pa and 9 Pa for mixer pumps 1 and 2 respectively, are thus in close agreement with the observed data that the entire sediment was eroded, (5.4 Pa calculated wall stress at the far wall compared to estimated 6.4 Pa and 9 Pa critical stress for erosion). Thus, these results provide some demonstration that the jet models of Section 7.1.1 are meaningful with respect to the performance of prototypic, scale jet mixers with actual waste.

Table 7-1. AZ-101 ECR and Mixer Pump Operating Conditions

Mixer Pump[a]	Nozzle Velocity (U_0) (m/s)	ECR (m)
Mixer Pump 1	12.3	8.8[b]
Mixer Pump 1	15.9	10.5[b]
Mixer Pump 1	18.2	11.3[b]
Mixer Pump 2[c]	12.3	6.7
Mixer Pump 2[c]	15.9	8.0
Mixer pump 2[c]	18.2	11.4

Notes:
a. RPP-6548 reported ECR data for AZ-101 at mixer pump oscillation rate of 0.05 rpm. Oscillation rates of 0.2 rpm were used in intermediary pump operations (see note b). Operations of 24 hours were conducted at each nozzle velocity.
b. Longer operation of mixer pump 1 as part of the concurrent mixer pump operation extended the ECR to 10.5 m at 12.3 m/s and 11.4 m at 15.9 and 18.2 m/s.
c. Prior and concurrent operation of mixer pump 1. The ECRs of the two mixer pumps overlap. Nozzle velocities of 12.3 m/s for mixer pump 2 could not be exceeded for 60º of the rotation. At higher speeds, mixer pump 2 was rotated manually; fixed orientation for nominally 1 to 2 hours, then manually rotated to the next fixed position, typically 10º from the prior position excepting the 60º at 12.3 m/s (pump speed was turned down for this region).

Figure 7-1. AZ-101 Jet Centerline Nozzle Velocity and Wall Shear Stress ($U_0 = 8.2$ m/s)
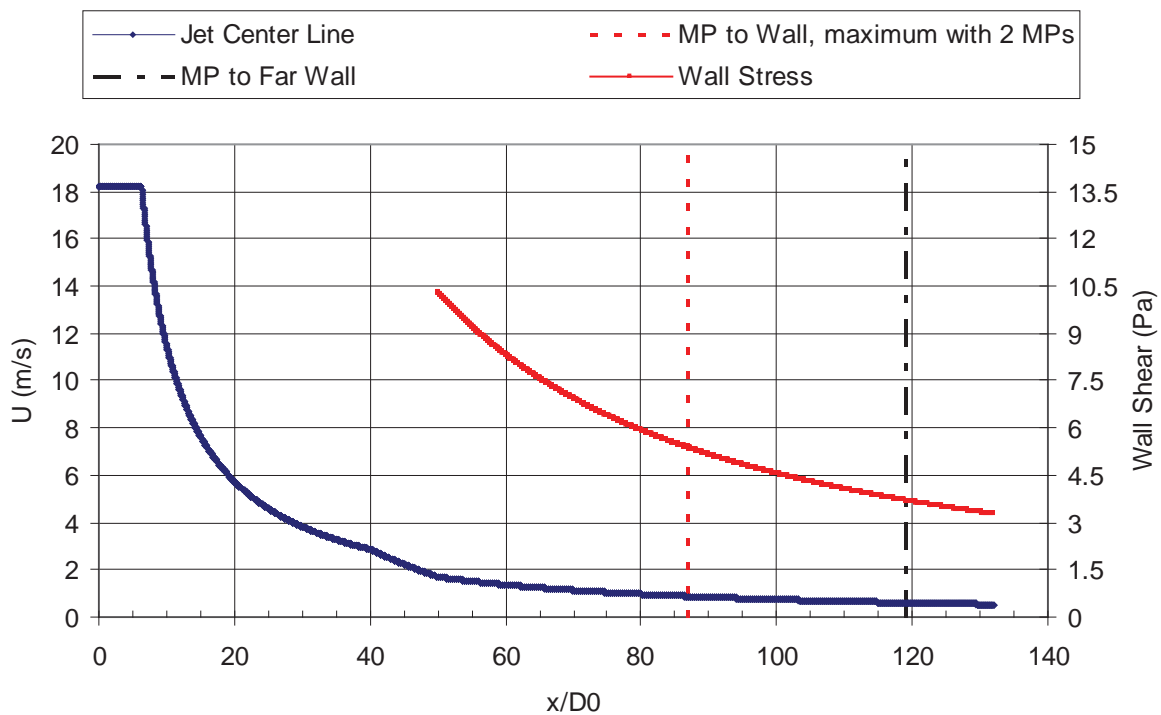
Figure 7-2. AZ-101 ECR as a Function of Nozzle Velocity, Test Data, and Predictions
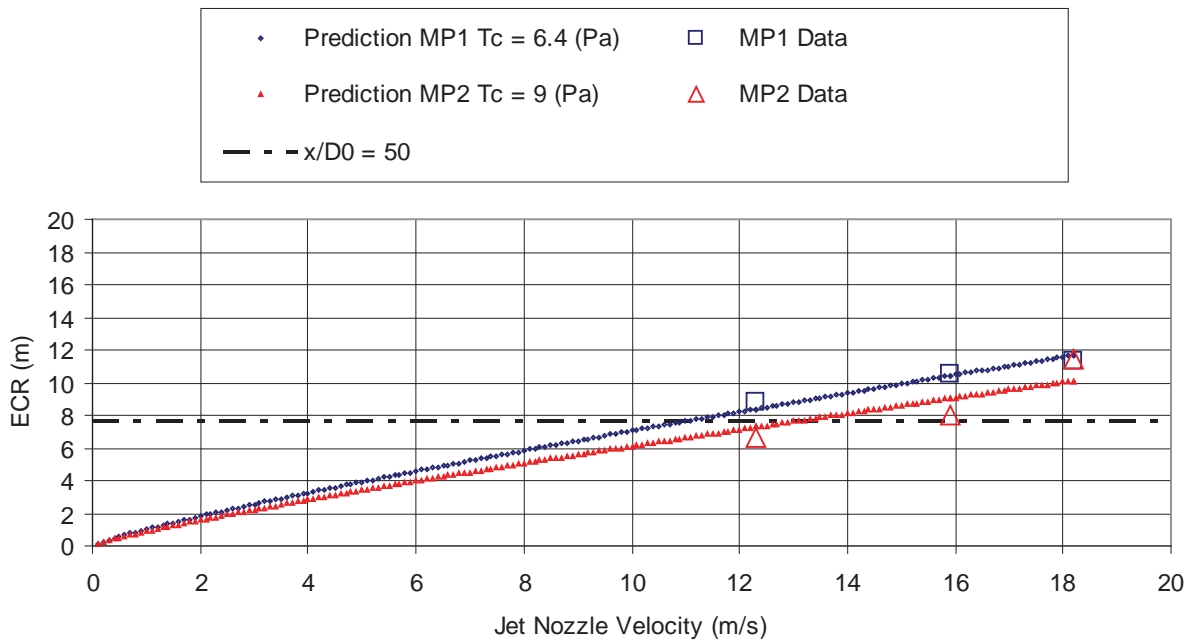
7.1.2.2 *Critical Stress for Erosion of Non-Cohesive Particles*

The Shields diagram (e.g., Vanoni 1975, Julien 1998) provides a relationship for the critical shear stress for erosion, τ_c, for a given particle. For non-cohesive solids (i.e., particles with negligible surface attractive forces, Parker (1984)), the Shields diagram with the shear Reynolds number ($Re*$) greater than approximately 2 determines the critical shear stress. For fine cohesive solids, $Re* < 2$, the Shields Diagram provides a qualitative trend of the critical shear stress, but does not provide specific critical shear stress values. The relation of Paphitis (2001) is presented in Beheshti and Ataie-Ashatiani (2008) as

$$\tau_* = \frac{0.273}{1 + 1.2D_*} + 0.046(1 - 0.576e^{-0.02D_*}) \qquad (7-17)$$

where $D* = Ar^{1/3}$

The Archimedes number (Ar) is given by Equation 7-2 and Equation 7-17 compares well with both the $Re* > 2$ relation from the Shields diagram and data of Mantz (1977) wherein the Shields diagram was extended below $Re* \sim 2$ for fine non-cohesive particles. This comparison is shown in PNNL-20637. As was also shown in PNNL-20637, the range of Ar for Hanford waste particulate in water is bounded by the data used for the Paphitis (2001) model for larger, more dense particulate. The non-dimensional critical shear stress for erosion, τ_*, of Equation 7-17, is related to the dimensional critical stress via the Shields diagram as

$$\tau_* = \frac{\tau_c}{(\rho_s - \rho_l)g d_s} \qquad (7-18)$$

Caution must be taken in applying the critical stress for erosion results for a given particulate directly. PNNL-18831 noted that there does not appear to be tools for predicting sediment erosion without obtaining data for similar or related types of material. Clark and Wynn (2007) compared different methods of determining the critical shear stress for erosion. Jet erosion test results were compared to estimates from the Shields diagram and empirical relations based on parameters of percent clay, plasticity index, particle size, and percent silt-clay. The experimental jet erosion test results were as much as four orders of magnitude greater than calculated results from the Shields diagram and empirical methods, indicating that caution should be taken in applying a model outside of the specific study area used to develop the model.

The estimated (via the Section 7.1.1 jet models as previously described for AZ-101) and calculated critical stress for erosion (via Equations 7-2, 7-17, and 7-18) are compared for the small-scale tests of the baseline WFD system of SRNL-STI-2011-00278. In that work, scoping tests were performed to determine the magnitude of the impact of non-Newtonian fluid rheology on mixing in a 40.5-inch diameter test vessel. That vessel was geometrically scaled to be similar to the prototypic AY-102 tank with two rotating horizontal-opposed-jet mixer pumps. These tests demonstrated that the batch transfer of settling particles (stainless steel (SS), 8 g/mL, median particle size $d_{50} = 106$ μm) in water transferred a lower quantity of solids when compared to similar tests in a non-Newtonian yield stress fluid. As shown in Figure 7-3 and Figure 7-4, ECRs were measured for the SS in water (1 g/mL, 1 cP) and a water/glycerin solution (1.13 g/mL, 6.2 cP). As for the AZ-101 data, reasonable agreement is achieved between the jet model and the measured data when a single value of critical stress is applied to the respective data sets (Figures 7-3 and 7-4 from SRNL-STI-2011-00278), and the estimated critical stress for erosion values are listed in the figure legends as 1.8 Pa and 2.8 Pa respectively. In water, the calculated critical stress for erosion of the SS is ~ 0.50 Pa, while in glycerol it is ~ 0.90 Pa.

**Figure 7-3. ECR as a Function of Nozzle Velocity, Stainless Steel in Water,
Test Data, and Predictions**
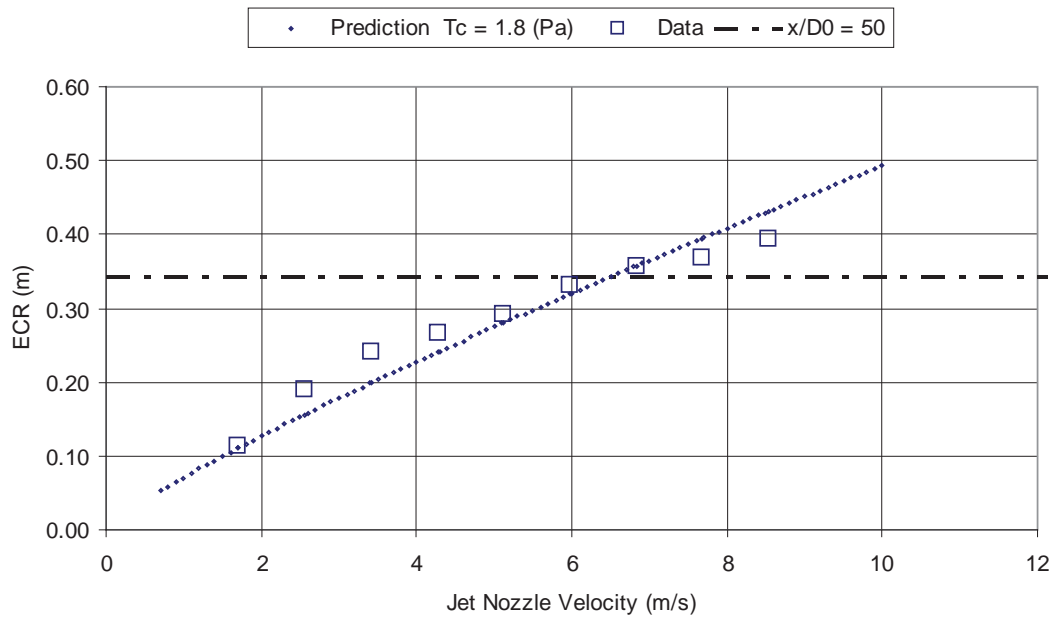
**Figure 7-4. ECR as a Function of Nozzle Velocity, Stainless Steel in Glycerol,
Test Data, and Predictions**
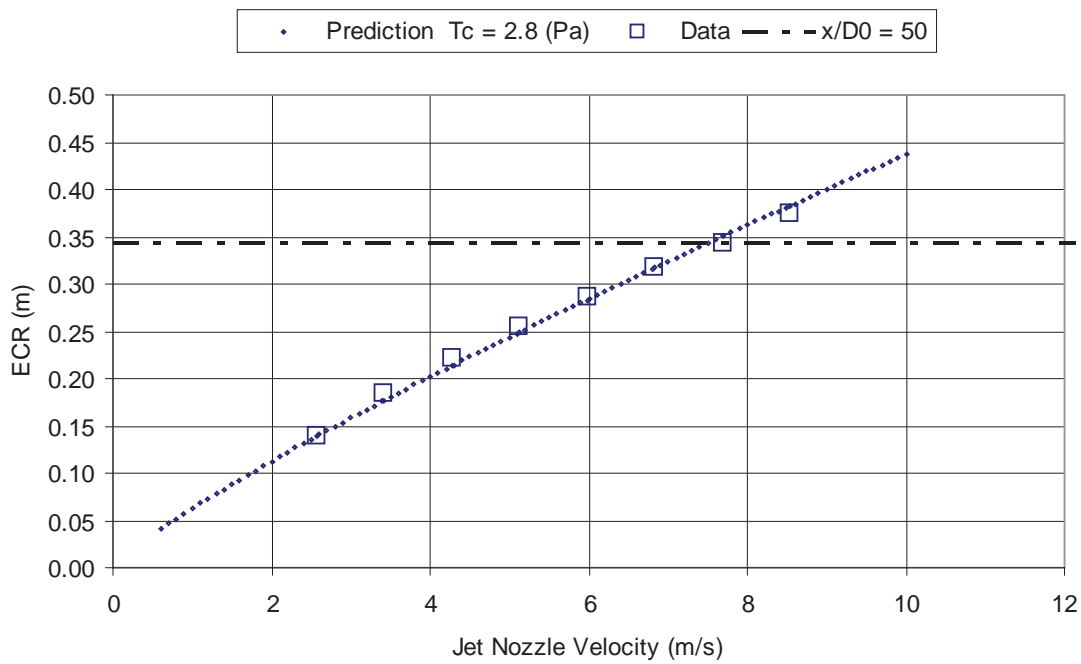
The ratios of the estimated and calculated critical stress for erosion for the small-scale tests (SRNL-STI-2011-00278) are approximately 3.8 and 3.1 with water and glycerol, respectively. This result compares favorably with that achieved for AZ-101 of 1.9 to 2.7, which had a calculated τ_c of approximately 3.3 Pa for a potential maximum size and density particle in AZ-101, 7.143 g/mL and 1441 µm (Table 4-9). However, as noted for AZ-101, the small-scale test ECR data were also likely impacted by the rotation of the jet mixers. For the SS in glycerol, SRNL-STI-2011-00278 found that the steady-state ECR could be increased by over 100% if the jet is operated at a fixed direction as opposed to rotating. The ratio of the estimated and calculated critical stress for erosion for the tests of Figure 7-3 and Figure 7-4 with the ECRs increased by 100% decreases to 0.74 to 0.60. Based on this comparison and that shown below for the erosion of cohesive sediment, it will be assumed for Section 7.1.3 that the calculated critical stress for erosion of a particle can be compared directly to the calculated applied stress of the jet.

7.1.2.3 *Cohesive Sediment Erosion*

The estimated (via the Section 7.1.1 jet models as previously described for AZ-101) critical stress for erosion and the measured shear strength of the sediment are compared with respect to the ECR model of PNL-10464. The model was developed to predict the ECR of horizontal jet mixer pumps in the Hanford tanks and is given by

$$ECR = 4.0 \, U_0 D_0 \tau_s^{-0.46} \tag{7 - 19}$$

where τ_s = shear strength of the sediment

Centimeter-gram-seconds units must be used in this model (ECR in cm, D_0 in cm, τ_s in dynes/cm^2, and U_0 in cm/s). The Equation 7-19 predicted ECR for the AZ-101 conditions and a median measured sediment shear strength of 1,769 Pa (as above, PNNL-20646) is shown in Figure 7-5 together with the jet model estimated ECR with an estimated critical stress value of 6.4 Pa. The result at 18.2 m/s is again consistent with the conclusion of RPP-6548 that at least 95% of the area of the tank bottom of the AZ-101 sediment was mobilized (with two mixer pumps, farthest distance to wall is ~ 43.5 feet, Section 7.1.2.1). The ratio of the estimated critical stress for erosion to the measured sediment shear strength is nominally 280. This ratio compares quite favorably with that of the estimated critical stress for the actual AZ-101 ECR data described above, which results in an average of nominally 240 to the same median shear strength (average of 1,769/6.4 and 1,769/9). The agreement of the PNL-10464 model results and the AZ-101 test data concurs with the conclusion of PNNL-19245 regarding these data and the agreement with the Section 7.1.1 model approach supports using that model.

The presented comparisons of ECRs predicted via the jet models described in Section 7.1.1 to prototypic and scaled data support the use of these models in predicting the limits of performance of the current baseline mixing system with respect to the UDS particle size and density.

Figure 7-5. Cohesive Sediment ECR as a Function of Nozzle Velocity
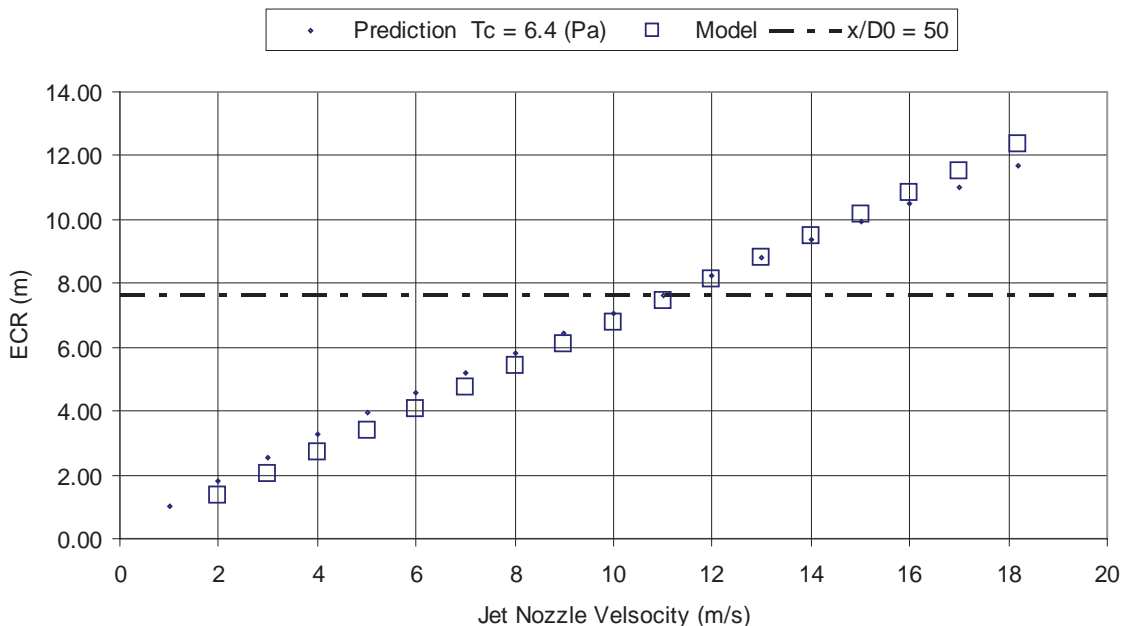
7.1.3 Estimates of the Limiting Particles, Jet Mixer Pump

This section evaluates the capability of the Hanford DST baseline mixing system (which employs two jet mixer pumps to mix and mobilize the waste as described earlier) to transfer large-dense particulate. The limits of performance of the jet mixer pumps to mobilize and transport UDS particulate such that it can be ingested into the transfer line are evaluated using the models presented in Section 7.1.1 which were shown to be meaningful with respect to ECR test data in Section 7.1.2.

The case in which the largest, most dense particle is available for transfer is of interest. As such, the probability that the limiting particle is available (with respect to actual waste concentration, initial particle location in the vessel, etc.) is not evaluated. The limiting case wherein a particle enters the jet pump inlet and is ejected towards the transfer pump inlet was described in Section 7.1.1 to have two elements: (1) The longitudinal distance traveled as a suspended particle based on the velocity distribution of the jet and the terminal falling velocity of the particle, and (2) the transport along the bottom of the vessel based on the wall shear stress generated by the jet.

As an example of element (1), the calculated velocity and trajectory of a gibbsite particle with a 700-μm diameter and 2.42-g/mL density are shown in Figures 7-6 and 7-7, respectively. This particle example is chosen so that the model predictions can be compared to the on the available process data for AZ-101 as described below. The nozzle velocity is 18.2 m/s, and the suspending fluid is water at 1 g/mL and 1 cP.

Figure 7-6. Calculated Particle Velocity Example
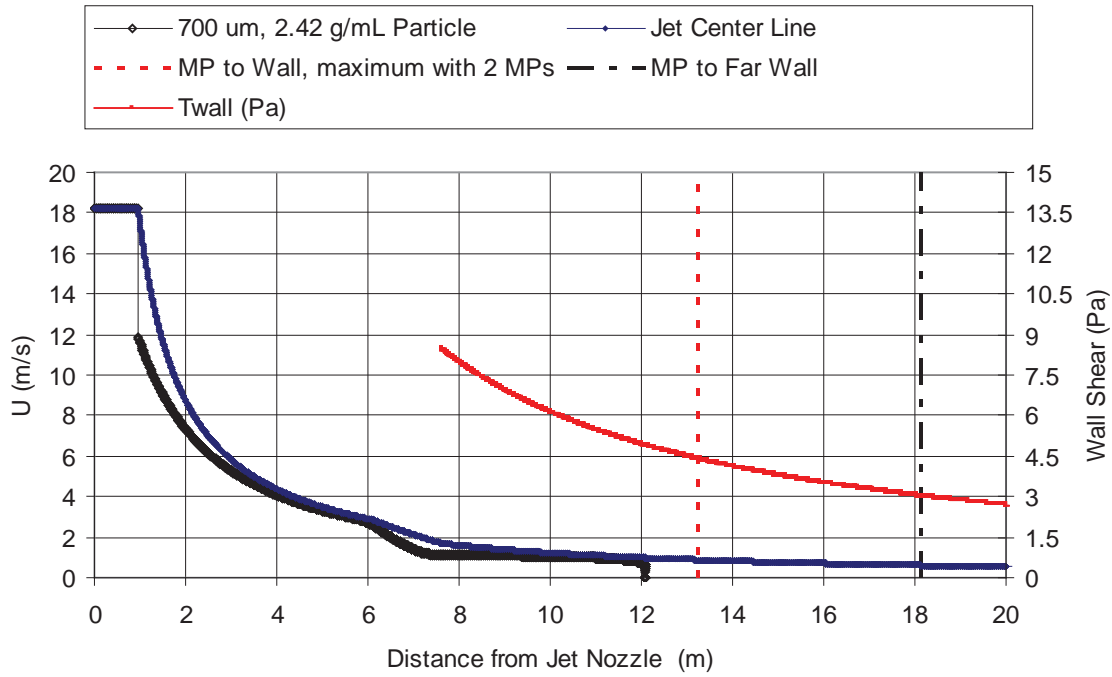
Figure 7-7. Calculated Particle Trajectory Example
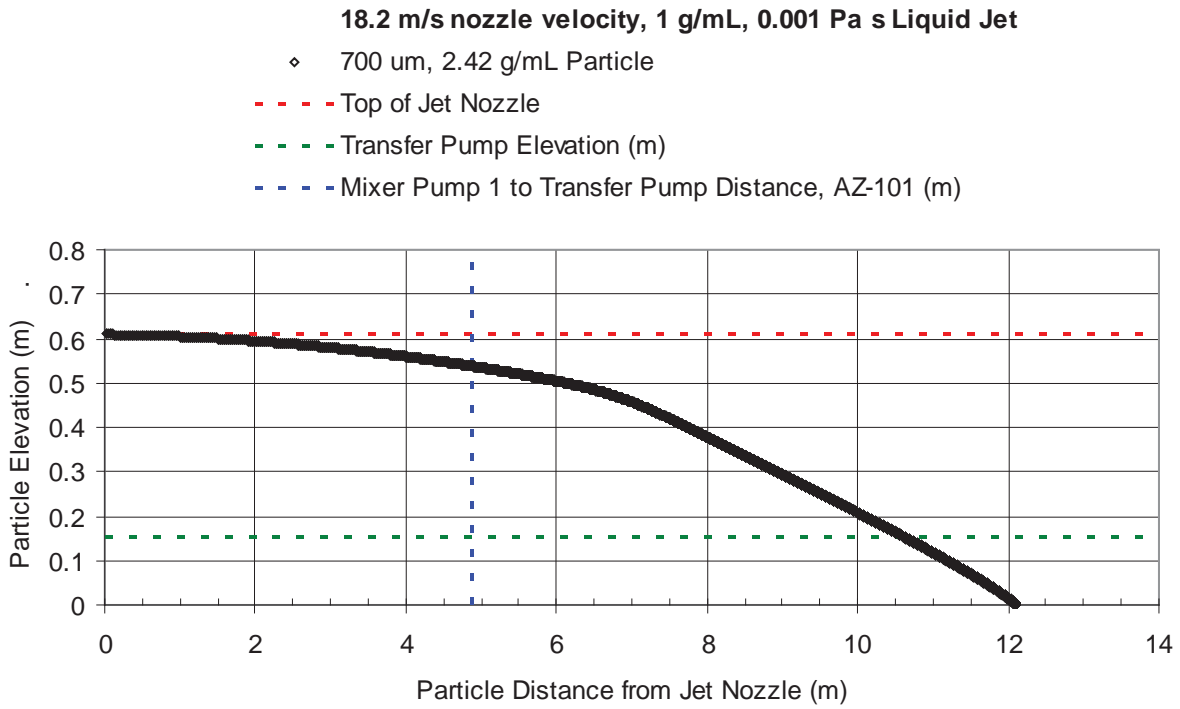
Also shown in Figure 7-6 (as in Figure 7-1) are the calculated jet centerline velocity, and wall shear stress. The distances from the mixer pump to the farthest vertical vessel wall with two mixer pumps (22-feet mixer pump radius to 90° wall off center-line - 37.5 tank radius, or approximately 43.5 feet) and with one mixer pump (22-feet mixer pump radius plus 37.5 tank radius) are also depicted. Figure 7-6 shows that the calculated particle velocity departs from the centerline velocity after the jet potential core and then rapidly decreases as the particle approaches the vessel floor at approximately 12.1 m. Because the calculated critical stress for erosion, 0.39 Pa (from Equations 7-2, 7-17, and 7-18) is less than the calculated wall stress to the farthest vessel wall, 4.4 Pa, the example particle is predicted to be mobilized regardless of its location in the vessel, and, if not suspended, will at least be mobilized along the vessel bottom.

The calculated trajectory of the example particle is shown in Figure 7-7. In AZ-101, the minimum radial distance from mixer pump 1 to the transfer pump is ~16 feet (Hanford Drawing H-14-010507 Rev. 0, Sheet 1 of 2. Mixer pump 1 is at a 22-feet radius, 180°, the transfer pump is at 6-feet radius, 180°). At the transfer pump inlet distance from the mixer pump of approximately 4.9 m, the particle is at an elevation of ~ 0.54 m, well above the transfer line inlet height of 0.1524 m (6 inches, see Section 3). It may therefore be assumed that the example particle of 2.42 g/mL and 700 μm can be available for ingestion into the transfer pump via the jet mixer pumps operated at a nozzle velocity of 18.2 m/s in water.

As summarized in RPP-PLAN-51625, it was concluded in PNNL-20637 that previous testing has shown that the batch transfer of settling SS particles in a slurry of dense salt solution and fine gibbsite particles was more effective than batch transfers of identical SS particles when the suspending fluid was water or glycerol/water solutions. Analysis via a simple model including the suspending-fluid density and viscosity gives the correct qualitative effect of the ECR increasing with increasing suspending-fluid density and decreasing with increasing viscosity. However, the analysis does not give good quantitative predictions based on the limited data. The PNNL-20637 summary of available data shows that a change in fluid properties, such as increased viscosity that decreases the ECR, may still increase the amount of settling particles transferred. The predicted ECR is higher in water, but the increased density and/or viscosity of the other fluids improves the overall suspension and transfer of particles. Thus, higher liquid density and viscosity are expected to increase the performance of the WFD system for transferring rapidly settling particles to the WTP.

The example particle (2.42 g/mL, 700 μm) is therefore considered for two cases of increased liquid properties. The first case considered is for the AZ-101 liquid, 1.22 g/mL, 2 cP (Section 7.1.2). The calculated particle elevation is ~ 0.56 m at the AZ-101 transfer pump inlet radius from mixer pump 1, further above the transfer line inlet height in comparison to water. The calculated critical stress for erosion, 0.37 Pa, is again less than the calculated wall stress at the farthest vessel wall, 5.3 Pa. This estimate of the particle elevation relative to the transfer pump inlet height is compared to AZ-101 process data for particle size and elevation to evaluate the model results relative to process data.

PNNL-19245 summarized test sequences conducted in AZ-101 to evaluate UDS suspension as a function of pump operation as reported in RPP-6548. In an initial sequence, both mixer pumps were simultaneously operated in oscillatory mode for 19 hours at nozzle velocities of

approximately 12.3, 15.9 and 18.2 m/s. The operating time of 19 hours was selected because it represents the time required to transfer approximately 160,000 gallons of HLW at a nominal flow rate of 530 L/min (140 gpm). A second test sequence was similar except that only mixer pump 1 was operated. Gamma profiles and Suspended Solids Profiler (SSP) readings were taken after the mixer pumps were shut off at the end of the 19-hour period. A gamma profile is produced by the gamma-monitoring system which detects radionuclides and the SSP uses light reflectance to determine turbidity. Both instruments can therefore be used to evaluate UDS concentration.

The SSP data collected nominally 40 minutes after cessation of mixing were qualitatively examined in RPP-6548 to determine the effect of pump operation on UDS suspension quantities and profile. Each SSP profile required 6 to 12 minutes to traverse from 33 to 300 inches above the tank bottom. RPP-6548 notes that the UDS concentration profiles throughout the range of pump operation are relatively similar in that the suspended UDS is uniformly distributed with the exception of reduced concentrations in the top 2 to 3 ft of the measurement range. More UDS appears to be suspended at higher pump speeds and with both mixer pumps operating. It is emphasized that the SSP data can only be used as relative values for comparison between different test conditions due to lack of instrument calibration. RPP-6548 notes that the estimated mass of UDS suspended determined from the SSP data appears to be consistent with that based on grab sample data for concurrent pump operation at maximum speed.

As reported in PNNL-18327 from analysis of the gamma data, only 32% of the UDS waste inventory was uniformly suspended above 38 inches at concurrent pump operation at maximum speed. PSDs of the UDS in grab samples taken at specific elevations and times during the time immediately following the final operation of the mixer pumps (the "settling test," RPP-6548) are reported in HNF-6062. It is noted in HNF-6062 that at the time of the particle size analysis, the samples had evaporated to dryness and were stored in that condition for an extended period. It is further noted that the particle size "...results should be treated as suspect as related to their representation of the PSDs of the originally sampled materials."

HNF-7078 provides PSDs of AZ-101 composite samples that were kept in a hydrated condition. The same PSD instrumentation and configuration thereof was used in both the HNF-6062 and HNF-7078 analyses. The samples in HNF-7078 analyzed for PSD were separated via laboratory scale gravity settling tests into slowest, intermediate, and fastest settling particulate by sampling from the top, middle, and bottom of the settled sediment. As concluded with respect to this data and other comparisons in PNNL-20646, Figure 7-8 illustrates that there is no conclusive evidence in the PSD results that the evaporation and rehydration of the samples impacted the PSD results.

Figure 7-8. AZ-101 PSD Comparison between Mixer Pump Test Re-Hydrated Grab Samples (HNF-6062) and Core Composite (HNF-7078)
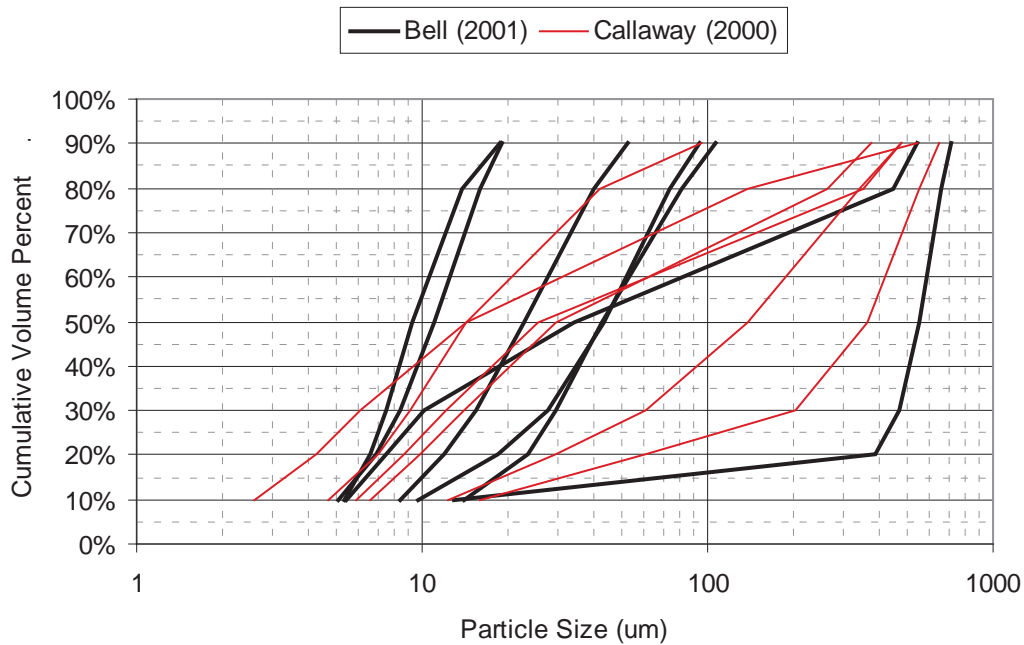
Although there is a lack of expected PSD trend results with settling for the HNF-7078 data in Figure 7-9,[13] the HNF-6062 data in Figure 7-10 are generally shown to be more plausible within the fraction of UDS waste inventory that was uniformly suspended above 38 inches. For the data of HNF-6062, the material suspended higher in the vessel (48 through 216 inches) is smaller, while the material initially near the tank bottom (6 inches) at 11 minutes after mixer pump operation is larger. Almost 25 hours after operation of the mixer pump, the 6-inch elevation sample PSD shows the contribution of the smaller, suspended particulate settling.[14]

---

[13] From Equation 7-1, it is reasonable to expect that faster settling particulate is comprised of larger particles. For the primary test, the intermediate settling particulate is shown to have the largest PSD, while for the duplicate test, the slowest settling particulate is shown to have the largest PSD.

[14] The solid-liquid interface data of RPP-6548 shows the suspended solids settling from at most 300 in to about 28 inches in approximately 2 days, PNNL-17707.

Figure 7-9. AZ-101 PSDs (HNF-7078)
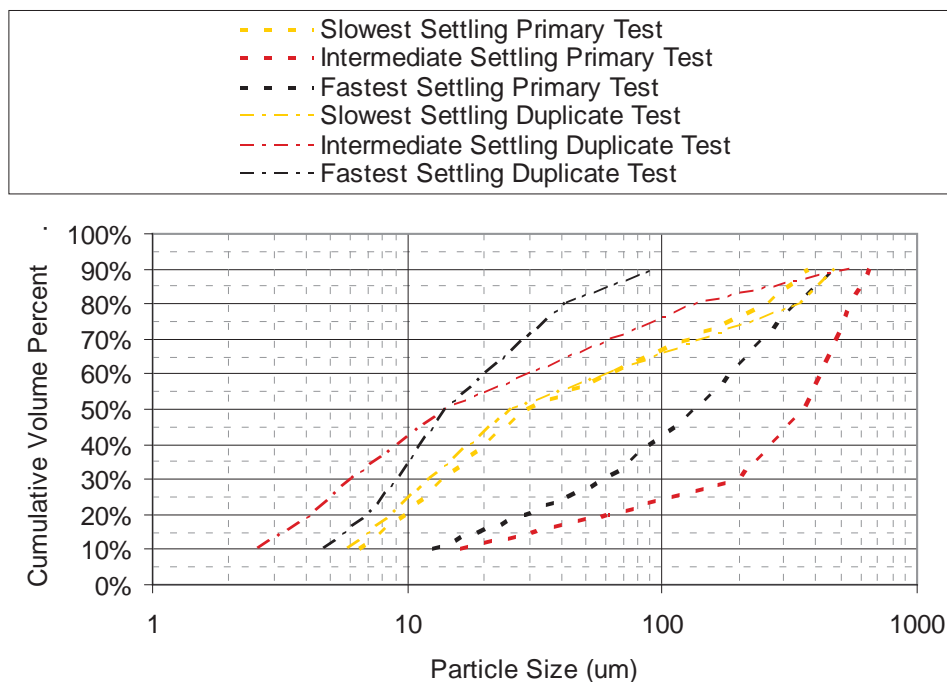
It can be argued that the mixer pump operation in AZ-101 resulted in (1) particulate of at least 100 μm being suspended to an elevation of 216 inches (i.e., 90th percentile of the 216-inch data, maximum size likely larger, Figure 7-10), and (2) particulate of at least 700 μm being at the elevation of 6 inches (90th percentile of the 6-inch data, maximum size likely larger, Figure 7-10). As described in Section 7.1.2, 100% of the sediment was mobilized. From PNNL-20646, the most predominate UDS phase in AZ-101 is gibbsite.

The data for composition of the centrifuged solids reported by HNF-6062 (data also briefly summarized in RPP-6548) showed only minor differences between grab samples taken at elevations of 6, 48, and 132 inches. Those results suggest that the particles suspended into the upper region had a similar composition to the larger particles that remained in the lower region. Therefore, the calculated result that a gibbsite particle (2.42 g/mL) of 700 μm could be present at or above the transfer line inlet (previously referenced calculated elevation is ~ 0.56 m) is not inconsistent with the prototypic test data (700 μm particle could be present up to 48 inches, the next higher elevation grab sample, Figure 7-10)[15].

---

[15] The RPP-6548 data is shown in PNNL-18327 to indicate that there was uniform suspension of solids above 38 inches. Thus, the 6 in. grab sample could be representative of material up to 38 inches.

Figure 7-10. AZ-101 PSDs (HNF-6062)
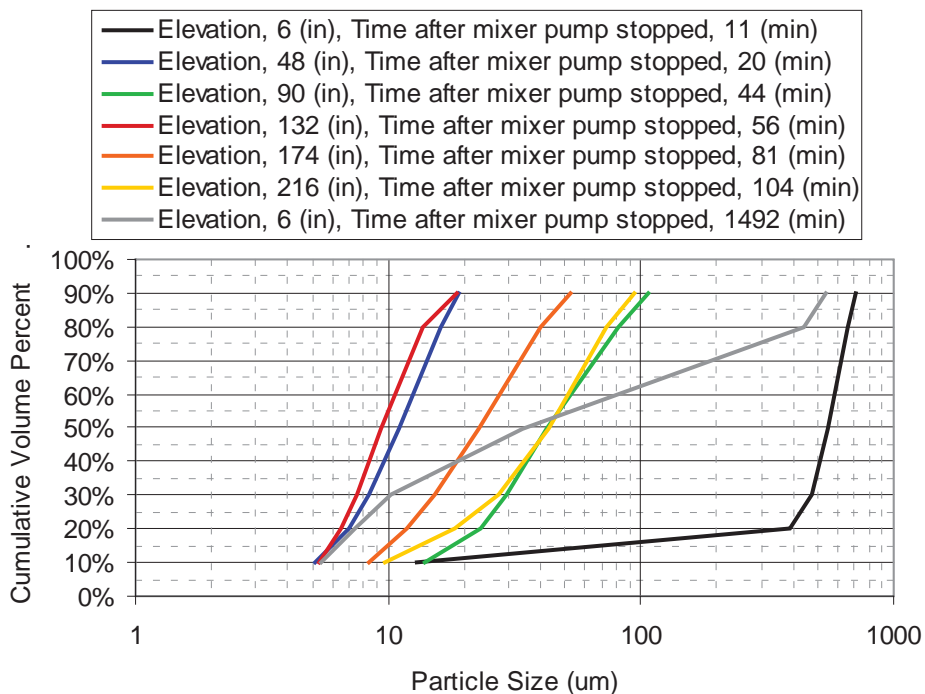
The second case of increased liquid properties considered is a representative upper limit of density and viscosity for the liquid feed to WTP. From Section 5, the maximum liquid density and viscosity for the HTWOS prior to end-of-mission activities data are 1.37 g/mL (Table 5-4, without uncertainties) and 14 cP (Table 5-7, viscosity for the 1.37 g/mL liquid with uncertainties) respectively.[16] The calculated elevation for a 700 μm, 2.42 g/mL particle is ~ 0.6 m at the AZ-101 minimum transfer pump inlet distance from the mixer pump and the calculated critical stress for erosion is 0.60 Pa (the jet has a 6 Pa calculated wall stress at the farthest vessel wall). The example particle is at a higher elevation at each increasing density and viscosity liquid case evaluated: (1) water at 1 g/mL and 1 cP, (2) AZ-101 liquid at 1.22 g/mL and 2 cP, and (3) the representative upper-limit liquid, 1.37 g/mL and 14 cP. The selected representative upper-limit liquid will therefore be used to evaluate the limits of performance of the jet mixer pumps to mobilize and transport UDS particulate relative to the potential limiting waste particles listed in Table 4-9.

The designated HLW commissioning feed tank is AY-102, Section 3. As listed in Table 3-2, the average jet nozzle velocity for the feed vessel mixer pumps is 59 ft/s (~18 m/s). In AY-102, the minimum radial distance from mixer pump 1 to the transfer pump is ~22.8 feet (Hanford Drawings H-14-109549 Rev. B, Sheet 1 of 1 and H-2-64447 Rev. 7. Mixer pumps are at 22-feet radius, 0º and 180º, the transfer pump is at 6-feet radius, 90º). The size and density limit for particles to be at the transfer line inlet elevation [0.1524 m, (6 inches) from Section 3] at the

---

[16] It is subsequently discussed why the WFD system capability with the liquid density with uncertainty (and associated liquid viscosity) is not evaluated.

radial distance to the transfer pump inlet (~6.95 m, AY-102, see above) upon ejection from the top of the mixer pump jet nozzle in the upper-limit liquid at 18 m/s is shown in Figure 7-11. Any particle that has a size and density pair at or below the calculated line in Figure 7-11, which corresponds to a constant particle settling velocity of ~ 0.27 m/s (Equation 7-1) in the representative upper-limit liquid, can be assumed to be available for ingestion into the transfer line inlet. Ingestion of particulate into the transfer pump inlet is considered further in Section 7-2.

At the maximum particle density of 19 g/mL (from Section 4), the limiting particle size is ~ 1,110 μm (Figure 7-11). This particle size is more than one order of magnitude larger than the estimated particle size for that density, 100 μm, from Table 4-10. The inlet height limit also shown to exceed the potential maximum size and density particles from AZ-101 and AY-102 from Table 4-9. At the limiting particle size of 9,525 μm (from Section 4), the calculated, inlet-height-limiting particle density (from Figure 7-11) is ~ 2.1 g/mL. This particle density is more than the estimated potential density of ~ 1.6 g/mL for an agglomerate of gibbsite having the same size in 1.37 g/mL liquid, as listed in Table 4-9.

Therefore, the potential limiting waste particles of Table 4-9 are exceeded by the calculated limits of performance of the jet mixer pumps to mobilize and transport UDS particulate such that it can be ingested into the transfer line (in the representative, upper-limit liquid of 1.37 g/mL, 14 cP). Given that higher liquid density and viscosity are expected to increase the performance of the WFD system for transferring rapidly settling particles to the WTP as described previously, liquid properties exceeding this representative upper limit (i.e., the maximum liquid density for the TWOS prior to end-of-mission activities with uncertainty, 1.47 g/mL, Table 5-4, and associated viscosity) are thus not evaluated. Some of the feed vessels (Figure 3-1) have shorter distances between the mixer pump and transfer pump (e.g., AZ-101, as specified previously) which would also increase the performance of the WFD system for transferring rapidly settling particles to the WTP, but this will also not be evaluated further.

Figure 7-11. Calculated Particle Size and Density Limits at Transfer Pump Inlet
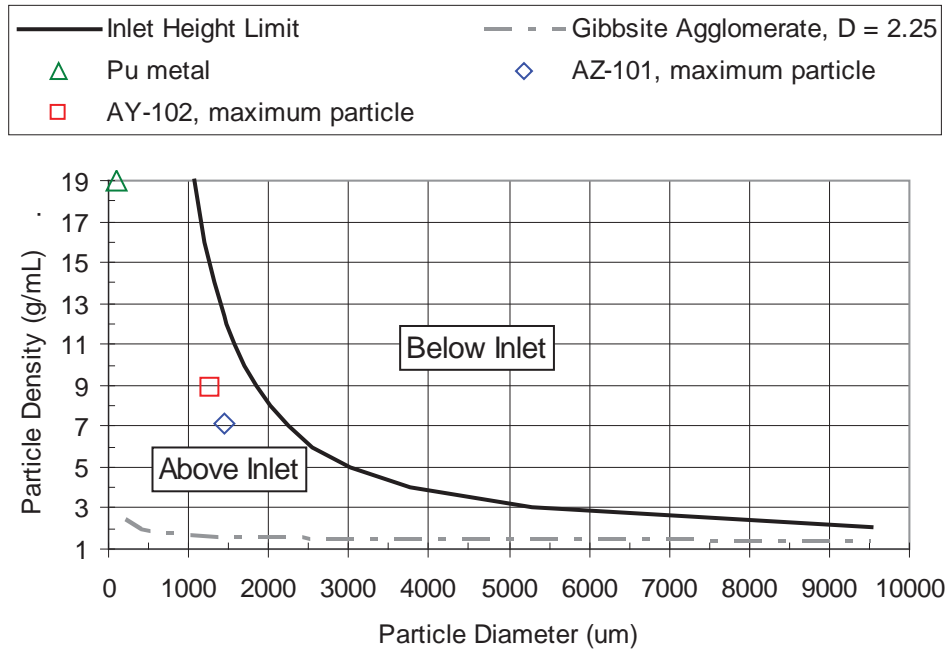
Mobilization of denser particles at a given size (than indicated in Figure 7-11) along the vessel bottom is considered by comparing the jet wall stress to the calculated particle critical stress for erosion (critical stress for erosion via Equations 7-2, 7-17, and 7-18). As described in Section 7.1.1, Equation 7-16 provides an expression for the wall stress from a wall jet after the attachment point of $x/D_0 = 50$ (~ 7.62 m, transfer line distance is ~ 6.95 m), which is the point of maximum stress for the wall jet, e.g., see Figure 7-1. Comparing the calculated maximum wall stress to the critical stress for erosion in Figure 7-12 shows that larger, denser particles than for the inlet height limit can likely be mobilized by the wall jet.

Figure 7-12. Calculated Particle Size and Density Limits for Mobilization via Wall Jet
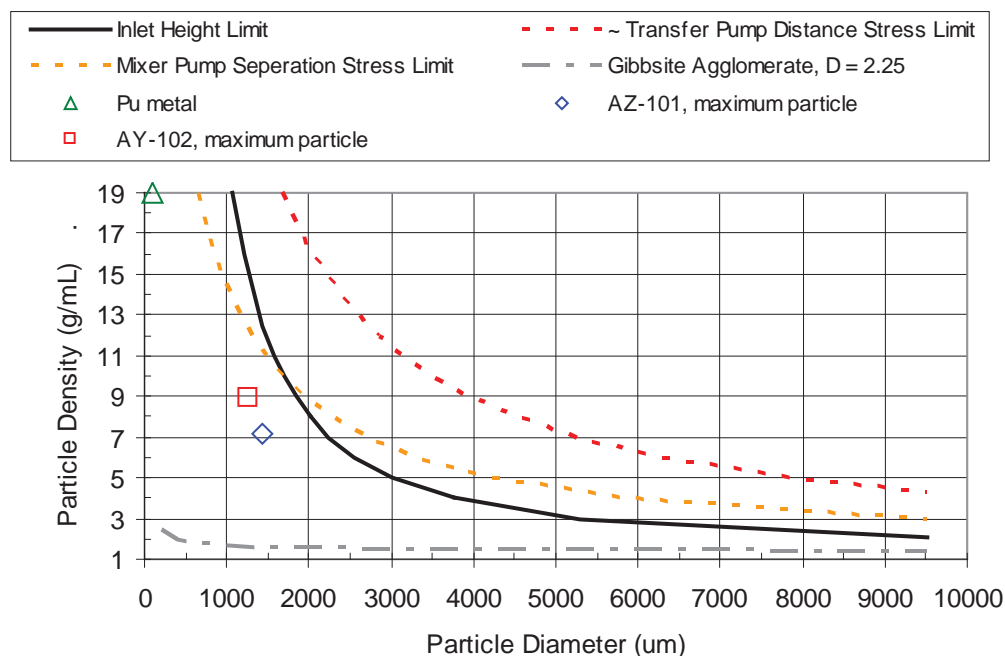
The mobilization of particles by one mixer pump at the radial location of the other mixer pump, 44 feet (~ 13.41 m, x/D_0 ~ 88), can be considered similarly. As shown in Figure 7-12, the mixer pump separation limit exceeds the potential limiting waste particles and exceeds the inlet height limit above ~ 9.85 g/mL and 1,710 μm.

7.1.3.1 *Non-Newtonian Yield Stress Fluid Effect*

The effect of a non-Newtonian yield stress fluid on the calculated limits of performance of the jet mixer pumps to mobilize and transport UDS particulate presented in Figures 7-11 and 7-12 is considered. RPP-PLAN-51625 described that the evaluation of PNNL-19245 showed that cohesive particle interaction will have multiple effects on UDS uniformity and mobilization during jet mixing through a number of different mechanisms. Scoping tests to determine the magnitude of the impact caused by cohesive particle interactions and hence non-Newtonian yield stress fluid rheology, on mixing were subsequently performed under the Small-Scale Mixing Demonstration (SSMD) program and are reported in SRNL-STI-2011-00278.

SRNL-STI-2011-00278 concluded that increasing the slurry yield stress tended to decrease in the ECR but the total transfer of settling particles increased with increasing yield stress. For jet mixing of non-Newtonian yield stress slurries, it is apparently more difficult to suspend particles from the tank bottom with increasing yield stress, but the particles stay suspended to a greater degree once lifted from the tank bottom. The combined effect of increasing the yield stress for the conditions tested is then an increase in the transfer of the settling particles.

It can thus be inferred that the calculated particle size and density limits of performance (in Figure 7-11 and Figure 7-12) may increase if the jet fluid is changed from a Newtonian fluid to one of the non-Newtonian yield-stress fluids described in Section 6.0. This inference presumes

that the yield stress does not prohibitively impact the ECR. SRNL-STI-2011-00278 considered the competing effects of particle settling and ECR via the yield Reynolds number and the critical gravity number. The yield Reynolds number is written as

$$Re_\tau = \frac{\rho U_0}{\tau} \qquad\qquad (7-20)$$

which has been used to quantify the size of a cavern (e.g., PNWD-3551), the region where the jet causes fluid (density ρ) motion, but outside of which the fluid remains quiescent due to the fluid yield stress in shear (τ) and the gravity yield parameter is defined by:

$$Y_G = \frac{\tau}{gd(\rho_s - \rho_L)} \qquad\qquad (7-21)$$

Equation 7-21 is a measure of the relative magnitudes of the yield stress in shear and gravitational effects and can be used to express the initiation or cessation of the motion of spherical particles in a quiescent yield stress fluid (Chhabra 1993).

From Equations 7-20 and 7-21, as the yield stress of the fluid is increased, the cavern size is reduced and the likelihood of a particle remaining suspended is increased. Limiting values for Re_τ and Y_G are material dependent, and thus the specific "optimum" yield stress (as in defining the maximum limiting particle) for Hanford waste is currently indeterminate. Given that the calculated limits of performance in a Newtonian fluid jet exceed the potential limiting waste particles (Figure 7-11 and Figure 7-12), quantification of an optimum yield stress is not pursued herein.

7.2 TRANSFER PUMP CAPABILITIES

Transfer pumps are utilized to transfer the waste mobilized by the jet mixers out of the DST and through a pipeline to the WTP. This section evaluates the limits of performance of the current baseline transfer system with respect to the UDS particle size and density. The mechanisms whereby the transfer pumps can ingest UDS particulate and transport that particulate up and out of the tank are described. As with the evaluation of the mixer pump capability in Section 7.1, the probability that the limiting particle is available (with respect to actual waste concentration, initial particle location in the vessel, etc.) is not evaluated.

The models describing the flow at the transfer pump inlet and vertical leg of the transfer pipeline are discussed in Section 7.2.1. Results of this modeling approach are briefly compared to prototypic results in Section 7.2.2. The models are applied to estimate the limiting particles in Section 7.2.3.

7.2.1 Transfer Pump Model

Calculations for the flow at the transfer pump inlet and vertical leg of the transfer line are described. Ingestion at the transfer line inlet is considered via the flow around the inlet and the tank bottom wall stress generated by that flow. The flow in the vertical leg of the transfer line is considered relative to the limiting particles.

7.2.1.1 *Inlet*

Particles are transported to the vessel bottom region near the transfer line inlet through a combination of longitudinal distance travelled as a suspended particle and transport along the bottom of the vessel based on the wall shear stress generated by the jet pump, as described in Section 7.1.3. The velocity field in the vessel formed by the flow into the transfer line inlet can ingest a particle. A literature search was performed for the flow distribution around an offset vertical pipe intake and no analytical solutions were found.

The ParaFlow computer program (PNNL-20637) was used to simulate the flow field surrounding the transfer line inlet. While not a validated model, Paraflow can be used to indicate flow patterns around the pump inlet. The ParaFlow program has been applied to a variety of multiphase processing systems, including slurry pipelines, ultrafiltration, pulsejet mixing and jet pump tank mixing (Rector et al. 2009, Rector and Stewart 2010). Based on Section 3.0, the transfer line inlet was assumed 2.25- inch diameter, the transfer line exterior was 3-inch diameter, the offset from the tank bottom was 6 inches, and the transfer line flow rate was 140 gpm. The transfer line is centered in a cylindrical domain over 6 feet in diameter with side and top boundary conditions that allow the bounding pressure and velocities to adjust to the domain flow field, resulting in an approximation of a semi-infinite domain. A RANS k-ε turbulence model was used.

7.2.1.2 *Vertical Transfer Leg*

The vertical pipeline downstream of the pump is assumed connected directly to the pump inlet. No consideration is given to the pump internals or any size reduction that may occur due to passage through the pump's rotor/stator. The modeling of the particle transfer assumes the vertical section of pipe is long enough for fully developed flow to be established. The evaluation considers single particles with no consideration made to the effects of solids concentration. The effects of concentration relative to the modeling of a single particle are accounted for by changes in the viscosity of the carrier fluid.

The modeling is based on a force balance for a solid spherical particle with no rotation of diameter d_s suspended in flow. The forces acting on the particle are the following:

- weight of the particle F_{Wt}
- particle buoyancy F_B
- drag force on the particle created by the flow field F_D

For steady state, fully developed conditions, the sum of the forces equals zero. Figure 7-13 provides a schematic of the solid sphere under consideration. The average velocity of the

surrounding fluid is U and the velocity of the sphere is V. If the positive direction is assumed upward then

$$F_D + F_B - F_{Wt} = 0 \qquad (7-22)$$

$$F_{Wt} = \frac{\pi d_s^3 \rho_s g}{6} \qquad (7-23)$$

$$F_B = \frac{\pi d_s^3 \rho_F g}{6} \qquad (7-24)$$

$$F_D = \frac{C_D A_P \rho_F U_r^2}{2} \qquad (7-25)$$

where d_S = particle (sphere) diameter
g = gravitational constant
ρ_S = solid particle density
ρ_F = carrier fluid density
C_D = dimensionless drag coefficient which is a function of the relative Reynolds Number, Re_r
A_P = projected area of the particle (sphere)

The projected particle area is calculated by the following:

$$A_P = \pi d_s^2/4 \qquad (7-26)$$

The average surrounding fluid velocity, U_r, is

$$U_r = |U - V| \qquad (7-27)$$

where V = particle (sphere) diameter

The Reynolds number is the following:

$$Re_r = \frac{\rho_F d_s U_r}{\mu_F} \qquad (7-28)$$

where μ_F = carrier fluid Newtonian viscosity

Figure 7-13. Schematic Showing Forces Exerted on a Spherical Particle

V = particle velocity
U = fluid velocity

F_B = buoyancy force
F_{wt} = gravity force
F_D = drag force
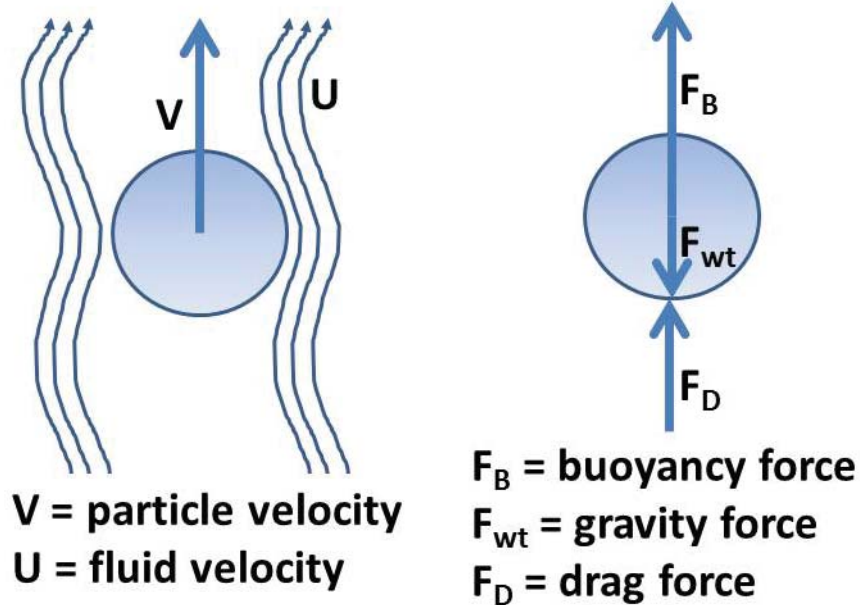
Substituting Equations 7-23 through 7-25 into Equation 7-22 yields the sum of the forces on the spherical particle, given by

$$\frac{C_D A_P \rho_F U_r^2}{2} + \frac{\pi d_s^3 \rho_s g}{6} - \frac{\pi d_s^3 \rho_s g}{6} = 0 \qquad (7-29)$$

Substituting Equation 7-26 for A_P and solving for U_r results in

$$U_r^2 = \frac{8\pi d_s^3 g(\rho_s - \rho_F)}{6 C_D \rho_F \pi d_s^2} \qquad (7-30)$$

$$U_r = \frac{4 d_s g}{3 C_D}\left(\frac{\rho_s}{\rho_F} - 1\right) \qquad (7-31)$$

To solve for U_r using Equation 7-31, the drag coefficient, C_D, for the sphere must be obtained. C_D is dependent on Re_r, which is a function of U_r. Therefore, Equation 7-31 must be implicitly solved. Table 7-2 provides a set of equations for obtaining C_D based on the value of Re_r along with the corresponding references. The combination of these empirical equations creates the standard steady-state drag coefficient curve, which is presented in most fluids texts and handbooks for spheres and/or cylinders (e.g., Crowe et al 2001, Crowe 2006, Govier, and Aziz 1987). The steady-state drag coefficient curve is characterized by the following:

- An initial decay of C_D, which is approximately linear and has been defined by Stoke's law, which under predicts the drag coefficient with increasing Re_r. The flow is attached to the sphere and no visible recirculation zone exists behind the sphere. Separation has been observed to occur at approximately $Re_r > 20$ (Crowe 2006).

- With an increase in Re_r a steady-state wake develops and the onset of separation of the flow from the surface of the sphere is experienced. The steady state wake has been observed in the region of $20 < Re_r < 150$ (Crowe 2006).

- The wake begins to become instable for Re_r in the range of 130 to 150. The instable wake results in a laminar flow oscillation with a long period of oscillation. The unsteady wake regime has been experimentally observed to exist in the range of $(130 \text{ to } 150) < Re_r < 270$ (Crowe 2006).

- For $270 < Re_r < 3 \times 10^5$ vortices are being shed at a regular high frequency from alternate sides of the sphere. While the wake is turbulent in this regime the flow is not turbulent. While experimental results vary the steady-state drag coefficient curve is relatively flat in this region and C_D is often approximated by a constant, refer to Equation 7-35 in Table 7-2.

- For a smooth surface sphere, the C_D abruptly decreases at $Re_r \approx 3 \times 10^5$ due to the onset of the transition to a turbulent wake, which begins at $Re_r \approx 2 \times 10^5$ and is completed at $Re_r \approx 3.7 \times 10^5$ (Crowe 1998, Crowe 2006). This phenomenon is entirely due to boundary layer effects. If the particle surface is rough or the free-stream turbulence is increased, transition to turbulence occurs at a lower Re_r and the drop in C_D is not as drastic occurring over a wider range of Re_r.

The calculated particle size and density limits for the Hanford waste presented in Figure 7-11 in combination with the transfer line velocity are not anticipated to result in $Re_r > 3 \times 10^5$. Therefore, Table 7-2 and the associated discussion provide no approximations for C_D beyond $Re_r = 3 \times 10^5$.

Table 7-2. Methods for Determining C_D for Ranges of Re_r

Equation	Min Re$_r$	Max Re$_r$	CD	Reference
7-32	0	0.1	$C_D = \dfrac{24}{Re_r}$	Stokesian flow, Crowe 2006
7-33	0.1	0.7	$C_D = \dfrac{24}{Re_r}\left[1 + \dfrac{3}{6}Re_r + \dfrac{9}{160}Re_r^2 \ln\left(\dfrac{Re_r}{2}\right)\right] + O(Re_r^2)$	Proudman and Pearson 1956*
7-34	0.7	800	$C_D = \dfrac{24}{Re_r}(1 + 0.15Re_r^{0.687})$	Schiller and Nauman 1933
7-35	750	300,000	$C_D \approx 0.445 \pm 0.059$ (0.059 $corresponds\ to \pm 13\%$	Crowe 1998

Notes: *This equation is often presented as $C_D = \frac{24}{Re_r}\left(1 + \frac{1}{6}Re_r^{2/3}\right)$ because it is easier to integrate analytically.

A solution for U_r using Equation 7-31 is obtained by selecting a value for C_D, calculating U_r, evaluating Re_r to check the validity of the original C_D and iterating until a value for U_r is obtained with the resulting Re_r corresponding to C_D. Once U_r is resolved, the particle velocity, V, is determined from Equation 7-27. Table 7-3 provides the interpretation of the possible results for V.

**Table 7-3. Vertical Pipeline Conditions Relative to Particle Transport
for a Range of Calculated Particle Velocities (V)**

Value of V	Resulting Phenomenon Relative to Transport in the Vertical Pipeline
$V < 0$	Particles are unable to be transported up the pipe in the region of fully developed flow. There is some range of calculated particle velocities less than zero that could indicate a condition where particles can be entrained into the developing flow at the discharge of the pump but they cannot be transported up the vertical line. This adverse condition can result in an accumulation of solids at the discharge of the pump.
$V = 0$	In this case $U_r = U$ and the flow is sufficient to suspend the particle. At this condition holdup of some of the particles is possible. The transport of particles is not imminent but the existence of holdup may begin to alter the system curve relative to pump operation.
$0 < V \leq U$	Particles are being transported up the pipe.
$V > U$	This condition cannot be sustained and is assumed not to exist within the vertical line.

7.2.1.3   *Effects Impacting Solids Transport in a Vertical Pipe*

The previous model development focused on a smooth surface sphere. Factors that impact this model include:

- particle surface condition

- particle shape

- non-Newtonian fluid behavior (discussed in Section 7.2.3)

As mentioned earlier, an increase in the particle surface roughness can lead to the onset of a turbulent wake at a smaller value of U_r. If the roughness and/or porosity of the particle are sufficiently large relative to the particle diameter, then these attributes can have an impact on the effective projected area of the particle. This is because the boundary layer effect on the particle can be influenced by flow through individual pores/caverns/divots in the particle. Again, these structures have to be large relative to the particle size.

Particle shape is again a factor relative to the effective projected area, A_P. The projected area of interest relative to the form drag is the projected area perpendicular to the flow field. However, the coefficient of drag represents the effects of both form and viscous drag. As the aspect ratio and aerodynamic shape of the particles deviate from that of a sphere, significant differences can be observed in the drag force for a given Re_r. An example of this can be observed by comparing the drag curves for a disk with its face perpendicular to the flow and for an airfoil (Crowe 1998). The importance of this relative to particle transport is in the interpretation of particle size data to evaluate particle transport. The particle shape must be taken into consideration. High aspect ratio particles can be transported under conditions that are prohibitive for spheres of the same size based on results from particle size analyses. This issue must also be considered for conditions of agglomeration, which may be broken up during characterization. Agglomeration not only changes the particle size but can impact the effective particle shape and thus A_P.

7.2.2   Comparison of Transfer Pump Model Estimates to Test Data

Estimates of the transfer system performance from the models described in Section 7.2.1 are qualitatively compared to prototypic operation data, specifically, the transfer of waste from C-106 to AY-102. Approximately 186 kgal of sludge (~97% of the initial inventory) was retrieved from C-106 using the Waste Retrieval Sluicing System and transferred to AY-102 via three sluicing campaigns from 11/98 through 10/99 (PNNL-13319). Supernatant from AY-102 was used as the sluicing fluid and nominally 16% of the original sludge volume of C-106 was removed via solids dissolution (RPP-5687).

AY-102 initially contained approximately 9 inches of sediment (PNNL-13319) and had nominally 67 inches of sediment after the completion of the sluicing campaigns.   It is noted in PNNL-17707 that this sediment level change of approximately 58 inches suggest that the solids settled in AY-102 to a similar condition as in C-106, because 186 kgal minus 16% is nominally 155 kgal of sludge transferred. With a tank diameter of 75 feet, this volume translates to approximately 56 inches, as compared to the 58-inch difference. It is considered further in PNNL-17707 that the > 500-day measurements of the ENRAF densitometer, riser 15S, and the temperature profiles on the opposite side of the tank, riser 5A, are similar and thus the sediment level is relatively uniform and does not appear to be a function of location in the tank.

The uniformity of the sediment deposition with settling may be attributed to a slurry distributor (Hanford Drawing H-2-818537 Rev. 3) that was located at a tank radius of 6 feet. The distributor is a fixed-length drop leg with four opposed 2-inch nozzles that discharge below the liquid surface (HNF-SD-WM-PCP-013). That report notes that the distributor is designed to provide equal distribution of solids throughout the tank. It is thus reasonable to assume that characterization of the waste in AY-102 from core samples taken after the C-106 retrieval is not impacted by the radial location of the samples.

As reported in HNF-SD-WM-PCP-013, the slurry pump system in C-106 consisted of a submersible pump and a booster pump located in the pit above. The submersible slurry pump was a centrifugal, direct drive, end suction, 40-hp pump with a 0.25 in mesh intake screen. The booster pump is likewise a centrifugal, direct drive that is 250-hp. The combined-pump nominal flow rate is 350 gpm, which corresponds to 2.7 m/s (8.9 ft/s) in the 4-inch (straight legs, Hanford Drawing H-2-81844) vertical leg.

The potential maximum size and density particle in AY-102 is listed in Table 4-9 as 1,268 μm, 8.9 g/mL. The transport of this particle up the vertical leg of the transfer pipeline is considered via the models presented in Section 7.2.1. For the actual transfers, this potential maximum particle, assuming that it originated in C-106, would have been transferred in a slurry of the supernatant liquid. The supernatant liquid is represented by the liquid properties in AY-102 (1.15 g/mL and 2.5 cP, PNNL-20646) and the remainder of the UDS (UDS concentration by volume in transfers estimated at ~ 6-vol% in PNNL-20646). As discussed in RPP-PLAN-51625, the limiting particle capability of a system is dependent on the remainder of the solids. Further, the rheology of the suspending fluid is likely increased by the presence of these solids. For this qualitative comparison the limiting case of the potential maximum size and density particle in the AY-102 liquid is considered. The limiting case is considered, given that AY-102 slurry at an

increased solids loading (6 wt%) is Newtonian, and increased density and rheology likely result in increased transfer of particulate, See Section 7.1.3 and Equations 7-27, and 7-31 through 7-35 of Section 7.2.1), The upward velocity of the 1268 μm, 8.9 g/mL particle in the 1.15 g/mL, 2.5 cP liquid at an upward velocity of 2.7 m/s is calculated to be ~ 2.3 m/s. Therefore, a potential particle of this size and density is predicted by the Section 7.2.1 model to be transferred through the vertical leg of the transfer line, a result that is consistent with the prototypic test data.

7.2.3   Limiting Particles in Transfer Pump and Vertical Leg

The inlet height limit shown in Figure 7-11 (Section 7.1.3) for particles calculated to be at the transfer line inlet elevation, because of the mixer pump, is compared to the ParaFlow predictions of the inlet flow. The velocity of the particle in the jet at this point is neglected in this evaluation. A minimum upward particle velocity of 0.01 ft/s is selected to establish the extent of the flow field around the inlet wherein a particle would be ingested. For a uniform liquid flow at the representative upper limit of density and viscosity of 1.37 g/mL and 14 cP, an upwards fluid velocity of ~ 0.32 m/s is calculated (Equations 7-27, and 7-31 through 7-35) for a minimum particle flow of ~ 4E-3 m/s (0.01 ft/s) for size and density pairs from the inlet height limit, Figure 7-14.

The predicted vertical velocity profile and velocity vectors near the transfer line inlet (2.25-inch diameter) at 140 gpm are shown in Figure 7-15. The region below the transfer line inlet with vertical velocities greater than 32 cm/s extends down approximately 6 cm and out between 0.5 and 1 cm beyond the inlet radius. This result does not include a screen around the inlet. However, it is likely, given that the screen housing is so much larger than the inlet, that there is minimal effect of the screen on the interior velocity profile. If the transverse velocities are taken into account, this expands the effective capture radius to over 2 cm beyond the radius of the transfer line inlet. In comparison, if a uniformly distributed flow of 32 cm/s is assumed over a hemisphere surrounding the inlet, the radius is 6.6 cm. A particle rising vertically at 4E-3 m/s will traverse the ~ 6 cm in 15 seconds, which is substantially less than the potential transfer time of 19 hours (see Section 7.1.3, AZ-101 mixer pump test discussion). Any particle at the Figure 7-11 inlet height limit or below will therefore likely be ingested into the transfer line. As described in Section 7.1.3, the inlet height limit encompasses the potential bounding waste particles.

Figure 7-14. Calculated Vertical Particle Velocity in 0.32 m/s Flow
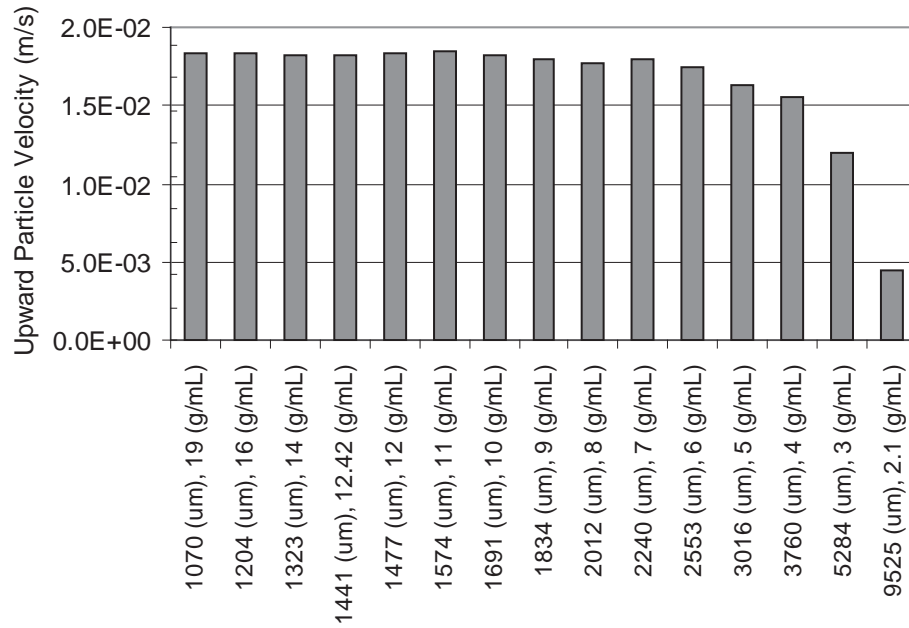
Figure 7-15. Vertical Velocity Profile and Vectors Near the Transfer Line Inlet
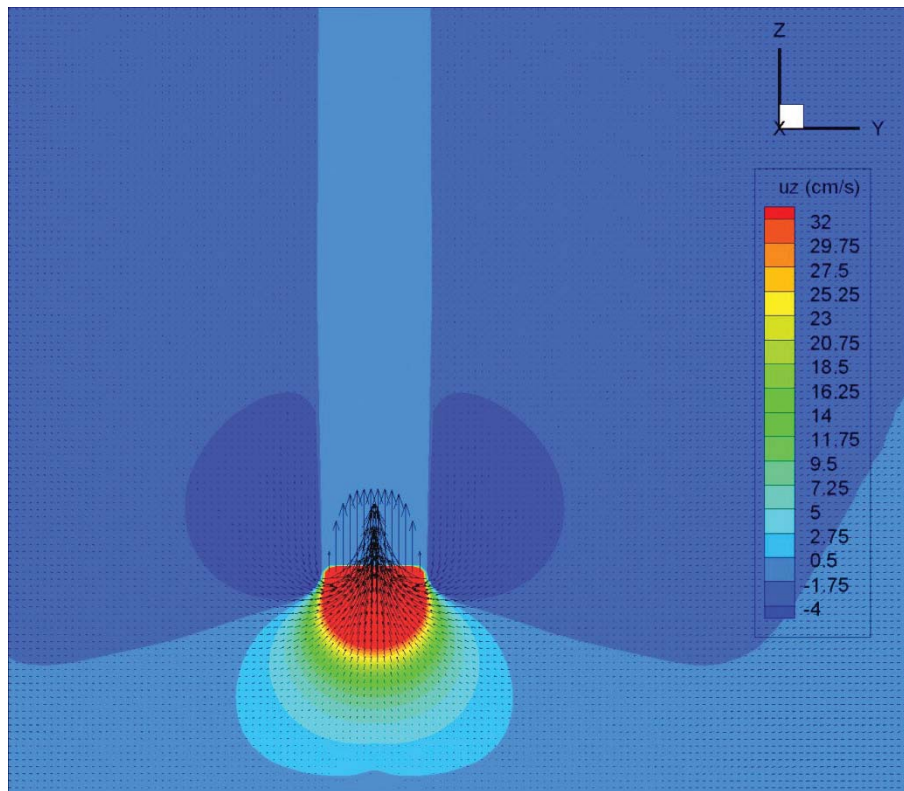
The size and density particle limit of Figure 7-11 corresponds to a constant particle settling velocity of ~ 0.27 m/s in the upper-limit liquid as noted in Section 7.1.3. For these particles less than approximately 3,760 μm in diameter and 4 g/mL density (Re_r ~ 110), the calculated upwards velocity is ~ 1.64 m/s. This velocity decreases to ~ 1.63m/s for the 9525 μm, 2.1 g/mL particle (Re_r ~ 290). Therefore, as for the transfer line inlet, any particle at the Figure 7-11 limit or below, which includes the potential limiting waste particles of Table 4-9 (see Section 7.1.3) will be transferred up the vertical leg of the transfer line.

The calculated mixer pump particle mobilization limits shown in Figure 7-12 can be exceeded (i.e., a larger, more dense particulate) in the vertical leg of the transfer line. For example, an upwards velocity of ~ 0.03 m/s (0.1 ft/s) is calculated for the same flow and liquid conditions for a 9,500 μm, 19 g/mL particle.

7.2.3.1 *Non-Newtonian Yield Stress Fluid Effects in Transfer Pump*

Non-Newtonian behavior of the carrier fluid can be difficult to quantify because the effect of drag on the particle is based on localized boundary effects. Rheological characterization of the carrier fluid alone may not be enough to understand the effects on a particle fully. The phenomenon causing the rheological impact must be understood. The following two examples are provided to illustrate these concepts:

- Consider a fine particle suspension that transports larger particles. For the evaluation of the viscosity relative to pipeline transport/system pressure drop, it may be possible to consider the fluid and fine solids a homogenous mixture that makes up the carrier fluid. However, depending on the fluid properties, the properties of the fine solids, and the relative aerodynamic response of the larger and finer particles the finer particles may exhibit a concentration gradient in the region surrounding each particle. Therefore, the rheological characterization of the bulk mixture may not represent the fluid imposing a drag force on the particle.

- Another issue is the effect of viscoplastic fluids exhibiting a yield stress in shear. Depending on the relative velocity, U_r, the potential exists for a sheared cavity to develop around the particle. The shape of this flow field and the non-Newtonian nature of the carrier fluid can make determining the applicable rheology to apply to the particle difficult because the shear stress is not uniform along the particle surface. Confounding the effects of viscoelastic material can be the nature of the material to adhere to the particle. Particle size can be increased due to adhered material similar to agglomeration or slip may occur at the material surface due to a lack of adhesion.

For the effects of non-Newtonian fluid behavior, the impact on C_D will be discussed for a power law fluid and a Herschel-Bulkley (viscoplastic) modeled fluid. The effects of non-Newtonian characteristics appear to be more important at low Re_r and the impact diminishes as the inertial effects become significant with increasing Re_r.

7.2.3.2 *Power Law and Herschel-Bulkley Modeled Fluids*

For a power law fluid, the shear stress is related to the strain rate by the following:

$$\tau_{yx} = K(\gamma_{yx})^n \qquad (7-36)$$

where τ_{yx} = shear stress

K = viscosity coefficient, an empirically determined parameter based on the curve fit of rheological data.

γ_{yx} = strain rate, $\frac{\partial u}{\partial y}$

n = behavior index, an empirically determined parameter based on the curve fit of rheological data. For $n < 1$ the fluid exhibits shear thinning behavior (the lower the value the greater the degree of shear thinning). For $n = 1$, Equation 7-36 reduces to that for Newtonian behavior. For $n > 1$ the fluid exhibits shear-thickening behavior (the greater the value the greater the degree of shear-thickening behavior).

For a power law fluid, the Reynolds Number (Re_{PLr}) is defined as

$$Re_{PLr} = \frac{\rho_F d_s^m U_r^{2-n}}{K} \qquad (7-37)$$

Creep flow is considered to exist for the condition

$$Re_{PLr} < 1 \qquad (7-38)$$

and

$$C_D = \frac{24 Z_{PL2}}{Re_{PLr}} \qquad (7-39)$$

where

$$C_D = \frac{1.33 + 0.37n}{1 + 0.7n^{3.7}} \qquad (7-40)$$

For the entire range of Re_{PLp}, Darby (1996) defines the coefficient of drag as the following:

$$C_D = \left[Z_{PL1} + \frac{4.8}{\left(Re_{PLr} \big/ Z_{PL2} \right)^{0.5}} \right]^2 \qquad (7-41)$$

This equation is implicit in Ur and to simplify the iterative process, Equation 7-41 is rearranged to yield

$$Re_{PLr} = Z_{PL2} \left(\frac{4.8}{C_D^{0.5} - Z_{PL1}} \right)^2 \qquad (7-42)$$

Based on past numerical analysis (Gu and Tanner 1985, Tripathi et al. 1994, Tripathi and Chhabra 1995) in the region of creep flow, shear-thinning behavior causes an increase in drag and drag reduction results for shear-thickening fluids.

7.2.3.3 *Viscoplastic Fluid*

A material whose rheology is modeled as a Bingham plastic will have a limiting viscosity, μ_B and Bingham plastic yield stress, τ_B. To assess the particle transport in a Bingham plastic, the Bingham number, Bn and Bingham plastic particle Reynolds number, Re_{Bp}, are defined as

$$Bn = \frac{\tau_B d_s}{\mu_B U_r} \qquad (7-43)$$

$$Re_{Bp} = \frac{\rho_F d_s U_r}{\mu_B} \qquad (7-44)$$

and the generalized drag coefficient, C_D, can be defined for a particle from the force balance described relative to Figure 7-13 (equivalent to Equation 7-31) as

$$C_D = \frac{4g d_s (s-1)}{3U_r^2} \qquad (7-45)$$

According to Chhabra and Richardson (1999), creeping flow exists for the condition

$$Re_{Bp} < 100 Bn^{0.4} \qquad (7-46)$$

For the condition of creeping flow,

$$C_D = \frac{24}{Re_{Bp}} Z_B = \frac{24\mu_B Z_B}{d_s \rho_F U_r} \qquad (7-47)$$

where

$$Z_B = 1 + 2.93 Bn^{0.83} \qquad (7-48)$$

For larger Re beyond creeping flow

$$C_D = \left[0.632 + \frac{4.8}{\left(Re_{Bp} \middle/ Z_B \right)^{0.5}} \right]^2 \qquad (7-49)$$

Equations 7-47 and 7-49 are implicit in U_r and are solved via iteration with Equations 7-43 through 7-45.

From the relations above, as the rheological properties increase, the velocity needed to transport particles in turbulent flow decreases. Given that the calculated limits of performance for the vertical leg of the transfer line exceed the potential limiting waste particles as previously described, quantification of the effect of a non-Newtonian fluid is not analyzed further.

7.3   TRANSFER PIPELINE CAPABILITIES

Waste mobilized by the jet mixers is transferred out of the DST via the transfer pump and through a pipeline to the WTP. The limits of performance of the current baseline transfer system with respect to the transfer of UDS particles through the horizontal pipeline are considered. Following Sections 7.1 and 7.2, the probability that the limiting particle is available (with respect to actual waste concentration, initial particle location in the vessel, etc.) is not evaluated.

The models describing the horizontal transfer pipeline flow are developed in Section 7.3.1. Results of this modeling approach are compared to prototypic test results in Section 7.3.2 and estimates of the limiting particles are made in Section 7.3.3.

7.3.1   Horizontal Transfer Pipe Model

This section considers the modeling of particle transport in liquid through a horizontal pipe. No attempt is made to consider:

- entrance effects associated with a developing flow field or slurry flow pattern

- the impact on flow or solids separation due to pipe components such as elbows, valves, etc.

- solids holdup within the transport line.

The assessment assumes fully established, steady-state flow in a continuous horizontal pipe. While the effects of fluid drag on the particle are the dominating factor contributing to solids transport, the methodology presented in Section 7.2.1 cannot be applied. For vertical transport, the effects of gravity occur parallel to the direction of flow, and the applied velocity can be assumed to be the bulk velocity existing across the center region of the pipe. For horizontal transport, the effects of gravity act perpendicular to the flow and therefore, act to concentrate (settle) particles at the bottom of the pipe where, due to the wall friction, the velocity is lower.

In considering the settling velocity of a particle under quiescent flow conditions, the time duration for a particle to traverse the width of the pipe is relatively short compared to the length of many transfer lines (e.g., minimum HLW transfer pipeline length to WTP of 5,232 feet, Section 3). Therefore, for a particle to remain in suspension, the lift forces applied to the particle must be sufficient to overcome or be in balance with the gravitational forces. The degree of particle suspension is dependent on the flow field, degree, and size of any turbulent structure within the flow, the density difference between the carrier fluid and the particulate, the particle shape and the rheology of the carrier fluid. The suspension is also dependent on the solids concentration and the size and density distribution of the particulate. The term carrier fluid is used to define the fluid or representative mixture assumed to act as a fluid, which may include small (i.e., ultra-fine < 10 μm, Govier and Aziz 1987), low-density particulate with relatively small settling velocities that remain homogeneously mixed within the pipe. For these particles, gravitational effects and concentration gradients (even localized) are negligible. The carrier fluid is taken to include the mixture of liquid and small/low-density particles and the corresponding mixture properties (e.g., density, viscosity) are applied for the liquid properties.

With the addition of particulate into a flow stream, the description of the flow condition/regime takes on meaning beyond just conditions of laminar, transitional and turbulent flow. Slurry transport can occur via a variety of mixture conditions that exist within the pipe. A high-level summary of these conditions for granular material in a horizontal pipeline is provided in a number of texts related to slurry transport (e.g., Crowe 2006, Govier, and Aziz 1987).

- Homogenous suspension – All particles are fully suspended and no stratification exists.

- Heterogeneous suspension – All particles are fully suspended, but a vertical stratification of material exists. The variation may be in solids concentration, size distribution, solids density, or a combination of these parameters.

- Sliding particles – Larger, denser particles are transported by sliding or bouncing along the bottom of the pipe. The particles transported along the bottom of the pipe can be individually identified and the particle-to-particle interactions on the bottom of the pipe are negligible.

- Sliding/moving bed or dune flow – A significant amount of particles accumulate at the bottom of the pipeline to create a continuous layer (bed) and travel by sliding along the bottom of the pipe. This transport may be either in the form of "dunes," in which groups of particles appear to summersault or leapfrog along the bottom of the pipe, or as a continuous moving bed. In this flow condition, all particles still possess some downstream velocity.

- Settled bed – For this flow regime, stationary particles exist on the bottom of the pipe. This condition may be the result of 1) a self-correcting condition in which settling occurs until an increased pipe velocity is established that maintains a constant transport condition, or 2) a continuous holdup of the larger/denser particles that will eventually lead to pipe plugging.

For solids transport, the previously mentioned conditions are often considered in terms of onset conditions or critical transport velocities. In other words, above and below prescribed velocity, defined conditions exists such as:

- critical velocity for homogeneous flow – U_{cH},

- critical velocity for full suspension or deposition – U_{cd}, which also corresponds to U_{cmb}, below which a moving bed begins to form,

- critical velocity for stationary bed – U_{csb}.

Therefore, a fully suspended heterogeneous flow would be expected for average pipeline velocities between U_{cH} and U_{cd}. It also is possible for a combination of conditions to exist simultaneously within the cross-section of the pipe flow. For example, in the case of a sliding bed:

- The flow above the sliding bed may be clear (pure liquid) as all solids are transported within the sliding bed.

- A heterogeneous flow may exist above the moving bed.

- The Particle Size Dispersion (PSDD) of the solids may result in a homogeneous flow occurring above the moving bed.

Within texts related to slurry transport (e.g., Crowe 2006, Govier and Aziz 1987), these slurry flow patterns are also often defined, based on industry applications, relative to particle size ranges, which are also density dependent. Table 7-4 provides a breakdown of anticipated particle size range and the corresponding flow patterns based on work with coal ash (1.2 to 1.5 g/mL), limestone (2.45 g/mL) and sand (2.65 g/mL), Govier and Aziz (1987). The range of particle density for Hanford waste can be nominally 1 to 19 g/mL. As given in Equation 7-50 below, the functionality of critical velocity for pipeline transport is more strongly dependent on particle density than size (e.g., $U_{cd} \rightarrow (S-1)^{0.545} d^{0.167}$, Equation 7-50, Case 0, Table 7-5). It is thus emphasized the relations between particle size and anticipated flow pattern described in Table 7-4 are likely dependent on the particle density.

Table 7-4. Slurry Flow Patterns for Particle Size Ranges at Densities between 1.2 and 2.65 g/mL

Particle Size Range (μm)	Anticipated Slurry Flow Pattern Based on Common Industrial Applications
0 -10	Almost always carried in fully homogeneous state.
10 – 100	Usually suspended as homogenous mixture, but localized concentration gradients can exist due to gravitational effects. Not considered challenging to maintain in full suspension.
100 – 1000	May be fully suspended at sufficiently high velocities, but forms a heterogeneous (stratified) suspension. Often will form a moving deposit.
1000 – 10000	Rarely fully suspended and usually will form a moving deposit.
≥ 10000	Not suspended at feasible velocities unless solids are relatively light compared to the carrier fluid. May be transported along bottom of pipe as individual particles or moving bed.

Attempts have been made to predict, analytically or computationally, slurry transport, which includes predicting the solids distribution within the pipe, the solids transport velocity/velocities, and the resulting pressure drop. However, for industry application, slurry pipeline design has relied on empirical results, which have generated a number of predictive models. The majority of slurry transport applications and associated design efforts aim to avoid solids deposition within the pipe. The occurrence of solids deposition within the pipe results in the following:

- an increased risk of plugging.

- an increase in wear for the lower portion of the pipe.

- increased segregation of the solids for wider size distributions.

Therefore, the majority of work relative to evaluating the solid flow patterns has been the prediction of the critical deposition velocity, U_{cd}. Full suspension can be expected at this minimum flow velocity. For determining the limit of performance, the initial approach assumes that the existence of solids deposition is a limiting condition for solids transport through the horizontal line. The majority of experimental work has been conducted for process streams that contain uniform solids relative to size distribution and density. No models have been developed addressing a wide range of particle sizes and densities that approach those existing in Hanford waste. The Hanford waste contains particles sizes spanning six orders of magnitude and a density range of one order of magnitude.

For the purpose of determining the limits of performance, relative to solids transport, the evaluation of the flow stream takes a conservative approach and assumes:

- That the flow stream consists of only one constituent with the potential to settle out in the pipe. Each combination of density and particle size evaluated will be independently assessed.

- The solids consist of non-cohesive coarse particles that can be approximated as spheres for the purpose of determined particle diameter (i.e., large aspect ratios are not considered).

- Any other solids assumed to exist within the flow will be considered fine, fully suspended material that can be assessed as part of the carrier fluid (e.g., effecting fluid density and viscosity).

- The concentration of a constituent being evaluated will be relatively low, on the order of one volume percent or less.

These simplifying assumptions make it an easier task to select a predictive model for the assessment. As stated earlier, numerous empirical methods and models have been developed for predicting U_{cd} (e.g., Durand and Condolois 1952, Gillies and Shook 1991, Turian et al. 1987, Wani et al. 1982, Wasp 1977). There are also models that have been developed that are independent of solids concentration (Shook et al. 2002), however, this comes with a greater uncertainty for the prediction of deposition velocity over the range of comparable results. For the purpose of this assessment, a model developed and/or assessed for non-cohesive, larger, denser, coarse particles and over a wide range of particle sizes was desired. The object was to identify a model that was dependent on concentration and had been assessed at low solids

loadings. Based on these goals, the Oroskar-Turian model (Oroskar and Turian 1980) has been selected for this assessment. The model has the form:

$$U_{cdyx} = \chi_1 \Phi_S^{\chi_2}(1 - \Phi_s)^{\chi_3}[2gd_s(s-1)]^{0.5}\left[\frac{D_T\rho_l[gd_s(s-1)]^{0.5}}{\mu_F}\right]^{\chi_4}\left(\frac{d_s}{D_T}\right)^{\chi_5} \qquad (7-50)$$

where $\chi_1, \chi_2, \chi_3, \chi_4, \chi_5$ = coefficients listed in Table 7-5 for Case 0
Φ_s = solids volume fraction
g = gravitational constant
d_s = particle size (median particle size)
s = density ratio between solids and carrier fluid, $s = \rho_s/\rho_F$
D_T = pipe inside diameter (ID)
μ_F = viscosity of carrier fluid

The Oroskar-Turian model was developed for fully turbulent Newtonian flow. PNNL-16857 conducted an assessment of the applicability of potential correlations/models for Hanford waste to determine the critical velocity for deposition. One of the drawbacks to most models was a relatively high limit on the lower particle size used in the development of the models (typically > 200 μm). The particle size range used for the development of the Oroskar-Turian model, which included a lower limit of 100 μm, was one of the widest employed. PNNL-16857 concluded that the application of the Oroskar-Turian model following the procedure of Hall (2006) yielded elevated results relative to their Newtonian test results. The Oroskar-Turian model is also presented for application to Hanford coarse solids in the assessment of Hanford waste physical and rheological properties (RPP-20646).

The Oroskar-Turian model does not take into account the effects of the range/width of the PSD because a single value is entered for particle size, d_s, and concentration, Φ_s. Turian et al. (1987) compared the model predictions to a collection of 864 data points for critical velocity. The data points included UDS densities of 1.15 to 7.475 g/mL, fluid densities of 0.77 to 1.35 g/mL, fluid viscosities of 0.77 to 38 cP, particle sizes of 20 to 19000 μm, and solids concentrations as low as 0.5 vol% and up to 50 vol%. Turian et al. (1987) also evaluated variations of the Equation 7-50 model in which the coefficients χ_1 through χ_5 are altered by setting some of the coefficients to zero and determining the other coefficients using all 864 data points. In addition to the Oroskar and Turian (1980) coefficients (Case 0), Table 7-5 provides the Turian et al. (1987) values for χ_1 through χ_5 for five different variations, Cases 1 through 5. For Cases 1 through 5 the table also contains the Turian et al. (1987) defined overall absolute average percent deviation and root mean square deviation obtained for the five variations of the model when compared to the experimental data. Turian et al. (1987) concluded that Cases 1 and 3 are the best overall at predicting U_{cd}. Following common Hanford practice, Equation 7-50 with the Case 0 coefficients is applied herein.

Table 7-5. Coefficient and Exponent Values for Oroskar-Turian and Subsequent Turian Models Predicting Critical Velocity for Solids Deposition Presented in Equation 7-50

Case No	χ_1	χ_2	χ_3	χ_4	χ_5	Overall Absolute Average Deviation[a] (%)	Root Mean Squared Deviation[a]
0	2.584[b]	0.1536	0.3564	0.09	-0.378	n/a[c]	n/a[c]
1	1.7951	0.1087	0.2501	0.00179	0.06623	20.53	0.3416
2	1.8471	0.1126	0.03421	-0.03093	0	21.53	0.3447
3	1.8176	0.1086	0.2525	0	0.06486	20.57	0.3412
4	1.3213	0.1182	0.3293	0	0	21.04	0.3552
5	1.1228	0.07367	0	0	0	21.35	0.3559

Notes:
a.   As reported in Turian et al. (1987).
b.   Value assumes fraction of eddies having velocities equal to or greater than the settling velocity is 0.96 (to the 0.3 power, Oroskar and Turian 1980), which is determined to be applicable for pipeline velocities between 0.06 ft/s and 5.3 ft/s (Oroskar and Turian 1980). The square root of 2 difference in the particle buoyancy term between Turian et al. (1987) and Oroskar and Turian (1980) is also included.
c.   Fit not evaluated by Turian et al. (1987).

The assessment of the limiting particle using the Oroskar-Turian model has focused on critical deposition in a Newtonian carrier fluid as the limiting condition. Additional factors considered in Section 7.3.3 include:

- non-Newtonian fluid behavior

- pipeline/Pump pressure limits

- sliding deposit; moving bed for particle transfer

7.3.2   Comparison of Horizontal Transfer Pipeline Model Estimates to Test Data

Estimates from the transfer pipeline model described in Section 7.3.1 are qualitatively compared to test results and operation data.

7.3.2.1   *Experimental Flow Loop Test Results*

PNNL-16857 performed experimental flow loop testing with Newtonian and non-Newtonian slurries. The test loop was constructed of 3-inch NPS piping and the simulant test particles were representative of Hanford waste with a nominal size range of 10 to 100 μm and density of 2.5 to 8 g/mL. Three different carrier fluids were used with target Bingham yield stress values of 0 (i.e., Newtonian fluid), 3, and 6 Pa. As noted in Section 7.3.1 for the Newtonian slurries, PNNL-17639 applied the Oroskar and Turian (1980) critical velocity model (Equation 7-50 with Case 0 coefficients) following the procedure of Hall (2006), to the test conditions and determined the model predicted values exceeded the experimentally measured critical velocity of these slurries.

It is concluded in PNNL-16857 with respect to Equation 7-50 relative to specific test data that using the 95th percentile by volume particle size in calculations is conservative (higher calculated than experimentally measured critical velocity value), but using an average UDS density is non-conservative (discrete particles with densities much greater than the average UDS density can settle in a pipeline). Thus it can be inferred that calculation of the critical transport velocity for a potential maximum size and density particle via Equation 7-50 is conservative relative to the same specific test data (i.e., a higher calculated than experimentally measured critical pipeline transfer velocity will be determined). PNNL-16857 also concluded that as rheological properties increase, the velocity needed to transport particles in turbulent flow decreases, but the transition velocity for turbulent-to-laminar flow increases, and thus particles can begin to settle in a pipeline at higher flow rates than for the same particles in a non-Newtonian fluid.

7.3.2.2 *Transfer of C-106 Waste to AY-102*

Details of waste retrieval from C-106 to AY-102 using the Waste Retrieval Sluicing System to AY-102 are described in Section 7.2.2. The horizontal transfer pipeline from C-106 to AY-102 consisted of an approximately 520-m long primary 4-inch pipe encased in a secondary 10-inch pipe (HNF-SD-WM-PCP-013). The nominal operating flow rate of 350 gpm thus corresponds to a flow velocity of ~ 2.7 m/s (8.9 ft/s). As listed in Table 4-9, the potential maximum size and density particle in AY-102 is 1268 μm, 8.9 g/mL, and the liquid properties are 1.15 g/mL and 2.5 cP (see Section 7.2.2). Again, the limiting particle capability of a system is dependent on the remainder of the solids and the slurry.

From the functionality of Equation 7-50 with UDS concentration, a higher concentration of UDS results in a higher calculated critical pipeline transfer velocity. If it assumed that the ~ 6 vol% UDS (see Section 7.2) in the C-106 to AY-102 transfers is comprised of 1 vol% of the potential maximum size and density particles (potential vol% of this size and density particle in AY-102 from PNNL-20646 is 1.14E-4), the calculated critical transport velocity in a 4-inch pipe with the 1.15 g/mL, 2.5 cP liquid is ~ 3.2 m/s, or ~19% greater than the actual transfer velocity. If the suspending fluid is altered to 1.26 g/mL (5 vol% UDS at an average density of 3.4 g/mL (PNNL-20646) in the 1.15 g/mL liquid) and 4.1 cP, the calculated critical transport velocity is ~ 2.9 m/s, ~ 4% greater than actual transfer velocity. Given the conservatism (likely higher calculated critical velocity than actual) of using the potential maximum size and density particle at an elevated concentration, it is thus indicated that the potential limiting particle would likely have been transferred, which is in qualitative agreement with the prototypic test data.

7.3.3 Estimates of the Limiting Particles, Horizontal Transfer Pipeline

The potential limiting waste particles (Table 4-9) are shown in Figure 7-11 to be exceeded by the particle size and density inlet height limit calculated for the mixer pump in Section 7.1.3. In Section 7.2.3, it was calculated that these inlet height limit particles will likely be ingested into and transported upward through the vertical leg of the transfer pipeline. The horizontal pipeline transfer of these particles is evaluated in this section.

The inlet height limit particles above approximately 2650 μm, 5.8 g/mL are shown in Figure 7-16 to be more limiting than calculated via Equation 7-50 for horizontal pipeline transfer

at a concentration of 1 vol% in a 3-inch horizontal pipeline at 6 ft/s. For smaller, denser particles, the 6 ft/s transfer pipeline limit is shown as the limiting case.

Figure 7-16. Calculated Particle Size and Density Limits, Mixer Pump and Horizontal Pipeline with Bounding Liquid
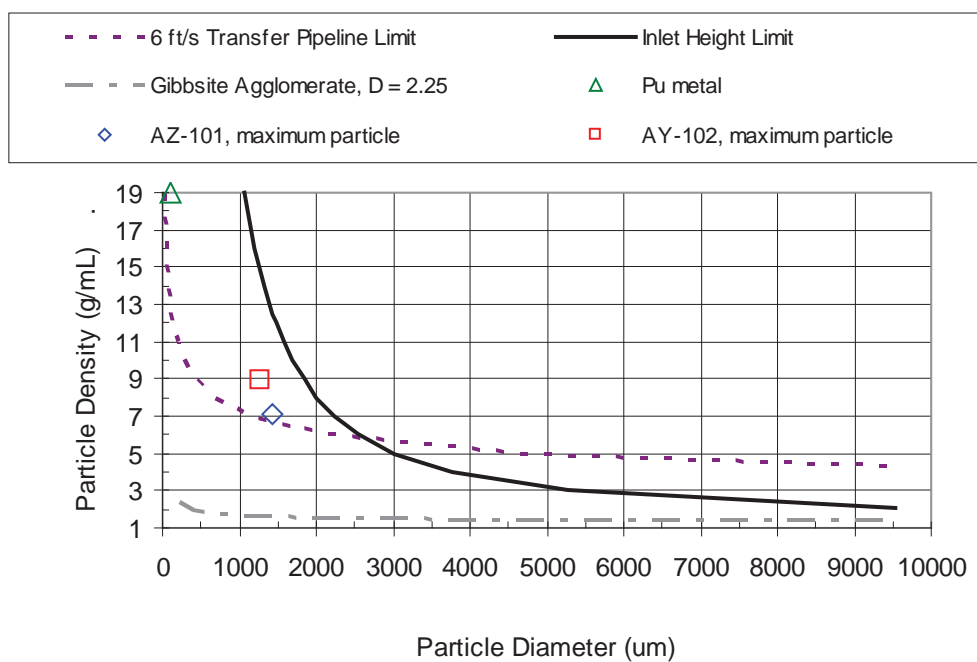
The potential maximum limiting particles in AZ-101 and AY-102 and the maximum particle density and size limit for that density, 19 g/mL and 100 μm, exceed the smaller, more dense particulate (than 2650 μm, 5.8 g/mL) limit for horizontal pipeline transfer, Figure 7-16. Therefore, the less-than 2650 μm, 5.8 g/mL particulate for the 6 ft/s transfer pipeline limit is evaluated for other, potentially less challenging flow conditions; non-Newtonian flow (Section 7.3.3.1) and an alternate flow regime (Section 7.3.3.5).

7.3.3.1 *Non-Newtonian Yield Stress Fluid, Horizontal Transfer Pipeline*

The horizontal pipeline transfer of the smaller, more dense particulate that fall below the inlet height limit (below 2650 μm, 5.8 g/mL, Figure 7-16) is evaluated in non-Newtonian flow. Methods are described for evaluating the rheology of the flow required to transfer these particles at 6 ft/s, and the resulting pressure drop of the flow.

The effects of non-Newtonian fluid behavior are not considered significant relative to the prediction of the critical deposition velocity via the Oroskar-Turian model. Slurry flows, unless at relatively low concentrations, tend to exhibit some form of non-Newtonian behavior with most exhibiting a shear-thinning behavior. The empirical development of the Oroskar-Turian model therefore suggests non-Newtonian effects may have had some impact on the model development. Note that it can be observed from Equation 7-50 that μ_F has minimal impact on U_{cd} as it is only an exponent of -0.09 (Case 0).

The important aspects of evaluating the deposition velocity for non-Newtonian conditions are to obtain a representative velocity, which is often obtained by calculating the effective viscosity, η, for the flow conditions, and to assure the application of the model is for turbulent conditions. The fluid flow regime must be determined based on the rheological behavior of the fluid and not by applying an effective or apparent viscosity to the Newtonian Re. The application of an effective viscosity to Equation 7-50 is considered for a Bingham plastic (viscoplastic) material having limiting viscosity, μ_B, and Bingham plastic yield stress, τ_B, where

$$\tau_{xy} = \tau_B + \mu_B \gamma \qquad (7-51)$$

The effective viscosity, η_{BP}, for a Bingham plastic in pipe flow is defined by Wasp (1977) as

$$\eta_{BP} = \mu_B + \frac{\tau_B D}{6V} \qquad (7-52)$$

This effective viscosity can then be applied to obtain U_{cd}. For the case of determining limiting conditions, U_{cd} can be set equal to the limiting condition of interest and the limiting material properties can be evaluated. In order for the application to be valid, the existence of turbulent flow within the pipe must be verified.

To evaluate a Bingham plastic modeled fluid for turbulent conditions, the Bingham Reynolds Number, Re_B, the Hedstrom Number, He, and the Yield Number, Y, need to be calculated, where

$$Re_B = \frac{D_T U_F \rho_F}{\mu_B} \qquad (7-53)$$

$$He = \frac{D_T^2 \rho_F \tau_B}{\mu_B^2} \qquad (7-54)$$

$$Y = \frac{He}{Re_{BP}} \qquad (7-55)$$

Govier and Aziz (1987) present a relationship from Hanks (1963) for the critical Bingham plastic Reynolds number., Re_{Bc}, which defines the transition from laminar to turbulent flow as

$$Re_{Bc} = \frac{He}{8x_{cB}}\left(1 - \frac{4x_c}{3} + \frac{x_c^4}{3}\right) \qquad (7-56)$$

where

$$\frac{x_c}{(1-x_c)} = \frac{He}{16,800} \qquad (7-57)$$

Govier and Aziz (1987) provide a plot of Re_{Bc} as a function of Y from Hanks and Frank (1967), Figure 7-17. Conditions above the solid line in Figure 7-17 are in the turbulent regime while those below that line are considered in the laminar regime.

Figure 7-17. Plot of Re_{Bc} as a Function of Y Providing the Limits of Turbulent Flow for a Bingham Plastic Modeled Fluid (from Govier and Aziz 1987)
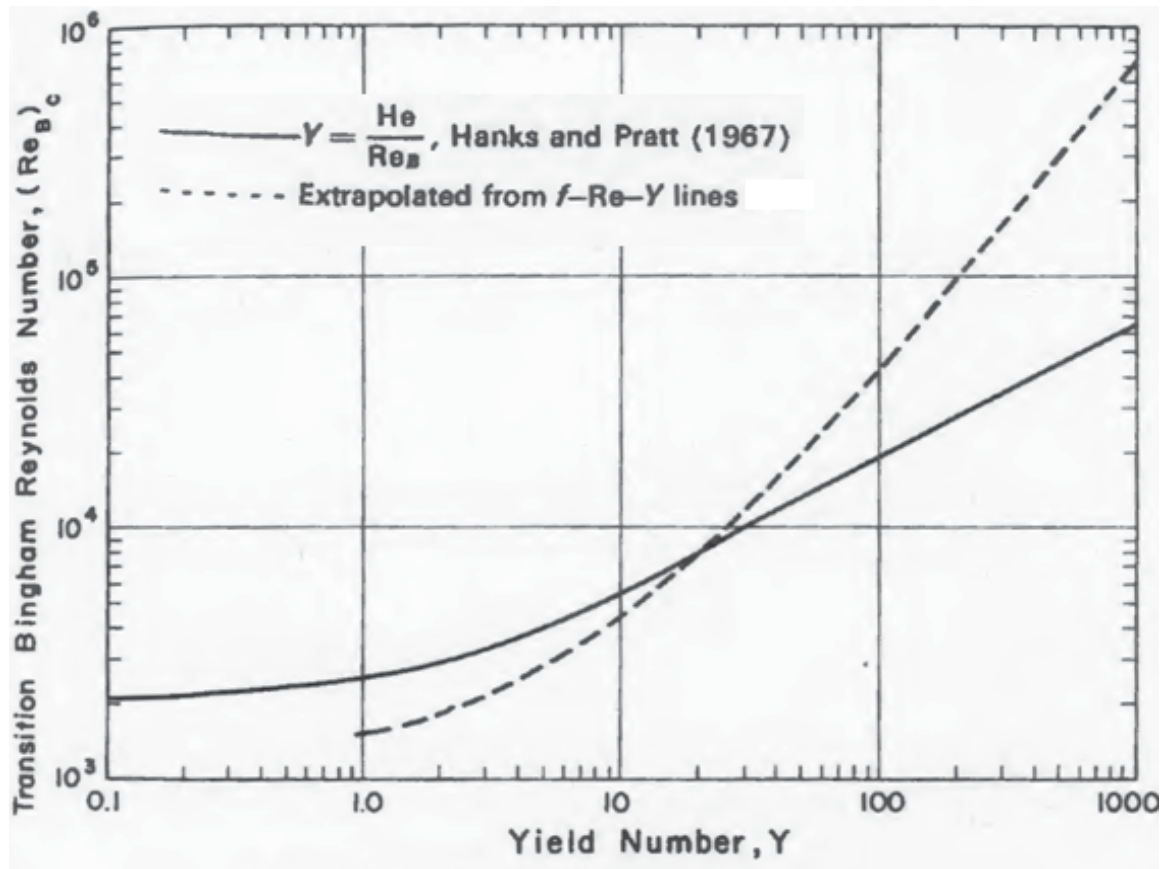
7.3.3.2 *Pressure Gradient Impact on Limiting Conditions*

With respect to the pressure limit, an increase in viscosity, solids loading, etc. can increase the pressure gradient through the transfer line. In determining limiting conditions for solids transport, it is important not to identify conditions beyond the limits of

- The pump capacity – The pump will only be capable of delivering a certain flow rate for a specific head and the performance for a dynamic type pump will be reduced with increases in viscosity. The pump capacity can also come into play relative to system startup from a condition of settled solids. This issue can be worse if the settled solids layer increases in strength with time. This is not of concern for this evaluation because the conservative approach is only applicable as the solids fraction approaches zero.

- Any pressure limiting devices provided for system protection.

The following discussion provides a methodology for predicting the pressure gradient for a multi-constituent slurry flowing under steady-state conditions. The presentation includes applications to Newtonian and Bingham plastic modeled fluids. Frictional pressure gradient within a pipe can be consider to be composed of both a pure fluid component and a solids component such that

$$\Delta P_m = \Delta P_F + \Delta P_S \qquad (7-58)$$

where ΔP_m, ΔP_F and ΔP_S represent the pressure gradients for the total mixture, the fluid component and the solid constituents, respectively (Saleh 2002). ΔP_F is obtained assuming pure fluid (no solids) but applying the average mixer velocity, U_m. ΔP_S is obtained using the Molerus diagram for suspension transport. The Molerus diagram (Selah 2002) was obtained from over 1000 data points for:

- pipe diameters of 25 mm to 315 mm

- particle diameters of 12 μm to 5.2 mm

- solid specific gravities of 1.27 to 5.25

- carrier fluids of both gas and liquid.

The relevant dimensionless groups associated with the suspension transport are the following:

The dimensionless, single-particle slip velocity.

$$U_{r0} = \frac{U_r}{U} \qquad (7-59)$$

The particle Froude Number.

$$Fr_p^2 = \frac{U_t^2}{(s-1)d_s g} \qquad (7-60)$$

The tube or pipe Froude Number.

$$Fr_T^2 = \frac{U_t^2}{(s-1)D_T g} \qquad (7-61)$$

The diameter ratio.

$$\frac{d_s}{D_T} \qquad (7-62)$$

Molerus (1993) modeled data in the form of:

$$\frac{U_{r0}}{s^{0.5}} = fn(Fr_p s^{0.5}, Fr_T^2) \qquad (7-63)$$

where U_r = the relative or "slip" velocity, $U_r = U_F - U_S$
U = the volumetric average velocity within the pipe
U_t = the unhindered terminal settling velocity
s = the density ratio, ratio of particle density to fluid density, ρ_s/ρ_F
fn = function
Fr_p = particle Froude Number
Fr_T = tube or pipe Froude Number
g = gravitational constant
d_s = the particle diameter
D_T = the tube or pipe diameter
ρ_F = fluid density
ρ_s = solids density

However, if some of the solids are uniformly suspended to create a homogenous mixture, this fraction of solids can be assumed to contribute to the fluid pressure gradient. If the carrier fluids or concentration of uniformly suspended solids result in non-Newtonian behavior, then the solution for the friction factor is more complex but the methodology is still applicable. The application of the process for a Bingham plastic modeled fluid is presented.

Molerus (1993) developed a relation for the dimensionless pressure gradient, $X_{\Delta P}$, resulting from the solids flow. His development is based on the rate of energy dissipation in the flow because of the solids and the rate of energy to the particles resulting from the relative velocity between the solids and the fluid. The resulting relation is

$$X_{\Delta P} = \frac{\Delta P_S}{\Phi_S \rho_F (s-1) g L} \left(\frac{U_t}{U}\right)^2 \qquad (7-64)$$

where Φ_s = total volumetric contribution of solids
L = relative pipe length.

The value of $X_{\Delta P}$ depends on the value of Φ_s. For $0 < \Phi_s < 0.25$,

$$X_{\Delta P} = X_{\Delta P0} = \frac{\left(U_r/U\right)^2}{\left[1 - \left(U_r/U\right)\right]} = \frac{U_{r0}^2}{1 - U_{r0}} \qquad (7-65)$$

For $\Phi_s > 0.25$,

$$X_{\Delta P} = X_{\Delta P0} + 0.1 Fr_T^2 (\Phi_s - 0.25) \qquad (7-66)$$

Darby (2000) and Selah (2002) both present a method for determining $X_{\Delta P}$, which is subsequently presented. The method involves the following five steps:

1. Determine U_t for the correct flow condition

2. Determine U_r by obtaining $U_{r0}/_{S^{0.5}}$ from the Molerus state diagram (refer to Figure 7-18) for solid suspension using the values calculated for $Fr_S s^{0.5}$ and Fr_T^2.

3. Calculate $X_{\Delta P0}$

4. If necessary ($\phi_S > 0.25$) calculate $X_{\Delta P}$ from Equation 7-66

5. $\frac{\Delta P_S}{L}$ is then calculated using Equation 7-64

Figure 7-18. Molerus Diagram for Suspension Transport Data. Diagram can be obtained from both Selah (2002) and Molerus (1993)
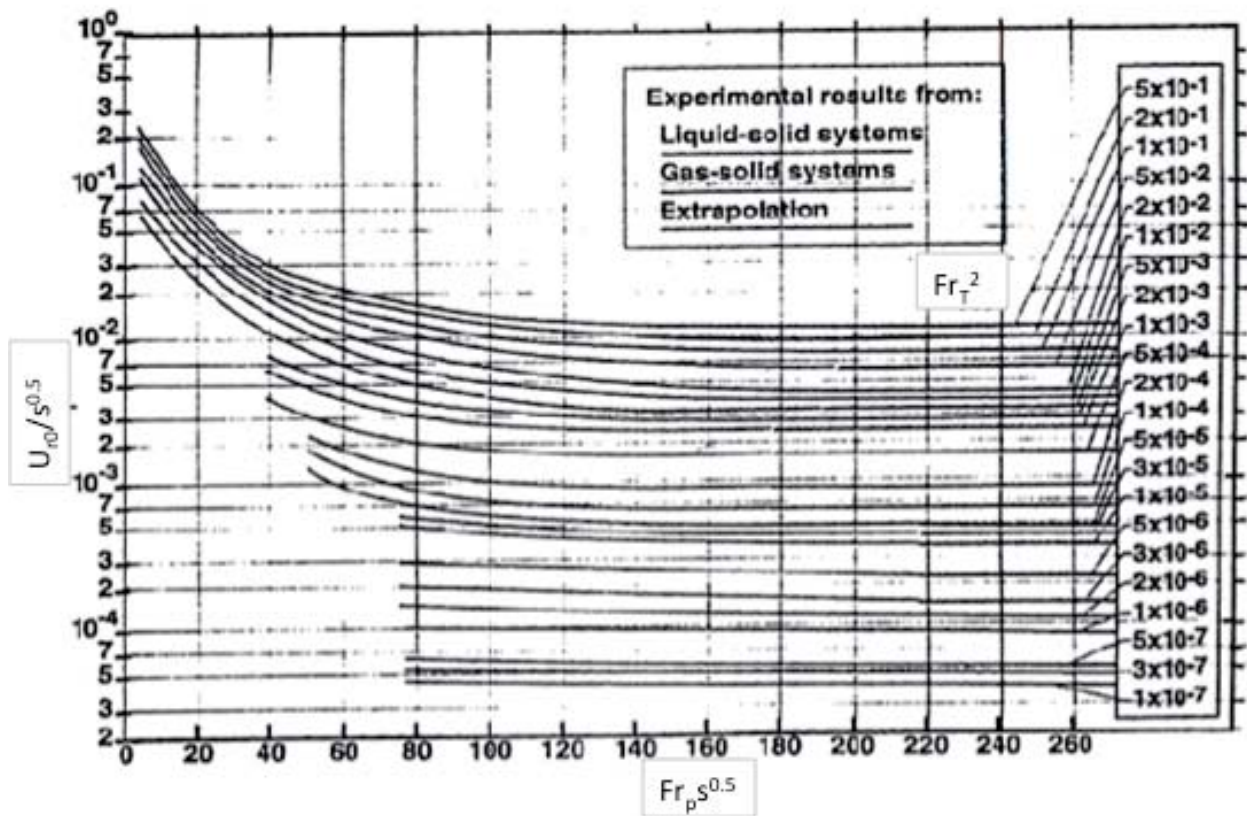
After obtaining $\frac{\Delta P_S}{L}$, the pressure gradient $\frac{\Delta P_F}{L}$ can be calculated from the Fanning equation

$$\frac{\Delta P_F}{L} = \frac{2f\rho_F U^2}{D_T} \qquad (7-67)$$

The friction factor for pipe flow (f) can be defined in terms of the shear stress at the pipe wall (τ_w) such that

$$f = \frac{2\tau_w}{\rho_m U^2} \qquad (7-68)$$

The pressure gradient resulting from solids for specific particle size ranges (bins) or species of solids can be considered individually such that n constituents of volume concentration Φ_{Si} having d_{si} and ρ_{si} would result in

$$\Delta P_m = \Delta P_F + \sum_{i=1}^{n} \Delta P_{si} \tag{7-69}$$

Again, a portion of the non-settling, uniformly suspended solid constituents may be considered part of the fluid and these materials would not be considered as part of the n solid constituents. For multiple solid materials and/or solid sizes, the five steps listed above are repeated for each of the n solid constituents/size ranges to obtain $\sum_{i=1}^{n} \frac{\Delta P_{si}}{L}$.

The particle terminal velocity, U_t and the friction factor, f, are dependent on the fluid rheology. Non-Newtonian behavior for the fluid changes the process by which these parameters are calculated. The following subsections will provide the method for obtaining these parameters for Newtonian and Bingham plastic modeled fluids.

7.3.3.3   *Settling Velocity*

For Newtonian flow in a quiescent fluid, a particle settling velocity can be determined via Equations 7-1 and 7-2. The equations for determining U_t for an un-sheared Bingham plastic were presented in Section 7.2.3 where $U_r = U_t$ in Equations 7-43 through 7-47.

7.3.3.4   *Friction Factor for Pipe Flow*

For Newtonian fluids, the friction factor can be obtained using the Moody diagram (Crane 1986), which was based on the following equation developed by Karman and modified by Colebrook (Crowe 2006).

$$\frac{1}{f^{0.5}} = -4.0 \log \left[\frac{\varepsilon/D_T}{3.7} + \frac{1.255}{\text{Re } f^{0.5}} \right] \tag{7-70}$$

where ε = absolute roughness or effective height of pipe wall irregularities (surface roughness of 0.0018 inch assumed for 304L SS)

Churchill (1977) provided an equation explicit in f and applicable to both smooth and rough pipe surfaces in either laminar or turbulent flows.

$$f = 2 \left[\left(\frac{8}{\text{Re}} \right)^{12} + (Z_1 + Z_2)^{-1.5} \right]^{1/12} \tag{7-71}$$

where

$$Z_1 = \left[2.457 \ln \left(1/Z_3 \right) \right]^{16} \quad Z_2 = \left(\frac{37,350}{\text{Re}} \right)^{16} \quad Z_3 = \left[\left(\frac{7}{\text{Re}} \right)^{0.9} + 0.27 \left(\frac{\varepsilon}{D_T} \right) \right] \tag{7-72}$$

Again, a Bingham plastic is modeled by defining a limiting viscosity, μ_B and Bingham plastic yield stress, τ_B. To determine the friction factor, f_B, in a Bingham plastic, the Bingham Reynolds number, Re_B and Hedstrom number, He, are calculated. The friction factor can be determined from a combination of the friction factors for laminar, f_L and turbulent flow, f_T as

$$F_B = (f_L^m + f_T^m)^{1/m} \qquad (7-73)$$

where

$$m = 1.7 + \frac{40{,}000}{Re_B} \qquad (7-74)$$

$$f_L = \frac{16}{Re_B}\left[1 + \frac{1}{6}\left(\frac{He}{Re_B}\right) - \frac{1}{3}\left(\frac{He^4}{f_B^3 Re_B^7}\right)\right] \qquad (7-75)$$

$$f_T = 10^\beta Re_B^{-0.193} \qquad (7-76)$$

$$\beta = -1.41\left[0.146\,e^{-2.9 \times 10^{-5} He}\right] \qquad (7-77)$$

7.3.3.5 *Calculations, Non-Newtonian Yield Stress Fluid, Horizontal Transfer Pipeline*

The possibility of horizontal pipeline transfer in a *n*-Newtonian yield stress fluid is considered for two particles having: (1) the maximum particle density and size limit for that density, 19 g/mL and 100 μm, and (2) the potential maximum size and density particle in AY-102, 1268 μm and 8.9 g/mL, in a non-Newtonian yield stress fluid. Both of these particle cases are included in Table 4.9. These particles were shown in Figure 7-16 to exceed the 6 ft/s transfer pipeline limit in Newtonian flow. It is assumed that the fluid is comprised of the bounding liquid at 1.37 g/mL and 10 wt% UDS at a typical UDS composite density of 2.46 g/mL (RPP-PLAN-51625) for a suspending fluid density of ~ 1.43 g/mL. The effective viscosity of this fluid is approximated by achieving a calculated critical velocity of 6 ft/s from the Oroskar and Turian (1980) model as listed in Table 7-6.[17] The Bingham viscosity required for this effective viscosity with the Bingham yield stress set to 10 Pa (reasonable upper bound, see Figure 6-2) is then determined via Equation 7-52. These Bingham parameters compare reasonably with the upper bounds of Section 6, thus indicting that it is plausible that the 19 g/mL, 100 μm and 1268 μm, 8.9 g/mL particles could potentially be transferred in the horizontal pipeline.

However, as described previously, the flow must be turbulent. With the Table 7-6 Bingham Reynolds number and yield number in Table 7-6, it is determined from Figure 7-17 that the flow required for the 19 g/mL, 100 μm particle is not turbulent, while the flow for the 1,268 μm, 8.9 g/mL particle is turbulent. The latter particle is thus demonstrated to be transferred at 6 ft/s

---

[17] From Section 7.3.1, the Oroskar and Turian (1980) model was developed for fully turbulent Newtonian flow. Application of the model to a non-Newtonian flow, noted as commonly applied with an apparent viscosity can over-predict the non-Newtonian pipeline transport test results of PNNL-17639 depending on the test case.

in a plausible non-Newtonian yield stress fluid, but the effect of the increased rheology must be considered relative to the maximum 400-psi transfer pipeline pressure limit, Table 3-4. The calculated pressure gradient per length of pipeline from Equations 7-58 through 7-77 are provided in Table 7-7 together with the limiting pipeline length at a limiting pressure of 400 psi. The calculated length is less than the WFD system feed tanks to WTP minimum pipeline length for HLW of 5,232 ft (0.99 miles) from Section 3 (see Figure 3-1 and Table 3-4; Tank AW-103[18]), indicating that the 1268 μm, 8.9 g/mL particle cannot be transferred at 6 ft/s in a plausible non-Newtonian yield stress fluid for that pipeline pressure limit and length.

Although the estimated Bingham parameters in Table 7-6 are plausible with respect to the waste data, ICD-19 (24590-WTP-ICD-MG-01-019) currently places an upper limit of 1 Pa for the Bingham yield stress for waste delivered to the WTP. However, this value is noted as still under investigation and may change (summarized in RPP-PLAN-51625). The upper limit for the Bingham viscosity is listed as 10 cP (24590-WTP-ICD-MG-01-019). If retrieved slurries exceed these limits, in-line dilution could be used as needed to reduce the rheology of the retrieved waste to meet the specified limit of waste feed to the WTP. Specific plans for waste retrieval, blending, and dilution to meet a specific rheology limit for delivered waste are not yet available, but it is expected that waste will be blended and staged in a manner that avoids the retrieval of waste with very high rheologies that will require a large amount of transfer line inlet dilution.

Also provided in Table 7-6 are the calculated parameters assuming a 1 Pa Bingham yield stress. As for the 10 Pa Bingham yield stress results, the flow required for the 19 g/mL, 100 μm particles is not turbulent, and although the rheology required for the 1268 μm, 8.9 g/mL particle could be plausible, the ICD-19 Bingham viscosity limit is exceeded. The calculated pressure gradient per length of pipeline for this latter particle is also provided in Table 7-7 as less than the minimum length of 0.99 miles. Regardless of the pipeline length limits, given the ICD-19 rheology limits, it is unlikely that the actual WTP feed delivery transfers will be conducted at the elevated rheology of Table 7-7 , which would again result in the limiting particle cases not transferring. Therefore, the transfer of the potential limiting particles via an alternate flow regime wherein these particles may be transferred is evaluated.

[18] AW-103 has a minimum distance of 17 feet between a mixer pump and transfer pump (Hanford Drawing 4-010502, Sheet 3). As described in Section 7.1.3, the potential limiting waste particles of Table 4-9 are exceeded by the calculated limits of performance of the jet mixer pumps for the AY-102 configuration (~22.8 ft mixer pump to transfer pump distance), so shorter distances between the mixer pump and transfer pump are not evaluated further.

Table 7-6 Non-Newtonian Parameters for Limiting Particle Cases

Particle		Calculated Effective Viscosity for 6 ft/s (cP)	Bingham Parameters		Re_B (Eq. 7-53)	He (Eq. 7-54)	Y (Eq. 7-55)	Turbulent Flow? [Fig. 7-17]
Size (μm)	Density (g/mL)		τ_B (Pa)	μ_B (cP)				
100	19	121	10	51	3,901	31,745	8.1	no
1268	8.9	76	10	6	32,561	2,211,470	67.9	yes
100	19	121	1	114	1,757	644	0.4	no
1268	8.9	76	1	69	2,910	1,767	0.6	yes

Table 7-7 Pressure Gradient and Pipeline Length for Limiting Particle Cases, Turbulent Flow Cases

Particle		Bingham Parameters		dP_S/dL (Pa/m) (Eq. 7-64)	dP_F/dL (Pa/m) (Eq. 7-67)]	dP_m/dL (Pa/m) (Eq. 7-58)	Pipeline Length, 400 psi limit (miles)
Size (μm)	Density (g/mL)	τ_B (Pa)	μ_B (cP)				
1,268	8.9	10	6	2,901	878	3,779	0.45
1,268	8.9	1	69	2,901	768	3,669	0.47

7.3.3.6 *Horizontal Transfer Pipeline Alternate Flow Regime*

While operating a slurry line in the presence of solids deposition is often considered undesirable, particle transport via sliding particles or a moving bed can still result in solids transport down the pipeline. This flow regime is beyond the limits of deposition as the limiting phenomena. Because particle transport via sliding particles or a moving bed is often considered an undesirable operating condition, the effort put forth to evaluate the flow of deposited solids has been limited in comparison to that applied toward predicting U_{cd}. In addition:

- For evaluating the limiting conditions for solids transport, the parameter of interest is the minimal velocity that can exist for sliding solids, referred to here as the minimal moving bed velocity, U_{mmb}.

- Past efforts have indicated that models of data for sliding solids have not been sufficient to obtain useful methods of prediction. The coupling of the various flow conditions and slurry profiles that occur simultaneously require physical or mechanistic models. To develop these complex types of models knowing "what happens" needs to be accompanied by a firm understanding of why things happen.

Based on additional analysis and empirical data, Doron and Barnea (1993, 1995, and 1996) have made an extensive effort to predict the occurrence of U_{mmb} through the development of a three-layer model presented in Crowe (2006). A schematic depicting the model conditions is presented in Figure 7-19 and the associated model assumptions are a uniform stationary bed of solids at the bottom of the pipe with an interface layer parallel to the axis of the pipe.

- A uniform moving bed of solids on top of the stationary bed with upper and lower interface layers parallel to the axis of the pipe.

- The moving bed has a uniform concentration of ϕ_{mb}, which is assumed 0.52 for cubic packing.

- A heterogeneous flow of suspended particulate exists in the upper region of the pipe.

- The pipe has an inclined angle of β.

The model is based on identifying a minimal bed velocity, U_{mmb}, which exists at the surface of the stationary layer. At velocities (and depths) below U_{mmb}, the velocity goes to zero and the particles are stationary while the moving bed above the location of U_{mmb} also moves at U_{mmb}. If the stationary bed does not exist, than the bed moves at U_{mb}. The three-layer model is described by a set of six equations for six unknowns: U_F, U_{mb} (which in the existence of a stationary bed is equal to U_{mmb}), U_{mmb}, ϕ_h (the solids concentration in the heterogeneous free stream), z_{mb} and z_{sb}, which respectively are the bed heights for the moving and stationary bed layers. The entire model will not be presented because assumptions made for determining the limiting transport conditions greatly simplify the model for application to this assessment.

Figure 7-19. Schematic for Presenting the Conditions of the Three-Layer Model

For the limiting case of particle transport for deposited solids, the following conditions apply.

- The depth of the stationary bed goes to zero and the condition of interest is when the moving bed is moving at its minimal velocity, U_{mmb}. In others words, any change in conditions that would increase the impedance to particle transport would result in the formation of a stationary bed being initiated. This conditions leads to $z_{sb} \approx 0$ (infinitely small) and $U_{mb} = U_{mmb}$.

- The solids loading in the process stream goes to zero as all solids that can settle have settled. Any suspended solids are fines that cannot settle and are considered part of the carrier fluid contributing to its bulk velocity and density. For this condition, $\phi_h = 0$.

- The free stream velocity U_F must be less than U_{cd}. In order for the previous assumption to hold, the flow conditions in the pipe have to be conducive for solids deposition.

- For the previous assumption to be assessed using Equation 7-50, the flow must be turbulent.

- The velocity of the free stream, U_F, is set to the transfer line operating velocity (velocity of condition to be assessed).

- The depth of the moving bed is set to the minimum depth, $z_{mb} = d_S$, as increases in depth result in an increase in the minimum bed velocity, U_{mmb} and increases U_{cd}.

- The inclined angle for the pipe is zero, $\beta = 0$.

This results in one equation with one unknown as

$$U_{mmb} = \frac{\sqrt{1.55(\rho_S - \rho_F)gd_s\left[\sin\left(\frac{\pi}{6} + \beta\right) + \frac{\cos\beta}{2}\phi_{mb}\left(\frac{z_{mb}}{d_S} - 1\right)\right]}}{\rho_F C_D} \qquad (7-78)$$

Because the drag coefficient, C_D, is dependent on the relative velocity of the particle, which is a function of U_{mmb}, Equation 7-78 must be implicitly solved for a convergence of C_D relative to $Re_r = f(U_r)$. Equation 7-27 is used to calculate U_r, where V is replaced by U_{mmb}. Equations 7-32 through 7-35 are used to determine C_D. The effects of non-Newtonian flow are accounted for in the determination of C_D, which is presented for a Bingham plastic model fluid in Equations 7-43 through 7-49.

It should be noted, the three-layer model is intended for use for any given set of operational slurry flow conditions. U_{cb} can be obtained when z_{mb} approaches zero (Doron and Barnea, 1995) and the applied assumptions for obtaining the limiting case of U_{mmb} did not impact the applicability of the model. The three-layer model was not employed in place of Equation 7-50, the Oroskar-Turian model, because of the wider range of conditions over which the Oroskar-Turian model has been successfully applied or verified. Future efforts to expand the application or verification of the three-layer model may prove it a more representative model than Oroskar-Turian.

The sliding bed velocities of the smaller, more dense particles (than 2,650 µm, 5.8 g/mL) for the mixer pump limit shown in Figure 7-16 are evaluated in the representative bounding liquid. The expression for the minimal bed velocity is evaluated for these particles using Equations 7-32 through 7-35 with the relative particle velocity dependent on the minimal bed velocity U_{mmb}, Equation 7-78, instead of the particle velocity V. With the height of the moving bed set to minimize the minimal bed velocity at the particle diameter, the smaller, more dense particles than 2650 µm, 5.8 g/mL are estimated to move along the pipeline floor at ~ 0.01 m/s. This indicates that they will traverse the pipeline length of a WFD system feed tank to the WTP of 0.99 miles in approximately 42 hours. If the height of the moving bed is increased to twice the particle diameter (i.e., the quantity of the material moving in the sliding bed is increased) with the total flow held constant, the calculated transit time is reduced to ~ 30 hours.

The pressure gradients for the larger, less dense particles (less than 2650 μm, 5.8 g/mL, Figure 7-16) for the mixer pump limit at a concentration of 1 vol% are evaluated using Equations 7-58 through 7-77 in the Newtonian bounding liquid. The calculated pipeline length at the 400-psi pressure limit is shown in Figure 7-20. These estimates based on the system pressure limit do not take into consideration elevation changes in the pipeline or pressure (head) loses due to pipe components/changes in flow direction. For the smaller, denser particles moving as the sliding bed, the pressure gradient for these particles is also evaluated.

7.3.3.7 *Pressure Drop for Sliding Bed*

In the case of a sliding bed, the methodology for predicting the pressure gradient that was applied in Section 7.3.3.2 is not applicable. The earlier discussion also applies to why limited developments exist for predicting of the pressure gradient associated with a moving bed. While the three-layer model can provide a prediction for the pressure gradient, a simplified approach has been chosen due the assumptions employed for assessing the limiting particle size for transport.

Turian and Yuan (1977) provide an approach that is applicable over a range of slurry flow patterns as presented in Crowe (2006). Friction factors f_F and f_S are defined for the liquid and solid phases, respectively, with both being applied at the same mean slurry velocity, U, and in terms of the carrier liquid density, ρ_F. Assuming a Newtonian fluid, Equation 7-71 is used to obtain f_F. The friction factor f_S is defined by Turian and Yuan (1977) as

$$f_s = K_1 \phi_S^{K_2} f_F^{K_3} C_D^{K_4} \left[\frac{U^2}{D_T g(s-1)} \right]^{K_5} + f_F \qquad (7-79)$$

where, K_1 through K_5 are slurry-flow regime-specific coefficients defined in Table 7-8 and C_D is calculated the same as for the vertical flow and the sliding bed particles, Equations 7-32 through 7-35. The pressure gradient is determined from

$$\frac{\Delta P}{L} = -\left(\frac{2 f_S \rho_F U^2}{D_T} \right) \qquad (7-80)$$

which is the same as Equation 7-67 except with the revised friction factor, f_S.

Table 7-8 Coefficients for Turian-Yuan Friction Factor Model of Equation 7-79

Slurry Flow Regime	K_1	K_2	K_3	K_4	K_5
Homogeneous suspension	0.8444	0.5024	1.428	0.1516	-0.3531
Heterogeneous suspension	0.5513	0.8687	1.200	-0.1677	-0.6938
Moving solids bed	0.9857	1.018	1.046	-0.4213	-1.354
Stationary solids layer	0.4036	0.7389	0.7717	-0.4054	-1.096

The calculated pipeline lengths at 400 psi for the smaller, denser particles (than 2,650 μm, 5.8 g/mL) moving as the sliding bed are also shown in Figure 7-20. The solid concentration is again 1 vol% in the bounding liquid.

Figure 7-21 provides a representative plot of the pressure gradient as a function of the mean slurry velocity. The assumptions imposed for determining U_{mmb} result in a mean velocity immediately to the right of U_{csb}. As observed from the plot, the pressure gradient for a given solids loading is expected to be at a minimum at the onset of the formation of a moving bed. Therefore, higher pressure gradients within the pipe will exist for fully suspended flows where $U > U_{cd}$, which explains the reduced limits in the calculated 400 psi pipeline length for the suspended particulate, Figure 7-20. The limiting particles for the mixer pump, which encompass the potential limiting waste particles, are shown to meet or exceed the pipeline length from the WFD system feed tank to WTP of 0.99 miles under the 400 psi limiting pressure.

Figure 7-20. Calculated Pipeline Length of Transfer with 400 psi Limit
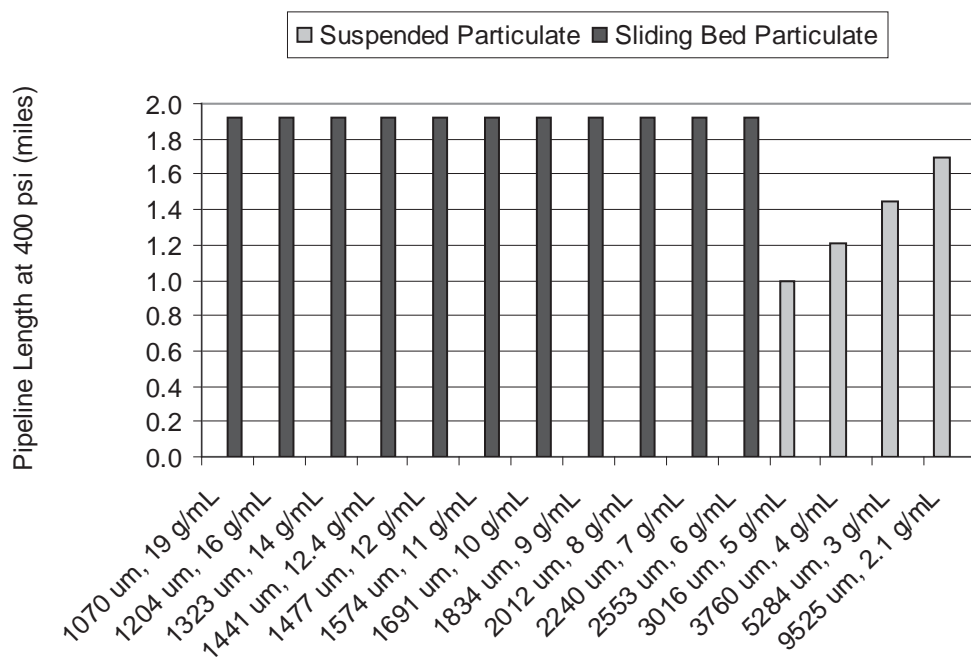
Figure 7-21. Pressure Gradient as a Function of Pipeline Superficial Velocity
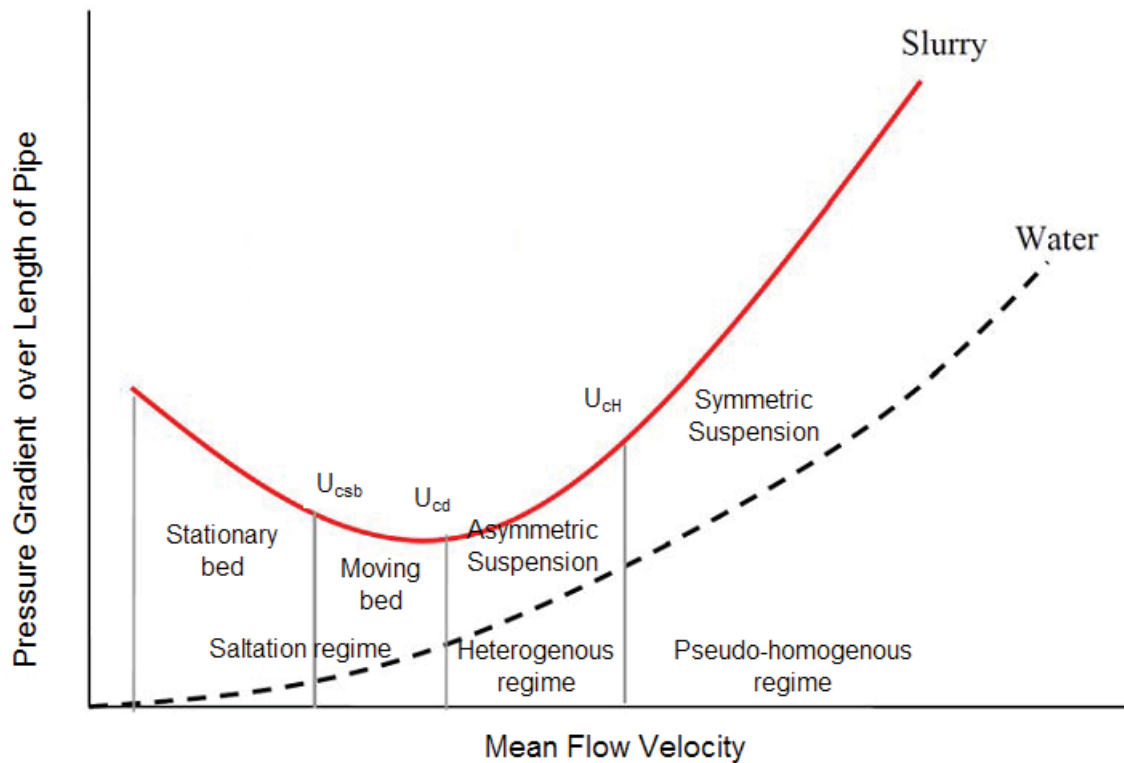
7.4 SYSTEM PERFORMANCE CAPABILITIES SUMMARY

The capabilities of the WFD system to transfer large-dense particulate were evaluated using simple models from the literature. The evaluation identified the limits of performance of the WFD system, including the mixer pumps and the vertical and horizontal legs of the transfer pipeline, with respect to UDS particle size and density. Where possible, a simple model approach was compared to full-scale process data and scaled test data, and reasonable agreement was demonstrated.

WFD system components analyzed for limits of performance with respect to UDS particle size and density include:

- Jet mobilization and transport of particles to the transfer pump.
- Particle entrainment into the transfer pump.
- Particle motion in the vertical transfer pipeline.
- Particle transfer in the horizontal pipeline.

Limiting cases were evaluated via literature-based models and/or force balance on individual particles. Assumptions made include:

- Single particle (density, size, minimum projected area (spherical particles).

- Rheology - Newtonian and Bingham plastic (homogeneous slurry for carrier fluid properties).

- Model uncertainties were not accounted for.

- The probability that the limiting particle is available (with respect to actual waste concentration, initial particle location in the vessel, etc.) is not evaluated.

- No limits or restrictions are evaluated between the WFD system components (e.g., elbows, valves, etc.).

- Assumed steady-state conditions.

The WFD system transport limit capabilities are determined for waste properties established by characterization of the Hanford waste and the evaluated uncertainties of that characterization data. The line in Figure 7-22 corresponds to the WFD system limit for particle transport, where particles are represented by size and density combinations. The WFD system is capable of delivering to the WTP the particles (as identified with size and density) that lie on or to the left of the line. The particles that lie to the right of the line exceed the WFD system capabilities. The potential limiting waste particles (maximum size and density) listed in Table 4-9 are to the left of the WFD system particle transport limit as denoted in Figure 7-22. Hence, it is concluded that the potential limiting waste particles from Table 4-9 do not exceed the limits of performance of the WFD system.

The limiting component and associated mechanism is the transport of particulate via the jet mixer pump to the transfer pump inlet assuming that transfer in the horizontal pipeline can occur via sliding particle beds. The influence of non-Newtonian yield stress fluid properties (Bingham plastic modeled fluid) on the evaluations was considered. While the influence of non-Newtonian fluid properties may increase the capability of one or more components in the WFD system, the potential limiting waste particles are always exceeded by the limits of performance with a Newtonian fluid. Thus the Newtonian fluid limits of performance provide a suitable upper bound for the WFD system capabilities. Because the identified WFD system limit exceeded the potential limiting waste particles, other potential less-limiting mechanisms for particle transport that exist were not considered as relevant.

Figure 7-22. WFD System Particle Transport Limit. Representative Bounding Liquid (1.37 g/mL, 14 cP), Limiting Pipeline Length, and Pressure, 0.99 miles, 400 psig
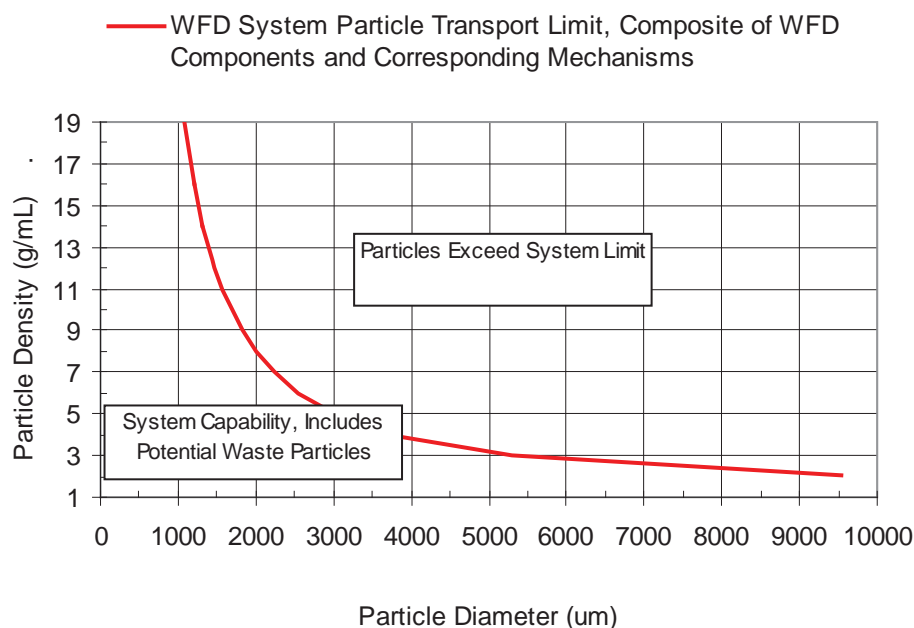
7.5   PLANNED LARGE-SCALE TESTS

Limits-of-performance testing using full-scale equipment is planned to determine the ranges of waste physical properties that can be mixed, sampled and transported under varying modes of operation. Small-scale test results (RPP-47557) will be used to help select instrumentation and placement of this instrumentation for an eventual full-scale demonstration of tank mixing performance.

7.5.1   Transfer Pump Evaluation

Commercially available pumps have been examined and no submersible slurry pump that is capable of conveying HLW slurry from the bottom of the DST to the WTP receipt tank (without an intermittent booster pump or exceeding the pressure limits of the transfer piping) is available. A customized pump to meet WFD requirements is under development, but this pump will not be completed in time to support limits-of-performance testing and the initial gap analysis. Therefore, a commercially available pump that has the flow capability and inlet velocity of the proposed pump without the high head requirements will be used for full-scale transfer pump limits-of-performance test activities. The final Gap Analysis (DNFSB 2010-2 Commitment 5.5.3.9) will address the impacts of testing results and the correlation to the final transfer pump design which is scheduled to be completed before the final Gap Analysis is issued.

The procured transfer pump will be placed into a mixing tank such that the pump inlet location is consistent with the AY-102 transfer system configuration. Simulant, including large diameter

spike particles, will be mixed and pumped through a network of pipes that mimic the flow from the bottom of a DST to the location of the Ultrasonic PulseEcho system in the WFD characterization flow loop. The slurry will be pumped vertically through 55 feet of 3-inch NPS, Schedule 40 piping, through a 90° bend and then horizontally through 20 feet of 3-inch NPS, transparent Schedule 40 plastic piping so that the flow can be observed. The spike particulates in the mobilized slurry will be collected and quantified from the end of the horizontal run so that the capability of the pump to transfer large and dense particles out of the DST can be assessed.

After testing is completed, the horizontal transfer line will be flushed (>140 gpm) and the discharge will be screened to collect the large and dense particles that were captured by the pump but settled out in the transfer line prior to reaching the sample location. The screened material will then be sieved to separate the different particle sizes. The spatial distribution of the large and dense particles remaining in the mixing tank will also be reported so that the mixing systems capability to deliver the large and dense particles to the area of influence of the transfer pump can be considered in the analysis of mixer pump capabilities.

7.5.2   Mixer Pump Demonstration

A full-scale demonstration is planned on the first WTP feed tank, AY-102. This work will be closely coordinated with the DST upgrade projects, which will be responsible for procuring and installing the baseline equipment anticipated to be needed for WTP feed acceptance and delivery. Any unique instrumentation necessary to verify the feed acceptance and delivery systems are performing up to requirements will be identified, procured, and installed.

Figure 7-23 shows an initial concept for equipment placement in tank AY-102. Slurry density monitors will evaluate vertical and radial mixing during mixer pump operation and results will be corroborated with data from small scale mixing results. The full-scale test will evaluate the effectiveness of the optimized system configuration and will ensure the tank farm systems are able to support delivery of the first waste to the WTP.

Figure 7-23. Initial Concept for Mixer Pump Demonstration
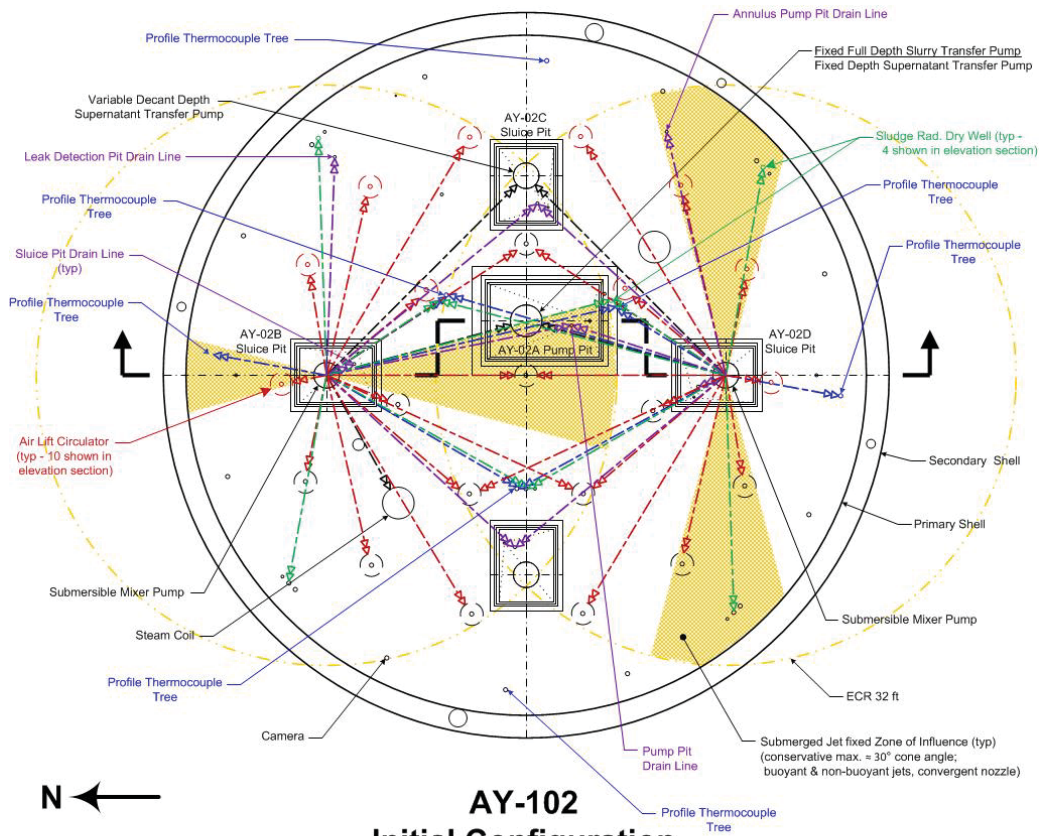
AY-102
Initial Configuration

SMP Jet Forces on In-Tank Equipment
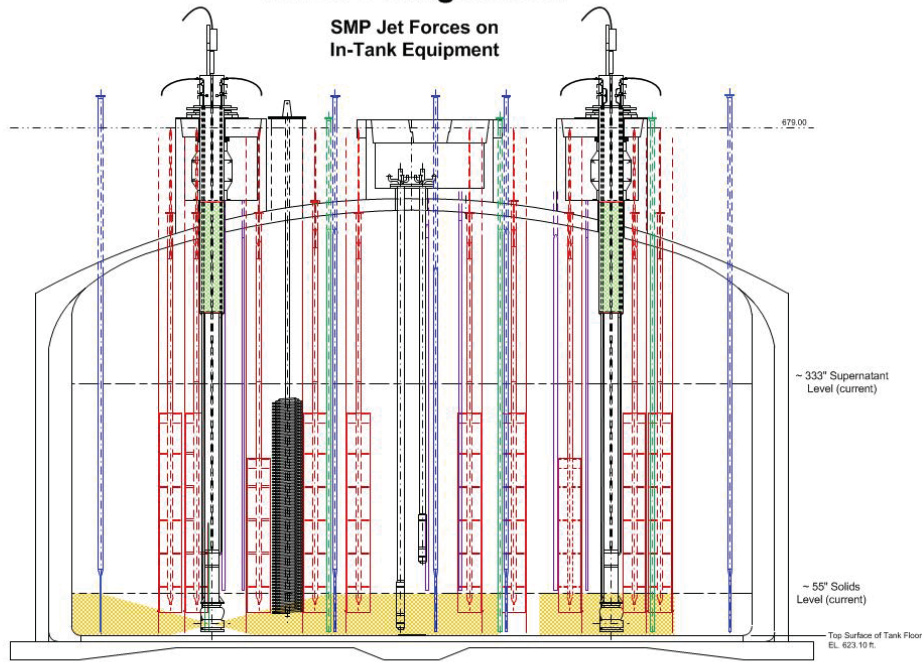
ITU-SK-037-02 Rev. 0

8.0   CONCLUSIONS

This report provides a preliminary examination of the ranges of physical properties for waste that is anticipated to be transferred to the WTP over the mission in response to DNFSB Recommendation 2010-2, *Pulse-Jet Mixing at the Waste Treatment and Immobilization Plant*, issued on December 17, 2010. The following are included in this report:

- A review of the retrieval and transfer system (Section 3).

- A description of waste undissolved solids, characterization uncertainties, and variation (Section 4).

- A description of waste liquid, characterization uncertainties, and variation (Section 5).

- A description of waste rheology, characterization uncertainties, and variation (Section 6).

- A determination of retrieval and transfer system capabilities (Section 7).

Important conclusions from each section are provided below.

8.1   WASTE FEED DELIVERY SYSTEM

Section 3 summarizes the WFD system including initial concepts for mixer pumps, transfers pumps and a flow loop with remote sampling capability. This section also summarizes transfer line pipe lengths that are used in the retrieval and transfer system capabilities section. Mixer pump performance parameters include the ability to discharge fluid at a velocity of 59 ft/s through two opposed 6-inch nozzles. The transfer pump specifications include the ability to transfer slurries of up to 1.5 SpG with a viscosity of up to 20 cP. The transfer line lengths from the proposed feed tanks to WTP range from 3,758 to 6,917 feet and are limited to a pressure of no more than 400 psig.

8.2   UNDISOLVED SOLIDS

Section 4 reviews the mineralogy, density, and particle size for UDS in Hanford Site tank farm waste. The largest particles or agglomerates are most likely predominately gibbsite. The densest particle is Pu metal (19 g/mL) and has been hypothesized to be as large as 100 µm. The largest UDS waste particle that might hypothetically be in waste feed is 9,525 µm (⅜-inch) and would most likely have a density of a gibbsite agglomerate (1.43 g/mL). Large agglomerates have been found in SST heel samples of retrieved tanks and some large particles will likely be in the HLW feed DSTs. Long-term storage in DSTs and planned WFD operations are judged not likely to eliminate large particles/agglomerates.

8.3 LIQUID WASTE

Section 5 discusses the available data, models, and model predictions for physical properties of the liquid phase of Hanford tank wastes. The physical properties include the liquid density, and liquid viscosity. Uncertainties in property data or model predictions and variation in properties (over the WTP mission) are discussed and quantified. Replicate measurements of SpG available for a large number of liquid waste samples from Hanford tanks were used to quantify the measurement uncertainty.

For individual SpG measurements, the SD was 0.0146 and the 95% PI was ±0.0286. A data set that had complete compositions of dissolved solids as well as measured SpGs (ranging from 0.97 to 1.58) was used to assess the performance of the liquid-density model included in HTWOS. That model tends to: slightly over-predict SpGs below 1.08, accurately predict for 1.08 to 1.34, over-predict for 1.34 to 1.54, and possibly under-predict above 1.54. The random uncertainty of SpG model predictions was SD = 0.0293 and 95% PI = ±0.0574 for SpG ≤ 1.27, and SD = 0.0489 and 95% PI = 0.0958 for SpG > 1.27.

A new model for liquid viscosity as a function of temperature and liquid density was developed to improve some aspects of the model used in PNNL-20646. The new liquid-viscosity model is still subject to considerable uncertainty because liquid density is an imperfect representative for the effects of dissolved solids on liquid viscosity. The data used to develop the model did not have complete compositions of dissolved solids, so it was not possible to develop a model as a function of dissolved solids composition. The models for liquid density and viscosity were applied to waste feed batches from the HTWOS run of the Baseline Case in ORP-11242. For batches dated from 5/31/2018 to 4/24/2039 (prior to the end-of-mission activities), the model-predicted values ranged from 1.14 to 1.37 kg/L for liquid density and 2.44 to 8.00 cP for liquid viscosity. Accounting for model uncertainties, the ranges are 1.08 to 1.47 kg/L for liquid density and 0.80 to 13.54 cP for liquid viscosity.

8.4 RHEOLOGY

Section 6 reviews the available rheology data and displays separate plots for each tank with data. Focusing on only the sludge data, viscosity ranged from near 1 cP at 0.1 wt% solids to slightly more than 100 cP at 18 wt% solids. Yield stress data ranged from near 0.3 Pa at 1-wt% solids to near 80 Pa at 18 wt% solids. Yield stress data were fit with a power law function for various temperature ranges and viscosity data were fit with an exponential function for various temperature ranges. These fits were then used to predict yield stress and viscosity at 10 wt% UDS through interpolation or extrapolation. Except for one outlier (C-109), yield stress predictions at 10-wt% UDS fell within a range of less than 0.01 to 12 Pa. Similarly, viscosity predictions fell within a range (except for the same C-109 outlier) of 0.42 to 7.1 cP.

A literature review for the potential effects from waste mixing and blending suggests a complicated relationship between particles sizes, solids fraction, particle and liquid densities, and repulsive and attractive forces. No good predictive tool exists for estimating yield stress and viscosity in mixed/blended wastes. Waste feed samples taken from the flow loop with the

remote sampler will be tested for rheological properties. It is likely that the ranges of yield stress and viscosity for all the future HLW feed batches will be greater than the data ranges listed here.

8.5   RETRIEVAL AND TRANSFER SYSTEM CAPABILTIES

Retrieval and transfer system capabilities were evaluated using simple models from the literature. The evaluation identified the limits of performance of the WFD system, including the mixer pumps and the vertical and horizontal legs of the transfer pipeline, with respect to UDS particle size and density. Where possible, a simple-model approach was compared to full-scale process data and scaled test data, and reasonable agreement was demonstrated.

WFD system components analyzed for limits of performance with respect to UDS particle size and density include:

- Jet mobilization and transport of particles to the transfer pump

- Particle entrainment into the transfer pump

- Particle motion in the vertical transfer pipeline

- Particle transfer in the horizontal pipeline

The WFD system transport limit capabilities are determined for waste properties established by characterization of the Hanford waste and the evaluated uncertainties of that characterization data. The limits of performance of the WFD system exceed the identified potential limiting waste particles, which are particles at the largest potential density and size that might occur in the waste. That is, transport of the postulated 100-µm, 19 g/mL Pu metal particle from a DST to WTP is possible. Similarly, transport of the large 9,525-µm 1.43 g/mL gibbsite agglomerate is also possible. The limiting component and associated mechanism is the transport of particulate via the jet mixer pump to the transfer pump inlet assuming that transfer in the horizontal pipeline can occur via sliding particulate. The influence of non-Newtonian yield stress fluid properties (Bingham plastic modeled fluid) on the evaluations is considered. While the influence of non-Newtonian fluid properties may increase the capability of one or more components in the WFD system, the potential limiting waste particles are always exceeded by the limits of performance with a Newtonian fluid. Thus the Newtonian fluid limits of performance provide a suitable upper bound for the WFD system capabilities. Because the identified WFD system limit exceeded the potential limiting waste particles, other potential less-limiting mechanisms for particle transport that exist were not considered as relevant.

9.0 REFERENCES

24590-HLW-PL-RT-07-0001, 2011, *IHLW Waste Form Compliance Plan for the Hanford Tank Waste Treatment and Immobilization Plant*, Rev. 3, Bechtel, Richland, Washington.

24590-WTP-ICD-MG-01-019, 2011, *ICD 19 – Interface Control Document for Waste Feed, Rev. 5, Bechtel*, Richland, Washington.

24590-WTP-RPT-MGT-04-001, 2011, *Regulatory Data Quality Objectives Optimization Report, Rev. 0, Bechtel,* Richland, Washington.

24590-WTP-RPT-MGT-11-014, 2011, *Initial Data Quality Objectives for WTP Feed Acceptance Criteria*, Rev. 0, Bechtel, Richland, Washington.

74A10-WSC-08-152, 2008, *Results of Testing Performed to Characterize Tank 241-S-112 Heel Solid*, Rev. 0, CH2M Hill Hanford Group, Inc., Richland, Washington.

Agelin-Chaab M. and M.F. Tachie, 2011, "Characteristics and Structure of Turbulent 3D Offset Jets," International Journal of Heat and Fluid Flow 32: 608-620.

ASTM D 4318 - 10, *Standard Test Methods for Liquid Limit, Plastic Limit, and Plasticity Index of Soils*, ASTM International, West Conshohocken, Pennsylvania.

Bain J.A., 1971, "A Plasticity Chart as an Aid to the Identification and Assessment of Industrial Clays," Clay Minerals 9: 1-17.

Beheshti A.A. and B. Ataie-Ashatiani, 2008, "Analysis of Threshold and Incipient Conditions for Sediment Movement," Coastal Engineering 55(5): 423-430.

Bhuiyan F., A. Habibzadeh, and N. Rajaratman, 2011, "Reattached Turbulent Submerged Offset Jets on Rough Beds with Shallow Tailwater," Journal of Hydraulic Engineering, December 2011, 1636-1648.

Buscall R., I.J. McGowan, P.D.A. Mills, R.F. Stewart, D. Sutton, L.R. White, and G.E. Yates, 1987, "The Rheology of Strongly Flocculated Suspensions," Journal of Non-Newtonian Fluid Mechanics 24: 183-202.

Camenen B., 2007, "Simple and General Formula for the Settling Velocity of Particles," Journal of Hydraulic Engineering 133(2): 229-233.

Channell G.M. and C.F. Zukoski, 1997, "Shear and Compressive Rheology of Aggregated Alumina Suspensions," AIChE Journal 43(7): 1700-1708.

Chhabra R.P., 1993, *Bubbles, Drops, and Particles in Non-Newtonian Fluids*, ISBN 0-8493-6718-2, CRC Press, Boca Raton, Florida.

Chhabra R.P. and J.F. Richardson, 1999, "Non-Newtonian Flow in the Process Industries," ISBN 0-7506-3770-6, Butterworth Heinemann, Woburn, Massachusetts.

Chun J., A.P. Poloski, and E.K. Hansen, 2010, "Stabilization and Control of Rheological Properties of Fe_2O_3/Al(OH)$_3$-rich Colloidal Slurries under High Ionic Strength and pH," Journal of Colloid Interface Science 348: 280-288.

Chun J., T. Oh, M. Luna, and M.J. Schweiger, 2011, "Effect of Particle Size Distribution on Slurry Rheology: Nuclear Waste Simulant Slurries," Colloids and Surfaces A: Physicochemical and Engineering Aspects 384: 304-310.

Clark L.A. and T.M. Wynn, 2007, "Methods for Determining Streambank Critical Shear Stress and Soil Erodibility: Implications for Erosion Rate Predictions," Transactions of the American Society of Agricultural Engineers 50(1): 95-106.

Crowe, C.T., 1998, *Multiphase Flows with Droplets and Particles*, ISBN 0-8493-9469-4, CRC Press, Boca Raton, Florida.

Crowe, C.T., J.A. Roberson, and D.F. Elger, 2001, *Engineering Fluid Mechanics*, ISBN 0-471-38482-8, John Wiley & Sons, Inc., New York, New York.

Crowe, C.T., 2006, *Multiphase Flow Handbook*, ISBN 0-8493-1280-9, CRC Press, Boca Raton, Florida.

Darby R, 1996, *Chemical Engineering Fluid Mechanics*, Marcel Dekker, New York, New York.

DE-AC27-01RV14136, 2001, Waste Treatment and Immobilization Plant (WTP) Contract, U.S. Department of Energy, Office of River Protection, Richland, Washington.

DNFSB Rec. 2010-2, 2011, *Department of Energy Plan to Address Waste Treatment and Immobilization Plant Vessel Mixing Issues, Implementation Plan for Defense Nuclear Facilities Safety Board Recommendation 2010-2*, Rev. 0, U.S. Department of Energy, Washington, D.C..

Dzuy N.Q. and D.V. Boger, 1985, "Direct Yield Stress Measurement with the Vane Method," Journal of Rheology 29(3): 335-347.

Dzuy N.Q. and D.V. Boger, 1983, "Yield Stress Measurement for Concentrated Suspensions," Journal of Rheology 24(7): 321-349.

Elimilech, M., J. Gregory, X. Jia, and R.A. Williams, 1995, "Particle Deposition and Aggregation: Measurement, Modeling, and Simulation," Butterworth and Heinemann, Woburn, Massachusetts.

Gao N. and D. Ewing. 2007, "Experimental Investigation of Planar Offset Attaching Jets with Small Distances, Exp Fluids 42: 941-954".

Goh R., Y.K. Leong, and B. Lehane, 2011, "Bentonite Slurries – Zeta Potential, Yield Stress, Adsorbed Additives and Time-dependent Behavior," Rheologica Acta 50: 29-38.

Gu R, 1996, "Modeling Two-Dimensional Turbulent Offset Jets," Journal of Hydraulic Engineering, November 1996, 617-624.

HNF-6062, 2001, *Tank 241-AZ-101 Grab Samples From Mixer Pump Test Events 5, 7, 8, and 9 Analytical Results for the Final Results for the Report*, Rev. 0, Fluor Hanford, Richland, Washington.

HNF7078, 2000, *Results of Retrieval Testing of Sludge from Tank 241-AZ-101*, Rev. 0, Fluor Hanford, Richland, Washington.

HNF-8862, 2002, *Particle Property Analyses of High-Level Waste Tank Sludges*, Rev. 0, Fluor Hanford, Inc., Richland, Washington

HNF-EP-0182, 2011, *Waste Tank Summary Report for Month Ending December 31, 2011*, Rev. 285, Washington River Protection Solutions, Richland, Washington.

HNF-SD-WM-PCP-013, 1999, *Tank 241-C-106 Waste Retrieval Sluicing System Process Control Plan*, Rev. 2, Lockheed Martin Hanford Corporation, Richland, Washington.

HNF-SD-WM-SP-012, 2007, *Tank Farm Contractor Operation and Utilization Plan*, Rev. 6, CH2MHill Hanford Group, Inc., Richland, Washington.

Hunter R.J, 2001, *Foundations of Colloid Science*, Oxford University Press, New York.

Julien P.Y, 1998, Erosion and Sedimentation, Cambridge University Press, Cambridge, United Kingdom.

Kosmulski M., E. Maczka, and J.B. Rosenholm, 2002, "Isoelectric Points of Metal Oxides at High Ionic Strengths," Journal of Physical Chemistry B 106(11): 2918-2921.

LAB-RPT-10-00001, 2010, *Results of Physicochemical Characterization and Caustic Dissolution Tests on Tank 241-C-108 Heel Solids*, Rev. 0, Washington River Protection Solutions, Richland, Washington

LAB-RPT-11-00008, 2011, *Solid Phase Characterization of Heel Samples from Tank 241-C-110*, Washington River Protection Solutions, Richland, Washington.

LAB-RPT-11-00009, 2011, *Final Report for the Initial Solid Phase Characterization of the 2011 Grab Samples and Composite for the C-109 Hard Heel Study*, Rev. 0, Washington River Protection Solutions, LLC., Richland, Washington.

Law A.W-K, and Herlina, 2002, "An Experimental Study on Turbulent Circular Wall Jets," Journal of Hydraulic Engineering, February 2002, 161-174.

Leong Y.K. and D.V. Boger, 1989, "Surface Chemistry Effects on Concentrated Suspension Rheology," Journal of Colloid and Interface Science 136(1): 249-258.

Leong Y.K., P.J. Scales, T.W. Healy, and D.V. Boger, 1995, "Effect of Particle Size on Colloidal Zirconia Rheology at the Isoelectric Point," Journal of the American Ceramic Society 78(8): 2209-2212.

Mantz P.A, 1977, "Incipient Transport of Fine Grains and Flakes by Fluids – Extended Shields Diagram," Journal of the Hydraulics Division, Proceedings of the American Society of Civil Engineers 103(6): 601-615.

Matlab, 2007, Version 7.5.0.342 (R2007b), August 15, 2007, The MathWorks Inc.," Natick, Massachusetts.

Myers, R.H., D.C., Montgomery and G.G. Vining, 2002, "Generalized Linear Models," Wiley Interscience, New York, New York.

Novotny, P. and O. Sohnel, 1988, "Densities of Binary Aqueous Solutions of 306 Inorganic Substances," Journal of Chemical and Engineering Data, 33: 49-55.

ORP-11242, 2011, *River Protection Project System Plan*, Rev. 6, Washington River Protection Solutions, Richland, Washington.

Pani B.S., and R.N. Dash, 1983, "Three-dimensional Reattached Wall Jet," La Houille Blanche/Nº, 38(1): 27-32.

Paphitis D., 2001, "Sediment Movement Under Unidirectional Flows: An Assessment of Empirical Threshold Curves," Coastal Engineering 43: 227-245.

Parker S.P, 1984, McGraw-Hill Dictionary of Scientific and Technical Terms, 3rd Edition, McGraw-Hill, New York.

Parks G.A., 1964, "The Isoelectric Points of Solid Oxides, Solid Hydroxides, and Aqueous Hydroxo Complex Systems," Chemical Reviews, 65(2): 177-198.

PNL-7758, 1989, *Characterization of the Second Core Sample of Neutralized Current Acid Waste from Double-Shell Tank 101-AZ*, Rev. 0, Pacific Northwest Laboratory, Richland, Washington.

PNL-10464, 1995, *Fiscal Year 1993 1/25th-Scale Sludge Mobilization Testing*, Rev. 0, Pacific Northwest National Laboratory, Richland, Washington.

PNL-11686, 1997, *Research on Jet Mixing of Settled Sludges in Nuclear Waste Tanks at Hanford and Other DOE Sites*, Rev. 0, Pacific Northwest Laboratory, Richland, Washington.

PNL-10582, 1995, *Fiscal Year 1994 1/25th-Scale Sludge Mobilization Testing*, Pacific Northwest National Laboratory, Richland, Washington.

PNNL-11685, 1997, *Retrieval Process Development and Enhancements Waste Simulant Compositions and Defensibility*, Rev. 0, Pacific Northwest National Laboratory, Richland, Washington.

PNNL-13319, 2000, *Review of Waste Retrieval Sluicing System Operations and Data for Tanks 241-C-016 and 241-AY-102*, Rev. 0, Pacific Northwest National Laboratory, Richland, Washington.

PNNL-14333, 2003, *Physical and Liquid Chemical Simulant Formulations for Transuranic Wastes in Hanford Single-Shell Tanks*, Rev. 0, Pacific Northwest National Laboratory, Richland, Washington.

PNNL-16857 (WTP-RPT-154), 2007, *Estimate of Hanford Waste Rheology and Settling Behavior*, Rev. 0, Pacific Northwest National Laboratory, Richland, Washington.

PNNL-17368 (WTP-RPT-157), 2008, *Characterization and Leaching Testing for REDOX Sludge and S-Saltcake Actual Waste Sample Composites*. Rev. 0, Pacific Northwest National Laboratory, Richland, WA

PNNL-17639 (WTP-RPT-175), 2009, *Deposition Velocities of Newtonian and Non-Newtonian Slurries in Pipelines*. Rev. 0, Pacific Northwest National Laboratory, Richland, Washington.

PNNL-17707 (WTP-RPT-177), 2009, *An Approach to Understanding Cohesive Slurry Setting, Mobilization, and Hydrogen Gas Retention in Pulsed Jet Mixed Vessels*, Rev. 0, Pacific Northwest National Laboratory, Richland, Washington.

PNNL-17965 (WTP-RPT-172), 2009, *Filtration and Leach Testing for REDOX Sludge and S-Saltcake Actual Waste Sample Composites*, Rev. 0, Pacific Northwest National Laboratory, Richland, Washington.

PNNL-17992 (WTP-RPT-166), 2009, *Characterization, Leaching, and Filtration Testing for Bismuth Phosphate Sludge (Group 1) and Bismuth Phosphate Saltcake (Group 2) Actual Waste Sample Composites*, Rev. 0, Pacific Northwest National Laboratory, Richland, Washington.

PNNL-18048 (WTP-RPT-181), 2009, *Filtration and Leach Testing for PUREX Cladding Sludge and REDOX Cladding Sludge Actual Waste Sample Composites*, Rev. 0, Pacific Northwest National Laboratory, Richland, Washington.

PNNL-18054 (WTP-RPT-167), 2009, *Characterization and Leach Testing for PUREX Cladding Waste Sludge (Group 3) and REDOX Cladding Waste Sludge (Group 4) Actual Waste Sample Composites*, Rev. 0, Pacific Northwest National Laboratory, Richland, Washington.

PNNL-18119 (WTP-RPT-169). 2009, *Characterization, Leaching, and Filtration Testing for Tributyl Phosphate (TBP, Group 7) Actual Waste Sample Composites*. Rev. 0), Pacific Northwest National Laboratory, Richland, Washington.

PNNL-18120 (WTP-RPT-170), 2009, *Characterization, Leaching, and Filtration Testing of Ferrocyanide Tank Sludge (Group 8) Actual Waste Composite*, Rev. 0, Pacific Northwest National Laboratory, Richland, Washington.

PNNL-18327, 2009, *Estimate of the Distribution of Solids within Mixed Hanford Double-Shell Tank AZ-101: Implications for AY-102*, Pacific Northwest National Laboratory, Richland, Washington.

PNNL-18831, 2009, *Assessment of Jet Erosion for Potential Post-Retrieval K-Basin Settled Sludge*, Pacific Northwest National Laboratory, Richland, Washington.

PNNL-18894 (WTP-RPT-197), 2009, *Pretreatment Engineering Platform Phase 1 Final Test Report*, Rev. 0, Pacific Northwest National Laboratory, Richland, Washington.

PNNL-19245, 2010, *The Role of Cohesive Particle Interactions on Solids Uniformity and Mobilization During Jet Mixing: Testing Recommendations*, Rev. 0, Pacific Northwest National Laboratory, Richland, Washington.

PNNL-20637, 2011, *Comparison of Waste Feed Delivery Small-Scale Mixing Demonstration Simulant to Hanford Waste*, Rev. 0, Pacific Northwest National Laboratory, Richland, Washington.

PNNL-20646, (EMSP-RPT-006), 2011, *Hanford Waste Physical and Rheological Properties: Data and Gaps*, Rev. 0, Pacific Northwest National Laboratory, Richland, Washington.

PNWD-3206 (WTP-RPT-043), 2003, *Filtration, Washing, and Caustic Leaching of Hanford Tank AZ-101 Sludge*, Rev. 1, Battelle - Pacific Northwest Division, Richland, Washington.

PNWD-3215, 2002, *Chemical Analysis and Physical Property Testing of 241-AZ-101 Tank waste – Supernatant and Centrifuged Solids*, Rev. 1, Battelle - Pacific Northwest Division, Richland, Washington.

PNWD-3228 (WTP-RPT-021), 2002, *Chemical and Physical Properties Testing of 241-AN-102 Tank Waste Blended with 241-C-104 Wash/Leachate Solutions*, Rev. 1, Battelle - Pacific Northwest Division, Richland, Washington.

PNWD-3300, 2004, *Identification of Washed Solids from Hanford Tanks 241-AN-102 and 241-AZ-101 with X-Ray Diffraction, Scanning Electron Microscopy, and Light-Scattering Particle Analysis*, Rev. 0, Battelle - Pacific Northwest Division, Richland, Washington.

PNWD-3551 (WTP-RPT-113), 2005, *Technical Basis for Testing Scaled Pulse Jet Mixing Systems for Non-Newtonian Slurries*, Rev. 0, Battelle-Pacific Northwest Division, Richland, Washington.

Probstein, R.F., 1994, *Physicochemical Hydrodynamics*, John Wiley & Sons Inc,, New York.

Proudman, I. and J.R.A Pearson, 1956, "Expansions at Small Reynolds Numbers for the Flow Past a Sphere and a Circular Cylinder," Journal of Fluid Mechanics, 2: 237-262.

Rajaratnam N, 1976, *Turbulent Jets*, ISBN 0-444-41372-3, Elsevier Scientific Publishing Company, Amsterdam, The Netherlands.

Rajaratnam N., and B.S. Pani, 1972, "Three-Dimensional Turbulent Wall Jets," Proceedings of the A.S.C.E., Journal of the Hydraulics Division, 100: 69-83.

Rector D.R., and M.L. Stewart, 2010, "Modeling of Leaching Filter Pressure Drop and Fouling Behavior," PNNL-SA-69594, Pacific Northwest National Laboratory, Presented at the 2010 Waste Management Conference, Phoenix, Arizona.

Rector D.R., M.L. Stewart, and A.P. Poloski, 2009, "Modeling of Sediment Bed Behavior for Critical Velocity in Horizontal Piping," PNNL-SA-63578, Pacific Northwest National Laboratory, Richland, Washington, Presented at the 2009 Waste Management Conference, Phoenix, Arizona.

RPP-5346, 2002, *Waste Feed Delivery Transfer System Analysis*, Rev. 2, CH2M Hill Hanford Group, Inc., Richland, Washington.

RPP-5687, 2000, *Waste Retrieval Sluicing System (WRSS) and Project W-320, Tank 241-C-106 Sluicing, Lessons Learned*, Rev. 0, CH2M HILL Hanford Group, Richland, Washington.

RPP-6548, 2001, *Test Report, 241-AZ-101 Mixer Pump Test*, Rev. 1, Numatec Hanford Corporation, Richland, Washington.

RPP-10006, 2011, *Methodology and Calculations for the Assignment of Waste Groups for the Large Underground Waste Storage Tanks at the Hanford Site*, Rev. 10, Washington River Protection Solutions, Richland, Washington.

RPP-14767, 2003, *Hanford Tank Waste Operations Simulator Specific Gravity Model - Derivation of Coefficients and Validation*, Rev. 0, CH2MHill Hanford Group, Inc., Richland, Washington.

RPP-15136, 2006, *System Design Description for the Replacement Cross-Site Transfer System between 200 West and 200East Tank Farms*, Rev. 3, CH2M Hill Hanford Group, Inc., Richland, Washington.

RPP-15137, 2011, *System Design Description for 200 Area Double-Shell Tank Waste Transfer System (DSA-Based)*, Rev. 5., Washington River Protection Solutions, Richland, Washington.

RPP-16922, 2012, *Environmental Specification Requirements,* Rev. 24, Washington River Protection Solutions, Richland, Washington.

RPP-17152, 2011, *Hanford Tank Waste Operations Simulation (HTWOS) Version 6.6.1 Model Design Document,* Rev. 6, Washington River Protection Solutions, LLC, Richland, Washington.

RPP-27591, 2007, *Volume 2 IQRPE DST System Integrity Assessment – Pipeline Integrity*, Rev. 1, CH2M Hill Hanford Group, Inc., Richland, Washington.

RPP-40149-VOL1, 2012, *Integrated Waste Feed Delivery Plan, Volume 1 – Process Strategy,* Rev. 2, Washington River Protection Solutions, LLC, Richland, Washington.

RPP-40149-VOL2, 2012, *Integrated Waste Feed Delivery Plan, Volume 2 – Campaign Plan*, Rev. 2, Washington River Protection Solutions, LLC, Richland, Washington.

RPP-40149-VOL3, 2012, *Integrated Waste Feed Delivery Plan, Volume 3 – Project Plan*, Rev. 2, Washington River Protection Solutions, LLC, Richland, Washington.

RPP-PLAN-51625, 2011, *Waste Feed Delivery Mixing and Sampling Program Simulant Definition for Tank Farm Performance Testing*, Rev. 0, Washington River Protection Solutions, LLC, Richland, Washington.

RPP-RPT-46112, 2010, *Transfer Line Reliability for the Waste Feed Delivery Operations Research Model Phase 2*, Rev. 0, Washington River Protection Solutions, Richland, Washington.

RPP-RPT-46618, 2011, *Hanford Waste Mineralogy Reference Report,* Rev. 2, Washington River Protection Solutions, Richland, Washington.

RPP-RPT-50941, 2011, *Review of Plutonium Oxide Receipts into Hanford Tank Farms*, Rev. 0, Washington River Protection Solutions, Richland, Washington.

RPP-RPT-52196, 2012, *Methods for Heel Retrieval for Tanks C-101, C-102, and C-111*, Rev. 0, Washington River Protection Solutions, Richland, Washington.

RPP-SPEC-43262, 2011, *Procurement Specification for Hanford Double-Shell Tank Submersible Mixer Pumps*, Rev. 3, Washington River Protection Solutions, Richland, Washington.

RPP-SSMD-EG-0007, Rev. 0, 2011, *SSMD Test Platform Small-Scale Mixing Demonstration Informal Demonstration Test Results Report*, Energy Solutions, Richland, Washington.

RPP-SSMD-EG-0008, Rev, 0, 2011, *SSMD Test Platform Small Scale Mixing Demonstration Second Informal Demonstration Test Results Report*, Energy Solutions, Richland, Washington.

Requisition 244607, *Design of Hanford Submersible Transfer Pump*, Rev. 1, dated April 23, 2012, Washington River Protection Solutions, Richland, Washington.

Russel W.B., D.A. Saville and W.R. Schowalter, 1989, *Colloidal Dispersions*, Cambridge University Press, New York, New York.

SciFinder, https: //scifinder.cas.org

Scales P.J., S.B. Johnson, T.W. Healy, and P.C. Kapur, 1998, "Shear Yield Stress of Partially Flocculated Colloidal Suspensions," AIChE Journal 44(3): 538-544.

Schiller L. and A. Nauman, 1933, "Uber die grundlegende Berechnung bei der Schwekraftaufbereitung," Ver Deutch Ing., 44: 318-320.

Sforza P.M., and G. Herbst, 1970, "A Study of Three-Dimensional Incompressible Turbulent Wall Jets," *Journal of the American Institute of Aeronautics and Astronautics*, 8: 276-283.

SRNL-STI-2011-00278, 2011, "Demonstration of Mixing and Transferring Settling Cohesive Slurry Simulants in the AY-102 Tank," Rev. 0. Savannah River National Laboratory, Aiken, South Carolina.

Subbanna M., Pradip, and S.G. Malghan, 1998, "Shear Yield Stress of Flocculated Alumina-Zirconia Mixed Suspensions: Effect of Solid Loading, Composition, and Particle Size Distribution," Chemical Engineering Science 53(17): 3073-3079.

SVF-2115, 2011, WTP_SPEC_7_Update for SP6 Baseline Case_V8.xlsm, Version 8, Rev. 1, Washington River Protection Solutions, Richland, Washington.

SVF-2117, 2011, WTP_TRACEBACK_4MINTIMESTEP(6MELTERS)-MMR-11-031-6.5-8.3R1-2011-03-18-AT-01-31-58_V8.XLSM," Rev. 1, Washington River Protection Solutions, LLC, Richland, Washington.

Turian R.M., J.F. Attal, D.J. Sung, and L.E. Wedgewood. 2002. "Properties and Rheology of Coal-Water Mixtures Using Different Coals." Fuel 81(16): 2019-2033.

Vanoni A.A. (ed.), 1975, *Sedimentation Engineering, the ASCE Task Committee for the Preparation of the Manual on Sedimentation of the Sedimentation Committee of the Hydraulic Division*, The American Society of Civil Engineers, New York, New York.

Verhoff A., 1963, *The Two-Dimensional Turbulent Wall Jet Without An External Stream*, Report No. 626, Princeton University, Princeton, NJ.

Weigel R.L, 1966, *Oceanographical Engineering*, Prentice-Hall, Inc., Upper Saddle River, New Jersey, pp. 424-427.

WHC-SD-W079-ES-001, 1995, *Hot Sample Archiving/W-079*, Rev. 3, Westinghouse Hanford, Richland, Washington.

WHC-SD-WM-ES-370, 1996, *Phase I High-Level Waste Pretreatment and Feed Staging Plan*, Rev. 1, Westinghouse Hanford Company, Richland, Washington.

WHC-SD-WM-TI-648, 1994, *Tank Characterization Reference Guid*e, Rev. 0A, Westinghouse Hanford Company, Richland, Washington.

Yoon S.H., K.C. Kim, D.S. Kim, and M.K. Chung, 1995, "Effect of Surface Roughness on a Turbulent Wall-attaching Offset Jet," Experiments in Fluids 19: 38-42.

Zhou Z., P.J. Scales, and D.V. Boger, 2001, "Chemical and Physical Control of the Rheology of Concentrated Metal Oxide Suspensions," Chemical Engineering Science 56: 2901-2920.

APPENDIX A. MODELS FOR CALCULATING SPECIFIC GRAVITY AND LIQUID
DENSITY

This appendix presents different versions of models for calculating specific gravity and liquid density of the liquid phase of Hanford tank wastes. The model forms used for data analyses in the main body of the report are identified.

A.1. MODELS FOR CALCULATING SPECIFIC GRAVITY AND LIQUID DENSITY

Several mathematically equivalent models for the specific gravity (SpG) of liquid waste can be written, depending on the quantities that are known (or estimated) for input to the model. One model for calculating the SpG of liquid waste assumes the molarities of components in solution are available. This form of the model is given by

$$SpG = \frac{\rho_L^{g/L}}{\rho_W^{g/L}} = 1 + \sum_i \gamma_i M_i \tag{A-1}$$

where

$\rho_L^{g/L}$ = density of liquid waste (g/L)

$\rho_W^{g/L}$ = density of water (g/L)

γ_i = density coefficient of the ith component (L/g-mol)

M_i = molarity of the ith component (g-mol/L).

The density of water ($\rho_W^{g/L}$) in Equation A-1 depends on temperature (T, °C) according to the following relationship

$$\rho_W^{g/L} = 999.65 + 0.20438T - 0.06174T^{1.5}, \tag{A-2}$$

which is Equation (2) in Novotney and Sohnel (1988). Note that this model is for $\rho_W^{g/L}$ in g/L units. For the density of water in kg/L units (denoted $\rho_W^{kg/L}$), Equation A-2 becomes

$$\rho_W^{kg/L} = 0.99965 + 0.00020438T - 0.00006174T^{1.5} \tag{A-3}$$

If the density coefficients (γ_i) in Equation A-1 are constants, then that model assumes that contributions to SpG of components dissolved in solution are additive, linear functions of the component molarities (M_i). Hence, it assumes there are no/negligible curvature effects or interactive effects between components. The density coefficients are discussed subsequently in Section A.2.

A mathematically equivalent model for SpG is obtained by replacing M_i in Equation A-1 with the formula for calculating M_i, which yields

$$SpG = \frac{\rho_L^{g/L}}{\rho_W^{g/L}} = 1 + \sum_i \gamma_i \left(\frac{1000 m_i}{V_t (mw_i)} \right) \tag{A-4}$$

where

$1000 =$ constant for converting kg to g for consistency of units (g/kg)

$m_i =$ mass of the ith component dissolved in the liquid waste (kg)

$V_t =$ total volume of the liquid waste (L)

$mw_i =$ molecular weight of the ith component (g/g-mol)

and all other notation is as defined following Equation A-1. Note that Equation A-4 requires estimates of the component masses (m_i) and total volume (V_t) of the liquid waste. A re-expression of the model in Equation A-4 is

$$SpG = \frac{\rho_L^{g/L}}{\rho_W^{g/L}} = 1 + \sum_i \gamma_i \left(\frac{1000 c_i}{mw_i} \right) \tag{A-5}$$

where

$c_i =$ concentration of the ith component dissolved in the liquid waste (kg/L)

and all other notation is as defined following Equations A-1 and A-4. Note that Equation A-5 requires estimates of the component concentrations (c_i) of the liquid waste.

Another model for SpG that is mathematically equivalent to the models in Equations A-1, A-4 and A-5 is derived by substituting the relationship $V_t = 1000 m_t / \rho_L^{g/L}$ into Equation A-4, yielding

$$SpG = \frac{\rho_L^{g/L}}{\rho_W^{g/L}} = 1 + \sum_i \gamma_i \left(\frac{1000 m_i}{V_t (mw_i)} \right)$$
$$= 1 + \left(\frac{\rho_L^{g/L}}{m_t} \right) \sum_i \gamma_i \left(\frac{m_i}{mw_i} \right) \tag{A-6}$$

where

$m_t =$ total mass of the liquid waste (kg)

and all other notation is as defined following Equations A-1 and A-4. Then, collecting the density and SpG terms and solving for SpG yields another mathematically equivalent model given by:

$$SpG = \frac{\rho_L^{g/L}}{\rho_W^{g/L}} = \frac{m_t}{m_t - \rho_W^{g/L} \sum_i \left(\frac{\gamma_i m_i}{mw_i} \right)},$$ (A-7)

where all notations are as previously defined. Note that Equation A-7) requires estimates of the component masses (m_i) and the total mass (m_t) of the liquid waste.

Models for liquid density ($\rho_L^{g/L}$) can be obtained from Equations A-1, A-4, A-5 and A-7 for SpG by multiplying both sides of those equations by $\rho_W^{g/L}$. In the case of Equation A-7, this yields

$$\rho_L^{g/L} = \frac{\rho_W^{g/L} m_t}{m_t - \rho_W^{g/L} \sum_i \left(\frac{\gamma_i m_i}{mw_i} \right)},$$ (A-8)

with all notations as previously defined. Note that Equation (A-8) uses units of g/L for $\rho_L^{g/L}$ and $\rho_W^{g/L}$. Rewriting this model to use units of kg/L for $\rho_L^{kg/L}$ and $\rho_W^{kg/L}$ yields

$$\rho_L^{kg/L} = \frac{\rho_W^{kg/L} m_t}{m_t - 1000 \rho_W^{kg/L} \sum_i \left(\frac{\gamma_i m_i}{mw_i} \right)}.$$ (A-9)

The Hanford Tank Waste Operation Simulator (HTWOS) uses a "reduced" version of Equation A-9 to calculate liquid density. Specifically, HTWOS assumes the waste will be at 30°C and that the density of water at 30°C is $d_w^* = 1.0$ kg/L, so that Equation A-9 reduces to

$$\rho_L^{kg/L} = \frac{m_t}{m_t - 1000 \sum_i \left(\frac{\gamma_i m_i}{mw_i} \right)}.$$ (A-10)

The model in Equation A-10 is the same as Equation 2-17 in RPP-17152, except for the typo in Equation 2-17 where the summation sign does not (but should) include the mw_i denominator. However, the HTWOS assumption that $\rho_W^{kg/L} = 1.0$ kg/L at 30°C is in conflict with the dependence of $\rho_W^{kg/L}$ on temperature given in Equation A-3, which calculates $\rho_W^{kg/L}(30°C) = 0.9956$ kg/L. As discussed subsequently in Section A.2, the γ_i coefficients used in the HTWOS model in Equation A-10 for liquid density were derived from empirical models that incorporated the temperature dependence of water density. Hence, the HTWOS simplification from Equation A-9 to Equation A-10 introduces a bias (systematic uncertainty) in calculated values of liquid density. Specifically, the model in Equation A-10 over-predicts the liquid density of waste at 30°C by a factor of 1.0/0.9956 = 1.0044.

Because Equation A-9 is mathematically equivalent to Equation A-1, it is useful for work elsewhere in this report to develop a revision of Equation A-1 that is mathematically equivalent to Equation A-10. The resulting model is given by

$$SpG(30°C) = \frac{\rho_L^{g/L}(30°C)}{\rho_W^{g/L}(30°C)} = (1 + \sum_i \gamma_i M_i) \qquad \text{(A-11)}$$

A.2   MODEL COEFFICIENTS FOR CALCULATING SPECIFIC GRAVITY AND DENSITY OF LIQUID WASTE

Two methods for calculating the component density coefficients γ_i in the models of Section A.1 are available. One method accounts for concentration and temperature dependence in calculating the γ_i. The second method (the one that is incorporated in HTWOS) uses selected, constant γ_i values at a temperature of 30°C (the assumed temperature of the waste). Because the coefficients in the second method are determined based on results from the first method, both are discussed.

A.2.1   Variable Density Coefficients

A method to calculate the γ_i that accounts for concentration and temperature dependence is discussed in this subsection. Because the γ_i density coefficients depend on concentration and temperature, they are referred to as *variable density coefficients*. This method uses 1) solute concentrations expressed as molarity and 2) empirical density correlations from the literature (Novotny and Sohnel 1988). This method is based on the SpG model in Equation A-4, where it is assumed the total volume of liquid waste and the masses of dissolved components are available, so that component molarities can be calculated, yielding the SpG model in Equation A-1.

The formula for the component density coefficient γ_i is

$$
\begin{aligned}
\gamma_i &= \frac{f_i(M_i, T)}{\rho_W M_i} \\
&= \frac{A_i M_i + B_i M_i T + C_i M_i T^2 + D_i M_i^{1.5} + E_i M_i^{1.5} T + F_i M_i^{1.5} T^2}{\rho_W M_i} \\
&= \frac{A_i + B_i t + C_i T^2 + D_i M_i^{0.5} + E_i M_i^{0.5} T + F_i M_i^{0.5} T^2}{\rho_W}
\end{aligned}
\qquad \text{(A-12)}
$$

where A_i, B_i, C_i, D_i, E_i and F_i are coefficients specific to the ith component and all other notation is as defined in Section A.1. The empirical function in the numerator of Equation A-12 was fit for over 100 salts, temperatures up to 100°C and concentrations up to saturation in an exhaustive study by Novotny and Sohnel (1988). Table A-1 lists the coefficients A_i, B_i, C_i, D_i, E_i and F_i for salts common to Hanford Site waste that were calculated by Novotny and Sohnel (1988).

Note that all of the salts listed in Table A-1 are sodium salts except for UO_2 nitrate. Sodium is the predominant cation in most Hanford waste tanks. A few tanks (e.g., AP-101 and AW-101) have potassium concentrations approaching one molar. Novotny and Sohnel (1988) listed A_i, B_i, C_i, D_i, E_i and F_i coefficients for several potassium salts. Coefficients for potassium salts might provide an incremental improvement to the liquid density current model, but using coefficients for sodium salts and potassium salts would require reprogramming HTWOS.

Table A-1. Coefficients for Calculating Component Liquid-Density Coefficients as Functions of Molarity and Temperature

Component	A	B	C	D	E	F
NaCl	44.85	-0.09634	0.000614	-2.712	0.01009	0
Na_2CO_3	124.1	-0.6213	0.006124	-18.36	0.3178	-0.003672
Na_2CrO_4	154.1	-0.3173	0.003623	-15.53	0.1308	-0.001521
NaF	49.40	-0.2985	0.003365	-4.752	0.1622	-0.001872
$NaNO_2$	51.42	-0.3362	0.004079	-3.242	0.07155	-0.00096717
$NaNO_3$	62.98	-0.2382	0.001520	-4.138	0.06626	-0.0004208
Na_3PO_4	147.3	1.306	-0.01043	11.76	1.113	0.008691
Na_2SO_4	141.2	-0.4535	0.003766	-17.51	0.2111	-0.001773
NaOH	49.16	-0.09064	0.00063081	-4.907	0.01633	-0.0001041
UO_2 nitrate	318.2	0.06041	0.002092	-5.374	-0.1683	-0.00013

Source: Novotny and Sohnel (1988).

A.2.2 Constant Density Coefficients

Table A-2 lists the components that HTWOS currently incorporates into the liquid-density calculation (Column 1), along with their molecular weights (Column 2). Where volume (and therefore, molarity) is not explicitly known, the approximate molarity ranges for components (Column 3) were determined in RPP-14767. Equation A-10 was used to establish the corresponding range of γ_i values for selected components (Column 4). RPP-14767 noted that the potential range of γ_i is wider for higher solubility components because their concentration range is wider. Column 4 shows that γ_i is a weak (and nearly constant) function of concentration over the expected molarity ranges of components in Hanford waste tanks selected in RPP-14767. Column 5 of Table A-2 lists γ_i values selected for each component, including coefficients for components not addressed by Novotny and Sohnel (1988). Where a range for γ_i is indicated in Column 4, the lower limit of the range was selected for the γ_i value (in Column 5) for HTWOS modeling. The lower (upper) limits correspond to the highest (lowest) expected molarity of the components. RPP-14767 noted that the lower limits are more consistent with the higher concentrations typically found in the Hanford wastes.

Table A-2. Component Coefficients at 30°C for the HTWOS Liquid-Density Model.

Component	mw_i (g/gmol)	Expected Range M_i (gmol/L)[a]	Expected Range γ_i (L/gmol)[b]	γ_i (L/gmol)[b]
Aluminum [Al^{+3}]	26.9815	–	–	0.04
(Al(OH)$_4$)$^-$	95.01	–	–	0.04
Carbonate [(CO$_3$)$^{-2}$]	60.01	0.1 – 0.6	0.102 – 0.108	0.102
Chloride [Cl$^-$]	35.453	0.1 – 0.3	0.041 – 0.042	0.041
Cr^{+3}	51.996	–	0.144	0.144
Cr(OH)$_4$$^-$	183.99	–	0.144	0.144
Chromate [(CrO$_4$)$^{-2}$]	115.99	0.1	0.144	0.144
Fluoride [F$^-$]	18.998	0.1 – 0.3	0.0428 – 0.0432	0.0428
H$^+$	1.008	–	–	0.031
Iron [Fe^{+3}]	55.847	–	–	0.173
Nitrite [(NO$_2$)$^-$]	46.0	0.1 – 3.0	0.0418 – 0.0446	0.0418
Nitrate [(NO$_3$)$^-$]	62.0	0.1 – 3.0	0.0531 – 0.0566	0.0531
Hydroxide [OH$^-$]	17.01	0.1 – 5.5	0.0394 – 0.0458	0.0394
Phosphate [(PO$_4$)$^{-3}$]	94.97	0.1	0.180	0.180
Sulfate [(SO$_4$)$^{-2}$]	96.058	0.1	0.128	0.128
Uranium (Total)	238.029	–	–	0.318[c]
Uranium [^{232}U]	232.037	–	–	0.318[c]
Uranium [^{233}U]	233.040	–	–	0.318[c]
Uranium [^{234}U]	234.041	–	–	0.318[c]
Uranium [^{235}U]	235.044	–	–	0.318[c]
Uranium [^{236}U]	236.046	–	–	0.318[c]
Uranium [^{238}U]	238.051	–	–	0.318[c]
Uranyl [(UO$_2$)$^{+2}$]	270.03	–	–	0.318[d]
Zirconium [Zr^{+4}]	91.22	–	–	0.243

Notes:
[a] From Appendix A of RPP-14767.
[b] Source is Table 2 in RPP-14767 except for H+, which is based on nitric acid.
[c] If different measurement methods yield concentration data for uranium isotopes and "Uranium (Total)", only the uranium isotope data are used. If concentration data are available only for "Uranium (Total)" and not the uranium isotopes, then only "Uranium (Total)" is used.
[d] Source is Table A-39 in HNF-SD-WM-SP-012.

Although aqueous chromium is mostly CrO_4^-, the HTWOS material balance carries Cr^{3+} and $Cr(OH)_4^-$ as the aqueous species by convention. It is valid to use the CrO_4^- coefficient with Cr^{3+} and $Cr(OH)_4^-$ because the SpG calculation is on a molarity basis.

Density results with the coefficients in Table A-2 were spot-checked in RPP-14767 against measured densities for moderate and high ionic strength solutions. It was found that assigning a fixed value to γ_i was only slightly less accurate than the more rigorous "variable density coefficients" method because the values for each given γ_i fall in a relatively narrow band. That is the basis for HTWOS using the "constant density coefficients" listed in the last column of Table A-2 to calculate liquid densities. Another assessment of using "constant density coefficients" instead of "variable density coefficients" was performed as part of the work documented in this report and is discussed in Section 5.2.4.

APPENDIX B. DEVELOPMENT OF A LIQUID-VISCOSITY MODEL AS A
FUNCTION OF TEMPERATURE AND LIQUID DENSITY

This section discusses the development of the liquid-viscosity model given by Equation 5-3. The first step in the model development was to consider what types of functional relationships exist between liquid viscosity and 1) temperature and 2) liquid density. The Arrhenius equation is commonly used to express the temperature dependence of liquid viscosity. The Arrhenius equation is given by

$$\mu_L = Ae^{B/T} \tag{B-1}$$

where μ_L denotes liquid viscosity (cP), T denotes temperature (K) and A and B are coefficients determined by fitting the equation to data. The Arrhenius equation was fit separately to the two or three pairs (T, μ_L) of data for each combination of waste tank and density in Table B-1 (which is a copy of Table I.1 of PNNL-20646). The results of the separate Arrhenius fits are shown graphically in Figure B-1.

Figure B-1. Fitted Arrhenius Equations for Each Set of Liquid Viscosities at Two or Three Temperatures for each Tank and Liquid Density Combination
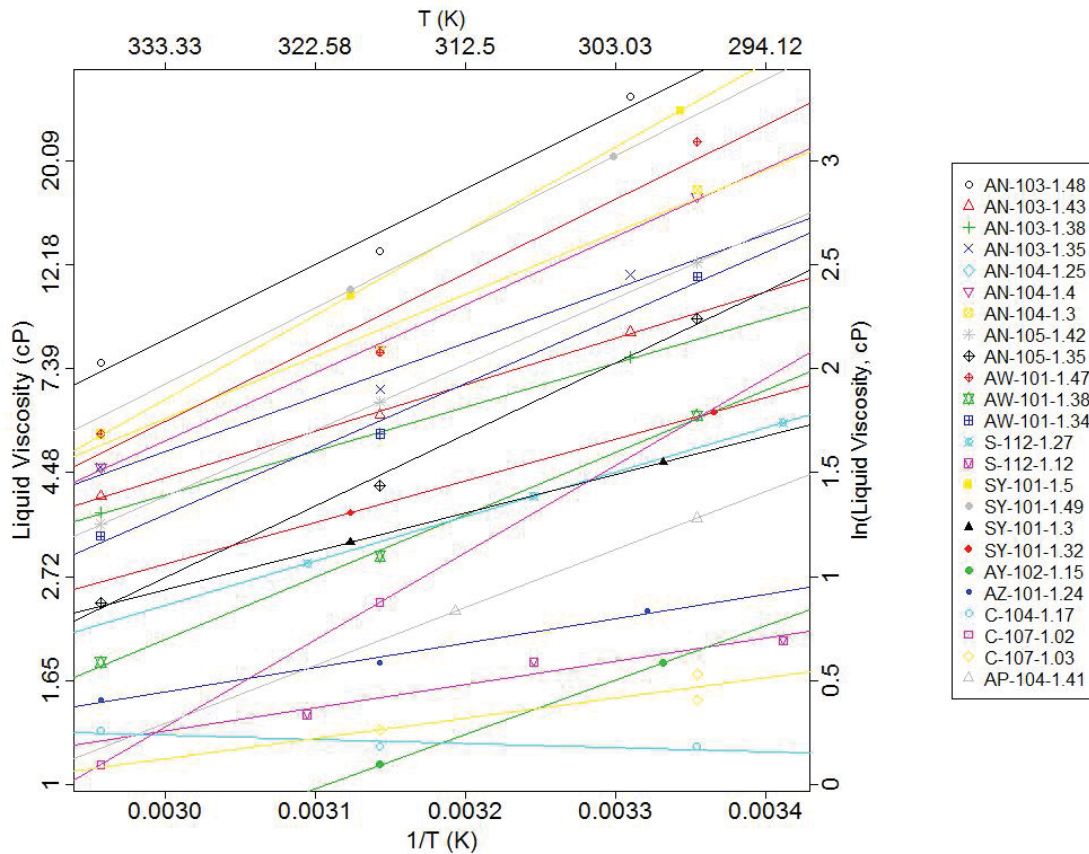
Table B-1. Density, Temperature and Viscosity Data for Samples of Liquid Wastes from Hanford Tanks (from Table I.1 of PNNL-20646)

Tank	Primary Waste Type	Primary Waste Type Fraction	Sample Density (g/mL)	Sample Temperature (°C)	Viscosity (cP)
AN-103	A2 saltcake	1.00	1.48	29	27.4
AN-103	-	-	1.48	45	13
AN-103	-	-	1.48	65	7.6
AN-103	-	-	1.43	29	8.8
AN-103	-	-	1.43	45	5.9
AN-103	-	-	1.43	65	4
AN-103	-	-	1.38	29	7.8
AN-103	-	-	1.38	45	5.4
AN-103	-	-	1.38	65	3.7
AN-103	-	-	1.35	29	11.6
AN-103	-	-	1.35	45	6.7
AN-103	-	-	1.35	65	4.6
AN-104	A2 saltcake	1.00	1.25	25	3.5
AN-104	-	-	1.4	25	16.9
AN-104	-	-	1.4	45	8.1
AN-104	-	-	1.4	65	4.6
AN-104	-	-	1.3	25	17.5
AN-104	-	-	1.3	45	8.1
AN-104	-	-	1.3	65	5.4
AN-105	A2 saltcake	1.00	1.42	25	12.3
AN-105	-	-	1.42	45	6.3
AN-105	-	-	1.42	65	3.5
AN-105	-	-	1.35	25	9.4
AN-105	-	-	1.35	45	4.2
AN-105	-	-	1.35	65	2.4
AW-101	A2 saltcake	1.00	1.47	25	22
AW-101	-	-	1.47	45	8
AW-101	-	-	1.47	65	5.4
AW-101	-	-	1.38	25	5.9
AW-101	-	-	1.38	45	3
AW-101	-	-	1.38	65	1.8
AW-101	-	-	1.34	25	11.5
AW-101	-	-	1.34	45	5.4
AW-101	-	-	1.34	65	3.3
S-112	S1 saltcake	0.99	1.27	20	5.7
S-112	-	-	1.27	35	4
S-112	-	-	1.27	50	2.9
S-112	-	-	1.12	20	2
S-112	-	-	1.12	35	1.8
S-112	-	-	1.12	50	1.4
SY-101	S2 saltcake	1.00	1.5	26	25.5
SY-101	-	-	1.5	47	10.5
SY-101	-	-	1.49	30	20.5
SY-101	-	-	1.49	47	10.8
SY-101	-	-	1.3	27	4.7
SY-101	-	-	1.3	47	3.2
SY-101	-	-	1.32	24	6
SY-101	-	-	1.32	47	3.7
AY-102	BL sludge	1.00	1.15	27	1.8
AY-102	-	-	1.15	45	1.1
AZ-101	P3 sludge	1.00	1.24	28	2.3
AZ-101	-	-	1.24	45	1.8
AZ-101	-	-	1.24	65	1.5
C-104	CWP1 sludge	0.34	1.17	25	1.2
C-104	-	-	1.17	45	1.2
C-104	-	-	1.17	65	1.3
C-107	IC sludge	0.54	1.02	45	2.4
C-107	-	-	1.02	65	1.1
C-107	-	-	1.03	25	1.5
C-107	-	-	1.03	45	1.3
C-107	-	-	1.03	25	1.7
AP-104	n/a	0.00	1.41	25	3.6
AP-104	-	-	1.41	40	2.3
n/a, not applicable, liquid only tank					

Figures B-2 and B-3 show, respectively, plots of the separate estimates of the *A* and *B* coefficients (from Equation B-1) plotted versus the corresponding liquid densities. Figure B-1 shows that the slopes for many tank/density combinations are similar, with noticeably different slopes (*B* coefficients) in some cases. The figure also shows considerable variation in the intercepts (*A* coefficients). Figures B-2 and B-3, respectively, show the values of the Arrhenius coefficients *A* and *B* from the separate fits plotted versus the measured liquid densities. Figures B-2 and B-3 show roughly linear relationships between the Arrhenius slope and intercept coefficients and liquid density, but these relationships are weak, partially as a result of the limited and scattered data for lower liquid densities. Also, the general weakness in the linear relationships in Figures B-2 and B-3 are presumably a result of liquid density being an inadequate stand-in for the concentrations of the dissolved solids in the liquid samples. Unfortunately, composition information was not available for all of the samples listed in Table B-1.

Figure B-2. Plot of Arrhenius Equation *B* Coefficients for the Various Tank-Liquid Density Combinations in Table B-1
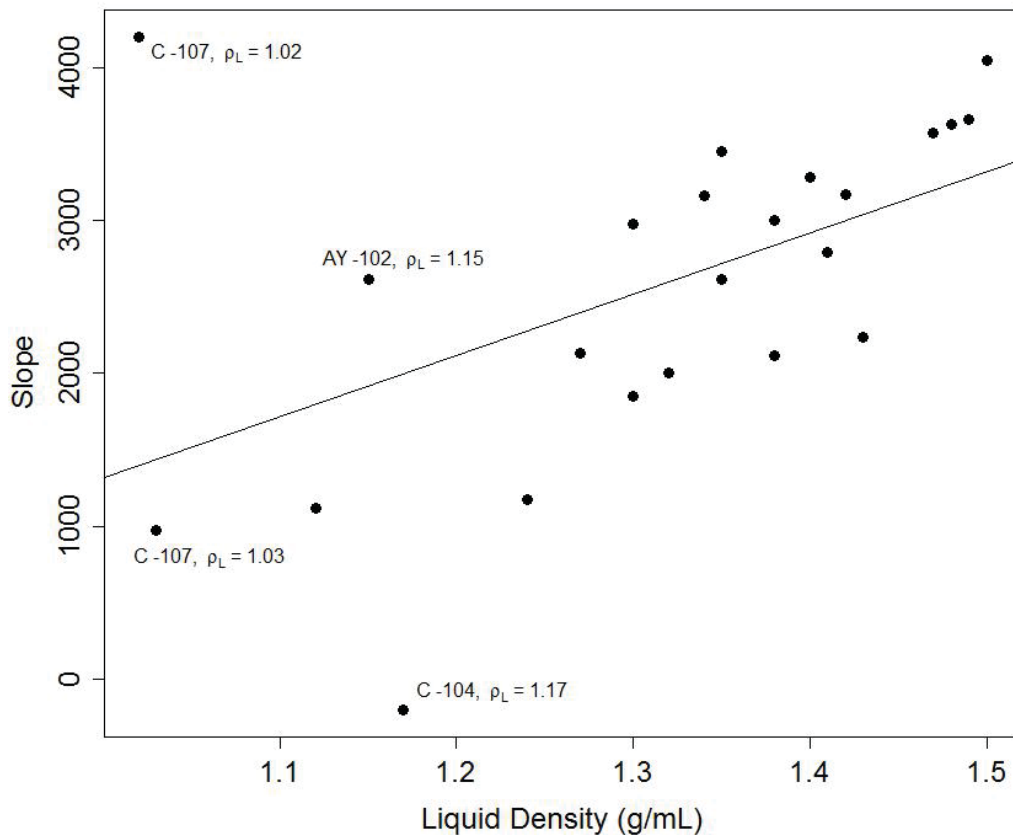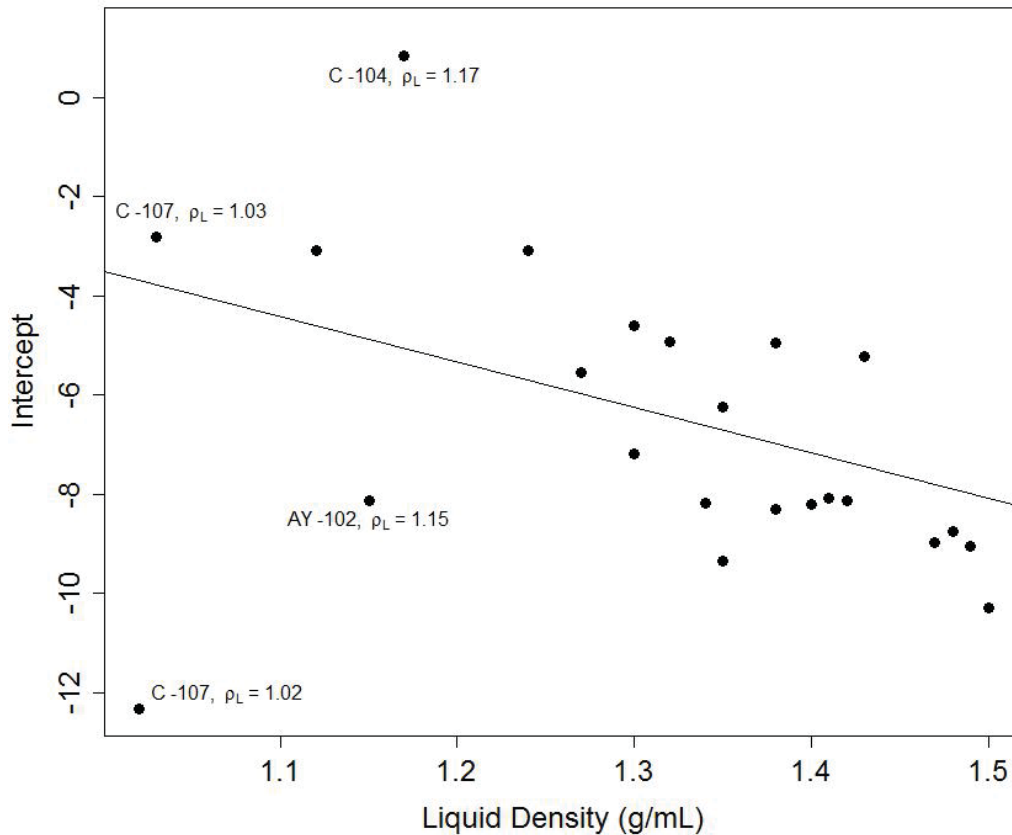
Figure B-3. Plot of Arrhenius Equation *A* Coefficients for the Various Tank-Liquid Density Combinations in Table B-1

Of particular note in Figures B-2 and B-3 are the labeled points for (C-107, $\rho_L = 1.02$) and (C-107, $\rho_L = 1.03$) which appear in very different locations of the figures. This suggests one of these data points might be an outlier—the one with $\rho_L = 1.02$ looks more likely (and would be the most influential on the fitted lines shown in Figures B-2 and B-3 if it was removed from the data set as an outlier). However, there was no basis to make a judgment on excluding potential outliers, such as (C-107, $\rho_L = 1.02$), so all data points were retained in developing a model for liquid viscosity as a function of temperature and liquid density.

Based on the results of Figures B-1 to B-3, an appropriate model form for liquid viscosity is

$$\mu_L = ae^{(b(\rho_L - 1) + c(\rho_L - 1) + d)/T} \tag{B-2}$$

which is the same as the model given in Equation 3.3 of PNNL-20646 (Section 3.2.2). The authors of that report concluded that this model form was not adequate and proposed a piecewise model

$$\mu_L = \begin{cases} a_1 e^{[b_1(\rho_L - 1) + (c_1(\rho_L - 1) + d_1)/T]} & \rho_L \le f \\ a_2 e^{[b_2(\rho_L - 1) + (c_2(\rho_L - 1) + d_2)/T]} & \rho_L > f \end{cases} \tag{B-3}$$

where μ_L is the liquid viscosity (cP), ρ_L is the liquid density (g/mL), T is the temperature in Kelvin and the model coefficients are a_1 and a_2 (cP), b_1 and b_2 (g/mL)$^{-1}$, c_1 and c_2 (K·mL/g), d_1 and d_2 (K) and f. In PNNL-20646, the 9 coefficients (a_1, a_2, b_1, b_2, c_1, c_2, d_1, d_2 and f) were fit by using OLS regression applied to the data in Table I.1 of PNNL-20646 (Table B-1 in this report). The model in Equation B-3 is discontinuous in ρ_L, which PNNL-20646 proposed an ad-hoc modification to address. The use of OLS regression to fit the model in (B-3) was inappropriate, because OLS assumes that the experimental and measurement uncertainties in the response variable (liquid viscosity) are relatively constant over the whole (temperature, density) space of interest. This corresponds to an additive uncertainty structure. Rather, it is well known that when viscosity can take relatively small values and varies by more than an order of magnitude, uncertainties of viscosity values tend to be relatively constant on a relative basis (corresponding to a multiplicative uncertainty structure). Hence, OLS regression is an inappropriate method for fitting the viscosity model with a multiplicative error structure.

The model in Equation 5-3 was developed applying generalized linear model regression to the data in Table B-1. Generalized linear models (GLM) are used to describe a regression approach where the variance of the response is a function of its expected value (the mean of the response). The type of functions relating the mean and the variance of the response in GLM are described using a member of the exponential family of distributions (Myers et al. 2002). In addition to having a function relating the variance and the mean of the response, in GLM the linear portion of the model, involving the predictors, is related to the expected value of the response via a link function.

A GLM was employed, applying Equation B-2 to the data in Table B-1 using the entire range of densities and temperatures available as predictors, but it was found that the model did not describe the viscosity response well. The model form was then expanded to a model like the one in Equation B-3, modified as shown in Equation 5-3 to ensure continuity over the entire space defined by the liquid density and temperature values available. The model in Equation 5-3 was fitted using a variety of error distributions and link functions while simultaneously searching in a grid for the value of the f coefficient that produced adequate model predictions, a statistically significant model, and no strong anomalies in a variety of goodness-of-fit statistics.

Starting with Equation B-3, reduced forms of the model were built and tested for goodness of fit and agreement with modeling assumptions. Terms that were not statistically significant at the 95% confidence level were eliminated and the model coefficients re-estimated, arriving finally at the model in Equation 5-3. The model coefficients and their standard errors, along with a predicted-versus-measured plot for the modeling data set are presented and discussed in Section 5.3.1.

DISTRIBUTION SHEET

To Distribution	From One System		Page 1 of 1
Project Title/Work Order One System Evaluation of Waste Transferred to the Waste Treatment Plant			Date 06/26/2012
			EDT No. N/A
			ECN No. N/A

Name	MSIN	Text With All Attach.	Text Only	Attach./ Appendix Only	EDT/ECN Only
S. A. Saunders	B1-55	X			
R. J. Skwarek	H3-28	X			
G. M. Duncan	B1-55	X			
C. K. Liu	H6-60	X			
C. L. Leung	B1-55	X			
T. W. Fletcher	H6-60	X			
B. J. Harp	H6-60	X			
W. R. Wrzesinski	H6-60	X			
S. M. Barnes	17-A	X			
R. L. Garrett	H3-25	X			
D. C. Larsen	H3-20	X			
D. M. Busche	17-A	X			
D. J. Washenfelder	R2-53	X			
N. W. Kirch	R2-58	X			
R. M. Kacich	14-3B	X			